

ELASTORESISTIVITY AS A PROBE OF ELECTRONICALLY
DRIVEN ROTATIONAL SYMMETRY BREAKING AND ITS
APPLICATION TO THE HIDDEN ORDER STATE IN URu₂Si₂

A DISSERTATION
SUBMITTED TO THE DEPARTMENT OF APPLIED PHYSICS
AND THE COMMITTEE ON GRADUATE STUDIES
OF STANFORD UNIVERSITY
IN PARTIAL FULFILLMENT OF THE REQUIREMENTS
FOR THE DEGREE OF
DOCTOR OF PHILOSOPHY

Maxwell C. Shapiro

May 2016

© 2016 by Maxwell Craig Shapiro. All Rights Reserved.
Re-distributed by Stanford University under license with the author.



This work is licensed under a Creative Commons Attribution-Noncommercial 3.0 United States License.

<http://creativecommons.org/licenses/by-nc/3.0/us/>

This dissertation is online at: <http://purl.stanford.edu/cw977dd4151>

I certify that I have read this dissertation and that, in my opinion, it is fully adequate in scope and quality as a dissertation for the degree of Doctor of Philosophy.

Ian Fisher, Primary Adviser

I certify that I have read this dissertation and that, in my opinion, it is fully adequate in scope and quality as a dissertation for the degree of Doctor of Philosophy.

Theodore Geballe

I certify that I have read this dissertation and that, in my opinion, it is fully adequate in scope and quality as a dissertation for the degree of Doctor of Philosophy.

Srinivas Raghu

Approved for the Stanford University Committee on Graduate Studies.

Patricia J. Gumport, Vice Provost for Graduate Education

This signature page was generated electronically upon submission of this dissertation in electronic format. An original signed hard copy of the signature page is on file in University Archives.

Abstract

Electronic nematic order refers to a phase of matter in which rotational symmetry is broken due to electronic correlations. For a large class of materials (including many cuprate and iron-pnictide superconductors), even though the crystal lattice possesses a certain degree of rotational symmetry at high temperatures, the electronic properties on cooling are much more strongly anisotropic. Such electronic anisotropy generically induces a corresponding structural distortion, however, and it is a challenge to the experimentalist to find appropriate means for differentiating electronically driven phase transitions from other types of structural instabilities.

In this thesis, I have advanced a technique (building on earlier work largely driven by our group) which can directly probe the tendency toward electronic nematic order. Since anisotropic strain acts as a conjugate field to nematic order, a central insight is that a divergence in the associated nematic susceptibility (the linear nematic response to an induced anisotropic strain) on approaching the phase boundary can identify a nematic instability. If the physical quantity chosen to characterize the nematic response is the induced resistivity anisotropy, then probing the nematic susceptibility involves measurement of select components of a fourth-rank tensor called the elastoresistivity.

Advancing the elastoresistivity technique has comprised two parts. First, I have formalized the mathematical description of the elastoresistivity tensor and elucidated its symmetry properties. This formalism involves the first discussion of elastoresistivity for a non-cubic system, inherently includes the presence of a magnetic field, and directly connects select components of the elastoresistivity tensor to order parameters

of continuous phase transitions within a Landau paradigm. Second, given this formalism, I have proposed and demonstrated a new class of elastoresistivity measurements based on transverse resistivity configurations. The transverse elastoresistivity technique confers several experimental advantages over earlier differential longitudinal methods, including direct determination of the induced resistivity anisotropy from a single measurement and minimization of symmetry-admixing errors which complicate symmetry-based statements of an associated order parameter.

In addition to describing an appropriate formalism for elastoresistivity and developing appropriate methods to measure specific components of the elastoresistivity tensor, I have also used elastoresistivity to investigate the electronic nematic properties of URu₂Si₂. This material is a heavy Fermion superconductor whose unconventional superconducting state condenses out of a novel Hidden Order state which has defied comprehensive understanding for over 30 years. Through a series of differential longitudinal and transverse elastoresistivity measurements, I have found evidence that the Hidden Order parameter is a multicomponent vector with a nematic component, the onset of which breaks fourfold rotational symmetry in addition to other symmetries. Preliminary measurements further indicate that this behavior persists to high magnetic fields even as Hidden Order is suppressed to zero temperature. Finally, I have observed a strong dependence of the elastoresistance on sample quality, indicating that while many thermodynamic properties associated with Hidden Order have large experimental signatures, the symmetry properties of Hidden Order are very sensitive to disorder.

Acknowledgements

I have been an extremely fortunate beneficiary of a lot of help and support throughout my thesis work—both at Stanford and at various labs across the world—without which the research presented in this dissertation would not have been possible.

First and foremost, there are not enough nor appropriate words to express the depth of my gratitude to my advisor Ian. I first met Ian as an aspiring undergraduate physics student in Fall 2006, and I still vividly remember my first conversation with him in my freshman cafeteria—we began with pleasantries, but the discussion quickly turned to his own research and his broader physics interests. His descriptions and excitement were simultaneously fascinating and contagious, and this is what motivated me to seek out a research opportunity under his guidance as an undergrad and to stay in his group for graduate school. Ian is authentic, deep, and inquisitive, a man of character who leads through his own professionalism and diligence and who correspondingly inspires and receives the best out of his students and those around him. He is also an extremely kind and generous person, one who is not above inviting a dispirited senior graduate student into his home to cook him dinner for no other reasons than it was a Monday and “You look like you need a meal.” I am very lucky and honored to have been a member of your group.

Ian has fostered a vibrant, productive, and fun lab environment. Since there is no fair way to organize this section, let’s do this chronologically in the order I met each of my colleagues. I am especially indebted to Eric, James, and Scott for imparting to me whatever experimental lab knowledge I have. Even though Eric is a Dodger fan who called me out in his thesis acknowledgement for talking too much about baseball and Bob Dylan, I am extremely grateful for his mentorship in the lab

and his friendship outside it. Despite being a fancy-pants Berkeley professor, James has always been extremely kind and warm—a vast repository of physics knowledge (still can't thank you enough for the qual guidance!), an enthusiastic fellow Bay Area sports fan, and someone who I have enjoyed befriending as much as I have enjoyed working alongside (to his chagrin, with a CeeLo Green musical ambience). Scott taught me what it means to be an experimentalist (the “Scott Riggs” is still a unit of magnet time fortitude), but just as important has been his personal friendship. I will forever cherish our times in the lab together (although if you change another furnace temperature setting to 801 C, I swear...), and I look forward to hanging with you more now that you're back in the Bay. All of the elasto-resistivity work I have done stands on the shoulders of the original work done by Jiun-Haw; it has been a great privilege to collaborate both daily and during magnet time with you, and I wish you the best in Washington. I had the longest overlap with Hsueh-Hui and Paula—together, you both made the lab a very special place to come to every day. Although we may never uncover the mystery of salty beans, ni es probable que enseñaré cómo se baila el reguetón, thank you both for your occasional commiseration, your frequent jokes, and your timeless friendship. It still bemuses me that I was tasked with mentoring Alex—there was an immediate and obvious knowledge asymmetry that made it pretty easy for the student to surpass the teacher. Thanks for rotating back into the lab, for being a fellow group theory crusader, and for your ongoing help and friendship (and also for the sweet Gunners jersey). Elliott has been a really great addition to the group; whether we are talking about physics or basketball or life, our conversations are always fun and enlightening. The lab is in great hands with you and Alex now as the two most senior graduate students. Philip K. Walmsley (a.k.a. P. K. Dubs)—professionally and personally, it's been real. Thank you for your dissertation-writing and end-of-thesis-related wisdom, for your friendship generally, and for teaching me that being a physicist doesn't preclude being a great soccer player and jazz musician. To all of you—and also Johanna, Simon, Harlyn, Felipe, Chris, Patrick, and Josh—thanks for being my Fisher group family.

I would like to thank Ted Geballe, Srinivas Raghu, Aharon Kapitulnik, and Steve Kivelson for their yeoman's work in serving on my committee, and to Ted and Sri

additionally for being on my reading committee. Ted has been a personal inspiration to me; along with Ian, I don't think I have ever met anyone who loves physics so much. Thank you for your friendship and generosity, for introducing me to Rohit Dilip, and for all that you have done to make it possible to do research in this fantastic department. My grad school trajectory changed dramatically upon collaborating with Sri about the original URS elasto-resistance data; thank you for your help and discussions over the years, which have always been elucidating and engaging.

I would be remiss if I failed to acknowledge the myriad of collaborators who enabled this thesis work. Thank you to Ryan Baumbach (then at Los Alamos National Laboratory, now at the NHMFL in Tallahassee), Eric Bauer (LANL), Sheng Ran (UCSD), and Brian Maple (UCSD) who grew the URu_2Si_2 samples, without whom this work very literally would not be possible. Special thanks to Ross McDonald (NHFML in Los Alamos), Dave Graf (NHFML in Tallahassee), Ju-Hyun Park (NHMFL in Tallahassee), Tim Murphy (NHMFL in Tallahassee), and all of the other scientists and staff at the Mag Labs who were essential to being able to do the high field experiments—these people are what make both of the high field labs into world class facilities that are wonderful places to do science. On the theory side, along with Sri, Akash Maharaj worked out the formalism predicting the heat capacity-like anomaly in the nematic susceptibility prior to seeing the data; aside from being an amazing scientist, Akash is someone who I hope is a lifelong friend. I'm very glad I wore my Barça jersey to our initial meeting, and my only regret is that we didn't meet sooner. Akash also introduced me to Patrik Hlobil (visiting scientist at Stanford from Karlsruhe), who, aside from teaching me most of what I know about symmetry and fourth-rank tensors, was always a source of entertainment. I'm very glad to call Patrik my friend.

Thanks to Lina Alsibai, Larry Candido, Mark Gibson, Margo Holley, Bob Jones, Sybille Katz, Claire Nicholas, Corrina Peng, Paula Perron, Arturas Vailionis, Alison Veith, Dora Yu, and all of the many other Applied Physics, GLAM, and SLAC staff who helped me over the years. You all are truly the backbone of the research enterprise, and your help with all of the administrative, financial, and scientific tasks made it possible for me to do my thesis work.

Whatever semblance of sanity I have was maintained by the support of many friends, both Stanford-affiliated and not. A brief list: Urusa Alaan, Santhi Analytis, Nicholas Breznay, David Bull, Ingmar Burstel, Emma Callister-Walmsley, Jimmy Chion, Elizabeth Colbert, Amelie Ehrhard, Nils Engelsen, Hannah Engholm, Jimmy Grayson, Natasha Holmes, Helen Howard, Michael Howard, Katja Kowalski, Rajiv Krishnakumar, Ryan Madsen, Akash Maharaj, Mirage Marrou, Tyler Merz, Rick Pam, Byron Philhour, David Ramirez, Aaron Rosenberg, Jared Salin, Elizabeth Schemm, Jeffrey Schox, Eric Spanton, Chris Stiedemann, Dickson Thian, Vijay Thirumalai, Zoe Unruh, Yonas Yemane, Lucas Zipp, Zahara Zipp, and so many others that I have embarrassingly left off with apologies. Your friendships mean more to me than I can adequately express.

Finally, but certainly not least, I would like to thank my family, whose importance needs no justification: Merle Shapiro (a.k.a. Mom), Sandy Shapiro (a.k.a. Dad), Jesus Portillo, Kasa Cotugno, Michaeline Kiss, Leonard Page, Ann Zuppann, Katie Zuppann, Jeffrey Tolin, Eve Tolin, Marc Goldman, Susan Goldman, Steve Shapiro, and everyone else. This thesis is also dedicated to the loving memory of Milly Shapiro: ¡Viva la Rally Dog!

Contents

Abstract	v
Acknowledgements	vii
1 Introduction and Background	1
1.1 Organizing Principles in Condensed Matter Physics	1
1.2 Electronic Nematic Order	6
1.3 Elastoresistivity as a Probe of Nematic Susceptibility	10
1.4 Hidden Order in URu ₂ Si ₂	12
1.4.1 Hidden Order, Magnetism, and Time-Reversal Symmetry . . .	16
1.4.2 Hidden Order and Translational Symmetry	18
1.4.3 Hidden Order and Point Group Symmetry	23
1.5 Thesis Layout	26
1.A Mulliken Symbols	27
2 Symmetry Constraints on the Elastoresistivity Tensor	32
2.1 Introduction	32
2.2 Definition and Inherited Symmetries	34
2.2.1 Directly Inherited Symmetries	35
2.2.2 Point Group Symmetry Constraints	36
2.3 Elastoresistivity Tensor for D_{4h}	41
2.4 Connection to Thermodynamic Susceptibilities	42
2.5 Measurements of Additional Coefficients	48
2.6 Conclusion	49

3	Differential Longitudinal and Transverse Elastoresistivity	50
3.1	Introduction	50
3.2	Coordinate Frames and the Elastoresistivity Tensor	55
3.3	Differential Longitudinal Configuration for Probing Nematic Susceptibility in D_{4h}	58
3.3.1	Ideal Configuration	58
3.3.2	Sources of Error	60
3.4	Transverse Configuration for Probing Nematic Susceptibility in D_{4h}	66
3.4.1	Ideal Configuration	66
3.4.2	Sources of Error	70
3.5	Transverse Elastoresistivity Measurements of BaFe_2As_2	74
3.5.1	Experimental Methods	74
3.5.2	Results	76
3.6	Conclusion	83
3.A	Elastoresistivity Tensor for D_{4h} and Transformation Properties	84
3.B	Quantifying Current and Strain Alignment Errors	88
3.C	Quantifying Strain Magnitude Errors	90
3.D	Isolating Transverse Elastoresistivities in a Longitudinally-Contaminated Elastoresistance Measurement	94
3.E	Evaluating Goodness of Fit of Curie-Weiss Model to the Measured Elastoresistivity Coefficient $2m_{xy,xy}$	99
4	Evidence for a Nematic Component to the Hidden Order Parameter in URu_2Si_2 from Differential Elastoresistance Measurements	103
4.1	Introduction	103
4.2	Results	106
4.3	Discussion	110
4.4	Methods	114
4.A	Nematic Susceptibility: Theory	115
4.A.1	Electronic Nematic Transition	116

4.A.2	Nematic \times (?) Symmetry	117
4.B	Crystal Growth	128
4.C	Elastoresistance Measurements	130
4.D	Proximity to Strain-induced Transition	131
4.E	Curve Fitting	136
4.E.1	Curie-Weiss Fit	136
4.E.2	General Power Law Fit	139
4.F	Nonlinear Elastoresistance Near T_{HO}	141
5	Additional Elastoresistivity Measurements on URu₂Si₂	145
5.1	Effect of Sample Quality on Elastoresistivity of URu ₂ Si ₂	145
5.2	Transverse Elastoresistivity Measurements on URu ₂ Si ₂	149
5.3	Magnetic Field Dependence of Elastoresistivity in URu ₂ Si ₂	154
6	Concluding Remarks and Future Outlook	160
6.1	Elastoresistivity Technique: Current Status	161
6.2	Hidden Order in URu ₂ Si ₂ : Current Status	162
6.2.1	Hidden Order and Fourfold Rotational Symmetry	162
6.2.2	Hidden Order and Time-Reversal Symmetry	166
6.2.3	Final Conclusions	167
	Bibliography	169

List of Tables

1.1	Possible \vec{Q}_C Hidden Order Parameters	22
1.2	Character Table for D_{4h}	27
2.1	Elastoresistivity Symmetry Properties	40
2.2	Irreducible Representations of D_{4h} with Representations in Strain	46
3.1	Fit Parameters from Transverse, Differential Longitudinal, and Modified Montgomery Methods	82
4.1	URu ₂ Si ₂ Sample Information (Dimensions in mm)	128

List of Figures

- 1.1 Schematic illustration of the isotropic liquid to nematic liquid crystal phase transition. In the high temperature isotropic liquid phase, the kinetic energy of the system dominates, favoring a configuration in which the molecules collectively display neither translational nor rotational order. On cooling, the molecules gain energy by spontaneously aligning along a preferred axis, thereby breaking the rotational symmetry of the disordered phase. 7
- 1.2 Schematic Fermi surface distortions in D_{4h} . For a quasi-2D tetragonal material, the electronic analog to the isotropic liquid to nematic liquid transition comprises a Fermi surface distortion in which the primary fourfold (C_4) rotational symmetry is broken. Such a distortion could be driven by electronic correlations (e.g., a Pomeranchuk instability) or by a structural distortion which is then reflected in the electronic structure due to electron-lattice coupling. There are two distinct ways in which the primary C_4 rotational symmetry could be relaxed in D_{4h} : (a) a B_{1g} distortion, in which the diagonal in-plane mirror symmetries are broken in addition to C_4 rotational symmetry; (b) a B_{2g} distortion, in which the secondary mirror symmetries are broken in addition to C_4 rotational symmetry. 9

1.3 (a) Reproduced from Tonegawa *et al.* [21]. At room temperature, URu₂Si₂ crystallizes in the ThCr₂Si₂ (*I4/mmm*) body-centered tetragonal crystal structure (with lattice parameters $a \approx 4.13 \text{ \AA}$, $c \approx 9.59 \text{ \AA}$ [11]). This layered structure consists of uranium spacer atoms situated between layers of ruthenium-silicon tetrahedra. The point group at each uranium site is D_{4h} . (b) Reproduced from Palstra *et al.* [11]. On cooling URu₂Si₂ in zero magnetic field, the specific heat features an abrupt anomaly at $T_{\text{HO}} \approx 17.5 \text{ K}$. Measuring the Sommerfeld coefficient γ admits an effective mass estimate (relative to the bare electron mass m_e) of $m^* \approx 50m_e$ [13], intermediate between most transition metals ($m^* \lesssim 10m_e$) and typical heavy fermion systems ($m^* \gtrsim 200m_e$). The heat capacity anomaly also corresponds to an entropy change (per formula unit) $\Delta S = \int_0^{T_{\text{HO}}} (\Delta C/T) dT \approx 0.2R \ln 2$, which, if magnetic in origin, would imply a magnetic moment that should be detectable by magnetic probes. (c) Reproduced from Kasahara *et al.* [22]. $T-H$ and $T-P$ phase diagrams for URu₂Si₂, illustrating how both a c -axis oriented magnetic field and hydrostatic pressure can suppress Hidden Order.

15

1.4 (a) Reproduced from Ikeda *et al.* [34]. Calculations of the paramagnetic (i.e., $T > T_{\text{HO}}$) Fermi surface in URu₂Si₂ by density functional theory. The Fermi surface is well-nested by the commensurate wave vector $\vec{Q}_C = (001)$, which connects the largest electron pocket (centered around the Γ point in the body-centered tetragonal Brillouin zone) with the largest hole pocket (centered around the Z point). The Fermi surface is colored by the z -component of the angular momentum j_z ; it is evident that \vec{Q}_C connects portions of the Fermi surface dominated by electrons/holes with $j_z = \pm 5/2$. The nested structure of the Fermi surface indicates that URu₂Si₂ has inherent tendencies to antiferroic order characterized by \vec{Q}_C ; it is then unsurprising that both Hidden Order and the pressure-induced antiferromagnetic phase both manifest as \vec{Q}_C orders which double the unit cell along the tetragonal c -axis. (b) Reproduced from Palstra *et al.* [37]. Temperature dependence of the in-plane and out-of-plane resistivities spanning T_{HO} , evincing the opening of an electronic energy gap on entering the Hidden Order state. When Hidden Order onsets, the Fermi surface gets backfolded by \vec{Q}_C . Correspondingly, the Γ and Z points of the original body-centered tetragonal Brillouin zone become equivalent (transforming to the Γ point in the new simple tetragonal Brillouin zone) and a significant portion ($\approx 40\%$ [12]) of the Fermi surface is lost. 20

1.5 Reproduced from Suzuki *et al.* [51]. Schematic illustration of an antiferro- $E_g^-(\vec{Q}_C)$ order arising from a magnetic multipole. The onset of a finite ordered magnetic multipole (with components oriented along the 45° direction relative to the high temperature primitive cell) results in a small orthorhombicity and doubles the size of the ordered primitive magnetic unit cell along the c -axis. 23

1.6 (a) Reproduced from Okazaki *et al.* [52]. Magnetic torque τ dependence on an in-plane angle ϕ (defined as the angle between the crystal axes and an applied 4 T magnetic field) on cooling through T_{HO} . Resolving the total torque signal $\tau(\phi)$ into its Fourier components $\tau_{2n\phi}$, it is observed that, for $T > T_{\text{HO}}$, the twofold term $\tau_{2\phi}$ is absent and $\tau(\phi)$ is dominated by the fourfold term $\tau_{4\phi}$, consistent with the full fourfold symmetry of the underlying tetragonal lattice. However, on cooling to temperatures $T < T_{\text{HO}}$, the twofold term $\tau_{2\phi}$ clearly onsets, suggesting that fourfold rotational symmetry has been broken. The twofold term follows the functional form $\tau_{2\phi} = A_{2\phi}(T) \cos 2\phi$, indicating that the off-diagonal susceptibility χ_{ab} becomes nonzero (i.e., the rotational symmetry breaking is a B_{2g} type distortion). Notably, $\tau_{2\phi} \neq 0$ only in the smallest samples measured, which the authors interpret in terms of pinned domains due to underlying features of the crystal (such as internal stress or disorder). (b) Reproduced from Tonegawa *et al.* [21]. The temperature dependence of the (880) Bragg peak as measured by high resolution X-ray scattering. A single peak is observed in the high temperature regime, as expected for a tetragonal system; however, the peak splits on cooling through T_{HO} , directly resolving an orthorhombic distortion in the absence of a symmetry breaking field. The orthorhombic distortion is consistent with the twofold torque measurements in at least two ways: 1) the resolved orthorhombicity is of a B_{2g} type, with the high temperature $I4/mmm$ space group lowering to the $Fmmm$ space group (with the in-plane primitive axes rotated by 45°) in the Hidden Order state; 2) the small orthorhombicity (of the order of 10^{-5} , much smaller than that of the ordered orthorhombic phase of the BaFe_2As_2 -based superconductors) can only be resolved for the highest RRR samples, with samples of $\text{RRR} \approx 10$ displaying no resolvable orthorhombic distortion. 25

2.1 Schematic illustration of an arbitrary shearless strain in D_{4h} as decomposed in terms of three irreducible components:

$$\begin{pmatrix} \epsilon_{xx} & 0 & 0 \\ 0 & \epsilon_{yy} & 0 \\ 0 & 0 & \epsilon_{zz} \end{pmatrix} = \epsilon_{A_{1g,1}} \begin{pmatrix} 1 & 0 & 0 \\ 0 & 1 & 0 \\ 0 & 0 & 0 \end{pmatrix} + \epsilon_{A_{1g,2}} \begin{pmatrix} 0 & 0 & 0 \\ 0 & 0 & 0 \\ 0 & 0 & 1 \end{pmatrix} + \epsilon_{B_{1g}} \begin{pmatrix} 1 & 0 & 0 \\ 0 & -1 & 0 \\ 0 & 0 & 0 \end{pmatrix},$$

where $\epsilon_{A_{1g,1}} = \frac{1}{2}(\epsilon_{xx} + \epsilon_{yy})$, $\epsilon_{A_{1g,2}} = \epsilon_{zz}$, and $\epsilon_{B_{1g}} = \frac{1}{2}(\epsilon_{xx} - \epsilon_{yy})$. The gray parallelepiped represents a crystalline sample; the yellow regions represent electrical contacts used for transport measurements. 45

- 3.2 Schematic diagram illustrating the relative orientations of the crystal (unprimed), normal strain (primed), and transport (double primed) coordinate frames. The crystal and normal strain frames are related by a relative angle ϕ about their mutual z/z' axis, while the crystal and transport frames are related by a relative angle θ about their mutual z/z'' axis. 57
- 3.3 Longitudinal elasto-resistivity configurations for extracting (a) $m_{xx,xx} - m_{xx,yy}$ (with $(\theta, \phi) = (0, 0)$) and (b) $2m_{xy,xy}$ (with $(\theta, \phi) = (-\pi/4, \pi/4)$), which characterize the B_{1g} and B_{2g} irreducible representations of $m_{ij,kl}$ in D_{4h} . In (a), one measures the differential longitudinal resistive response to strain $(\Delta\rho/\rho)_{(xx)''} - (\Delta\rho/\rho)_{(yy)''}$ to a strain $\epsilon_{(xx)'} - \epsilon_{(yy)'}$ with the transport, crystal, and normal strain frames all coincident; the differential longitudinal elasto-resistivity then yields the elasto-resistivity coefficients $m_{xx,xx} - m_{xx,yy}$. In (b), one measures the differential resistive response to strain $(\Delta\rho/\rho)_{(xx)''} - (\Delta\rho/\rho)_{(yy)''}$ to a strain $\epsilon_{(xx)'} - \epsilon_{(yy)'}$ with the crystal frame oriented at the angles $(\theta, \phi) = (-\pi/4, \pi/4)$ relative to the transport and normal strain frames; the differential longitudinal elasto-resistivity then yields the elasto-resistivity coefficient $2m_{xy,xy}$ 59
- 3.4 Schematic diagrams illustrating transverse elasto-resistivity configurations for extracting (a) $m_{xx,xx} - m_{xx,yy}$ (with $(\theta, \phi) = (\pi/4, 0)$) and (b) $2m_{xy,xy}$ (right, with $(\theta, \phi) = (0, \pi/4)$). In (a), one measures the sum of the transverse resistive response to strain $(\Delta\rho/\rho)_{(xy)''} + (\Delta\rho/\rho)_{(yx)''}$ to a strain $\epsilon_{(xx)'} - \epsilon_{(yy)'}$ with the transport frame rotated by $\pi/4$ radians relative to the crystal and normal strain frames; the summed elasto-resistivity then yields the elasto-resistivity coefficients $m_{xx,xx} - m_{xx,yy}$. In (b), one measures the sum of the transverse resistive response to strain $(\Delta\rho/\rho)_{(xy)''} + (\Delta\rho/\rho)_{(yx)''}$ to a strain $\epsilon_{(xx)'} - \epsilon_{(yy)'}$ with the normal strain frame rotated by $\pi/4$ radians relative to the crystal and transport frames; the summed transverse elasto-resistivity then yields the elasto-resistivity coefficient $2m_{xy,xy}$ 67

3.5 Transverse elasto-resistivity configurations for extracting (a) $m_{xx,xx} - m_{xx,yy}$ (with $(\theta, \phi) = (\pi/4, 0)$) and (b) $2m_{xy,xy}$ (with $(\theta, \phi) = (0, \pi/4)$). Mounted in these configurations and in the presence of a finite field, the appropriate elasto-resistivity coefficients can be measured from $(\Delta\rho/\rho)_{(xy)''}(H_z) + (\Delta\rho/\rho)_{(xy)''}(-H_z)$; in zero field, the same coefficients can be extracted with a single measurement $(\Delta\rho/\rho)_{(xy)''}(H_z = 0)$. The primary advantage of the transverse technique is that one can measure the same elasto-resistivity coefficients from a single mounting without A_{1g} contamination. 69

3.6 Schematic diagram showing contact geometry for a practical transverse elasto-resistance measurement. Contacts 1 and 2 are used to measure $R_{(xy)''}$; however, partial misalignment can lead to $R_{(xx)''}$ contamination in a nominal $R_{(xy)''}$ measurement. This contamination can be accounted for by subtracting out a down-weighted longitudinal contribution, with the down-weighting given by the factor Δ_ℓ . Δ_ℓ is defined as the ratio of the misalignment distance l_{12} to the distance between longitudinal contacts l_{13} , which is related to the ratio of the transverse and longitudinal voltages on a free-standing crystal: $\Delta_\ell \equiv l_{12}/l_{13} = V_{(xy)''}(H=0, \text{free-standing})/V_{(xx)''}(H=0, \text{free-standing})$ (see Appendix 3.D). This subtraction procedure is analogous to the antisymmetrization procedure that is used for Hall effect measurements. To use this geometry to probe $\chi_{B_{1g}}$ or $\chi_{B_{2g}}$ requires mounting the crystal such that $(\theta, \phi) = (\pi/4, 0)$ or $(\theta, \phi) = (0, \pi/4)$, respectively, as described in the main text. 73

3.7 Photograph showing a BaFe_2As_2 crystal affixed to the surface of a PZT stack and mounted in the transverse elasto-resistivity configuration $(\theta, \phi) = (0, \pi/4)$, appropriate for measuring $2m_{xy,xy}$ ($\propto \chi_{B_{2g}}$). Contacts 1, 2, and 3 are labeled with reference to Figure 3.6. The twisted pairs used for performing the voltage measurements are evident. 75

- 3.8 Resistance measurements for the BaFe₂As₂ sample showing R_{xx} (top panel), R_{xy} (middle panel), and the ratio $\Delta_\ell \equiv R_{xy}/R_{xx}$ (bottom panel). For temperatures above the coupled structural and magnetic transition at $T_{S,N}$ (vertical dashed gray line), Δ_ℓ is small and temperature-independent; by taking the average value for temperatures > 150 K, we estimate $\Delta_\ell \sim 4.1 \pm 0.1\%$ (horizontal dashed blue line). Since this measurement was performed on a free-standing (unglued) sample in zero magnetic field, the measured R_{xy} in the tetragonal state is due to R_{xx} contamination from contact misalignment; Δ_ℓ characterizes the physical extent of this misalignment. 77
- 3.9 Representative data for BaFe₂As₂ showing strain-induced changes in resistance $\Delta R_{(xy)''}$, $\Delta R_{(xx)''}$, and $\Delta_\ell \Delta R_{(xx)''}$ at a temperature of 100 K as a function of the voltage applied to the PZT stack. Values of Δ_ℓ are extracted from Figure 3.8 as described in the main text. In order to correct for ρ_{xx} contamination, the relatively small amount $\Delta_\ell \Delta R_{(xx)''}$ is subtracted from $\Delta R_{(xy)''}$ 78
- 3.10 Representative data showing the temperature dependence of the elastoresistive response of BaFe₂As₂ in the transverse configuration (θ, ϕ) = $(0, \pi/4)$ as a function of the induced shear strain ($\epsilon_{xy} = -\frac{1}{2}(\epsilon_{(xx)'} - \epsilon_{(yy)'})$) experienced by the crystal. This is the appropriate configuration for measuring $2m_{xy,xy}$ ($\propto \chi_{B_{2g}}$). Slopes have been corrected for ρ_{xx} contamination, as described in the main text and Appendix 3.D. All responses were linear in the applied strain for all measured temperatures. 79
- 3.11 Temperature dependence of the elastoresistivity coefficient $2m_{xy,xy}$ of BaFe₂As₂ from the transverse configuration. Error bars represent 95% confidence intervals from the linear fits to the elastoresistive slopes at each temperature. The vertical dashed bar marks the coincident structural and magnetic transition temperature $T_{S,N}$ of the sample. . 80

- 3.12 Temperature dependence of $[-2(m_{xy,xy} - m_{xy,xy}^0)]^{-1}$, proportional to the inverse nematic susceptibility $\chi_{B_{2g}}^{-1}$ in this configuration. Error bars represent 95% confidence intervals from both the linear fits to the elastoresistive slopes at each temperature and the estimation of $2m_{xy,xy}^0$. The red line shows a linear fit (i.e., Curie-Weiss functional form) between 136 K and 220 K, with fit parameters given in Table 3.1. The vertical dashed line marks the coincident structural and magnetic transition temperature $T_{S,N}$ of the sample ($T_{S,N} = 134$ K). 82
- 3.13 (a) Schematic diagram illustrating contact misalignment in a transverse measurement. The transverse voltage is to be measured between contacts 1 and 2, while the longitudinal voltage can be measured between contacts 1 and 3. The degree of transverse contact misalignment (horizontal offset between contacts 1 and 2) has been greatly exaggerated for pedagogical purposes. Contact 4 (dark gray) is a hypothetical contact which is perfectly vertically aligned with contact 2, which means that the relative voltages between these contacts $V_2 - V_4 = 0$ in zero magnetic field for zero strain. (b) Primitive crystal frame and its relative alignment to the transport frame. 95
- 3.14 Bullseye plot of the $2m_{xy,xy}$ elastoresistivity coefficient, illustrating the minimized RMSE from the Curie-Weiss form as a function of a varying temperature window. While an ideal fit over a particular range would produce a local minimum in the RMSE in that range and hence a bullseye-like pattern in the contour map, no such bullseye pattern is observed for the present data. This indicates that there is no “optimal” temperature range over which the data best conforms to the Curie-Weiss form. Without such a best-fit range, we opt to fit over the maximal range from 220 K (the highest temperature measured) down to 136 K (just above $T_{S,N} \approx 134$ K). 100

3.15 Contour map of estimated Weiss temperatures θ as a function of a varying temperature window. The star in the top-left region again corresponds to the maximal temperature range, which we use due to the absence of any particular best fit range. The distribution of Weiss temperatures is heavily concentrated around ~ 120 K for the ranges close to the maximal window, which is the value of θ quoted in the main text. 102

4.1 **Measurement of elastoresistivity coefficients.** Anisotropic strain is achieved by gluing thin crystals of URu₂Si₂ to the side of a PZT piezoelectric stack such that ϵ_{xx} is opposite in sign to ϵ_{yy} . The Cartesian axes are defined relative to the piezo stack itself, with the x -(y -)direction parallel to the short (long) axis of the piezo. (a) Photograph of [100] oriented URu₂Si₂ crystals mounted in the $(\frac{\Delta R}{R})_{yy}$ and $(\frac{\Delta R}{R})_{xx}$ directions on the surface of a PZT piezoelectric stack. Strain gauges mounted on the opposite face of the piezo stack measure ϵ_{yy} and ϵ_{xx} , which are related by the effective Poisson ratio of the PZT stack, $\nu_p \equiv -\frac{\epsilon_{xx}}{\epsilon_{yy}}$. Panels (b) and (c) show representative $(\frac{\Delta R}{R})_{yy}$ elastoresistance data for five different temperatures as a function of ϵ_{yy} for $[1\bar{1}0]$ and $[100]$ orientations, respectively. Data are plotted for both warming and cooling cycles and are identical within the resolution of the experiment. The resistive response to anisotropic strain is considerably larger (by a factor of ~ 4) for measurements made in the $[1\bar{1}0]$ direction compared to the $[100]$ direction. 107

4.2 Temperature dependence of the elastoresistivity coefficients.

The $2m_{66}$ (red circles) and the $m_{11} - m_{12}$ (cyan diamonds) elastoresistivity coefficients reveal a large directional anisotropy, with $2m_{66}$ reaching very large values close to and below the Hidden Order transition. The dashed vertical black line indicates the Hidden Order transition, $T_{HO} = 17.17$ K, determined from the peak in the temperature derivative of the resistivity. The green curve is a fit of $2m_{66}$ to a Curie-Weiss temperature dependence $2m_{66} = \frac{C}{T-\theta} + 2m_{66}^0$ from 60 K to 30 K, as described in the main text. The fit is extrapolated below 30 K to emphasize deviations from Curie-Weiss behavior below this temperature. The best-fit values for the parameters are $C = 375$ K, $\theta = 15.2$ K, and $2m_{66}^0 = -7.9$. The inset shows $(2m_{66} - 2m_{66}^0)^{-1}$ versus temperature, with $2m_{66}^0$ determined from the green fit in the main figure. 109

4.3 Temperature dependence of $2m_{66}$ and heat capacity near T_{HO} .

Temperature dependence of (a) the $2m_{66}$ elastoresistivity coefficient, (b) the in-plane resistivity ρ , (c) the temperature derivative of the in-plane resistivity $\frac{d\rho}{dT}$, and (d) the electronic specific heat in the immediate vicinity of T_{HO} , all measured on the same $[1\bar{1}0]$ oriented crystal. The phonon component to the specific heat was subtracted out by using ThRu_2Si_2 , such that $C_{elec}(\text{URu}_2\text{Si}_2) = [C(\text{URu}_2\text{Si}_2) - C(\text{ThRu}_2\text{Si}_2)]$. Data for all four panels are plotted as a function of $T - T_{HO}$, with the absolute temperature scale for the transport measurements shown on the upper axis. The temperature range in absolute units for all four plots is the same. The position ($T_{HO} = 17.17$ K) and width of the peak in $2m_{66}$ exactly match that of $\frac{d\rho}{dT}$, while there is a slight temperature offset ($T_{HO} = 17.47$ K) relative to the heat capacity measurement (but with the same width). Differences between T_{HO} obtained from transport and electronic specific heat are attributed to slight differences in thermometry between the two measurements. 111

4.4	In-plane resistivity as a function of temperature for samples detailed in Supplementary Table 4.1. Sample 1 [100] and Sample 3 [1 $\bar{1}$ 0] were used for the elastoresistivity measurements in the main text. Sample 2 [100] was also measured and showed the same temperature dependence in $m_{11} - m_{12}$ as Sample 1.	129
4.5	Temperature dependence of the individual elastoresistance measurements (slopes of the normalized resistivity change to strain) for both the $(\frac{\Delta R}{R})_{xx}$ (black boxes) and $(\frac{\Delta R}{R})_{yy}$ (gray stars) configurations for all three samples. (a) [1 $\bar{1}$ 0] oriented crystal. Along with a very large elastoresistance signal ($(\frac{\Delta R}{R})_{xx}, (\frac{\Delta R}{R})_{yy} \gg 1$), there is a pronounced difference between the individual orthogonal configurations. Because the $(\frac{\Delta R}{R})_{xx}$ orientation has an opposite sign to that of $(\frac{\Delta R}{R})_{yy}$, the difference, which is proportional to the nematic susceptibility, is larger than either individual orientation. (b, c) [100] oriented crystals. There is a decidedly smaller elastoresistance signal in each individual measurement and a correspondingly smaller difference between the $(\frac{\Delta R}{R})_{xx}$ and $(\frac{\Delta R}{R})_{yy}$ configurations. Near T_{HO} , the [100] data resemble those from the [1 $\bar{1}$ 0] sample, likely reflecting slight sample misalignment on the piezo stack. Sample 2 and Sample 3 are the samples that appear in the main text.	132
4.6	In-plane resistivity as a function of temperature on [1 $\bar{1}$ 0] Sample 3, both free-standing and glued to the piezo stack with zero volts applied. The slight difference between the curves is attributed to differential thermal contraction of the PZT and the URu ₂ Si ₂ sample. There is no discernible shift in T_{HO} between the two curves.	137
4.7	A plot of the elastoresistivity coefficient $2m_{66}$ as a function of temperature. The data were fit to (4.E.1) with $\alpha = 1$. The red curve is a fit from 18 K to 60 K, the green from 30 K to 60 K, and the blue from 42 K to 60 K. The inset shows the reduced χ^2 for temperature windows of varying sizes (from a lower cut-off temperature to 60 K). The best fit is over the region 30 K to 60 K, as defined by χ_{red}^2 closest to 1. . .	138

4.8 Inverse elastoresistivity coefficient (with a subtracted temperature-independent term) versus temperature. For the case where $2m_{66}$ obeys a power law divergence with a critical exponent α , we should observe a curve that is linear in temperature. This linear relationship is not observed for any α spanning the range $0.5 \leq \alpha \leq 3$ over the entire temperature window. The data can be fit to a Curie-Weiss form over a smaller temperature range. Inset: Zoom-in version on the $\alpha = 0.5$ and $\alpha = 1$ curves, highlighting nonlinear behavior. The $\alpha = 0.5$ curve is rescaled by a factor of 50 for illustrative purposes. 142

4.9 (a) $(\frac{\Delta R}{R})_{yy}$ as a function of applied strain ϵ_{yy} around the Hidden Order transition for Sample 3 ($[1\bar{1}0]$). There is a clear sign change in the slope of $(\frac{\Delta R}{R})_{yy}$ at $T_{HO} = 17.17$ K. In a small temperature range (± 0.15 K) about T_{HO} , the resistive response to applied strain is nonlinear. The slopes in (a) are fit and plotted in (b) for different strain regions. Black points refer to the full strain region of -50 V to $+150$ V (which correspond to strains $\sim -0.25 \times 10^{-4}$ to 1×10^{-4}). Orange points in (b) are from slopes fit over a 0 V to 150 V strain region in (a) (strains of ~ 0 to 1×10^{-4}). Blue points in (b) are from slopes fit over a -50 V to 0 V strain region in (a) (strains of $\sim -0.25 \times 10^{-4}$ to 0). Red points in (b) are from slopes fit over a -50 V to 50 V region in (a) (strains of $\sim -0.25 \times 10^{-4}$ to 0.25×10^{-4}). Comparing the black points and the red points in (b), it can be seen that the magnitude of the elastoresistivity coefficients are slightly underestimated if the data are fit to a linear function over the entire strain range and overestimated if fitting only the negative strain region. In (c) we plot resistance as a function of temperature for a fixed strain in the $[1\bar{1}0]$ sample (see main text for further details). From the shift in the point of inflection in the resistance, application of $+5 \times 10^{-4}$ strain (red curve) and of -5×10^{-4} strain (green curve) shifts the transition temperature T_{HO} by approximately 100 mK per 10^{-3} of strain. 144

5.1 (a) Temperature dependence of the in-plane resistivity for three separate URu₂Si₂ samples, with contacts oriented along [110]. The quoted RRR value is given by $RRR = R(300 \text{ K})/R(2 \text{ K})$. (b) The elastoresistive response $d(\Delta\rho/\rho)_{yy,[110]}/d\epsilon_{yy}$ for the three samples presented in (a). The elastoresistance for the RRR 970 and the RRR 168 samples both show an anomaly centered at T_{HO} that tracks the heat capacity. For these two samples, T_{HO} occurs at essentially the same temperature, but the magnitude of the elastoresistive response is much smaller for the lower RRR sample. The RRR 7 sample not only shows a smaller elastoresistive response but also displays the anomaly at a slightly lower temperature than the higher RRR samples, in agreement with the published RRR dependence of T_{HO} [90]. 148

5.2 (a) Picture of a mounted sample for transverse elastoresistivity measurements. For the orientation of currents (along [100]) and strains (along [110]) relative to the crystallographic axes, the configuration shown admits measurement of the B_{2g} component of the elastoresistivity tensor. $(\Delta\rho/\rho)_{(xy)''}$ and $(\Delta\rho/\rho)_{(xx)''}$ are simultaneously measured, and the difference (with $(\Delta\rho/\rho)_{(xx)''}$ down-weighted by Δ_ℓ) is related to $2m_{xy,xy}$. (b) Measurement of R_{xy} and R_{xx} on the free-standing crystal (i.e., before mounting to a PZT) in order to extract $\Delta_\ell \equiv R_{xy}/R_{xx}$. $\Delta_\ell \approx 13\%$ is observed to be roughly temperature independent. RRR for this sample is ≈ 240 . As noted in the main text, this relatively low value of RRR is not ideal given the strong dependence of $2m_{xy,xy}$ on RRR (Section 5.1). A further nonideality is associated with the sample geometry, which deviates significantly from a perfect rectilinear shape, potentially affecting symmetry-based conclusions. 151

5.3 (a) Strain-induced resistance changes $\Delta R_{(xy)''}$, $\Delta R_{(xx)''}$, and $\Delta_\ell \Delta R_{(xx)''}$ as a function of voltage applied to the PZT. For the sample measured, $\Delta R_{(xx)''}$ is actually larger than $\Delta R_{(xy)''}$, although the down-weighted contribution $\Delta_\ell \Delta R_{(xx)''}$ is smaller than $\Delta R_{(xy)''}$. This contrasts sharply with the differential longitudinal measurements performed on a higher RRR sample. (b) Representative transverse elastoresistivity measurements of the down-weighted $(\Delta\rho/\rho)_{xy}$ versus strain for a sample of RRR ≈ 240 . These slopes are used to extract the elastoresistivity coefficient $2m_{xy,xy}$. All slopes are observed to be roughly linear in the anisotropic strain at all temperatures except for a very small temperature window of $\approx \pm 150$ mK around T_{HO} . Very close to the Hidden Order transition, the elastoresistive slope changes sign, evincing the anomaly in the nematic susceptibility which follows the heat capacity. The absolute magnitude of the elastoresistive slope is smaller than in the earlier differential longitudinal case, presumably due to the RRR effect. . . . 152

5.4 (a) Temperature dependence of $2m_{xy,xy}$ as extracted from the transverse method for the sample with RRR 240. The anomaly associated with Hidden Order at T_{HO} is evident, but the absolute magnitude of the elastoresistivity coefficient is comparable to the differential longitudinal case for samples with a similar RRR value (see Figure 5.1(b)). (b) Temperature dependence of $d(\Delta\rho/\rho)_{xx,[100]}/d\epsilon_{xy}$ in the transverse method. The qualitative behavior of $d(\Delta\rho/\rho)_{xx,[100]}/d\epsilon_{xy}$ follows nearly exactly with the estimated $2m_{xy,xy}$, with nearly the same values. This is in sharp contrast to the differential longitudinal measurements on higher RRR samples in which $2m_{xy,xy}$ was significantly larger than the isotropic contributions. 153

5.5 Reproduced from Jaime *et al.* [19]. The zero field heat capacity jump in URu₂Si₂ is reminiscent of a mean field second order phase transition. On increasing the magnetic field, the heat capacity anomaly evolves into a sharp first-order-like feature and also shifts downward towards zero temperature. Both of these behaviors are qualitatively followed in the elastoresistance. 155

5.6 (a) Picture of mounted samples for differential longitudinal elastoresistivity measurements in a high magnetic field. For the orientation of currents (along [110]) and strains (along [100]) relative to the crystallographic axes, the configuration shown admits measurement of the B_{2g} component of the elastoresistivity tensor. The top sample corresponds to measurements of $(\Delta\rho/\rho)_{yy,[110]}$, the bottom sample corresponds to measurements of $(\Delta\rho/\rho)_{xx,[110]}$, and the difference is related to $2m_{xy,xy}$. (b) Representative measurements of $(\Delta\rho/\rho)_{yy,[110]}$ versus strain at a magnetic field of $H = 20$ T directed along the crystallographic c -axis. These slopes (and similar ones from measurements of $(\Delta\rho/\rho)_{xx,[110]}$) are used to extract the elastoresistivity coefficient $2m_{xy,xy}(H_z = 20$ T). In agreement with the zero field measurements, all slopes are observed to be linear in the anisotropic strain at all temperatures except for a very small temperature window around T_{HO} . Very close to the Hidden Order transition (which is ≈ 17.5 K in zero field but shifts down in an applied magnetic field), the elastoresistive slope changes sign, evincing the anomaly in the nematic susceptibility which follows the temperature dependence of the heat capacity. 157

5.7 (a) (Top Left) Differential elastoresistance measurements for a range of fields approaching the critical magnetic field of ≈ 35.1 T at which Hidden Order is suppressed. The measurements are proportional to the elastoresistivity coefficient $2m_{xy,xy}$, although the data need to be normalized by $(1 + \nu_p)$ (where ν_p is the Poisson ratio of the PZT) to obtain the exact elastoresistivity coefficient. Both the onset of a resolvable elastoresistive response and the heat capacity anomaly shift downwards in temperature with increasing field. (b) (Top Right) Expanded view of (a) at low temperatures. The differential elastoresistance tracks the field dependence of Hidden Order; furthermore, the height of the anomaly increases with increasing field and the width of the anomaly decreases with increasing field. These observations are consistent with the field dependence of the heat capacity. (c) (Bottom Left) A version of (a) but also including data taken at the critical magnetic field. A large response is observed, but the heat capacity anomaly is harder to resolve because of the sharp first-order nature of the transition and the large negative magnetoresistance of URu₂Si₂ near this field. (d) (Bottom Right) Differential elastoresistance at a base temperature of 1.85 K as a function of magnetic field. The elastoresistance diverges on approaching the critical magnetic field from below, but the signal-to-noise becomes limiting on the high magnetic field side due to the large negative magnetoresistance. 159

Chapter 1

Introduction and Background

In this chapter, the general principles of broken symmetries associated with continuous phase transitions are reviewed within the paradigm of Landau theory. Particular attention is paid to characterizing electronic nematic order via measurements of select elastoresistivity coefficients, which connect to corresponding thermodynamic susceptibilities of a material. In addition, a discussion is given of symmetry constraints on the Hidden Order parameter in URu_2Si_2 as inferred from earlier and concurrent work.

1.1 Organizing Principles in Condensed Matter Physics

Condensed matter physics comprises the study of how large numbers (often of order Avogadro's number) of particles organize themselves collectively when they interact with each other individually. There are countless examples of many-body systems in nature (to wit, a few: phonons in solid state materials, Bose-Einstein condensates in dilute gases, quark-gluon plasmas, cells in biological organisms); condensed matter physics involves studying these systems via a combination of classical mechanics, quantum mechanics, statistical mechanics, thermodynamics, electrodynamics, atomic and molecular physics, and other fields. Even if we perfectly understood all fundamental physical laws underlying these many-body interactions, finding analytical solutions

for the equations of motion of all of the particles would be prohibitively difficult and without obvious practical application; however, we can observe the macroscopic state variables (e.g., entropy, pressure, magnetization, etc.) that characterize a system's ground state. These state variables and their perturbative responses to external fields (e.g., temperature, volume, and magnetic field, respectively, for the the state variables listed above) often distinguish the different states of matter.

One of the most fundamental insights gleaned from condensed matter physics is that conservation laws and broken symmetries dictate a system's macroscopic properties [1]. At sufficiently high temperatures, a system of particles is uniform, isotropic, and disordered—the probability of finding a constituent particle at any point in space is completely independent of the other particles, and the system respects the full translational and rotational symmetry of free space. Conservation laws corresponding to these symmetries (momentum and angular momentum, respectively, for the cases of complete translational and rotation symmetry) then completely determine the equations of motion of the system. As the temperature is lowered, however, the group of particles can minimize their free energy by condensing into states that progressively lower the total symmetry of the system. The equations of motion of the particles abruptly change and, under a set of reasonably broad conditions, the system's low-temperature ground state (in the absence of thermal fluctuations) does not possess all of the symmetries of its underlying Hamiltonian [2]. On cooling, the system undergoes a phase transition.

In the absence of disorder, a symmetry of a system is a binary property of that system, either present or absent. In the context of a phase transition which breaks a symmetry across a phase boundary, the broken symmetry state can be characterized by an order parameter ψ which vanishes in the disordered (fully symmetric) state and assumes a nonzero expectation value which uniquely specifies the ordered state when the symmetry is broken. Often, defining such an order parameter is clear given context; for example, for the case of a paramagnetic-ferromagnetic phase transition, ψ can be taken as the z -component of the magnetization M_z , which characterizes the degree to which time-reversal symmetry is preserved ($M_z = 0$) or broken ($M_z \neq 0$).

Quite generally, requiring the inclusion of the order parameter ψ to specify the

broken symmetry state implies that the free energy is a non-analytic function at the phase transition, with ψ characterizing the degree of non-analyticity. The system's Helmholtz free energy $\mathcal{F}(T, V)$ (the thermodynamic potential which depends on its temperature T and volume V) can, at least in principle, be computed according to

$$\begin{aligned}\mathcal{F}(T, V) &= -\beta^{-1} \ln \mathcal{Z} \\ \mathcal{Z} &= \text{Tr } e^{\beta \hat{H}},\end{aligned}\tag{1.1}$$

where \mathcal{Z} is the system's partition function, \hat{H} is the Hamiltonian of the system, the implicit sum in the trace is performed over all microstates of the system, and where $\beta^{-1} \equiv k_B T$. Explicitly including the order parameter ψ in the free energy as $\mathcal{F}(T, V, \psi)$, we demand that the system minimize its free energy by imposing the equilibrium condition

$$\frac{\partial}{\partial \psi} [\mathcal{F}(T, V, \psi)] = 0.\tag{1.2}$$

Eq. (1.2) implicitly defines ψ as a function of the other state variables, which we can then substitute back into $\mathcal{F}(T, V, \psi)$ to solve for $\mathcal{F}(T, V)$. Above the phase transition temperature, the condition Eq. (1.2) is trivial (since $\psi \equiv 0$), and thus $\mathcal{F}(T, V, \psi) = \mathcal{F}(T, V)$. Below the phase transition temperature, $\psi \neq 0$ and the condition Eq. (1.2) results in a new function $\mathcal{F}(T, V, \psi) = \mathcal{F}'(T, V)$, where in general $\mathcal{F}(T, V) \neq \mathcal{F}'(T, V)$. The result is that $\mathcal{F}(T, V, \psi)$ abruptly changes form across the phase boundary and is thus non-analytic at the phase transition.

Within the Landau paradigm of phase transitions, the non-analytic component of $\mathcal{F}(T, V, \psi)$ is an analytic function of the order parameter ψ which is explicitly constrained by symmetry. In particular, while the system's Hamiltonian \hat{H} and free energy $\mathcal{F}(T, V, \psi)$ are invariant under a group of transformations G , ψ itself is invariant only under a subgroup Y of G (since ψ explicitly breaks certain symmetries of the system at the phase transition). If, for example, G comprises a certain set of symmetries (which may include time reversal symmetry, spatial translation symmetry, p -fold rotational symmetry about different axes, mirror symmetry about different

planes, gauge symmetry, spin rotational symmetry, etc.), ψ will in general only be invariant under a certain subset of these symmetries. That ψ is invariant only under a subgroup of G also restricts the functional form of the ψ -containing terms in $\mathcal{F}(T, V, \psi)$, since the free energy as a whole must remain invariant under all of the symmetry operations in G . For instance, referencing back to the previous example of a paramagnetic-ferromagnetic phase transition where $\psi = M_z$ (the z -component of the magnetization), because the paramagnetic phase possesses time reversal symmetry \mathcal{T} (i.e., $\mathcal{T}[\mathcal{F}(T, V, \psi)] = \mathcal{F}(T, V, \psi)$), $\mathcal{F}(T, V, \psi)$ cannot contain a term of the form wM_z (with w a constant), since such a term changes sign under time reversal (i.e., $\mathcal{T}[wM_z] = -wM_z$).

A complete description of the ordered phase requires specifying the particular subgroup Y of G to which ψ belongs. In general, ψ will transform under an n -dimensional representation of G —that is, if ψ is an n -dimensional vector with components ψ_i ($i = 1, 2, \dots, n$), for each symmetry element g contained in G , we can define a set of matrices $t_{ij}(g)$ such that $t_{ij}(g)\psi_j = \psi_i$. For a particular choice of the $t_{ij}(g)$, the set of all of the chosen $t_{ij}(g)$ matrices forms a particular representation of G . Any set of the components of the order parameter ψ_i that transforms under some representation of G can be decomposed into disjoint subsets that do not mix under the operations of G —that is, by choosing the representation (i.e., the set of $t_{ij}(g)$ mappings) intelligently, the operation of the $t_{ij}(g)$ will only ever send ψ_j to a subset of the n total ψ_i . Each of these disjoint subsets can be labeled by an index ℓ containing k_ℓ elements of the ψ_i , where the action of $t_{ij}(g)$ on ψ_j^ℓ will never send $\psi_j^{\ell_1}$ to a $\psi_i^{\ell_2}$ with $\ell_1 \neq \ell_2$. These k_ℓ elements of ψ_i^ℓ transform among themselves under a k_ℓ -dimensional irreducible representation of G , and the enumeration of all of the possible irreducible representations of G constrain the possible subgroups Y to which ψ can belong.

One experimental method for determining the symmetry character of ψ (i.e., identifying the particular irreducible representation of G to which ψ belongs) is to measure a divergence in the associated thermodynamic susceptibility, which in turn requires an experimental tuning field h that is conjugate to ψ (and therefore admits a bilinearly coupled term in $\mathcal{F}(T, V, \psi)$ of the form $-\lambda\psi h$, where λ is a constant). When a

system undergoes a phase transition, it becomes extremely sensitive to external perturbations of the appropriate symmetry. For temperatures T much larger than the transition temperature T_c , applying a finite value of the conjugate field h will result in the order parameter acquiring a nonzero expectation value (i.e., $h \neq 0$ induces $\langle \psi \rangle \neq 0$). As $T \rightarrow T_c$, the same value of $\langle \psi \rangle$ can be achieved for decreasingly small values of h until, right at criticality, ψ orders even in the absence of any externally applied field at all (i.e., a symmetry is spontaneously broken and the phase transition occurs). The system's critical sensitivity to external perturbations proximal the phase transition can be quantified in terms of a thermodynamic susceptibility defined as

$$\chi_{\psi,\pm} \equiv \lim_{h \rightarrow 0} \frac{d\langle \psi \rangle}{dh} \propto \left| \frac{T - T_c}{T_c} \right|^{-\gamma_{\pm}}, \quad (1.3)$$

where the particular form of the divergence of the response function χ_{ψ} as $T \rightarrow T_c$ is characterized by the two critical exponents γ_+ (when $T \rightarrow T_c$ from above T_c) and γ_- (when $T \rightarrow T_c$ from below T_c). The critical exponents γ_{\pm} , which generically depend on the symmetry of the order parameter and the effective dimensionality of the system, specify the universality class of the transition. This notion of universality, whereby diverse systems display universal behavior in their thermodynamic response functions regardless of the microscopic details leading to phase transition (at least close to the critical temperature T_c and in a scaling limit) makes the study of condensed matter systems potentially elucidative in fields far beyond just condensed matter itself.

Within the context of the paramagnetic-ferromagnetic phase transition example given previously, where the order parameter can be taken as the z -component of the magnetization M_z , the corresponding conjugate field would be the z -component of the magnetic field H_z . The thermodynamic response function is then the magnetic susceptibility χ_{M_z} ($\equiv \lim_{H_z \rightarrow 0} \frac{d\langle M_z \rangle}{dH_z}$), which diverges as $T \rightarrow T_c$ with mean-field exponents $\gamma_+ = \gamma_- = 1$ in $d \geq 4$ dimensions [3].

1.2 Electronic Nematic Order

In the previous section, we introduced the concept of an order parameter and illustrated how its symmetry properties constrain the free energy and therefore determine a material's thermodynamic properties. We further explained that the symmetry properties of the order parameter can be experimentally determined by measuring a divergent thermodynamic susceptibility when a conjugate field to the order parameter is available. In this section, we focus on a particular type of electronic order that has recently attracted attention in the context of strongly correlated electron systems (SCES) and which is a primary focus of this thesis: electronic nematic order.

Electronic nematic order refers to a particular phase of matter in which a rotational symmetry is broken due to electronic correlations. For a large class of materials (including many cuprate [4, 5] and iron-pnictide [6, 7] superconductors), even though the crystal lattice possesses a certain degree of rotational symmetry at high temperatures, the electronic properties on cooling are much more strongly anisotropic. For example, in the case of the iron-pnictide $\text{Ba}(\text{Fe}_{0.965}\text{Co}_{0.035})_2\text{As}_2$ (which is structurally tetragonal at high temperature but develops an orthorhombic symmetry below a critical temperature T_S), the ratio of the twofold electronic anisotropy $\frac{\rho_{aa}-\rho_{bb}}{\frac{1}{2}(\rho_{aa}+\rho_{bb})}$ [8] to the structural orthorhombicity $\frac{a-b}{\frac{1}{2}(a+b)}$ [9] is ≈ 500 below T_S . By analogy with their classical counterparts, the homogeneous anisotropic phase of these quantum SCES is said to be an electronic nematic phase [10]. As we will discuss below, electronic nematic order necessarily results in a simultaneous structural phase transition.

A schematic illustration of a classical nematic liquid crystal transition is depicted in Figure 1.1, where an isotropic liquid (consisting of orientable molecules that are neither positionally nor rotationally ordered) condenses on cooling into a nematic state (defined by a state in which the molecules become aligned along a particular axis). The nematic state preserves the translational symmetry of the isotropic liquid state but spontaneously breaks the rotational symmetry of the isotropic state. The order parameter describing such a transition is a traceless symmetric tensor \mathcal{N}_{ij} called a director; \mathcal{N}_{ij} defines a preferred axis (but has no preferred direction) and preserves time-reversal symmetry. \mathcal{N}_{ij} belongs to the continuous group $SO(3)$, which describes

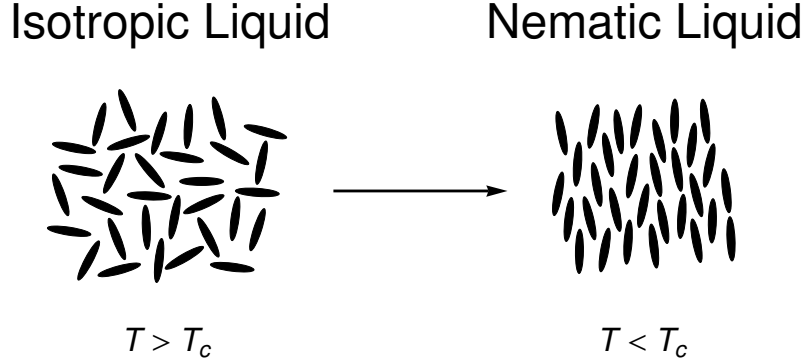


Figure 1.1: Schematic illustration of the isotropic liquid to nematic liquid crystal phase transition. In the high temperature isotropic liquid phase, the kinetic energy of the system dominates, favoring a configuration in which the molecules collectively display neither translational nor rotational order. On cooling, the molecules gain energy by spontaneously aligning along a preferred axis, thereby breaking the rotational symmetry of the disordered phase.

the group of all three-dimensional rotations about arbitrary axes passing through an origin in \mathbf{R}^3 ; condensation into the uniaxial nematic state corresponds to fixing a unique one-dimensional linear subspace of \mathbf{R}^3 which differentiates the preferred axis (defining the z -axis) and reduces the group from $SO(3)$ to $SO(2)$.

A quantum analog of the classical nematic liquid phase transition appropriate for many SCES is that of a Fermi surface distortion which spontaneously breaks the underlying rotational symmetry of the crystal lattice. In the context of a quasi-2D tetragonal material characterized by a D_{4h} point group symmetry (of relevance to many materials of current interest), the lattice symmetry confines the director \mathcal{N}_{ij} to lie within the xy plane (i.e., the plane orthogonal to the primary fourfold rotational axis, which is conventionally taken as the z -axis); this then simplifies the traceless symmetric nematic order parameter \mathcal{N}_{ij} to an Ising-like scalar \mathcal{N} .

There are two principal ways in which the primary C_4 rotational symmetry can be relaxed in D_{4h} by an in-plane distortion, and so there are correspondingly two types of

nematic order parameters in the group. The first corresponds to a B_{1g} distortion¹, in which the initially fourfold symmetric Fermi surface elongates into a rectangular-like shape by breaking the diagonal in-plane mirror symmetries in addition to C_4 (Figure 1.2(a)). The second corresponds to a B_{2g} distortion, in which the initially fourfold symmetric Fermi surface elongates into a parallelogram-like shape by breaking the secondary mirror symmetries in addition to C_4 (Figure 1.2(b)). To measure the tendency towards either type of order, one can apply a stress that results in an anisotropic strain $\epsilon_{B_{1g}} = \frac{1}{2}(\epsilon_{xx} - \epsilon_{yy})$ or $\epsilon_{B_{2g}} = \epsilon_{xy}$ (which serves as the conjugate field) and measure the corresponding induced electronic anisotropy (characterized by the nematic order parameters $\langle \mathcal{N} \rangle_{B_{1g}}$ or $\langle \mathcal{N} \rangle_{B_{2g}}$). The nematic susceptibilities in either symmetry channel then characterize the linear response to the perturbation and are given by

$$\chi_{\mathcal{N}_{B_{1g}}} \equiv \lim_{\epsilon_{B_{1g}} \rightarrow 0} \frac{d \langle \mathcal{N}_{B_{1g}} \rangle}{d \epsilon_{B_{1g}}} \quad (1.4a)$$

$$\chi_{\mathcal{N}_{B_{2g}}} \equiv \lim_{\epsilon_{B_{2g}} \rightarrow 0} \frac{d \langle \mathcal{N}_{B_{2g}} \rangle}{d \epsilon_{B_{2g}}}. \quad (1.4b)$$

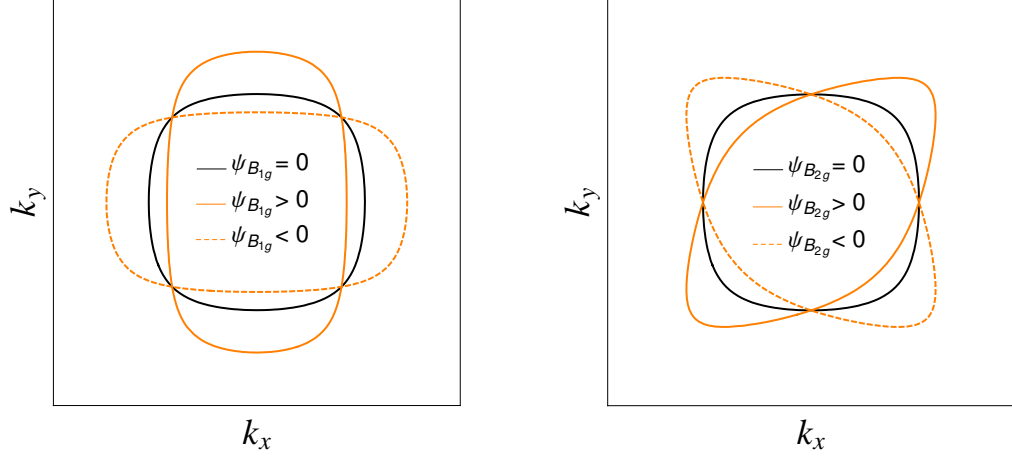
A divergence in either susceptibility on approaching the phase transition signals a nematic instability in that symmetry channel.

What permits the measurement of these susceptibilities is that $\langle \mathcal{N} \rangle_{B_{1g}}$ (or $\langle \mathcal{N} \rangle_{B_{2g}}$) has available to it a corresponding conjugate field $\epsilon_{B_{1g}}$ (or $\epsilon_{B_{2g}}$). The lowest order coupling between the two in the non-analytic component of the free energy $\Delta \mathcal{F}(T, \mathcal{N}, \epsilon)$ is a bilinear coupling in which $\Delta \mathcal{F}(T, \mathcal{N}, \epsilon)$ retains the form

$$\Delta \mathcal{F}(T, \mathcal{N}, \epsilon) = \frac{1}{2} a_0 (T - T_{\mathcal{N}}) \mathcal{N}^2 + \frac{1}{4} b \mathcal{N}^4 + \frac{1}{2} c \epsilon^2 + \frac{1}{4} d \epsilon^4 - \lambda \mathcal{N} \epsilon. \quad (1.5)$$

Written in this way, it becomes clear that once $\langle \mathcal{N} \rangle \neq 0$, $\Delta \mathcal{F}(T, \mathcal{N}, \epsilon)$ can be minimized by ϵ also acquiring a finite value; that is, nematic order implies a corresponding structural distortion.

¹“ B_{1g} ” is an example of a Mulliken symbol, which is used to label different irreducible representations of a group. For a brief discussion of Mulliken symbols, see Appendix 1.A.



(a) B_{1g} electronic nematic distortions for a tetragonal material with a D_{4h} point group symmetry. $\psi_{B_{1g}}$ is an order parameter with Ising symmetry, where the sign characterizes the type of B_{1g} orthorhombic distortion. For $\psi_{B_{1g}} > 0$, the Fermi surface breaks its original fourfold symmetry by elongating along one of the in-plane principal axes and contracting along the other in-plane principal direction; $\psi_{B_{1g}} < 0$ corresponds to the complementary distortion.

(b) B_{2g} electronic nematic distortions for a tetragonal material with a D_{4h} point group symmetry. $\psi_{B_{2g}}$ is an order parameter with Ising symmetry, where the sign characterizes the type of B_{2g} orthorhombic distortion. For $\psi_{B_{2g}} > 0$, the Fermi surface breaks its original fourfold symmetry by elongating along one of the in-plane diagonal axes and contracting along the other diagonal direction; $\psi_{B_{2g}} < 0$ corresponds to the complementary distortion.

Figure 1.2: Schematic Fermi surface distortions in D_{4h} . For a quasi-2D tetragonal material, the electronic analog to the isotropic liquid to nematic liquid transition comprises a Fermi surface distortion in which the primary fourfold (C_4) rotational symmetry is broken. Such a distortion could be driven by electronic correlations (e.g., a Pomeranchuk instability) or by a structural distortion which is then reflected in the electronic structure due to electron-lattice coupling. There are two distinct ways in which the primary C_4 rotational symmetry could be relaxed in D_{4h} : (a) a B_{1g} distortion, in which the diagonal in-plane mirror symmetries are broken in addition to C_4 rotational symmetry; (b) a B_{2g} distortion, in which the secondary mirror symmetries are broken in addition to C_4 rotational symmetry.

As a final comment in this section, we note that electronic nematic order refers to a homogeneous state in which the translational symmetry of the high temperature phase is not further broken. The iron-pnictide superconductors for which $T_S > T_N$ fall into this class of materials. More broadly, electronic phases that break rotational symmetry *and* other symmetries, while not technically pure “nematic” phases, can nevertheless be considered as having a nematic component. A central result of this thesis, to be discussed in greater detail in subsequent chapters, is that URu₂Si₂ appears to belong to this wider class of materials.

1.3 Elastoresistivity as a Probe of Nematic Susceptibility

In the previous section we defined the two in-plane nematic susceptibilities in D_{4h} , but it is then a challenge to the experimentalist to find appropriate means to measure this quantity. Although \mathcal{N} is generally not uniquely defined in terms of an experimentally measurable quantity, any physical quantity reflecting the rotational anisotropy that onsets at the transition can function equally well as a probe of \mathcal{N} . In particular, the strain-induced change in resistivity is convenient to measure experimentally and its linear response (which is directly proportional to the nematic susceptibility) defines a fourth-rank tensor called *elastoresistivity*.

In a situation in which the onset of electronic nematic order induces a corresponding anisotropy in the material’s Fermi surface, electrical resistivity can be a precise measure characterizing the nematicity. Electrical resistivity is determined by the electronic dynamics at the Fermi level, and so it is often extremely sensitive to Fermi surface changes. To leading order in the anisotropy, the nematic order parameters in either the B_{1g} or B_{2g} symmetry channels can be expressed in terms of the normalized, strain-induced resistivity changes according to

$$\langle \mathcal{N} \rangle_{B_{1g}} \sim (\Delta\rho/\rho)_{xx} - (\Delta\rho/\rho)_{yy} \quad (1.6a)$$

$$\langle \mathcal{N} \rangle_{B_{2g}} \sim (\Delta\rho/\rho)_{xy} + (\Delta\rho/\rho)_{yx}, \quad (1.6b)$$

where the strain-induced resistivity change is defined by

$$\Delta\rho_{ij} \equiv \rho_{ij}(\hat{\epsilon}) - \rho_{ij}(\hat{\epsilon} = \hat{0}). \quad (1.7)$$

In order to respect the group structure of the underlying crystal lattice and to preserve the transformation properties of $(\Delta\rho/\rho)_{ij}$ as a second-rank tensor, the appropriate normalization scheme is given by (in the limit $\rho_{ii} \gg \rho_{ij}$ for $i \neq j$)

$$(\Delta\rho/\rho)_{ij} \equiv (\Delta\rho_{ij}/\sqrt{\rho_{ii}\sqrt{\rho_{jj}}}). \quad (1.8)$$

On using Eq. (1.6) to measure the nematic susceptibilities in D_{4h} according to Eq. (1.4), the resulting ratios then yield

$$\chi_{\mathcal{N}B_{1g}} \sim m_{xx,xx} - m_{xx,yy} \quad (1.9a)$$

$$\chi_{\mathcal{N}B_{2g}} \sim 2m_{xy,xy}, \quad (1.9b)$$

where $m_{xx,xx} - m_{xx,yy}$ and $2m_{xy,xy}$ are, respectively, the B_{1g} and B_{2g} irreducible components of a fourth-rank tensor $m_{ij,kl}$ defined by

$$m_{ij,kl} \equiv \lim_{\epsilon_{kl} \rightarrow 0} \frac{\partial (\Delta\rho/\rho)_{ij}}{\partial \epsilon_{kl}}. \quad (1.10)$$

$m_{ij,kl}$ is called the *elastoresistivity*, which characterizes changes in a material's normalized resistivity due to the effects of strain. Defined for vanishing strains, it describes a material's linear response. From an experimental perspective in the field of SCES, elastoresistivity is an especially promising quantity for a number of reasons. First, as a fourth-rank tensor, elastoresistivity embeds additional information about directional anisotropies and broken point group symmetries which might more subtly manifest

in the resistivity itself or in other lower-rank physical quantities. Elastoresistivity can therefore contribute as a valuable experimental tool that more directly identifies subtle forms of broken symmetry, which is of particular utility in the field of SCES, where strong electronic and magnetic interactions can give rise to such novel phase transitions. Second, since electron-lattice coupling in SCES is often large, the order parameter characterizing an electronically-driven phase transition in these materials is often strongly tuned by strain and strongly reflected in transport; the coefficients in the elastoresistivity tensor are then likely to be large.

By measuring $m_{xx,xx} - m_{xx,yy}$ and $2m_{xy,xy}$ across a phase boundary and observing a divergence in one of the channels, one can infer the behavior of the corresponding nematic susceptibilities (up to potentially parameter-dependent coefficients of proportionality). In this way, one can determine the symmetry character of the order parameter. The central work of this thesis is associated with 1) defining the elastoresistivity tensor and elucidating its transformation properties for specific point group symmetries, 2) developing novel methods to efficiently and accurately measure the B_{1g} and B_{2g} components of this tensor in D_{4h} , and 3) applying these techniques to the specific material URu₂Si₂.

1.4 Hidden Order in URu₂Si₂

One particular material of ongoing interest in which the relevance of fourfold rotational symmetry breaking has been hotly debated is the heavy fermion material URu₂Si₂, especially as it relates to the elusive nature of its “Hidden Order” phase transition. URu₂Si₂ has been extensively studied since its initial discovery in the mid-1980s [11–13], and so a full recounting of the current state of knowledge of the material (and especially its low temperature unconventional, d -wave superconducting ground state) is beyond the scope of this thesis. Instead, the exclusive focus here is given to what is currently known about the symmetries that are conserved and broken at the Hidden Order transition, and the interested reader is referred elsewhere for more extensive reviews on URu₂Si₂ generally (see, for example, Mydosh and Oppeneer [14]).

The novel physics displayed in URu₂Si₂ fundamentally emerges from the valence $5f$ U electrons and the competition of several electronic energy scales (namely, the exchange interaction, the $5f$ bandwidth, the spin-orbit interaction, and Coulomb repulsion). Unlike lanthanides, which have more compact $4f$ orbitals that give a tendency to local magnetism due to small wave function overlap, $5f$ orbitals are more extended and, depending on the U-U atomic spacing as dictated by the host lattice, can give rise to both local and itinerant behavior. When intra-atomic U-U distances are large, conduction electrons have limited mobility (since the $5f$ wave functions do not strongly overlap) and there is a strong tendency to local magnetic ground states. As the U-U spacing decreases, the increasing $5f$ orbital overlap produces narrow f -bands that hybridize strongly with $6d$ and $7s$ bands, and, in a Kondo-like scenario, give rise to two effects. First, local $5f$ moments are screened by conduction electrons, tending to favor nonmagnetic ground states characterized by large effective masses (as typically observed in a large Sommerfeld coefficient and an enhanced Pauli susceptibility). For this reason, these materials are often heavy fermion systems. Second, the magnetic moments simultaneously interact with their neighboring magnetic ions via inter-atomic RKKY-like interactions. This can produce unconventional magnetic or superconducting behavior (or sometimes both). URu₂Si₂ is a material displaying both of these effects, featuring both intermediate heavy Fermion behavior and superconductivity; however, the superconducting state only emerges from a mysterious Hidden Order state which has strong thermodynamic signatures but which is still not well understood.

URu₂Si₂ also possesses a strong spin-orbit interaction, which entangles the orbital and spin electronic degrees of freedom and leads to the possibility that Hidden Order belongs to a class of high rank multipolar magnetic order. In a j - j coupling scheme (appropriate when spin-orbit is not a small perturbation), the f ($\ell = 3$) electrons have $7 (= 2\ell + 1)$ available orbital electronic states, which double to 14 total electronic states due to spin degeneracy. The spin-orbit interaction $\lambda \vec{L} \cdot \vec{S}$ splits these 14 electronic states; for $\lambda > 0$, it is energetically favorable for \vec{L} and \vec{S} to be anti-aligned, which lowers the energy of 6 of the entangled electronic states into an effective $j_{\text{eff}} = 5/2$ manifold. In a picture where U possesses a $5f^2$ electronic configuration,

two f electrons populate the $j_{\text{eff}} = 5/2$ manifold, and so operators that relate to physical observables belong to a two $j_{\text{eff}} = 5/2$ electron Hilbert space. These operators can be expressed in the individual electron basis (with states expressed in terms of $|j_{\text{eff},1}j_1\rangle \otimes \mathbb{1} \oplus \mathbb{1} \otimes |j_{\text{eff},2}j_2\rangle$), but these operators can also be expressed in the total angular momentum product basis (useful since the total angular momentum commutes with the Hamiltonian) by taking the tensor product of the two individual $j_{\text{eff}} = 5/2$ spaces (with states expressed in terms of $|j_{\text{eff},1}j_{\text{eff},2}JM\rangle$, where J and M are total angular momenta quantum numbers). The Clebsch-Gordan decomposition of $|j_{\text{eff},1}j_1\rangle \otimes \mathbb{1} \oplus \mathbb{1} \otimes |j_{\text{eff},2}j_2\rangle$ in terms of $|j_{\text{eff},1}j_{\text{eff},2}JM\rangle$ then involves total J quantum numbers up to $J = 5$, since $5/2 \otimes 5/2 = 0 \oplus 1 \oplus \dots \oplus 5$. If we project the $|j_{\text{eff},1}j_{\text{eff},2}JM\rangle$ states into spherical coordinates, the results are spherical harmonics Y_J^M , which are tensor operators of rank J which form a $(2J+1)$ -dimensional representation of the 3D rotation group $SO(3)$. Since the rotational group of a crystal belongs to a subgroup of $SO(3)$ and all physical observables must at least respect the symmetry of the crystal, any physical observable can be expressed in terms of the Y_J^M . As the maximum total angular momentum is $J = 5$, observable operators are then allowed up to rank 5 (called a dotriacontapole).

URu₂Si₂ crystallizes in the ThCr₂Si₂ ($I4/mmm$) body-centered tetragonal crystal structure at room temperature (Figure 1.3(a)), a common structure for many materials of ongoing interest (including many superconductors). This layered structure consists of uranium spacer atoms situated between planes of tetrahedrally coordinated ruthenium atoms, and the point group at each uranium site is D_{4h} . On cooling URu₂Si₂ in zero magnetic field, the specific heat features an abrupt anomaly at $T_{\text{HO}} \approx 17.5$ K (Figure 1.3(b)), evincing a phase transition to a Hidden Order state which reduces the entropy (per formula unit) by $\Delta S = \int_0^{T_{\text{HO}}} (\Delta C/T) dT \approx 0.2R \ln 2$. The phrase ‘‘Hidden Order’’ was coined to signify that while the presence of a phase transition to an ordered state is beyond doubt, the nature of the ordered state is not clear. This phase transition, which can be suppressed with hydrostatic pressure [15–18] and a c -axis oriented magnetic field [19, 20] (Figure 1.3(c)), would correspond to a measurable magnetic moment that should be detectable by magnetic probes if it was magnetic in origin. In addition to its magnetic properties, it is also

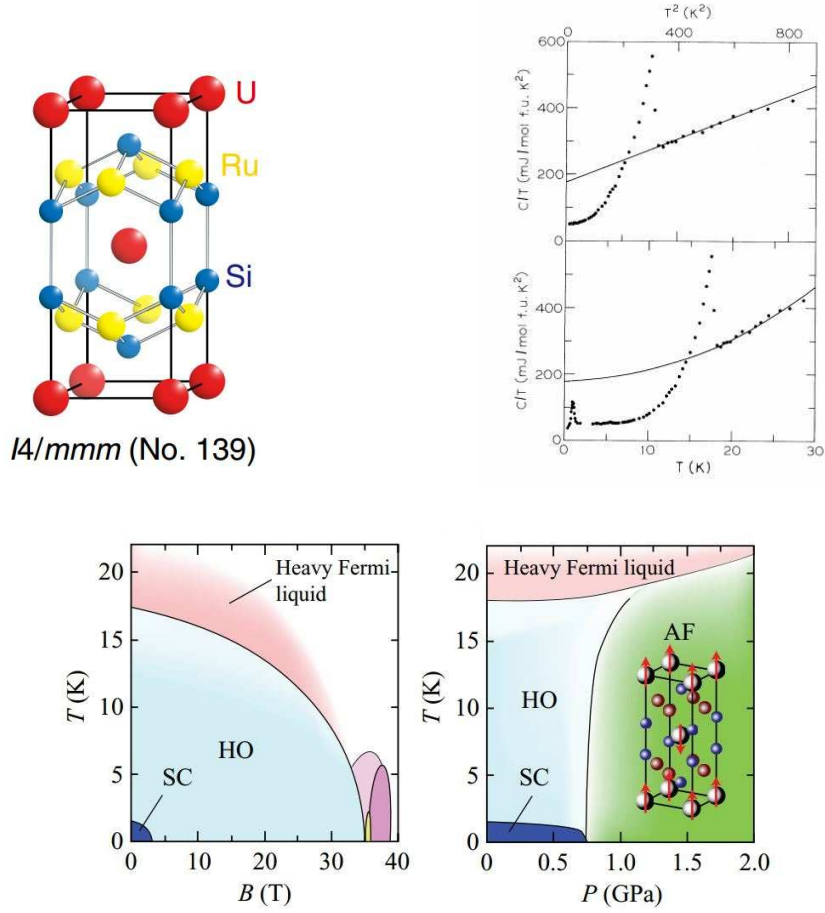


Figure 1.3: (a) Reproduced from Tonegawa *et al.* [21]. At room temperature, URu_2Si_2 crystallizes in the $ThCr_2Si_2$ ($I4/mmm$) body-centered tetragonal crystal structure (with lattice parameters $a \approx 4.13$ Å, $c \approx 9.59$ Å [11]). This layered structure consists of uranium spacer atoms situated between layers of ruthenium-silicon tetrahedra. The point group at each uranium site is D_{4h} . (b) Reproduced from Palstra *et al.* [11]. On cooling URu_2Si_2 in zero magnetic field, the specific heat features an abrupt anomaly at $T_{HO} \approx 17.5$ K. Measuring the Sommerfeld coefficient γ admits an effective mass estimate (relative to the bare electron mass m_e) of $m^* \approx 50m_e$ [13], intermediate between most transition metals ($m^* \lesssim 10m_e$) and typical heavy fermion systems ($m^* \gtrsim 200m_e$). The heat capacity anomaly also corresponds to an entropy change (per formula unit) $\Delta S = \int_0^{T_{HO}} (\Delta C/T) dT \approx 0.2R \ln 2$, which, if magnetic in origin, would imply a magnetic moment that should be detectable by magnetic probes. (c) Reproduced from Kasahara *et al.* [22]. $T-H$ and $T-P$ phase diagrams for URu_2Si_2 , illustrating how both a c -axis oriented magnetic field and hydrostatic pressure can suppress Hidden Order.

important to establish the symmetry properties of the Hidden Order parameter, especially as it relates to the breaking or preservation of time-reversal, translational, and point group symmetry. A discussion of each type of symmetry in relation to the Hidden Order state follows.

1.4.1 Hidden Order, Magnetism, and Time-Reversal Symmetry

Early neutron scattering experiments probing magnetism within the Hidden Order state of URu₂Si₂ found a small ($\approx 0.03\mu_B$) antiferromagnetic dipole moment with ordering vector $\vec{Q} = (001)$ directed along the tetragonal c -axis [23]; even at that time, this ordered moment was understood to be unusually small, both compared to the inferred ordered dipole moment from the high temperature magnetic susceptibility and given the large entropy change at the phase transition. Subsequent ²⁹Si NMR [24, 25] and elastic neutron scattering [26] measurements on higher quality samples have clarified that the small detected dipole moment is associated with a spatially inhomogeneous antiferromagnetism which is characterized by a progressively smaller ordered moment with increasing sample purity and that progressively onsets below T_{HO} in the purest samples; on this basis, it seems that no intrinsic ordered dipole moment along the c -axis is associated with Hidden Order [27]. As regards the in-plane magnetic dipole moment, recent neutron scattering measurements [28, 29] place an experimental upper bound of $10^{-3}\mu_B/\text{U}$. While Ross *et al.* [29] do not quote the measured residual resistivity ratio (abbreviated RRR, and used as a cursory metric for crystal purity) of their samples, their data are in quantitative agreement with data from Das *et al.* [28] obtained on samples with $\text{RRR} \approx 10$. While large for typical metals, this RRR has been shown to be too small to observe thermodynamic signatures characteristic of Hidden Order in high-resolution X-ray diffraction measurements [21]. Thus, at present, it is unclear whether or not Hidden Order develops a small in-plane magnetic moment in the ordered state, motivating further studies on the in-plane dipole moment for samples that are characterized by significantly higher RRR values.

A related question to the inherent magnetism associated with the Hidden Order

state is the presence or absence of time-reversal symmetry breaking. Conclusive evidence for or against time-reversal symmetry breaking has not been obtained to date. One suggestive piece of evidence is inferred from ²⁹Si NMR measurements [25], in which additional broadening in the NMR line width ΔH_{add} onsets just below the Hidden Order transition temperature. The unusual temperature dependence of ΔH_{add} includes an abrupt jump at T_{HO} followed by a gradual decrease on cooling below the transition. Notably, ΔH_{add} has a roughly linear magnetic field dependence for in-plane magnetic fields, but the ΔH_{add} intercept in vanishing field only acquires a finite value of ≈ 0.6 Oe below T_{HO} . These features, consistent with an ordering hyperfine field at Si sites induced from an ordered multipole moment on U sites, have been interpreted in terms of broken time-reversal symmetry within the Hidden Order state [25] and would correspond to an in-plane antiferromagnetic dipole moment smaller than the resolution of previous neutron scattering measurements [27].

Another direct probe of time-reversal symmetry breaking is measurement of the Kerr angle θ_K , which characterizes the angular difference between the polarization axes of normally incident and reflected light on the surface of a material (the polar Kerr effect) and which can only acquire a nonzero value if time-reversal symmetry is broken [30]. The temperature dependence and behavior under training magnetic fields of θ_K in URu₂Si₂ display an unusual behavior around the Hidden Order transition [31]; θ_K acquires a finite value at ≈ 25 K (significantly above $T_{\text{HO}} \approx 17.5$ K) and can be trained with a *c*-axis magnetic field in a manner independent from the superconducting state. While time-reversal symmetry breaking was unambiguously observed in the superconducting state, the polar Kerr measurements regarding the Hidden Order state are not conclusive in a geometry probing net dipole moments along the *c*-axis, possibly due to residual magnetic impurities or other features extrinsic to Hidden Order. Further polar Kerr measurements in geometries probing the in-plane dipole moments might also be elucidating.

Muon spin relaxation (μ SR) [32] is a third experimental technique that has been used to characterize the nature of time-reversal symmetry in the Hidden Order state. By implanting muons (which have spin 1/2) at interstitial sites in a sample and measuring the resulting distribution of spin precession frequencies, one can determine the

time evolution of the muon spin polarization (expressed in terms of an asymmetry function, measuring the difference between the total detected muon events at forward and backward detectors), which is sensitive to the development of a local magnetic field that (if present) breaks time-reversal symmetry. The functional form of the muon spin polarization comprises a spin-lattice relaxation rate λ , characterizing the (typically stretched-exponential) time scale for muon spin depolarization due to a hyperfine interaction between the muons and electronic spins in the crystal lattice. Kawasaki *et al.* observe an enhancement in the zero-field relaxation rate λ_{ZF} at T_{HO} , reflecting the onset of a static time-reversal symmetry breaking magnetic field. Since enhancements in the muon spin relaxation rates λ_{TF}^a and λ_{TF}^c under transverse magnetic field conditions are observed for magnetic fields applied along both the crystallographic a - and c -axes on cooling through T_{HO} , the authors conclude that the static magnetic field has components along both the a - and c -axes. These μ SR results are consistent with either the development of an in-plane dipole moment of $\approx 10^{-4}\mu_B/U$ or a Hidden Order parameter that intrinsically breaks time-reversal symmetry but without the development of an associated in-plane moment (for example, a higher order magnetic multipole).

Although there is no consensus yet in the community, it is important to establish the time-reversal symmetry character of the Hidden Order parameter, as it is a clear delineating line between various multipolar theories of Hidden Order (e.g., electric multipoles such as hexadecapolar order [33] preserve time-reversality, magnetic multipoles such as dotriacontapolar order [34] break time-reversality, and hastatic order [35] breaks both time-reversality and double time-reversality; for a more exhaustive theoretical overview and each theory's relation to time-reversality, see [36]).

1.4.2 Hidden Order and Translational Symmetry

Translational symmetry breaking associated with condensation into the Hidden Order state appears to be firmly established. The volume of the primitive magnetic unit cell in the high temperature phase doubles in the ordered state, thereby increasing the number of uranium atoms in the primitive magnetic unit cell from 1 to 2. The

doubling occurs due to an antiferro-like order along the c -axis.

Calculations of the paramagnetic (i.e., $T > T_{\text{HO}}$) Fermi surface in URu₂Si₂ by density functional theory [34] reveal that the Fermi surface is well-nested by the commensurate wave vector $\vec{Q}_C = (001)$ (Figure 1.4(a)), which connects the largest electron pocket (centered around the Γ point in the body-centered tetragonal Brillouin zone) with the largest hole pocket (centered around the Z point). The nested parts of the Fermi surface are predominantly of angular momentum $j_z = \pm 5/2$ character. Its strongly nested Fermi surface inherently predisposes URu₂Si₂ to ordered states characterized by \vec{Q}_C , a feature shared by both Hidden Order and a proximal antiferromagnetic ground state which can be stabilized with hydrostatic pressure. When Hidden Order onsets, the unit cell doubles and the Fermi surface gets back-folded by \vec{Q}_C , which transforms the Γ and Z points of the original body-centered tetragonal Brillouin zone into each other (sending both to the Γ point in the new primitive tetragonal Brillouin zone). This results in the opening of an electronic energy gap, which is a characteristic experimental feature of Hidden Order. This gap is seen in resistivity (for example, as in Figure 1.4(b), reproduced from [37]), carrier concentration as inferred from Hall effect measurements (for example, [38, 39]), heat capacity (for example, [12]), inelastic neutron scattering (for example, [40, 41]), and many other measurements (see [14] for a more extensive review). Further, this back-folding scenario with ordering vector \vec{Q}_C is also consistent with cyclotron resonance measurements [42, 43], ARPES measurements [44–47], and the nearly identical Fermi surfaces in the Hidden Order and antiferromagnetic phases as inferred from quantum oscillations measurements [48–50]. On this basis, Hidden Order seems to result from the onset of a Hidden Order parameter which is inherently a finite \vec{Q}_C order, inducing a translational symmetry breaking which doubles the magnetic unit cell along the tetragonal c -axis.

Changes in the space group of a material due to a magnetic phase transition are frequently investigated via diffraction experiments, where the result of translational symmetry breaking can be inferred in one of two ways. In the first case, a diffraction experiment can observe additional Bragg peaks directly via a probe sensitive to the magnetism (e.g., neutron diffraction as a probe of dipolar antiferromagnetic order).

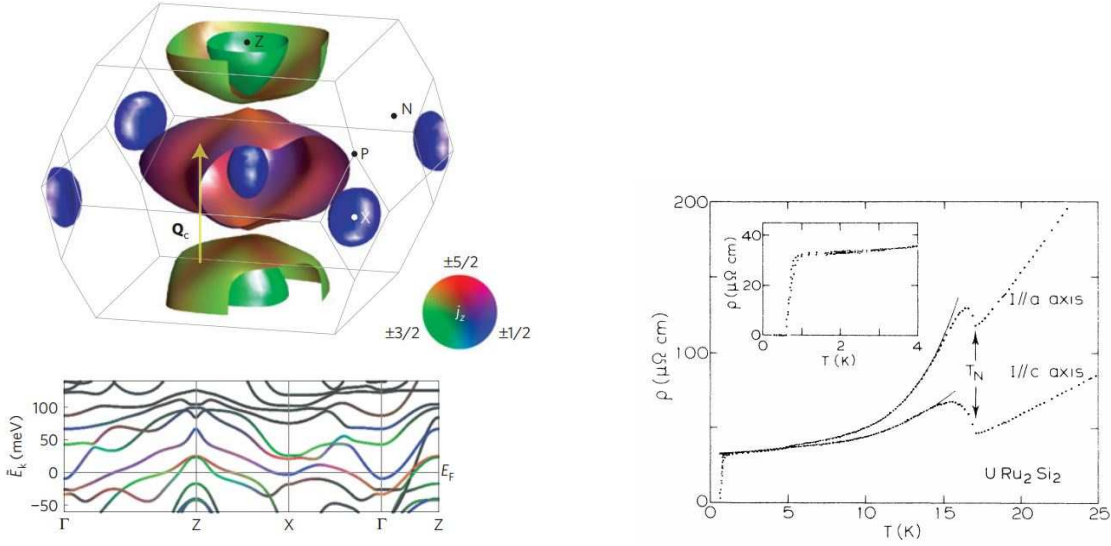


Figure 1.4: (a) Reproduced from Ikeda *et al.* [34]. Calculations of the paramagnetic (i.e., $T > T_{\text{HO}}$) Fermi surface in URu_2Si_2 by density functional theory. The Fermi surface is well-nested by the commensurate wave vector $\vec{Q}_C = (001)$, which connects the largest electron pocket (centered around the Γ point in the body-centered tetragonal Brillouin zone) with the largest hole pocket (centered around the Z point). The Fermi surface is colored by the z -component of the angular momentum j_z ; it is evident that \vec{Q}_C connects portions of the Fermi surface dominated by electrons/holes with $j_z = \pm 5/2$. The nested structure of the Fermi surface indicates that URu_2Si_2 has inherent tendencies to antiferroic order characterized by \vec{Q}_C ; it is then unsurprising that both Hidden Order and the pressure-induced antiferromagnetic phase both manifest as \vec{Q}_C orders which double the unit cell along the tetragonal c -axis. (b) Reproduced from Palstra *et al.* [37]. Temperature dependence of the in-plane and out-of-plane resistivities spanning T_{HO} , evincing the opening of an electronic energy gap on entering the Hidden Order state. When Hidden Order onsets, the Fermi surface gets backfolded by \vec{Q}_C . Correspondingly, the Γ and Z points of the original body-centered tetragonal Brillouin zone become equivalent (transforming to the Γ point in the new simple tetragonal Brillouin zone) and a significant portion ($\approx 40\%$ [12]) of the Fermi surface is lost.

In the second case, a diffraction experiment insensitive to the magnetism can infer the translational symmetry breaking indirectly from a Bragg peak splitting, which can occur only for a subset of magnetic order parameters which admit nontrivial magnetoelastic coupling terms (in leading order) in the free energy. Such symmetry-permitted magnetoelastic terms only result in cases in which the magnetic order parameter belongs to a multi-dimensional irreducible representation of the high temperature magnetic space group (i.e., magnetic space group in the disordered state). The high temperature crystallographic space group of URu_2Si_2 (denoted \mathcal{G}_{CSG} , and sometimes referred to as a Fedrov group) is $I4/mmm$ (No. 139), while the high temperature magnetic space group (denoted \mathcal{G}_{MSG} , and sometimes referred to as a Shubnikov group) is given by the tensor product of \mathcal{G}_{CSG} with the set $T = \{E, \theta\}$ (θ is the time-reversal operator): $\mathcal{G}_{\text{MSG}} = \mathcal{G}_{\text{CSG}} \otimes T$. Considering only those irreducible representations of D_{4h} that preserve spatial inversion,² one can completely enumerate the possible order parameters for Hidden Order characterized by a finite \vec{Q}_C and which either preserve or break time-reversality. The onset of the different order parameters correspondingly reduces the ordered crystallographic space group $\mathcal{G}_{\text{CSG}}^{\text{ordered}}$ and magnetic space group $\mathcal{G}_{\text{MSG}}^{\text{ordered}}$ to subgroups of \mathcal{G}_{CSG} and \mathcal{G}_{MSG} , respectively.

The possible Hidden Order parameters characterized by a finite \vec{Q}_C are given in Table 1.1. All of the space groups included in Table 1.1 (with the exception of the space groups given for the A_{1g}^{\pm} cases) belong to nonsymmorphic space groups with extra translation corresponding to the real space vector $\vec{\tau} = (0, 0, c/2)$. For those order parameters which preserve time-reversal symmetry (i.e., ‘electric’ order parameters), the full symmetry of the ordered state can be described by the crystallographic space group $\mathcal{G}_{\text{CSG}}^{\text{ordered}}$ (i.e., $\mathcal{G}_{\text{MSG}}^{\text{ordered}}$ coincides with $\mathcal{G}_{\text{CSG}}^{\text{ordered}}$ in its spatial character but also includes time-reversal θ). For those order parameters which break time-reversal symmetry (i.e., ‘magnetic’ order parameters), the ordered crystallographic space group $\mathcal{G}_{\text{CSG}}^{\text{ordered}}$ and the ordered magnetic space group $\mathcal{G}_{\text{MSG}}^{\text{ordered}}$ differ in both their spatial and time-reversal characters. The first column of Table 1.1 labels the point group and time-reversal symmetry character of the possible Hidden Order parameters, where the

²i.e., those irreps labeled by a Mulliken symbol with a g subscript. These are the only irreps considered because non-centrosymmetry has never been reported in the literature.

Table 1.1: Possible \vec{Q}_C Hidden Order Parameters

Irrep	$\mathcal{G}_{\text{CSG}}^{\text{ordered}}$	$\mathcal{G}_{\text{MSG}}^{\text{ordered}}$	Time-Reversal	Fourfold Rotation
A_{1g}^+	$P4/mmm$	$P4/mmm1'$	Preserved	Preserved
A_{2g}^+	$P4/mnc$	$P4/mnc1'$	Preserved	Preserved
B_{1g}^+	$P4_2/mmc$	$P4_2/mmc1'$	Preserved	Preserved
B_{2g}^+	$P4_2/mnm$	$P4_2/mnm1'$	Preserved	Preserved
E_g^+	$Cmce$	$Cmce1'$	Preserved	Broken
A_{1g}^-	$I4/mmm$	P_14/mmm	Broken	Preserved
A_{2g}^-	$I4/mmm$	P_14/mnc	Broken	Preserved
B_{1g}^-	$I4/mmm$	P_14_2/mmc	Broken	Preserved
B_{2g}^-	$I4/mmm$	P_14_2/mnm	Broken	Preserved
E_g^-	$Fmmm$	C_Amce	Broken	Broken

Reproduced from Suzuki *et al.* [51]. The first column labels the point group and time-reversal symmetry character of the possible Hidden Order parameters, where the Mulliken symbols label irreducible representations of the high temperature crystallographic point group (i.e., D_{4h} in $I4/mmm$) and \pm superscripts indicate time-reversal preservation or breaking (respectively). $\mathcal{G}_{\text{CSG}}^{\text{ordered}}$ and $\mathcal{G}_{\text{MSG}}^{\text{ordered}}$ label the ensuing crystallographic and magnetic space groups upon ordering of the corresponding order parameter, using Hermann-Mauguin space group notation (Note: crystallographic space groups indicate the presence and types of rotations/mirrors/translations that are symmetries, but the Hermann-Mauguin notation is presently modified for the magnetic space groups to further indicate the presence/absence of time-reversal symmetry by the presence/absence of the $1'$ symbol). The final two columns indicate the time-reversal and fourfold rotational symmetry character of the corresponding ordered states in the ordered unit cell (i.e., after imposing the \vec{Q}_C order).

Mulliken symbols label irreducible representations of the *high temperature crystallographic point group* (i.e., D_{4h} in $I4/mmm$) and \pm superscripts indicate time-reversal preservation or breaking (respectively). Because of this, while a $B_{1g}^\pm(\vec{Q}_C)$ or $B_{2g}^\pm(\vec{Q}_C)$ type order breaks the fourfold rotational symmetry of the high temperature primitive unit cell, after imposing the \vec{Q}_C order (i.e., doubling the primitive unit cell), the ensuing $B_{1g}^\pm(\vec{Q}_C)$ or $B_{2g}^\pm(\vec{Q}_C)$ ordered state still retains fourfold rotational symmetry (in the new doubled primitive unit cell). The possible order parameters belonging

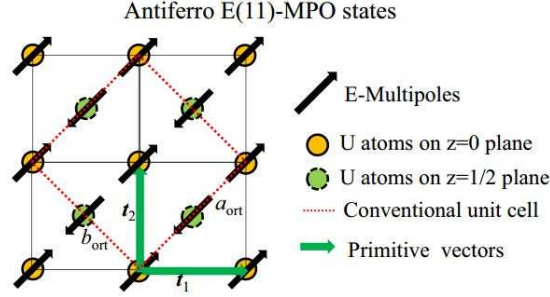


Figure 1.5: Reproduced from Suzuki *et al.* [51]. Schematic illustration of an antiferro- $E_g^-(\vec{Q}_C)$ order arising from a magnetic multipole. The onset of a finite ordered magnetic multipole (with components oriented along the 45° direction relative to the high temperature primitive cell) results in a small orthorhombicity and doubles the size of the ordered primitive magnetic unit cell along the c -axis.

to one-dimensional and two-dimensional irreducible representations are clearly distinguished based on their associated crystallographic space groups $\mathcal{G}_{\text{CSG}}^{\text{ordered}}$; all \vec{Q}_C one-dimensional irreps result in ordered states still characterized by fourfold rotational symmetry, while the two-dimensional irreps further break the original fourfold rotational symmetry of the high temperature crystallographic space group. Evidence for a two-dimensional E_g^- Hidden Order parameter was inferred on this basis from high resolution X-ray [21] measurements performed concurrently with this thesis, where the assignment of the crystallographic space group $\mathcal{G}_{\text{CSG}}^{\text{ordered}} = Fmmm$ was resolved in the highest RRR samples. A schematic illustration for a Hidden Ordered state which would correspond to such an $E_g^-(\vec{Q}_C)$ order is given in Figure 1.5 (from [51]).

1.4.3 Hidden Order and Point Group Symmetry

A final consideration in classifying the symmetry character of the Hidden Order parameter (and the one most relevant to the work presented in this thesis) is its point group symmetry properties and, in particular, whether Hidden Order preserves or breaks the primary fourfold rotational symmetry of the tetragonal lattice. For over two decades, no fourfold rotational symmetry breaking associated with Hidden Order had been reported in the literature. The first report of rotational symmetry breaking

occurred in 2011 with the magnetic torque measurements of Okazaki *et al.* [52]. They measured the dependence of the magnetic torque τ on an in-plane angle ϕ (defined as the angle between the crystal axes and an applied 4 T magnetic field) on cooling through T_{HO} (Figure 1.6(a)). Resolving the total torque signal $\tau(\phi)$ into its Fourier components $\tau_{2n\phi}$, it is observed that, for $T > T_{\text{HO}}$, the twofold term $\tau_{2\phi}$ is absent and $\tau(\phi)$ is dominated by the fourfold term $\tau_{4\phi}$, consistent with the full fourfold symmetry of the underlying tetragonal lattice. However, on cooling to temperatures $T < T_{\text{HO}}$, the twofold term $\tau_{2\phi}$ clearly onsets, suggesting that fourfold rotational symmetry has been broken. The twofold term follows the functional form $\tau_{2\phi} = A_{2\phi} \cos 2\phi$, indicating that the off-diagonal susceptibility χ_{ab} becomes nonzero (i.e., the rotational symmetry breaking is a B_{2g} type distortion). Notably, $\tau_{2\phi} \neq 0$ only in the smallest samples measured (i.e., the magnitude of the torque signal does not scale with volume), which the authors interpret in terms of pinned domains (of an estimated size of order $10\mu\text{m}$) that arise from underlying features of the crystal (such as internal stress or disorder). B_{2g} -like magnetic anisotropy associated with Hidden Order was also subsequently reported from cyclotron resonance [42, 43] and nuclear magnetic resonance [53] measurements.

Importantly, however, the above cited magnetic torque measurements require gluing samples to a cantilever; therefore, one cannot rule out the possibility that the sample experiences strain due to adhesion to the cantilever that induces the observed rotational symmetry breaking in the broken symmetry state. One way to address this concern is to directly determine the crystal symmetry in the Hidden Order state in the absence of a symmetry-breaking field. Such an experiment (performed concurrently with the present work of this thesis) using high-resolution X-ray diffraction was performed by Tonegawa *et al.* [21]. Using high resolution X-ray scattering, they measured the temperature dependence of the (880) Bragg peak, which should remain a single peak for a tetragonal material. A single peak is observed in the high temperature regime, as expected for URu_2Si_2 ; however, the peak splits on cooling through T_{HO} , directly resolving the orthorhombic distortion. The orthorhombic distortion is consistent with the twofold torque measurements in at least two ways: 1) the resolved orthorhombicity is of a B_{2g} type, with the high temperature $I4/mmm$ space group

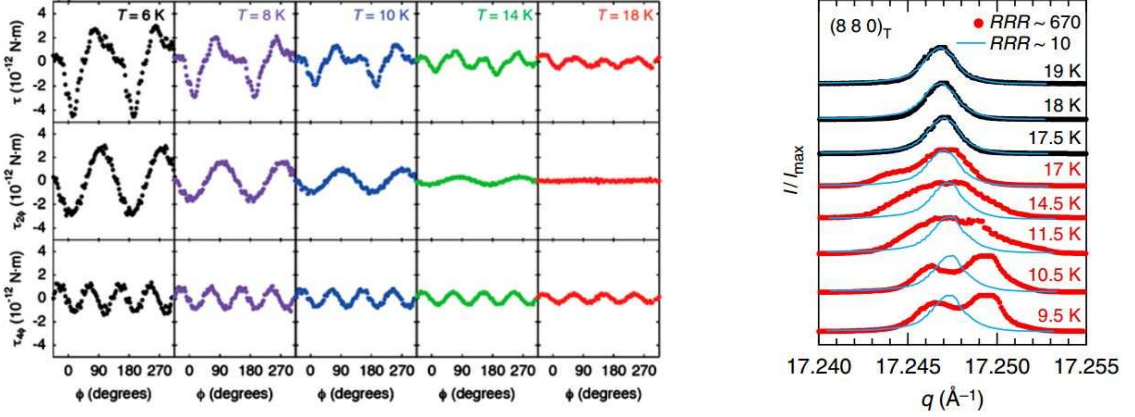


Figure 1.6: (a) Reproduced from Okazaki *et al.* [52]. Magnetic torque τ dependence on an in-plane angle ϕ (defined as the angle between the crystal axes and an applied 4 T magnetic field) on cooling through T_{HO} . Resolving the total torque signal $\tau(\phi)$ into its Fourier components $\tau_{2n\phi}$, it is observed that, for $T > T_{HO}$, the twofold term $\tau_{2\phi}$ is absent and $\tau(\phi)$ is dominated by the fourfold term $\tau_{4\phi}$, consistent with the full fourfold symmetry of the underlying tetragonal lattice. However, on cooling to temperatures $T < T_{HO}$, the twofold term $\tau_{2\phi}$ clearly onsets, suggesting that fourfold rotational symmetry has been broken. The twofold term follows the functional form $\tau_{2\phi} = A_{2\phi}(T) \cos 2\phi$, indicating that the off-diagonal susceptibility χ_{ab} becomes nonzero (i.e., the rotational symmetry breaking is a B_{2g} type distortion). Notably, $\tau_{2\phi} \neq 0$ only in the smallest samples measured, which the authors interpret in terms of pinned domains due to underlying features of the crystal (such as internal stress or disorder). (b) Reproduced from Tonegawa *et al.* [21]. The temperature dependence of the (880) Bragg peak as measured by high resolution X-ray scattering. A single peak is observed in the high temperature regime, as expected for a tetragonal system; however, the peak splits on cooling through T_{HO} , directly resolving an orthorhombic distortion in the absence of a symmetry breaking field. The orthorhombic distortion is consistent with the twofold torque measurements in at least two ways: 1) the resolved orthorhombicity is of a B_{2g} type, with the high temperature $I4/mmm$ space group lowering to the $Fmmm$ space group (with the in-plane primitive axes rotated by 45°) in the Hidden Order state; 2) the small orthorhombicity (of the order of 10^{-5} , much smaller than that of the ordered orthorhombic phase of the $BaFe_2As_2$ -based superconductors) can only be resolved for the highest RRR samples, with samples of $RRR \approx 10$ displaying no resolvable orthorhombic distortion.

lowering to the $Fmmm$ space group (with the in-plane primitive axes rotated by 45°) in the Hidden Order state; 2) the small orthorhombicity (of the order of 10^{-5} , much smaller than that of the ordered orthorhombic phase of the BaFe_2As_2 -based superconductors) can only be resolved for the highest RRR samples, with samples of RRR ≈ 10 displaying no resolvable orthorhombic distortion. This observation, however, has been disputed by different (as yet unpublished) X-ray measurements by a group in Sapporo [36, 54].

The very small orthorhombicity in the cleanest URu_2Si_2 samples that is unresolvable in the lower RRR samples suggests a novel interplay between crystalline disorder (e.g., impurities, defects, or internal stress) and electronic nematic order (especially as it couples to the crystal lattice). In this context, elastoresistivity can serve as a useful tool, providing additional experimental evidence that can help to adjudicate the existence and implications of rotational symmetry breaking associated with Hidden Order.

1.5 Thesis Layout

The organization of this thesis is as follows. Chapter 2 (published in [55]) provides a symmetry analysis for the elastoresistivity tensor in D_{4h} and explains how certain admixtures of elastoresistivity coefficients connect to thermodynamic susceptibilities of a material, particularly where they are sensitive to critical fluctuations proximate to a critical point at which a point group symmetry is spontaneously broken. Chapter 3 (published in [56]) presents a proof-of-principle transverse elastoresistivity experiment on the representative iron-pnictide BaFe_2As_2 , motivated by the theoretical exposition of the preceding chapter and also providing several experimental advantages. Chapter 4 (published in [57]) then contains results related to differential elastoresistance measurements on URu_2Si_2 , tracking the temperature dependence of the in-plane nematic susceptibilities that can be explained in terms of a Landau-Ginzburg free energy in which the Hidden Order parameter belongs to a two-dimensional irreducible representation of D_{4h} and breaks fourfold rotational symmetry in a B_{2g} -like fashion. Chapter 5 addresses certain additional elastoresistivity measurements on URu_2Si_2 , and in

particular the magnetic field and RRR dependence of the $2m_{xy,xy}$ elastoresistivity coefficient from the differential longitudinal method and as extracted from preliminary transverse elastoresistivity measurements. Chapter 6 concludes with an overall discussion of where the present measurements leave the state of elastoresistivity and our understanding of Hidden Order.

The work presented in this thesis is published in several references [55–57]. Additional contributions as part of this thesis have also been published [58, 59].

1.A Mulliken Symbols

Mulliken symbols are a succinct notation for conveying the symmetry properties of an irreducible representation for a group. In this appendix, the notation is briefly explained; for concreteness in this discussion, specific reference will be made to the D_{4h} character table, reproduced in Table 1.2.

Table 1.2: **Character Table for D_{4h}**

Irrep	E	$2C_4$	C_2	$2C'_2$	$2C''_2$	i	$2S_4$	σ_h	$2\sigma_v$	$2\sigma_d$	Linears, Rotations	Quadratic
A_{1g}	1	1	1	1	1	1	1	1	1	1		$x^2 + y^2, z^2$
A_{2g}	1	1	1	-1	-1	1	1	1	-1	-1	R_z	
B_{1g}	1	-1	1	1	-1	1	-1	1	1	-1		$x^2 - y^2$
B_{2g}	1	-1	1	-1	1	1	-1	1	-1	1		xy
E_g	2	0	-2	0	0	2	0	-2	0	0	(R_x, R_y)	(xz, yz)
A_{1u}	1	1	1	1	1	-1	-1	-1	-1	-1		
A_{2u}	1	1	1	-1	-1	-1	-1	-1	1	1	z	
B_{1u}	1	-1	1	1	-1	-1	1	-1	-1	1		
B_{2u}	1	-1	1	-1	1	-1	1	-1	1	-1		
E_u	2	0	-2	0	0	-2	0	2	0	0	(x, y)	

A Mulliken symbol consists of either two components (e.g., the E and the g in the E_g symbol) or three components (e.g., the B , 1 , and u in the B_{1u} symbol); however, to understand these components, one first needs to understand the underlying symmetry elements of the group. For the D_{4h} point group, 16 operations are symmetry elements of the group:

1. E , the identity element;
2. C_4 , the primary 90° rotation, the axis about which is conventionally taken as the z -axis;
3. $C_4^2 \equiv C_2$, 180° rotation about the z -axis;
4. C_4^3 , 270° rotation about the z -axis;
5. $C_2'(x)$, a first secondary 180° rotation about an axis perpendicular to the primary axis, which by convention is taken as the x -axis;
6. $C_2'(y)$, a second secondary 180° rotation about an axis perpendicular to the primary axis, which by convention is taken as the y -axis;
7. $C_2''(1)$, a first tertiary 180° rotation about an axis perpendicular to the primary axis and 45° to the secondary axes, which by convention is taken as the in-plane diagonal axis defined by the line $x = y$;
8. $C_2''(2)$, a second tertiary 180° rotation about an axis perpendicular to the primary axis and 45° to the secondary axes, which by convention is taken as the in-plane diagonal axis defined by the line $x = -y$;
9. i , spatial inversion;
10. $\sigma_h \equiv \sigma_z$, the primary mirror symmetry which is oriented by a normal vector pointing along the z -direction (by convention, this plane is referred to as a horizontal mirror plane);
11. $\sigma_v(1) \equiv \sigma_x$, a first secondary mirror symmetry which is oriented by a normal vector pointing along the x -direction (by convention, this plane is referred to as a vertical mirror plane);
12. $\sigma_v(2) \equiv \sigma_y$, a second secondary mirror symmetry which is oriented by a normal vector pointing along the y -direction (by convention, this plane is also referred to as a vertical mirror plane);
13. $\sigma_d(1) \equiv \sigma_{x=y}$, a first tertiary mirror symmetry which is oriented by a normal vector pointing along an in-plane diagonal axis defined by the line $x = y$ (by convention, this plane is referred to as a diagonal mirror plane);
14. $\sigma_d(2) \equiv \sigma_{x=-y}$, a second tertiary mirror symmetry which is oriented by a normal vector pointing along an in-plane diagonal axis defined by the line $x = -y$ (by convention, this plane is also referred to as a diagonal mirror plane);

15. S_4 , a first “improper rotation” or roto-reflection corresponding to the composition of the primary rotation C_4 and the primary mirror σ_h (i.e., $S_4 \equiv C_4 \circ \sigma_h = \sigma_h \circ C_4$); and
16. S_4^3 , a second improper rotation corresponding to the composition of the 270° rotation about the z -axis C_4^3 and the primary mirror σ_h (i.e., $S_4^3 \equiv C_4^3 \circ \sigma_h = \sigma_h \circ C_4^3$).

Of particular importance for Mulliken symbols in D_{4h} is the primary rotation C_4 , the secondary rotations $C_2'(x)$ and $C_2'(y)$, and inversion i .

An irrep is first labeled based on its dimensionality: if one-dimensional, then A or B ; if two-dimensional, then E ; if three-dimensional, then T ; if four-dimensional, then G ; if five-dimensional, then H ; etc. Note that D_{4h} does not possess any irreps with dimensionality higher than two, but both the cubic O_h point group (with four three-dimensional irreps) and the icosahedral I_h point group (with four three-dimensional irreps, two four-dimensional irreps, and two five-dimensional irreps) do. For the one-dimensional cases, an irrep is labeled according to how it transforms under the primary rotation of the group: if symmetric, then as an A ; if antisymmetric, then as a B . For the specific case of D_{4h} , we see that the basis function $x^2 + y^2$ is left invariant under C_4 (since C_4 takes $x \rightarrow y$ and $y \rightarrow -x$, $x^2 + y^2 \rightarrow x^2 + y^2$ under C_4) while the basis function xy is negated under C_4 ($x \rightarrow y$ and $y \rightarrow -x$ sends the product $xy \rightarrow -xy$). Therefore, $x^2 + y^2$ belongs to an irrep labeled by an A Mulliken symbol, while xy belongs to an irrep labeled by a B (see Table 1.2).

An irrep is then labeled according to how it transforms under the secondary rotations of the group: if symmetric, then by the number 1 in the subscript; if antisymmetric, then by the number 2 in the subscript. For the specific case of D_{4h} , we see that the basis function $x^2 - y^2$ is left invariant under $C_2'(x)$ (since $C_2'(x)$ takes $x \rightarrow x$ and $y \rightarrow -y$, $x^2 - y^2 \rightarrow x^2 - y^2$ under $C_2'(x)$) while the basis function xy is negated under $C_2'(x)$ ($x \rightarrow x$ and $y \rightarrow -y$ sends the product $xy \rightarrow -xy$). Therefore, $x^2 - y^2$ belongs to an irrep labeled by a Mulliken symbol with a 1 in the subscript, while xy belongs to an irrep labeled by a Mulliken symbol with a 2 in the subscript (see Table 1.2).

An irrep is finally labeled according to how it transforms under spatial inversion i :

if symmetric, then by the letter g (*gerade*, German for “symmetric”) in the subscript; if antisymmetric, then by the letter u (*ungerade*, German for “antisymmetric”) in the subscript. For the specific case of D_{4h} , we see that the basis function xy is left invariant under i (since i takes $x \rightarrow -x$ and $y \rightarrow -y$, $xy \rightarrow xy$ under i) while the basis function (x, y) is negated under i ($x \rightarrow -x$ and $y \rightarrow -y$ sends $(x, y) \rightarrow (-x, -y)$). Therefore, xy belongs to an irrep labeled by a Mulliken symbol with a g in the subscript, while (x, y) belongs to an irrep labeled by a Mulliken symbol with a u in the subscript (see Table 1.2).

As a final comment for completeness, we briefly discuss the basis functions involving the rotations R_x , R_y , and R_z which also appear in Table 1.2. These basis functions represent three Cartesian components of a pseudovector \vec{R} formed from the cross product of two polar vectors. For ease of recall, one can think of R_i as the i -th component of the angular momentum vector or the magnetic dipole moment; however, if one does so, it is important to remember that the R_i basis functions do *not* imply anything about time-reversality even though the physical quantities angular momentum and magnetic moment *do* break time-reversal symmetry. Order parameters belonging to irreps transforming under point group operations as R_i may or may not break time reversal symmetry, but if we restrict ourselves to discussing only point group symmetry operations, we can imagine how an angular momentum vector would transform in order to visualize the symmetry properties of an irrep.

To be fully concrete, consider the basis function R_z , which can be imagined as the z -component of angular momentum according to $R_z = xp_y - yp_x$ (where x, y and p_x, p_y are components of the displacement and momentum vectors, respectively) and which can be assigned a Mulliken symbol in view of above. First, under C_4 , $x \rightarrow y$, $p_x \rightarrow p_y$, $y \rightarrow -x$, and $p_y \rightarrow -p_x$, and so $R_z = xp_y - yp_x \rightarrow (y)(-p_x) - (-x)(p_y) = R_z$ (i.e., invariant under C_4). Second, under $C_2'(x)$, $x \rightarrow x$, $p_x \rightarrow p_x$, $y \rightarrow -y$, and $p_y \rightarrow -p_y$, and so $R_z = xp_y - yp_x \rightarrow (x)(-p_y) - (-y)(p_x) = -R_z$ (i.e., antisymmetric under $C_2'(x)$). Finally, under i , $x \rightarrow -x$, $p_x \rightarrow -p_x$, $y \rightarrow -y$, and $p_y \rightarrow -p_y$, and so $R_z = xp_y - yp_x \rightarrow (-x)(-p_y) - (-y)(-p_x) = R_z$ (i.e., invariant under i). Thus, R_z belongs to the A_{2g} irrep in D_{4h} (see Table 1.2). However, despite the

fact that the z -component of the angular momentum is antisymmetric under time-reversality (since time-reversal leaves the displacement vector invariant and negates the momentum vector), there are classes of order parameters which belong to A_{2g} (and thus transform like R_z under point group operations) that nevertheless preserve time-reversal symmetry.

Chapter 2

Symmetry Constraints on the Elastoresistivity Tensor

In this chapter, a symmetry analysis is given for the elastoresistivity tensor $m_{ij,kl}$ based on the crystalline point group, focusing for pedagogic purposes on the D_{4h} point group (of relevance to several materials of current interest, including URu_2Si_2). The relation between $m_{ij,kl}$ and various thermodynamic susceptibilities is also discussed, particularly where the susceptibilities are sensitive to critical fluctuations proximate to a critical point at which a point group symmetry is spontaneously broken. This chapter is taken nearly verbatim from [55].

2.1 Introduction

Although the occurrence of a phase transition in a material is often reflected by anomalies in its resistivity, such transport measurements do not generally identify the precise nature of the underlying broken symmetry. However, as a derivative of the resistivity, the *elastoresistivity*—a fourth-rank tensor that linearly relates normalized resistivity changes and strain—is also sensitive to directional anisotropies and other point group symmetries which more subtly manifest in the resistivity itself. Yet despite its importance in the semiconductor industry [60], elastoresistivity has only

recently been exploited as a probe of broken symmetry in the field of strongly correlated electron systems [57, 58, 61–63]. Since the electrons in these materials are often strongly coupled to the crystal lattice as compared to simple metals, and because transport measurements are sensitive to long wavelength electronic excitations at the Fermi level, elastoresistivity is a potentially valuable tool in elucidating the nature of broken symmetries in these complex systems [59].

By measuring the temperature dependence of the in-plane elastoresistance, recent experiments have probed the nematic susceptibility of a series of iron-pnictide [58, 61, 62] and heavy fermion [57] superconductors, signaling in both cases the nematic character of the fluctuations associated with the underlying order parameter. However, earlier discussions were limited in scope, considering the zero magnetic field limit and mostly reasoning by analogy with the elastic stiffness tensor. To advance the technique, what is needed is a full theoretical exposition of the structure of the elastoresistivity tensor, including its symmetry constraints and its magnetic field dependence.

In this manuscript, we pedagogically discuss the constraints that symmetry imposes on the elastoresistivity tensor, both in the presence and absence of an externally applied magnetic field. Several aspects of this treatment are nontrivial due to the different ways in which the resistivity and strain tensors transform. To our knowledge, this is the first discussion of the symmetry properties of the full elastoresistivity tensor in the presence of a magnetic field or for a point group other than cubic O_h . We illustrate this with the specific point group of D_{4h} but emphasize that the symmetry principles that are outlined can be straightforwardly generalized to any point group. Given the constraints imposed by directly inherited and point group symmetries (Section 2.2), we derive in Section 2.3 the explicit form of the elastoresistivity tensor in D_{4h} (Eq. (2.13)). We then discuss how particular combinations of elastoresistivity coefficients are related to various thermodynamic susceptibilities of the material within the framework of the Landau paradigm of phase transitions (Section 2.4); it is this connection that makes elastoresistivity a powerful experimental quantity for determining the symmetry of an order parameter for a continuous phase transition.

2.2 Definition and Inherited Symmetries

The elastoresistivity tensor $m_{ij,kl}(\mathbf{H})$ is of fourth-rank and linearly relates the (normalized) strain-induced resistivity change $(\Delta\rho/\rho)_{ij}(\mathbf{H})$ and the strain ϵ_{kl} according to

$$m_{ij,kl}(\mathbf{H}) \equiv \left. \frac{\partial (\Delta\rho/\rho)_{ij}(\mathbf{H})}{\partial \epsilon_{kl}} \right|_{\hat{\epsilon}=\hat{0}}, \quad (2.1)$$

where we write $(\Delta\rho/\rho)_{ij}(\mathbf{H})$ and ϵ_{kl} as the nine component vectors

$$(\Delta\rho/\rho)_{ij}(\mathbf{H}) = \begin{pmatrix} (\Delta\rho/\rho)_{xx}(\mathbf{H}) \\ (\Delta\rho/\rho)_{yy}(\mathbf{H}) \\ (\Delta\rho/\rho)_{zz}(\mathbf{H}) \\ (\Delta\rho/\rho)_{yz}(\mathbf{H}) \\ (\Delta\rho/\rho)_{zy}(\mathbf{H}) \\ (\Delta\rho/\rho)_{zx}(\mathbf{H}) \\ (\Delta\rho/\rho)_{xz}(\mathbf{H}) \\ (\Delta\rho/\rho)_{xy}(\mathbf{H}) \\ (\Delta\rho/\rho)_{yx}(\mathbf{H}) \end{pmatrix} \quad \text{and} \quad \epsilon_{kl} = \begin{pmatrix} \epsilon_{xx} \\ \epsilon_{yy} \\ \epsilon_{zz} \\ \epsilon_{yz} \\ \epsilon_{zy} \\ \epsilon_{zx} \\ \epsilon_{xz} \\ \epsilon_{xy} \\ \epsilon_{yx} \end{pmatrix}$$

in order to represent $m_{ij,kl}(\mathbf{H})$ as a 9×9 matrix. Whereas the strain tensor is defined in a manifestly symmetric manner¹ ($\epsilon_{kl} \equiv \frac{1}{2}(\frac{\partial u_k}{\partial x_l} + \frac{\partial u_l}{\partial x_k})$) and so there is no need to distinguish between off-diagonal terms (e.g., $\epsilon_{zx} = \epsilon_{xz}$), the same is not generally true of changes in resistivity in a magnetic field, where for example the Hall effect explicitly requires $(\Delta\rho/\rho)_{ij}(\mathbf{H}) \neq (\Delta\rho/\rho)_{ji}(\mathbf{H})$ for finite \mathbf{H} ; therefore, we choose not to use the compactified Voigt notation and instead include all nine components of both the change in resistivity and strain tensors.

As written, there is some ambiguity about the normalization constant ρ in each component of the change in resistance tensor, and in particular in the off-diagonal

¹As written here, ϵ_{kl} refers to the infinitesimal strain tensor; however, there is an alternative convention when using the Voigt notation (which we have used in earlier work [58,62]) involving the engineering strain e_{kl} . The two are related by $e_{kl} = \epsilon_{kl}$ for $k = l$ and $e_{kl} = 2\epsilon_{kl}$ for $k \neq l$.

terms where $\rho_{ij} = 0$ in vanishing magnetic field. From the perspective of symmetry, and in order to preserve the transformation properties of $(\Delta\rho/\rho)_{ij}(\mathbf{H})$ as a second-rank tensor, the following normalization scheme is motivated. Perturbatively, the strained resistivity tensor $\rho_{ij}(\hat{\epsilon})$ is equal to the unstrained resistivity $\rho_{ij}(\hat{\epsilon} = \hat{0})$ plus a strain-induced resistivity change $\Delta\rho_{ij}(\hat{\epsilon})$:

$$\rho_{ij}(\hat{\epsilon}) = \rho_{ij}(\hat{\epsilon} = \hat{0}) + \Delta\rho_{ij}(\hat{\epsilon}). \quad (2.2)$$

If the tensors were scalars, we would unambiguously factor out ρ to define $\Delta\rho/\rho$; however, since $\rho_{ij}(\hat{\epsilon} = \hat{0})$ is a tensor which does not generally commute with $\Delta\rho_{ij}(\hat{\epsilon})$, one would obtain a different result depending on whether $\rho_{ij}(\hat{\epsilon} = \hat{0})$ was factored on the left or right. Instead, we define the symmetric factorization

$$(\Delta\rho/\rho) \equiv (\boldsymbol{\rho}(\hat{\epsilon} = \hat{0}))^{-1/2} \cdot \boldsymbol{\Delta\rho}(\hat{\epsilon}) \cdot (\boldsymbol{\rho}(\hat{\epsilon} = \hat{0}))^{-1/2}, \quad (2.3)$$

which in the limit of $\rho_{ii} \gg \rho_{ij}$ ($i \neq j$) results in

$$(\Delta\rho/\rho)_{ij} \equiv (\Delta\rho_{ij}/\sqrt{\rho_{ii}\rho_{jj}}). \quad (2.4)$$

This normalization scheme preserves the transformation properties of $(\Delta\rho/\rho)_{ij}$ as a second-rank tensor and ensures that all symmetries of $\Delta\rho_{ij}(\hat{\epsilon})$ are retained in $(\Delta\rho/\rho)_{ij}$ (i.e., preserves the group structure of $\Delta\rho_{ij}(\hat{\epsilon})$).

2.2.1 Directly Inherited Symmetries

The symmetry properties possessed by the change in resistivity and strain tensors are retained by the elastoresistivity tensor as well, and correspondingly constrain the number of independent coefficients. For the change in resistivity tensor, the relevant symmetry is given by the Onsager relationship² [64] $(\Delta\rho/\rho)_{ij}(\mathbf{H}) = (\Delta\rho/\rho)_{ji}(-\mathbf{H})$,

²Strictly, the Onsager relation applies to $\rho_{ij}(\mathbf{H})$; however, it carries over to $(\Delta\rho/\rho)_{ij}(\mathbf{H})$ as well. Since Onsager obtains for both $\rho_{ij}(\hat{\epsilon} = \hat{0})$ and $\rho_{ij}(\hat{\epsilon})$, it necessarily holds for $\Delta\rho_{ij}(\hat{\epsilon}) \equiv \rho_{ij}(\hat{\epsilon}) - \rho_{ij}(\hat{\epsilon} = \hat{0})$ too. Using the normalization scheme of Eq. (2.4), it follows that

$$(\Delta\rho/\rho)_{ij}(\mathbf{H}) = (\Delta\rho_{ij}(\mathbf{H})/\sqrt{\rho_{ii}(\mathbf{H})\rho_{jj}(\mathbf{H})}) = (\Delta\rho_{ji}(-\mathbf{H})/\sqrt{\rho_{ii}(-\mathbf{H})\rho_{jj}(-\mathbf{H})}) = (\Delta\rho/\rho)_{ji}(-\mathbf{H}).$$

which directly implies that $m_{ij,kl}(\mathbf{H}) = m_{ji,kl}(-\mathbf{H})$. The symmetry of the strain tensor $\epsilon_{kl} = \epsilon_{lk}$ transfers as well, requiring that $m_{ij,kl}(\mathbf{H}) = m_{ij,lk}(\mathbf{H})$. These symmetries reduce the 81 independent $m_{ij,kl}(\mathbf{H})$ to 54.

2.2.2 Point Group Symmetry Constraints

In addition to the directly inherited symmetries, the form of the elastoresistivity tensor depends on the point group symmetry of the crystal lattice³ and the presence and direction of a magnetic field. Under generic coordinate transformations, the elastoresistivity tensor is transformed as $m \rightarrow m'$ according to

$$m'_{ij,kl} = O_{ia}O_{jb}O_{kc}O_{ld}m_{ab,cd}, \quad (2.5)$$

where O_{ia} is the appropriate transformation matrix relating the two coordinate systems.⁴ However, when the coordinate transformation is a group element of the crystalline point group, this physical response function is necessarily invariant, i.e.,

³For a bulk single crystal characterized by a particular point group, there is no ambiguity as to the relevant symmetry operations that are included in the group; the general form of the constraints that these symmetries impose on the elastoresistivity tensor are elucidated in the main text. The situation is less clear for the cases of thin film heterostructures or topological materials, where the electrons conduct at an interface or surface, respectively. The present elastoresistivity formalism can be applied to these cases as well, but the relevant point group that constrains the elastoresistivity tensor is not necessarily the point group of the bulk; instead, the relevant point group consists only of those operations that are global symmetries of the bulk and interface/surface, which is in general a subgroup of the bulk.

⁴We note that in our compactified notation where the fourth rank tensor $m_{ij,kl}$ is represented as a single matrix, Eq. (2.5) is simply a basis transformation of matrices $m_{\alpha\beta} = \Lambda_{\alpha\mu}\Lambda_{\beta\nu}m_{\mu\nu}$, where $\Lambda_{\alpha\mu}$ is a Kronecker product of the coordinate transformation matrices O by $\Lambda = O \otimes O$. In particular, in the basis of strain where $\vec{\epsilon} = (\epsilon_{xx}, \epsilon_{yy}, \epsilon_{zz}, \epsilon_{yz}, \epsilon_{zy}, \epsilon_{zx}, \epsilon_{xz}, \epsilon_{xy}, \epsilon_{yx})^T$ (and likewise for change in resistivity), the transformation Λ is a 9×9 matrix given by

$$\Lambda = \begin{pmatrix} O_{xx}O_{xx} & O_{xx}O_{yy} & \cdots & O_{xx}O_{yx} \\ O_{yy}O_{xx} & O_{yy}O_{yy} & \cdots & O_{yy}O_{yx} \\ \vdots & \vdots & \ddots & \vdots \\ O_{yx}O_{xx} & O_{yx}O_{yy} & \cdots & O_{yx}O_{yx} \end{pmatrix}.$$

The specific values of the elements of the O matrices depend on how the particular transformation operates on the basis vectors. As an illustrative example, for the σ_z transformation, $O_{xx} = O_{yy} = 1$, $O_{zz} = -1$, and all other $O_{ij} = 0$.

$m'_{ij,kl} = m_{ij,kl}$, and this equation leads to constraints on the individual elements of the elastoresistivity tensor. This is the essence of Neumann's principle.

From hereon, we will specialize to symmetry operations of the point group D_{4h} , which consists of 16 symmetry elements involving mirrors, rotations, and improper rotations. Our motivation for choosing this particular point group to illustrate the symmetry properties of the elastoresistivity tensor is due to the fact that several materials of current interest have such a symmetry; in particular, but not exclusively, materials that have the common ThCr_2Si_2 structure type crystallize in this point group. However, the symmetry considerations that we outline below can be readily applied to other point groups. Generally, the presence of a finite \mathbf{H} reduces the symmetry of the point group to a subgroup of D_{4h} , with the particular subgroup depending on the orientation of the field relative to the primitive axes;⁵ for simplicity and throughout, we will assume that all magnetic fields are oriented along the primary rotation axis (i.e., c axis) of the crystal, which we choose to label as the z direction (i.e., $\mathbf{H} = H_z \hat{z}$). To derive the symmetry constraints imposed by the point group, we need only consider the set of all rotations and reflections that are group elements;⁶ we now consider all such elements of D_{4h} independently and enumerate their implications for the elastoresistivity tensor.

First, consider the mirror operation about the xy plane (denoted by σ_z), which is represented in matrix form (with a Cartesian basis) as

$$\sigma_z = \begin{pmatrix} 1 & 0 & 0 \\ 0 & 1 & 0 \\ 0 & 0 & -1 \end{pmatrix}. \quad (2.6)$$

σ_z takes $z \rightarrow -z$ while leaving the other spatial dimensions unchanged and correspondingly transforms the elastoresistivity tensor according to $m_{ij,kl}(H_z \hat{z}) \xrightarrow{\sigma_z}$

⁵For example, a magnetic field $\mathbf{H} = H_z \hat{z}$ (oriented along the [001] crystallographic direction) reduces the crystalline point group from D_{4h} to C_{4h} , a field $\mathbf{H} = H_x \hat{x}$ (oriented along the [100] crystallographic direction) reduces the point group from D_{4h} to C_{2h} , and an arbitrarily oriented magnetic field reduces D_{4h} to C_i .

⁶Improper rotations are compositions of reflections and rotations, and so they do not impose additional constraints on the elastoresistivity tensor beyond those from the reflections and rotations individually.

$(-1)^{\mathcal{N}_z} m_{ij,kl}(\sigma_z H_z \hat{z})$, where \mathcal{N}_z is the number of times a z index appears among the $\{i, j, k, l\}$. In order to discern how the mirror operation $\sigma_{\hat{n}}$ acts on the magnetic field (where \hat{n} denotes the normal vector to the mirror plane), we decompose its action into an inversion and a rotation by π radians about the \hat{n} axis: $\sigma_{\hat{n}} = O_{\hat{n}}(\pi) \cdot \mathcal{I}$. Since the magnetic field is a pseudovector, it rotates as a regular vector but is invariant under inversion; therefore, since $O_{\hat{z}}(\pi) H_z \hat{z} = H_z \hat{z}$, $\sigma_z H_z \hat{z} = H_z \hat{z}$ and for a crystal with mirror symmetry about the xy plane

$$m_{ij,kl}(H_z) = (-1)^{\mathcal{N}_z} m_{ij,kl}(H_z) \begin{bmatrix} \sigma_z \end{bmatrix}. \quad (2.7)$$

There are analogous relations for the mirror symmetries about the yz and xz planes as well (σ_x and σ_y , respectively, where again the subscripts denote normal directions to the mirror plane), although care must be taken to account for the transformation of the magnetic field. Since $\sigma_{\hat{x}} H_z \hat{z} = \sigma_{\hat{y}} H_z \hat{z} = -H_z \hat{z}$, these mirror symmetries then require

$$\begin{aligned} m_{ij,kl}(H_z) &= (-1)^{\mathcal{N}_x} m_{ij,kl}(-H_z) \begin{bmatrix} \sigma_x \end{bmatrix} \\ m_{ij,kl}(H_z) &= (-1)^{\mathcal{N}_y} m_{ij,kl}(-H_z) \begin{bmatrix} \sigma_y \end{bmatrix}. \end{aligned} \quad (2.8)$$

The final mirror symmetries contained in D_{4h} are the diagonal reflections about the planes spanned by the lines $x = \pm y$ and the z axis. These symmetry operations (denoted $\sigma_{x=y}$ and $\sigma_{x=-y}$, respectively, where again the subscripts denote normal directions to the mirror plane) take (in the Cartesian basis) the matrix form

$$\sigma_{x=y} = \begin{pmatrix} 0 & -1 & 0 \\ -1 & 0 & 0 \\ 0 & 0 & 1 \end{pmatrix}, \quad \sigma_{x=-y} = \begin{pmatrix} 0 & 1 & 0 \\ 1 & 0 & 0 \\ 0 & 0 & 1 \end{pmatrix} \quad (2.9)$$

and transform the magnetic field as $\sigma_{x=\pm y} H_z \hat{z} = -H_z \hat{z}$; correspondingly, the elastoresistivity tensor is constrained according to

$$\begin{aligned}
m_{ij,kl}(H_z) &= (-1)^{N_x+N_y} m_{ij,kl}(-H_z) \Big|_{x \leftrightarrow y} \left[\sigma_{x=y} \right] \\
m_{ij,kl}(H_z) &= m_{ij,kl}(-H_z) \Big|_{x \leftrightarrow y} \left[\sigma_{x=-y} \right],
\end{aligned} \tag{2.10}$$

where $\Big|_{x \leftrightarrow y}$ conveys that all initial x and y indices are to be interchanged upon the symmetry operation.

The final set of symmetry constraints is imposed by rotational symmetries. D_{4h} possesses a primary fourfold rotational symmetry about the z axis (C_4), two secondary twofold rotations about the x and y axes ($C'_2(x)$ and $C'_2(y)$, respectively), and two tertiary twofold rotations about the lines $x = \pm y$ ($C''_2(1)$ and $C''_2(2)$, respectively). The operations are represented in matrix form (in the Cartesian basis) as

$$\begin{aligned}
C_4 &= \begin{pmatrix} 0 & -1 & 0 \\ 1 & 0 & 0 \\ 0 & 0 & 1 \end{pmatrix}, & C'_2(x) &= \begin{pmatrix} 1 & 0 & 0 \\ 0 & -1 & 0 \\ 0 & 0 & -1 \end{pmatrix}, & C'_2(y) &= \begin{pmatrix} -1 & 0 & 0 \\ 0 & 1 & 0 \\ 0 & 0 & -1 \end{pmatrix}, \\
C''_2(1) &= \begin{pmatrix} 0 & 1 & 0 \\ 1 & 0 & 0 \\ 0 & 0 & -1 \end{pmatrix}, & C''_2(2) &= \begin{pmatrix} 0 & -1 & 0 \\ -1 & 0 & 0 \\ 0 & 0 & -1 \end{pmatrix}.
\end{aligned} \tag{2.11}$$

The primary rotational symmetry preserves the magnetic field orientation while the secondary and tertiary rotations invert the field, and so the rotational symmetry operations collectively require that the elastoresistivity tensor obey

Table 2.1: **Elastoresistivity Symmetry Properties**

(Assuming $\mathbf{H} = H_z \hat{z}$)

Principle / Symmetry	Elastoresistivity Constraint
Onsager	$m_{ij,kl}(H_z) = m_{ji,kl}(-H_z)$
Strain Definition	$m_{ij,kl}(H_z) = m_{ij,lk}(H_z)$
σ_x Mirror	$m_{ij,kl}(H_z) = (-1)^{\mathcal{N}_x} m_{ij,kl}(-H_z)$
σ_y Mirror	$m_{ij,kl}(H_z) = (-1)^{\mathcal{N}_y} m_{ij,kl}(-H_z)$
σ_z Mirror	$m_{ij,kl}(H_z) = (-1)^{\mathcal{N}_z} m_{ij,kl}(H_z)$
$\sigma_{x=y}$ Mirror	$m_{ij,kl}(H_z) = (-1)^{\mathcal{N}_x + \mathcal{N}_y} m_{ij,kl}(-H_z) \Big _{x \leftrightarrow y}$
$\sigma_{x=-y}$ Mirror	$m_{ij,kl}(H_z) = m_{ij,kl}(-H_z) \Big _{x \leftrightarrow y}$
C_4 Rotation	$m_{ij,kl}(H_z) = (-1)^{\mathcal{N}_y} m_{ij,kl}(H_z) \Big _{x \leftrightarrow y}$
$C'_2(x)$ Rotation	$m_{ij,kl}(H_z) = (-1)^{\mathcal{N}_y + \mathcal{N}_z} m_{ij,kl}(-H_z)$
$C'_2(y)$ Rotation	$m_{ij,kl}(H_z) = (-1)^{\mathcal{N}_x + \mathcal{N}_z} m_{ij,kl}(-H_z)$
$C''_2(1)$ Rotation	$m_{ij,kl}(H_z) = (-1)^{\mathcal{N}_z} m_{ij,kl}(-H_z) \Big _{x \leftrightarrow y}$
$C''_2(2)$ Rotation	$m_{ij,kl}(H_z) = (-1)^{\mathcal{N}_x + \mathcal{N}_y + \mathcal{N}_z} m_{ij,kl}(-H_z) \Big _{x \leftrightarrow y}$

$$\begin{aligned}
m_{ij,kl}(H_z) &= (-1)^{\mathcal{N}_y} m_{ij,kl}(H_z) \Big|_{x \leftrightarrow y} && [C_4] \\
m_{ij,kl}(H_z) &= (-1)^{\mathcal{N}_y + \mathcal{N}_z} m_{ij,kl}(-H_z) && [C'_2(x)] \\
m_{ij,kl}(H_z) &= (-1)^{\mathcal{N}_x + \mathcal{N}_z} m_{ij,kl}(-H_z) && [C'_2(y)] \\
m_{ij,kl}(H_z) &= (-1)^{\mathcal{N}_z} m_{ij,kl}(-H_z) \Big|_{x \leftrightarrow y} && [C''_2(1)] \\
m_{ij,kl}(H_z) &= (-1)^{\mathcal{N}_x + \mathcal{N}_y + \mathcal{N}_z} m_{ij,kl}(-H_z) \Big|_{x \leftrightarrow y} && [C''_2(2)].
\end{aligned} \tag{2.12}$$

The totality of these symmetries and their consequences for the elastoresistivity tensor

are summed up in Table 2.1.

2.3 Elastoresistivity Tensor for D_{4h}

We now explicitly write down the elastoresistivity tensor for the D_{4h} point group, which possesses all of the symmetries in Table 2.1. These conditions require that certain coefficients vanish (e.g., σ_z symmetry requires $m_{xx,yz}(H_z) = -m_{xx,yz}(H_z) = 0$) while equating certain others (e.g., C_4 symmetry requires $m_{yy,xx}(H_z) = m_{xx,yy}(H_z)$). Imposing all symmetry constraints, the elastoresistivity tensor is given as⁷

$$m_{ij,kl}^{D_{4h}}(H_z) = \begin{pmatrix} m_{xx,xx} & m_{xx,yy} & m_{xx,zz} & 0 & 0 & 0 & 0 & 0 & 0 & 0 \\ m_{xx,yy} & m_{xx,xx} & m_{xx,zz} & 0 & 0 & 0 & 0 & 0 & 0 & 0 \\ m_{zz,xx} & m_{zz,xx} & m_{zz,zz} & 0 & 0 & 0 & 0 & 0 & 0 & 0 \\ 0 & 0 & 0 & m_{yz,yz} & m_{yz,yz} & \boxed{m_{yz,zx} \quad m_{yz,zx}} & 0 & 0 & 0 & 0 \\ 0 & 0 & 0 & m_{yz,yz} & m_{yz,yz} & \boxed{-m_{yz,zx} \quad -m_{yz,zx}} & 0 & 0 & 0 & 0 \\ 0 & 0 & 0 & \boxed{m_{yz,zx} \quad m_{yz,zx}} & \boxed{m_{yz,zx} \quad m_{yz,zx}} & m_{yz,yz} & m_{yz,yz} & 0 & 0 & 0 \\ 0 & 0 & 0 & \boxed{-m_{yz,zx} \quad -m_{yz,zx}} & \boxed{-m_{yz,zx} \quad -m_{yz,zx}} & m_{yz,yz} & m_{yz,yz} & 0 & 0 & 0 \\ \hline m_{xy,xx} & m_{xy,xx} & m_{xy,zz} & 0 & 0 & 0 & 0 & m_{xy,xy} & m_{xy,xy} & 0 \\ -m_{xy,xx} & -m_{xy,xx} & -m_{xy,zz} & 0 & 0 & 0 & 0 & m_{xy,xy} & m_{xy,xy} & 0 \end{pmatrix}. \quad (2.13)$$

This tensor has 10 independent coefficients, all implicitly dependent on the magnetic field. Those coefficients (of which there are seven) that have an even number of x and an even number of y indices are correspondingly even functions of the magnetic field due to the σ_x and σ_y symmetry constraints; conversely, those coefficients (of which there are three, demarcated by surrounding boxes) that have an odd number of x and an odd number of y indices are odd functions of the magnetic field (and consequently vanish in zero field).

⁷Earlier work [58] incorrectly stated that $m_{xx,zz} = m_{zz,xx}$ (in the earlier notation, that $m_{13} = m_{31}$). This is incorrect because there is no general reason why $m_{xx,zz} = \partial(\Delta\rho/\rho)_{xx}/\partial\epsilon_{zz}$ should be related to $m_{zz,xx} = \partial(\Delta\rho/\rho)_{zz}/\partial\epsilon_{xx}$, although they could be if the point group symmetry constrains it so (e.g., $m_{xx,zz} = m_{zz,xx}$ for the case of the cubic O_h point group).

The asymmetric appearance of $m_{ij,kl}^{D_{4h}}(H_z)$ in (2.13) is fundamentally due to the definition of the elastoresistivity tensor in (2.1), which does not generally admit interchanging the ij and kl indices; this stands in contrast to the elastic stiffness tensor $C_{ij,kl}$, which generally does have the symmetry $ij \leftrightarrow kl$ because of its symmetric definition as the second derivative of the elastic energy density \mathcal{U} : $C_{ij,kl} \equiv \partial^2 \mathcal{U} / \partial \epsilon_{ij} \partial \epsilon_{kl}$. The zeros in the upper right corner are enforced by Onsager and either σ_x or σ_y symmetry, but these symmetries only constrain the boxed terms to be odd functions of the magnetic field (i.e., they only vanish in zero field).

2.4 Connection to Thermodynamic Susceptibilities

A primary motivation for measuring elastoresistivity coefficients is their connection to thermodynamic susceptibilities. Building on our earlier work [57–59, 61, 62] and employing a more general formalism, we outline this connection in greater detail.

Continuous phase transitions can be experimentally identified by the observation of a diverging thermodynamic susceptibility across a phase boundary. For example, in the thermal phase transition of an Ising ferromagnet with a Curie temperature θ_C , the magnetic susceptibility $\chi_M \equiv \lim_{H \rightarrow 0} \frac{dM}{dH}$ (i.e., the rate that the order parameter M changes in response to its conjugate field H , the magnetic field) progressively increases on cooling from $T > \theta_C$ until it diverges at the phase transition. Crucially, the measurement of such a susceptibility is only possible when an available external experimental probe has the same symmetry as (and hence is conjugate to) the order parameter describing the phase transition. Here, we discuss the classes of order parameters which couple nontrivially (i.e., in a manner which can convey symmetry information about the order parameter) to externally applied strain fields. We emphasize that this discussion is limited to mean field analyses where Landau theory applies; however, treatments beyond mean field do not change the symmetry classifications of the order parameter inferred from a measurement. In fact, many elastoresistivity experiments to date can be well described within the framework of mean field theory [57, 58, 61, 62].

Within the Landau paradigm of phase transitions, the singular part of the free

energy at a symmetry breaking transition is an analytic function of the order parameter which respects all of the symmetries of the disordered phase of the system. Thus, near a generic phase transition, one can expand the free energy in powers of the order parameter(s) and conjugate field(s), with each term transforming as the identity in the space group of the symmetric phase of the crystal. A generic externally applied strain can only break point group symmetries, and so only order parameters (or products of order parameters, i.e., composite order parameters) which break *exclusively* point group symmetries may couple nontrivially to strain. In this instance, nontrivial coupling refers to terms which are *linear* in the strain ϵ_{kl} ; terms that are quadratic in strain, with the form $\epsilon^2|\Delta|^2$, are allowed for any order parameter Δ (since both ϵ^2 and $|\Delta|^2$ transform individually as the identity) and so generically provide no symmetry information (since they are allowed for any strain or order parameter).

We can therefore identify two classes of order parameters for which external strain proves to be a useful probe: (i) a scalar order parameter ψ that breaks only point group symmetries; (ii) a composite order parameter (derived from a vector order parameter $\vec{\phi}$) that breaks only point group symmetries. In the former case, the general form of the free energy expansion to quartic order near a continuous phase transition is

$$f(\psi, \epsilon) = f_0 + \frac{1}{2}a_0(T - T_c)\psi_{\Gamma_i}^2 + \frac{1}{4}b\psi_{\Gamma_i}^4 + \frac{1}{2}c\epsilon_{\Gamma_i}^2 + \frac{1}{4}d\epsilon_{\Gamma_i}^4 + \lambda\psi_{\Gamma_i}\epsilon_{\Gamma_i}, \quad (2.14)$$

where f_0 is a nonsingular contribution to free energy, the quadratic coefficient changes sign at the transition temperature T_c , b and d are positive to assure f is bounded from below, the coefficient c is the symmetry-dictated combination of elastic moduli, and in the bilinear term ψ_{Γ_i} and ϵ_{Γ_i} both belong to the same nontrivial irreducible representation⁸ of the point group. It is this last term which allows one to measure a thermodynamic susceptibility: any measurement sensitive to the strain ϵ_{Γ_i} has contributions from the fluctuations of ψ_{Γ_i} which diverge at the phase transition.

For concreteness, let us once more consider the specific case of the D_{4h} point

⁸If Γ_i transformed like the identity of the point group, no symmetry would be broken, and hence the order parameter would not be well-defined.

group, where an arbitrary strain can be decomposed into five distinct combinations: $\frac{1}{2}(\epsilon_{xx} + \epsilon_{yy})$, ϵ_{zz} , $\frac{1}{2}(\epsilon_{xx} - \epsilon_{yy})$, ϵ_{xy} , and $\begin{pmatrix} \epsilon_{xz} \\ \epsilon_{yz} \end{pmatrix}$ (Figure 2.1, Table 2.2). Only the last three involve a breaking of point group symmetries, and so the bilinear coupling term in (2.14) can correspondingly have three forms depending on the particular irrep of the strain, with an associated thermodynamic susceptibility defined by

$$\chi_{\Gamma_i} \equiv \lim_{\epsilon_{\Gamma_i} \rightarrow 0} \frac{d\psi_{\Gamma_i}}{d\epsilon_{\Gamma_i}}. \quad (2.15)$$

Thus, one can experimentally determine the irreducible representation to which ψ_{Γ_i} belongs by applying a strain with a definite Γ_i character. Any observed divergence in χ_{Γ_i} signals that ψ belongs to Γ_i , exactly in analogy to the ferromagnetic case. A recent example of this corresponds to the case of electronic nematic order in $\text{Ba}(\text{Fe}_{1-x}\text{Co}_x)_2\text{As}_2$ for which the tetragonal to orthorhombic transition precedes the subsequent magnetic order [58, 61, 62]. Because there is a continuous transition to a phase in which only C_4 symmetry has been broken (down to C_2) in these materials, *at the level of mean field theory*, the order parameter is a scalar belonging to the B_{2g} representation of D_{4h} and so belongs in this first class of theories. We note that this statement is independent of the microscopic origin of nematicity (whether induced by spin fluctuations or a result of orbital ordering [65]).

In the second class of theories, while the order parameters break extra symmetries (e.g., translation, time reversal, gauge invariance, etc.), there is some product of the order parameter fields which breaks solely point group symmetries. Focusing once more on systems with the point group D_{4h} , we note that despite the breaking of additional symmetries by the order parameter, terms that are linear in strain but quadratic in order parameters are possible when the order parameter is a (generally complex) vector $\vec{\phi} = (\phi_a, \phi_b)$ that transforms like any of the two dimensional (E_u or E_g) representations of D_{4h} . In such a scenario, the generic form of the free energy is

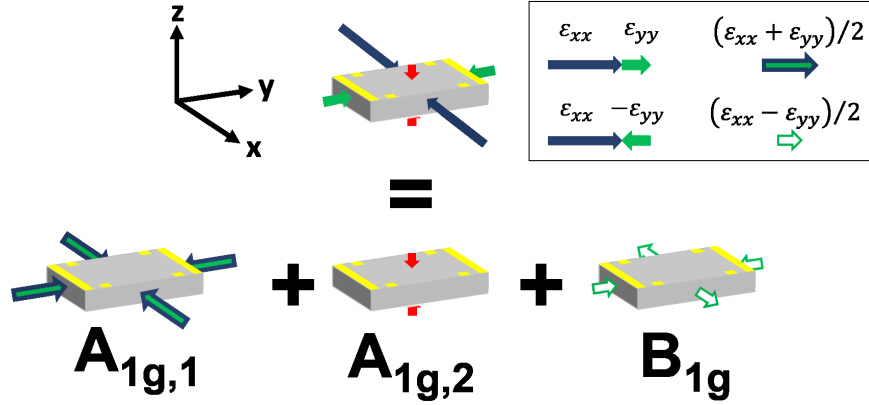


Figure 2.1: Schematic illustration of an arbitrary shearless strain in D_{4h} as decomposed in terms of three irreducible components:

$$\begin{pmatrix} \epsilon_{xx} & 0 & 0 \\ 0 & \epsilon_{yy} & 0 \\ 0 & 0 & \epsilon_{zz} \end{pmatrix} = \epsilon_{A_{1g,1}} \begin{pmatrix} 1 & 0 & 0 \\ 0 & 1 & 0 \\ 0 & 0 & 0 \end{pmatrix} + \epsilon_{A_{1g,2}} \begin{pmatrix} 0 & 0 & 0 \\ 0 & 0 & 0 \\ 0 & 0 & 1 \end{pmatrix} + \epsilon_{B_{1g}} \begin{pmatrix} 1 & 0 & 0 \\ 0 & -1 & 0 \\ 0 & 0 & 0 \end{pmatrix},$$

where $\epsilon_{A_{1g,1}} = \frac{1}{2}(\epsilon_{xx} + \epsilon_{yy})$, $\epsilon_{A_{1g,2}} = \epsilon_{zz}$, and $\epsilon_{B_{1g}} = \frac{1}{2}(\epsilon_{xx} - \epsilon_{yy})$. The gray parallelepiped represents a crystalline sample; the yellow regions represent electrical contacts used for transport measurements.

$$\begin{aligned} f(\phi, \epsilon) = & \frac{1}{2}a_0(T - T_c) (|\phi_a|^2 + |\phi_b|^2) + \frac{1}{4}b (|\phi_a|^2 + |\phi_b|^2)^2 \\ & + \frac{1}{4}g (|\phi_a|^2 - |\phi_b|^2)^2 + \frac{1}{2}c\epsilon_{\Gamma_i}^2 + \frac{1}{4}d\epsilon_{\Gamma_i}^4 + \lambda (|\phi_a|^2 - |\phi_b|^2) \epsilon_{\Gamma_i}, \end{aligned} \quad (2.16)$$

where the combination $(|\phi_a|^2 - |\phi_b|^2)$ transforms as an irreducible representation Γ_i of the point group. Examples of such a theory include superconducting states with degenerate p_x and p_y symmetry (where the coupling is to $\epsilon_{B_{1g}}$) or an incommensurate charge density wave⁹ with wave vectors oriented along the $[110]$ and $[1\bar{1}0]$ directions (where the coupling is to $\epsilon_{B_{2g}}$). Because there is no longer a bilinear coupling between strain and the order parameter, a diverging susceptibility is not generically

⁹We emphasize incommensurate CDWs because the Landau theory of commensurate CDWs may include other terms consistent with the commensurability. For example, a period 3 CDW with order parameter ϕ_Q also has terms in the free energy of the form $\delta f = \kappa\phi_Q^3$.

Table 2.2: Irreducible Representations of D_{4h} with Representations in Strain

Irreducible Representation (Koster Notation [66, 67] & Mulliken Symbol [68, 69])	Strain	Strain-Induced Resistivity Change
$\Gamma_1^+ = A_{1g}$	$\epsilon_{A_{1g,1}} = \frac{1}{2}(\epsilon_{xx} + \epsilon_{yy})$ $\epsilon_{A_{1g,2}} = \epsilon_{zz}$	$(\Delta\rho/\rho)_{A_{1g,1}}(H_z) = \frac{1}{2} \left[(\Delta\rho/\rho)_{xx}(H_z) + (\Delta\rho/\rho)_{yy}(H_z) \right]$ $(\Delta\rho/\rho)_{A_{1g,2}}(H_z) = (\Delta\rho/\rho)_{zz}(H_z)$
$\Gamma_3^+ = B_{1g}$	$\epsilon_{B_{1g}} = \frac{1}{2}(\epsilon_{xx} - \epsilon_{yy})$	$(\Delta\rho/\rho)_{B_{1g}}(H_z) = \frac{1}{2} \left[(\Delta\rho/\rho)_{xx}(H_z) - (\Delta\rho/\rho)_{yy}(H_z) \right]$
$\Gamma_4^+ = B_{2g}$	$\epsilon_{B_{2g}} = \frac{1}{2}(\epsilon_{xy} + \epsilon_{yx}) = \epsilon_{xy}$	$(\Delta\rho/\rho)_{B_{2g}}(H_z) = \frac{1}{2} \left[(\Delta\rho/\rho)_{xy}(H_z) + (\Delta\rho/\rho)_{yx}(H_z) \right]$
$\Gamma_5^+ = E_g$	$\epsilon_{E_g} = \frac{1}{2} \begin{pmatrix} \epsilon_{xz} + \epsilon_{zx} \\ \epsilon_{yz} + \epsilon_{zy} \end{pmatrix} = \begin{pmatrix} \epsilon_{xz} \\ \epsilon_{yz} \end{pmatrix}$	$(\Delta\rho/\rho)_{E_g}(H_z) = \frac{1}{2} \left(\begin{matrix} (\Delta\rho/\rho)_{xz}(H_z) + (\Delta\rho/\rho)_{zx}(H_z) \\ (\Delta\rho/\rho)_{yz}(H_z) + (\Delta\rho/\rho)_{zy}(H_z) \end{matrix} \right)$

In enumerating the irreps of D_{4h} with representations in strain, we have chosen $\frac{1}{2}(x^2 + y^2)$ and z^2 as the two quadratic basis functions for A_{1g} . This is a standard choice, but there is another equally standard choice involving the basis functions $\frac{1}{3}(x^2 + y^2 + z^2)$ and $\frac{1}{6}(2z^2 - x^2 - y^2)$, which when represented in strain corresponds to decomposing an arbitrary deformation into a volume-changing component and a volume-preserving component.

measured. Instead, any measurement which is sensitive to the symmetry class Γ_i will track fluctuations of the composite order parameter ($|\phi_a|^2 - |\phi_b|^2$) close to the transition. While at temperatures far above the transition one anticipates a Curie-Weiss-like temperature dependence (as long as there is a broad fluctuational regime of $\vec{\phi}$), when ϕ_a or ϕ_b orders at the transition, these fluctuations are proportional to the square of the fundamental order parameter, and so such a measurement is essentially proportional to the singular contribution to the heat capacity associated with this order parameter; heat capacity-like singularities in the susceptibility may then be observed [57].

With such considerations in mind, we now return to the case of an order parameter which breaks solely point group symmetries and discuss its relation to transport measurements. While the order parameter ψ is strictly a thermodynamic quantity, it is linearly proportional to all other physical quantities (including non-thermodynamic ones) in the same symmetry class for small values of the order parameter. In particular, if ψ belongs to the Γ_i irrep of the point group, then the strain-induced resistivity

change in the same symmetry channel scales as $(\Delta\rho/\rho)_{\Gamma_i} \sim \psi_{\Gamma_i} + \mathcal{O}(\psi_{\Gamma_i}^3)$. For the strains accessible in D_{4h} , the conjugate resistivity change is given in Table 2.2, and so the corresponding susceptibilities are

$$\chi_{B_{1g}} \propto \lim_{(\epsilon_{xx}-\epsilon_{yy}) \rightarrow 0} \frac{d\left[(\Delta\rho/\rho)_{xx}(H_z) - (\Delta\rho/\rho)_{yy}(H_z)\right]}{d\left[\epsilon_{xx} - \epsilon_{yy}\right]} = m_{xx,xx} - m_{xx,yy} \quad (2.17a)$$

$$\chi_{B_{2g}} \propto \lim_{(\epsilon_{xy}+\epsilon_{yx}) \rightarrow 0} \frac{d\left[(\Delta\rho/\rho)_{xy}(H_z) + (\Delta\rho/\rho)_{yx}(H_z)\right]}{d\left[\epsilon_{xy} + \epsilon_{yx}\right]} = 2m_{xy,xy} \quad (2.17b)$$

$$\begin{aligned} \chi_{E_g} &\propto \lim_{\begin{pmatrix} \epsilon_{xz} + \epsilon_{zx} \\ \epsilon_{yz} + \epsilon_{zy} \end{pmatrix} \rightarrow 0} \left(\frac{d\left[(\Delta\rho/\rho)_{xz}(H_z) + (\Delta\rho/\rho)_{zx}(H_z)\right]/d\left[\epsilon_{xz} + \epsilon_{zx}\right]}{d\left[(\Delta\rho/\rho)_{yz}(H_z) + (\Delta\rho/\rho)_{zy}(H_z)\right]/d\left[\epsilon_{yz} + \epsilon_{zy}\right]} \right) \\ &= \begin{pmatrix} 2m_{zx,zx} \\ 2m_{yz,yz} \end{pmatrix} = \begin{pmatrix} 2m_{yz,yz} \\ 2m_{yz,yz} \end{pmatrix}. \end{aligned} \quad (2.17c)$$

The ratios appearing in these susceptibilities correspond to select admixtures of elastoresistivity coefficients, and so by measuring symmetry-motivated combinations of the components of the elastoresistivity tensor, we can infer the behavior of the thermodynamic susceptibilities (up to potentially parameter-dependent coefficients of proportionality) and therefore identify the symmetry class of the order parameter.

We mention in passing that a nematic distortion by definition refers to reduced rotational symmetry, which for in-plane distortions in D_{4h} corresponds to the B_{1g} and B_{2g} irreps; it is for this reason that we have referred to $\chi_{B_{1g}}$ and $\chi_{B_{2g}}$ as nematic susceptibilities and have in previous publications (using the Voigt notation [57]) denoted them by $\chi_{\mathcal{N}_{[100]}} = m_{11} - m_{12}$ and $\chi_{\mathcal{N}_{[110]}} = 2m_{66}$, respectively. In principle, there are also nematic susceptibilities in D_{4h} that correspond to the E_g irrep, but these distortions are out-of-plane and respond to out-of-plane shears (see ϵ_{E_g} in Table 2.2).

2.5 Measurements of Additional Coefficients

There are two additional classes of elastoresistivity coefficients which, while they do not correspond to thermodynamic susceptibilities, may nevertheless be sensible to measure. In the first class, time-reversal odd resistive responses to strain (e.g., $[(\Delta\rho/\rho)_{yz}(H_z) - (\Delta\rho/\rho)_{zy}(H_z)]/[\epsilon_{xz} + \epsilon_{zx}]$) cannot probe susceptibilities because time-reversal odd order parameters cannot bilinearly couple to strain; however, such a ratio does correspond to a distinct elastoresistivity coefficient (in this instance, $2m_{yz,zx}$). Similarly, in the second class, resistive responses to A_{1g} strains (e.g., $(\Delta\rho/\rho)_{zz}/\epsilon_{zz}$) also do not correspond to susceptibilities (because $\epsilon_{A_{1g}}$ does not break a symmetry) but can still be related to elastoresistivity coefficients; in this instance, care must be taken because the two A_{1g} strains can cause distinct elastoresistivity coefficients to mix into each other if one of the A_{1g} strains is not constrained to vanish. For completeness, we have enumerated below additional coefficients in both of these classes:

$$\lim_{(\epsilon_{xx} + \epsilon_{yy}) \rightarrow 0} \frac{d \left[(\Delta\rho/\rho)_{xx}(H_z) + (\Delta\rho/\rho)_{yy}(H_z) \right]}{d \left[\epsilon_{xx} + \epsilon_{yy} \right]} \Big|_{\epsilon_{zz}=0} = m_{xx,xx} + m_{xx,yy} \quad (2.18a)$$

$$\lim_{\epsilon_{zz} \rightarrow 0} \frac{d \left[(\Delta\rho/\rho)_{zz}(H_z) \right]}{d \left[\epsilon_{zz} \right]} \Big|_{\epsilon_{xx} + \epsilon_{yy} = 0} = m_{zz,zz} \quad (2.18b)$$

$$\lim_{(\epsilon_{xx} + \epsilon_{yy}) \rightarrow 0} \frac{d \left[(\Delta\rho/\rho)_{zz}(H_z) \right]}{d \left[\epsilon_{xx} + \epsilon_{yy} \right]} \Big|_{\epsilon_{zz}=0} = m_{zz,xx} \quad (2.18c)$$

$$\lim_{\epsilon_{zz} \rightarrow 0} \frac{d \left[(\Delta\rho/\rho)_{xx}(H_z) + (\Delta\rho/\rho)_{yy}(H_z) \right]}{d \left[\epsilon_{zz} \right]} \Big|_{\epsilon_{xx} + \epsilon_{yy} = 0} = 2m_{xx,zz} \quad (2.18d)$$

$$\lim_{(\epsilon_{xx} + \epsilon_{yy}) \rightarrow 0} \frac{d \left[(\Delta\rho/\rho)_{xy}(H_z) - (\Delta\rho/\rho)_{yx}(H_z) \right]}{d \left[\epsilon_{xx} + \epsilon_{yy} \right]} \Big|_{\epsilon_{zz}=0} = 2m_{xy,xx} \quad (2.18e)$$

$$\lim_{\epsilon_{zz} \rightarrow 0} \frac{d \left[(\Delta\rho/\rho)_{xy}(H_z) - (\Delta\rho/\rho)_{yx}(H_z) \right]}{d \left[\epsilon_{zz} \right]} \Big|_{\epsilon_{xx} + \epsilon_{yy} = 0} = 2m_{xy,zz} \quad (2.18f)$$

$$\lim_{(\epsilon_{xz} + \epsilon_{zx}) \rightarrow 0} \frac{d \left[(\Delta\rho/\rho)_{yz} (H_z) - (\Delta\rho/\rho)_{zy} (H_z) \right]}{d \left[\epsilon_{xz} + \epsilon_{zx} \right]} = 2m_{yz,zx} \quad (2.18g)$$

$$\lim_{(\epsilon_{yz} + \epsilon_{zy}) \rightarrow 0} \frac{d \left[(\Delta\rho/\rho)_{zx} (H_z) - (\Delta\rho/\rho)_{xz} (H_z) \right]}{d \left[\epsilon_{yz} + \epsilon_{zy} \right]} = 2m_{yz,zx} \quad (2.18h)$$

As mentioned above, since quantities with the same symmetry can mix into each other and there are two forms of $\epsilon_{A_{1g}}$, the ratios in (2.18) involving $\epsilon_{xx} + \epsilon_{yy}$ and ϵ_{zz} are only equal to the indicated coefficients provided that the other A_{1g} strain is constrained to vanish, which we have denoted by $\big|_{\epsilon_{A_{1g}}=0}$. Achieving such constraints in practice might be challenging, but we emphasize that in this discussion we are more concerned with formal definitions than with the practical means that might be employed to realize such an experiment.

2.6 Conclusion

The primary goal of this work has been twofold. First, we have tried to explain the general ways in which the elastoresistivity tensor is constrained due to the structure of the resistivity and strain tensors and also the point group symmetry of the crystal. We focused in detail on the tetragonal point group D_{4h} , but extensions to other point groups would proceed in an analogous way. Our treatment also readily incorporates the presence of a magnetic field. Second, our motivation in pursuing elastoresistance measurements has been to elucidate the role of electronic nematicity (broken rotational symmetry driven by electronic correlations) in a number of strongly correlated electron systems. To this end, we have discussed how elastoresistivity coefficients can be connected to thermodynamic susceptibilities in order to characterize the symmetry of an order parameter for a continuous phase transition.

Chapter 3

Differential Longitudinal and Transverse Elastoresistivity

In this chapter, transverse elastoresistance is introduced as a complementary technique to the earlier differential longitudinal elastoresistance method for extracting the B_{1g} and B_{2g} components of the elastoresistivity tensor for tetragonal materials. Whereas the differential longitudinal method determines the induced resistivity anisotropy arising from anisotropic in-plane strain based on the difference of two longitudinal resistivity measurements, the transverse approach directly determines the strain-induced resistivity anisotropy from a single transverse measurement. To demonstrate the efficacy of the new transverse experimental protocol, transverse elastoresistance measurements of the $2m_{xy,xy}$ elastoresistivity coefficient of $BaFe_2As_2$ (a representative iron-pnictide that has previously been characterized via differential longitudinal elastoresistance measurements) are also presented. This chapter is taken nearly verbatim from [56].

3.1 Introduction

Resistivity measurements are employed extensively in the field of strongly correlated electron systems (SCES). Since transport properties are determined by the electronic

dynamics at the Fermi level, resistivity is often extremely sensitive to Fermi surface changes and electronically-driven phase transitions; however, since resistivity is a second-rank tensor, transport measurements are generically limited in their ability to identify the *symmetry* properties of the underlying order. In contrast, the elastoresistivity (a fourth-rank tensor defined as the strain derivative of the resistivity) can convey additional information about directional anisotropies and broken point group symmetries which might more subtly manifest in the resistivity itself [55, 59]. Furthermore, since electron-lattice coupling in SCES is often large, the order parameter characterizing an electronically-driven phase transition in these materials is often strongly tuned by strain and strongly reflected in transport; the coefficients in the elastoresistivity tensor are then likely to be large, making elastoresistivity very promising from an experimental perspective. Although elastoresistance measurements have been applied to semiconductors [60], this physical quantity has only recently been measured in the context of SCES [55, 57, 58, 61–63, 70, 71]; in both cases, however, measurements have been confined to *longitudinal* geometries (Figure 3.1 (a) and (b)), and the wider class of *transverse* (Figure 3.1 (c)) measurements (which are the subject of this paper) have not been investigated.

For a tetragonal material, the B_{1g} and B_{2g} components of the elastoresistivity tensor characterize the material’s linear response to the anisotropic strains $\epsilon_{xx} - \epsilon_{yy}$ and ϵ_{xy} , respectively. These two components of the elastoresistivity tensor directly connect to the nematic susceptibility for the same two symmetry channels, $\chi_{B_{1g}}$ and $\chi_{B_{2g}}$ [55, 58]. We have recently shown how these coefficients can be determined from differential longitudinal elastoresistance measurements and have used this technique to investigate a series of materials which exhibit electronic nematic instabilities [57, 58, 61, 62, 70].

Anisotropic strain can be achieved by a variety of means. In one specific realization, crystals are glued to the side surface of a piezoelectric lead zirconate titanate (PZT) stack with a strain-transmitting epoxy [72]. In this implementation, the crystals are mechanically coupled to and hence deform with the PZT, which expands (contracts) along its poling direction (perpendicular to its poling direction) upon application of a positive external voltage. The strain can be measured by attaching

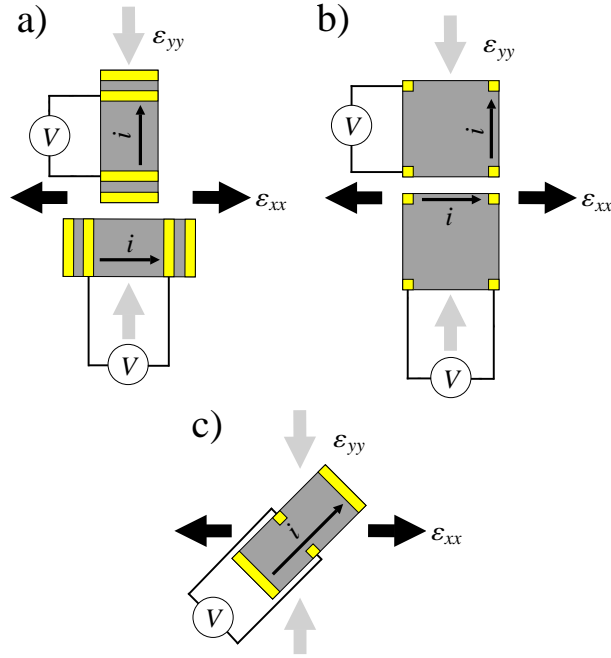


Figure 3.1: Schematic diagrams illustrating three different methods that can be used to measure the B_{1g} or B_{2g} elasto-resistivity coefficients of a tetragonal material. The appropriate orientation of the principal crystal axes with respect to the current \mathbf{i} and the strains ϵ_{xx} (horizontal black arrows) and ϵ_{yy} (vertical gray arrows) for the two irreducible components is discussed in Sections 3.3 and 3.4 of the main text. Gray bars represent single crystal samples and yellow regions depict electrical contacts used for the transport measurements; current paths and schematic voltmeters are also indicated. The samples are caused to experience an induced anisotropic strain by some external means and the strains ϵ_{xx} and ϵ_{yy} are separately determined. In the configuration shown in panel (a), a standard four-point contact geometry is used to measure the differential longitudinal elasto-resistivity (i.e., $(\Delta\rho/\rho)_{xx} - (\Delta\rho/\rho)_{yy}$). In panel (b), a modified Montgomery geometry is used to measure the same quantities with a single sample; however, two measurement configurations are still required to extract $(\Delta\rho/\rho)_{xx}$ and $(\Delta\rho/\rho)_{yy}$, as illustrated by the two schematic diagrams. In both cases, the relevant elasto-resistivity coefficients are determined from the difference of the two longitudinal measurements. As described in the main text, these configurations have some practical drawbacks; in particular, one infers a (potentially small) resistive anisotropy from the difference of two (potentially larger) longitudinal resistivity measurements. In this paper we describe an alternative *transverse* (i.e., $(\Delta\rho/\rho)_{xy}$) measurement that can be performed on one single crystal (depicted in panel (c)) that yields the same elasto-resistivity coefficients by directly determining the resistivity anisotropy from a single measurement.

strain gauges directly to the surface of larger samples or estimated by measuring the strain on the PZT surface. Longitudinal resistances are then measured while the strain is varied and the differential longitudinal elastoresistance determined from the difference of the two measurements [58]. In the original realization of this experiment, two separate transport bars were used in order to separately determine the longitudinal elastoresistivities $(\Delta\rho/\rho)_{xx}$ and $(\Delta\rho/\rho)_{yy}$ (illustrated schematically in Figure 3.1 (a)). While these measurements unambiguously identified a divergence of the nematic susceptibility in the B_{2g} symmetry channel for the iron-based superconductors [58], nevertheless this specific experimental configuration leads to several experimental concerns. In particular, the technique relies upon equal strain transmission for the two samples used in the differential measurement (which might be difficult to realize in practice, in part due to geometric factors and in part due to differences in the adhesion of the two samples to the PZT stack [73]). Expressed in the context of group theory, such nonidealities (which we describe in greater detail in Section 3.3) admix elastoresistivity coefficients with an A_{1g} character (i.e., isotropic in-plane, or symmetric with respect to rotation about the c -axis), potentially affecting the determination of the associated elastoresistivity coefficients in other symmetry channels.

To avoid the possible contamination of isotropic strain that can manifest in a differential longitudinal elastoresistivity measurement, it is preferable to extract the differential elastoresistivity from a measurement performed on just one single crystal sample that is held under conditions of anisotropic strain. One such method is to use the modified Montgomery technique to measure the induced anisotropy in the longitudinal resistivity of a square shape sample (Figure 3.1 (b)). We recently applied such a technique to measure the differential elastoresistance of several families of iron-based superconductors [70]. While this technique obviates concerns over strain transmission to the sample, nevertheless it still requires separate measurement of two (potentially large) longitudinal resistivities as a function of strain, the (potentially small) difference of which yields the desired B_{1g} or B_{2g} components of the elastoresistivity tensor. Ideally, one would determine this difference directly.

We note that it is indeed possible to measure the induced resistivity anisotropy (and hence the B_{1g} and B_{2g} components of the elastoresistivity tensor) from a single

measurement. In particular, we note that a tetragonal material which undergoes an orthorhombic distortion by breaking symmetry about its σ_x and σ_y mirror planes (i.e., undergoes a B_{2g} distortion in which the in-plane square lattice deforms into a parallelogram) acquires finite off-diagonal terms in the resistivity tensor (ρ_{xy} and ρ_{yx}) which are proportional to the amount of orthorhombicity regardless of the magnetic field environment. Hence, one can obtain the same information *from a single measurement* of the *transverse* elastoresistivity (Figure 3.1 (c)). The primary advantage of the transverse method is that it directly measures the associated resistive anisotropy from a single measurement of a single sample. Furthermore, by symmetry, the measured quantity cannot be affected by isotropic strain in the linear regime.

In this manuscript, we propose and demonstrate a new method for probing the nematic susceptibility in the B_{2g} channel $\chi_{B_{2g}}$ based on measuring the transverse elastoresistivity $(\Delta\rho/\rho)_{xy}$. One common problem that can arise with measurements of a transverse resistivity is ρ_{xx} contamination in a nominal ρ_{xy} measurement due to contact misalignment, and so we also provide a practical means for subtracting such contamination. Since transverse elastoresistivity measurements have to date neither been discussed nor measured, we provide here a detailed description of the relevant tensor quantities and a suitable technique that enables such a measurement.

We proceed by first describing appropriate coordinate frames and associated transformations of the elastoresistivity tensor, necessary for the subsequent discussion. We then explain the various configurations for measuring the corresponding elastoresistivity coefficients, along the way characterizing certain forms of experimental error. We conclude by presenting $2m_{xy,xy}$ data acquired via the new method for the representative iron-pnictide BaFe_2As_2 , which was chosen since it has previously been well-characterized by differential longitudinal measurements [58, 61, 62] and has a large elastoresistive response. The temperature dependence of the elastoresistivity coefficients as observed by the transverse method agree with the earlier differential measurements, revealing a nematic instability in the B_{2g} symmetry channel. Similar to our earlier differential longitudinal measurements, anisotropic strain for the transverse elastoresistance measurements was achieved by gluing the sample to the surface of a piezoelectric PZT stack; however, we note that the proposed technique does not

rely on this specific realization, and alternative methods to strain the sample can be readily envisioned.

3.2 Coordinate Frames and the Elastoresistivity Tensor

As a consequence of strains experienced by a material, terms in the resistivity tensor ρ_{ij} acquire a strain-induced change

$$\Delta\rho_{ij}(\mathbf{H}) \equiv \rho_{ij}(\mathbf{H}, \hat{\epsilon}) - \rho_{ij}(\mathbf{H}, \hat{\epsilon} = \hat{0}). \quad (3.1)$$

The elastoresistivity $m_{ij,kl}(\mathbf{H})$ is a fourth-rank tensor that linearly relates the (normalized) strain-induced resistivity change $(\Delta\rho/\rho)_{ij}(\mathbf{H})$ and the strain ϵ_{kl} according to

$$(\Delta\rho/\rho)_{ij}(\mathbf{H}) \equiv m_{ij,kl}(\mathbf{H})\epsilon_{kl}, \quad (3.2)$$

where we choose to represent the second-rank tensors $(\Delta\rho/\rho)_{ij}(\mathbf{H})$ and ϵ_{kl} as the column vectors

$$(\Delta\rho/\rho)_{ij}(\mathbf{H}) = \begin{pmatrix} (\Delta\rho/\rho)_{xx}(\mathbf{H}) \\ (\Delta\rho/\rho)_{yy}(\mathbf{H}) \\ (\Delta\rho/\rho)_{zz}(\mathbf{H}) \\ (\Delta\rho/\rho)_{yz}(\mathbf{H}) \\ (\Delta\rho/\rho)_{zy}(\mathbf{H}) \\ (\Delta\rho/\rho)_{zx}(\mathbf{H}) \\ (\Delta\rho/\rho)_{xz}(\mathbf{H}) \\ (\Delta\rho/\rho)_{xy}(\mathbf{H}) \\ (\Delta\rho/\rho)_{yx}(\mathbf{H}) \end{pmatrix} \text{ and } \epsilon_{kl} = \begin{pmatrix} \epsilon_{xx} \\ \epsilon_{yy} \\ \epsilon_{zz} \\ \epsilon_{yz} \\ \epsilon_{zy} \\ \epsilon_{zx} \\ \epsilon_{xz} \\ \epsilon_{xy} \\ \epsilon_{yx} \end{pmatrix} \quad (3.3)$$

in order to represent $m_{ij,kl}(\mathbf{H})$ as a 9×9 matrix. The appropriate normalization

scheme is given by [55]

$$(\Delta\rho/\rho)_{ij}(\mathbf{H}) \equiv (\Delta\rho_{ij}(\mathbf{H})/\sqrt{\rho_{ii}(\mathbf{H})}\sqrt{\rho_{jj}(\mathbf{H})}). \quad (3.4)$$

Because of Onsager’s relation [64], the resistivity tensor is not in general symmetric in the presence of a magnetic field and so we avoid usage of the compactified Voigt notation in order to present a generalized description appropriate for finite \mathbf{H} . The point group symmetry of the crystal lattice constrains the number of independent nonzero coefficients in the elastoresistivity tensor; for example, the elastoresistivity tensor for the specific case of the D_{4h} point group (appropriate for BaFe_2As_2 and derived elsewhere [55]) is given in Appendix 3.A.

In labeling the elastoresistivity coefficients by spatial coordinates, we have implicitly assumed a Cartesian system referenced to the crystal itself and defined by its primitive lattice vectors. We refer to this reference frame as the “crystal frame” and denote it by unprimed x , y , and z axes. In order to extract symmetry information about the crystal, one is generally concerned with measured quantities in the crystal frame. We consider an experiment in which the crystal experiences a purely normal (i.e., shear-free) homogeneous strain in a given Cartesian frame of reference defined by x' , y' , and z' basis vectors. For example, this could be realized with a piezoelectric PZT stack, where the basis vectors are defined by the lateral dimensions of the stack. We refer to this reference frame as the “normal strain frame”, which (by choice) shares a mutual z/z' axis with the crystal frame but is oriented at an in-plane angle ϕ relative to the primitive axes of the crystal frame (i.e., $\hat{x} \cdot \hat{x}' = \hat{y} \cdot \hat{y}' = \cos \phi$, where ϕ is positive when the crystal frame is oriented counterclockwise relative to the normal strain frame). The relative angle ϕ reflects our freedom to strain the crystal along arbitrary directions relative to the primitive crystal cell.

Additionally, when we perform an in-plane resistivity measurement, we have the freedom to direct the current along an arbitrary in-plane direction with respect to the crystal axes. We define this “transport frame” by double-primed Cartesian vectors x'' , y'' , and z'' ; x'' is the direction in which the current is sourced, y'' is the in-plane direction perpendicular to x'' , and z'' is the out-of-plane direction perpendicular to

$$\begin{aligned}
(\Delta\rho/\rho)_{(ij)''} &= \hat{\alpha}_\theta(\Delta\rho/\rho)_{ij} = \hat{\alpha}_\theta m_{ij,kl} \epsilon_{kl} \\
&= \hat{\alpha}_\theta m_{ij,kl} \hat{\alpha}_\phi \epsilon_{(kl)'} \\
&\equiv m_{(ij)'', (kl)'} \epsilon_{(kl)'},
\end{aligned} \tag{3.5}$$

where the $\hat{\alpha}_\phi$, $\hat{\alpha}_\theta$ are suitable transformation matrices given in Appendix 3.A and the subscripts in the elastoresistivity coefficients denote that the strains are measured in the normal strain frame (primes) while the normalized changes in resistivity are measured in the transport frame (double primes).

3.3 Differential Longitudinal Configuration for Probing Nematic Susceptibility in D_{4h}

3.3.1 Ideal Configuration

The elastoresistivity tensor takes a particularly simple form when decomposed in terms of its irreducible representations (as determined by the point group symmetry of the crystal lattice). Such a decomposition motivates making specific combinations of elastoresistance measurements in order to isolate particular elastoresistivity coefficients in the same symmetry class. For example, for the D_{4h} point group, the normalized resistivity changes in the B_{1g} and B_{2g} irreducible representations are proportional to the corresponding elastoresistivity coefficients ($m_{xx,xx} - m_{xx,yy}$ and $2m_{xy,xy}$, respectively) in the same symmetry channel and are related to the nematic susceptibilities $\chi_{B_{1g}}$ and $\chi_{B_{2g}}$ in those irreps [55, 57, 58]. There are, however, different experimental geometries that can be used to extract these combinations of coefficients. Previously, we have shown how a differential longitudinal elastoresistance measurement can be used to measure $m_{xx,xx} - m_{xx,yy}$ and $2m_{xy,xy}$, which is illustrated schematically in Figure 3.3. By taking the symmetry-motivated combination $(\Delta\rho/\rho)_{(xx)''} - (\Delta\rho/\rho)_{(yy)''}$ and expressing it in terms of the elastoresistivity coefficients in the crystal frame (Appendix 3.A), we find that

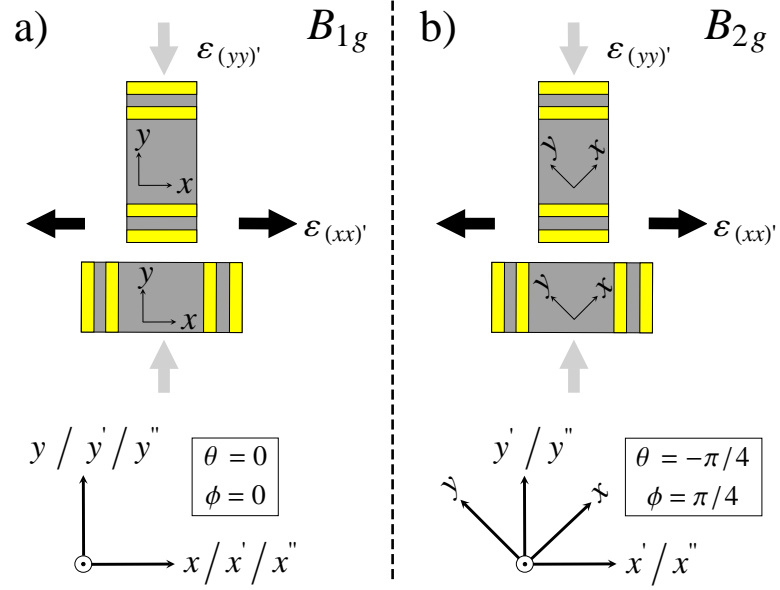


Figure 3.3: Longitudinal elasto-resistivity configurations for extracting (a) $m_{xx,xx} - m_{xx,yy}$ (with $(\theta, \phi) = (0, 0)$) and (b) $2m_{xy,xy}$ (with $(\theta, \phi) = (-\pi/4, \pi/4)$), which characterize the B_{1g} and B_{2g} irreducible representations of $m_{ij,kl}$ in D_{4h} . In (a), one measures the differential longitudinal resistive response to strain $(\Delta\rho/\rho)_{(xx)''} - (\Delta\rho/\rho)_{(yy)''}$ to a strain $\epsilon_{(xx)'} - \epsilon_{(yy)'}$ with the transport, crystal, and normal strain frames all coincident; the differential longitudinal elasto-resistivity then yields the elasto-resistivity coefficients $m_{xx,xx} - m_{xx,yy}$. In (b), one measures the differential resistive response to strain $(\Delta\rho/\rho)_{(xx)''} - (\Delta\rho/\rho)_{(yy)''}$ to a strain $\epsilon_{(xx)'} - \epsilon_{(yy)'}$ with the crystal frame oriented at the angles $(\theta, \phi) = (-\pi/4, \pi/4)$ relative to the transport and normal strain frames; the differential longitudinal elasto-resistivity then yields the elasto-resistivity coefficient $2m_{xy,xy}$.

$$\begin{aligned}
& (\Delta\rho/\rho)_{(xx)''} (H_z) - (\Delta\rho/\rho)_{(yy)''} (H_z) = \\
& \left[\epsilon_{(xx)'} - \epsilon_{(yy)'} \right] \cdot \left[(m_{xx,xx} - m_{xx,yy}) \cos(2\theta) \cos(2\phi) - 2m_{xy,xy} \sin(2\theta) \sin(2\phi) \right].
\end{aligned} \tag{3.6}$$

Unsurprisingly, despite the fact that each crystal experiences $\epsilon_{(zz)'}$ strain (and so the individual transport measurements experience the effects of strain in the A_{1g} symmetry channel in addition to the B_{1g} or B_{2g} channels), the quantity $(\Delta\rho/\rho)_{(xx)''} - (\Delta\rho/\rho)_{(yy)''}$ is unaffected by such strains since they are of a different symmetry class. Equivalently, the effects of rotationally invariant strains are subtracted out in taking the B_{1g} or B_{2g} combination, as we originally noted [58]. However, arbitrary in-plane rotations are not symmetry elements of D_{4h} (only the discrete $\pi/2$ rotations about the mutual $z/z'/z''$ axis are symmetries of the point group), and so rotating the crystal frame by an arbitrary angle θ relative to the transport frame and/or by an arbitrary angle ϕ relative to the strain frame can mix B_{1g} ($m_{xx,xx} - m_{xx,yy}$) and B_{2g} ($2m_{xy,xy}$) quantities (measured in the crystal frame) into each other. For certain high symmetry directions of the current and normal strains relative to the crystal axes, though, one can isolate the B_{1g} and B_{2g} coefficients and hence infer the behavior of the corresponding susceptibilities in those symmetry channels. The high symmetry configuration for $m_{xx,xx} - m_{xx,yy}$ ($\propto \chi_{B_{1g}}$) is $(\theta, \phi) = (0, 0)$ (i.e., the transport, current, and normal strain frames are all coincident), while the high symmetry configuration for $2m_{xy,xy}$ ($\propto \chi_{B_{2g}}$) is $(\theta, \phi) = (-\pi/4, \pi/4)$ (i.e., the crystal frame is oriented at $\pi/4$ radians relative to the transport and normal strain frames); these arrangements are depicted in Figure 3.3 and can be confirmed with (3.6). This was precisely the configuration used in our initial measurements of the elastoresistance of iron-based [58, 61] and heavy fermion [57] superconductors. The same information can also be extracted from a modified Montgomery geometry [70].

3.3.2 Sources of Error

There are two broad categories of systematic error associated with elastoresistivity measurements. In the first class are errors which affect the magnitude of the measured

elastoresistivity coefficients but which do not mix coefficients belonging to different symmetry channels. Systematic errors of this type include geometric factors and (for homogeneously strained samples) imprecision in determining the strain experienced by the sample. Since these types of errors do not mix responses from different symmetry channels, they do not impugn one's ability to assign an instability to a particular symmetry channel. Such uncertainties are therefore less of a concern from the perspective of characterizing the symmetry of an associated order parameter, which has been a primary motivation for considering elastoresistivity measurements of strongly correlated materials. In contrast, in the second class of systematic errors are those which mix responses from different symmetry channels in a given measurement. Errors of this type can arise, for example, due to angular misalignment of the transport or normal strain frames relative to the crystal frame or if the two samples that are used in a differential measurement experience unequal strain. Both of these examples not only result in errors in the magnitude of the extracted elastoresistivity coefficients but can also complicate symmetry-based conclusions by admixing symmetry channels. In this section, we briefly comment on several sources of systematic errors in both classes as they relate to a differential longitudinal measurement configuration, with a particular focus on those errors of the second class. The primary reason for doing so in the context of this paper is then to motivate the alternative transverse measurement configuration which does not suffer some of these drawbacks. Here we focus specifically on errors associated with the standard four-contact geometry (Figure 3.1 (a)), but a similar analysis could be applied to the modified Montgomery technique.

(a) Angular misalignment: In order to measure $m_{xx,xx} - m_{xx,yy}$ or $2m_{xy,xy}$, crystals should be oriented such that $(\theta, \phi) = (0, 0)$ and $(\theta, \phi) = (-\pi/4, \pi/4)$, respectively. In practice, misalignment will occur which will affect the measured elastoresistivity coefficients. Within the present formalism, we can propagate this error to leading order; in this section, we quote the main results, referring the reader to Appendix 3.B for the full derivation.

Suppose that in attempting to measure $(\Delta\rho/\rho)_{(xx)''}$, we intended to orient the crystal in a high-symmetry configuration characterized by the angles (θ, ϕ) but actually did so in a configuration given by $(\theta + \delta\theta_{xx}, \phi + \delta\phi_{xx})$. To probe nematic susceptibility, we subtract $(\Delta\rho/\rho)_{(yy)''}$ from $(\Delta\rho/\rho)_{(xx)''}$, which we also intend to be measured in a configuration (θ, ϕ) but which may also be misaligned according to $(\theta + \delta\theta_{yy}, \phi + \delta\phi_{yy})$. For full generality, we assume $\delta\theta_{xx} \neq \delta\theta_{yy}$ and $\delta\phi_{xx} \neq \delta\phi_{yy}$. Expanding these errors to leading order about the high symmetry configurations $(\theta, \phi) = (0, 0)$ and $(\theta, \phi) = (-\pi/4, \pi/4)$, the elastoresistivity coefficients $m_{xx,xx} - m_{xx,yy}$ (in the first configuration) and $2m_{xy,xy}$ (in the second configuration) are misestimated by a factor

$$1 - \left[\delta\theta_{xx}^2 + \delta\theta_{yy}^2 + \delta\phi_{xx}^2 + \delta\phi_{yy}^2 \right]. \quad (3.7)$$

The angular alignment errors systematically induce an underestimate of the true elastoresistivity coefficients and come in at second order in the misalignment; even if all angles were off by as much as 5° (a typical experimental uncertainty), the total error would only be $\sim 3\%$, and so the high symmetry configurations are relatively insensitive to minor angular offsets.

Additionally, misalignment with respect to the high symmetry configurations also mixes B_{1g} coefficients into a nominal measurement of the B_{2g} symmetry channel and vice versa. The amount of mixing from the other symmetry channel is proportional to

$$-2 \left[\delta\theta_{xx}\delta\phi_{xx} + \delta\theta_{yy}\delta\phi_{yy} \right], \quad (3.8)$$

which again is at second order in the misalignment. This mixing due to misalignment could be significant if the relative difference in the magnitudes of the elastoresistivity coefficients in the two symmetry channels is large. For example, for the specific case of the iron-based superconductors in which $\chi_{B_{2g}}$ diverges, measurement of $m_{xx,xx} - m_{xx,yy}$ is affected by admixture of the much larger $2m_{xy,xy}$ coefficient, whereas measurement of $2m_{xy,xy}$ is essentially unaffected by admixture of a small amount of the much smaller $m_{xx,xx} - m_{xx,yy}$ [58].

(b) Unequal strain experienced by the two samples: The differential longitudinal technique relies on both samples experiencing the same homogeneous strain. If the samples experience a different strain due to experimental nonidealities (see next section for a discussion relevant to the specific technique we have employed), this will also affect the deduced elastoresistivity coefficients.

Relative strain errors are of potentially greater concern than misalignment errors since any strain offset error occurs at first order. Strain offsets also erroneously mix in A_{1g} -like coefficients and hence contaminate a nominal nematic susceptibility measurement with the effects of isotropic strain (see discussion in Appendix 3.C).¹ Comparison of nominal B_{1g} and B_{2g} coefficients can help bound the amount of A_{1g} contamination (since such rotationally invariant contamination would manifest equally in both B_{1g} and B_{2g} measurements). Hence, it is still possible to classify which symmetries are broken at the phase transition (i.e., assigning the order parameter to a particular irreducible representation of the space group); however, these concerns motivate development of a technique that does not rely on separate measurements of different samples but which is based instead on measurement of a single sample. This is the primary motivation for adopting either the modified Montgomery technique (Figure 3.1 (b)) or the transverse elastoresistance technique (Figure 3.1 (c)) that we introduce in Section 3.4.

(c) Systematic errors originating with the specific technique: In addition to the sources of systematic error discussed above, additional errors can be introduced which are specific to the particular technique that is used to strain the samples. For our experimental realization in which single crystals are glued to the side surface of a PZT stack, these errors are related to measurement of the strain experienced by

¹For our initial elastoresistance measurements on the iron-based superconductors, A_{1g} strain contamination does not affect any of the conclusions since the observation of a singular divergence in $\chi_{B_{2g}}$ is immune to imperfect A_{1g} subtraction. A divergence in the A_{1g} symmetry channel would manifest equally in both $\chi_{B_{1g}}$ and $\chi_{B_{2g}}$ (which is not observed), and so an imperfect A_{1g} subtraction at worst contributes a small, non-singular, temperature-dependent background.

the sample, differential thermal contraction, and strain homogeneity. We emphasize, however, that these factors are not generic to elastoresistivity measurements; alternative methodologies may be able to mitigate or circumvent these particular sources of error while potentially incurring others.

For the analysis so far, it has been assumed that the strain experienced by the sample can be accurately determined. In practice, there are different ways this could be achieved, each of which would introduce an associated uncertainty. For the specific realization of the experiment that we present in this manuscript, we measure the strain on the PZT surface using two strain gauges mounted perpendicularly along the PZT stack axes and use this value to estimate the strain experienced by the sample. Strain transmission has been characterized for samples with a similar aspect ratio by comparing measurements for strain gauges mounted on top of the sample with one mounted directly on the PZT stack [61, 70]. Those measurements revealed a strain transmission in excess of 80% for the temperature range of our current experiments with only a weak temperature dependence.

Differential thermal contraction between the sample and the PZT stack on which it is mounted implies that the sample is strained even when no voltage is applied to the piezoelectric. At high temperatures, this is a small effect since the dynamic range over which the sample can be strained exceeds the “bias” strain due to such thermal effects.² However, the situation is reversed at cryogenic temperatures. Upon cooling to 100 K, the crystal experiences a large, anisotropic strain (of about $\sim 0.1\%$ [78]) solely from the PZT due to an expansion along its poling direction; depending on the voltage range that is applied to the PZT stack, this can be much larger than the dynamic strain that the PZT can apply due to an applied voltage at this temperature ($\sim 0.01\%$ at 150 V [58, 77]), which means that the strain experienced by the crystal may not be able to be tuned through zero. So long as the material is still in the regime

²On cooling from room temperature to 250 K, the PZT expands by $\sim 0.02\%$ along its poling direction [74], which is opposite to the typical thermal contraction of most materials. Silver (a representative material) and BaFe_2As_2 (the test material used in this manuscript) contract by $\sim 0.08\%$ and $\sim 0.05\%$ on cooling to 250 K, respectively [75, 76], and so by adhering either material to a PZT, the materials are placed under uniaxial tension of $\sim 0.1\%$ and $\sim 0.07\%$, respectively. These strains are smaller than the strain change of $\sim 0.15\%$ that is obtained by sweeping the applied voltage to the PZT between -50 V to $+150$ V at 250 K [58, 77].

of linear response, which can be checked, the elastoresistivity coefficients can still be faithfully measured; however, alternative methodologies [78] can also be employed which mitigate such effects and more closely yield zero strain conditions.

So far, our analysis has assumed no relaxation of the strain through the thickness of the crystal. In practice, the strain will relax towards its unstrained edges on a certain length scale determined by the elastic stiffness of the sample and the extent to which the sides of the crystal are “clamped” by the epoxy. To mitigate such effects, samples to be measured must have a thickness that is much smaller than the in-plane dimensions. Concerns about strain relaxation in the narrow in-plane direction relative to the long in-plane direction can be completely allayed by using a modified Montgomery technique for crystals with a square shape (Figure 3.1 (b)) [70].

An additional source of uncertainty associated with the specific experimental protocol we have discussed in which samples are glued to the surface of a PZT stack arises from strain inhomogeneity. For crystals with dimensions comparable to the separation distance between two PZT layers, and depending on where the crystal is mounted relative to a PZT layer junction, the strain that the crystal experiences can at least in principle vary with position on the PZT surface. The PZT stacks that we have employed have been stacked along their poling direction with an individual layer thickness of $\sim 200 \mu\text{m}$ and a separation between layers of $\sim 50 \mu\text{m}$. If a crystal with a width roughly equal to these thicknesses is adhered along the multilayer interface (as is required in a differential longitudinal elastoresistance measurement) and inauspiciously placed in the interfacial separation region, the crystal will experience little strain even with a voltage applied to the piezo. This sort of inhomogeneity can be ameliorated by spreading the strain transmitting epoxy to encompass more area than just the interface region, attention to placement on the PZT substrate, and use of larger crystals. Modified techniques can also be readily envisaged that yield a more homogeneous strain.

(d) **Geometric effects:** Finally, we note that geometric effects also impact the determination of the elastoresistivity coefficients in a differential longitudinal configuration. Specifically, for a uniformly strained sample the relative change in longitudinal resistance $(\Delta R/R)_{xx}$ is a sum of the intrinsic elastoresistivity $(\Delta\rho/\rho)_{xx}$ and a geometric term due to the change in the shape of the crystal. This latter term can in principle be exactly determined with full knowledge of the elastic constants $C_{ij,kl}$ of the material [58]. The geometric effects are small (contributing an additive factor of order unity to the measured elastoresistivity coefficients) and temperature independent. Consequently, in practice they can be neglected when considering a material with large elastoresistivity coefficients that diverge with temperature on approaching a phase transition.

3.4 Transverse Configuration for Probing Nematic Susceptibility in D_{4h}

3.4.1 Ideal Configuration

An alternative method for obtaining the same symmetry information involves *transverse* elastoresistance measurements, as depicted in Figure 3.4. The underlying intuition is that by appropriately rotating the crystal frame relative to the transport and normal strain frames, the quantity $(\Delta\rho/\rho)_{(xy)''} + (\Delta\rho/\rho)_{(yx)''}$ can mix into $(\Delta\rho/\rho)_{(xx)''} - (\Delta\rho/\rho)_{(yy)''}$ and hence probe the same B_{1g} and B_{2g} susceptibilities. Expressing $(\Delta\rho/\rho)_{(xy)''} + (\Delta\rho/\rho)_{(yx)''}$ in terms of strains in the normal strain frame and elastoresistivity coefficients in the crystal frame (Appendix 3.A), we find that

$$\begin{aligned} & (\Delta\rho/\rho)_{(xy)''} (H_z) + (\Delta\rho/\rho)_{(yx)''} (H_z) = \\ & - \left[\epsilon_{(xx)'} - \epsilon_{(yy)'} \right] \cdot \left[2m_{xy,xy} \cos(2\theta) \sin(2\phi) + (m_{xx,xx} - m_{xx,yy}) \sin(2\theta) \cos(2\phi) \right], \end{aligned} \quad (3.9)$$

and so the elastoresistivity coefficients corresponding to the B_{1g} and the B_{2g} irreducible representations can be isolated for appropriate high-symmetry configurations.

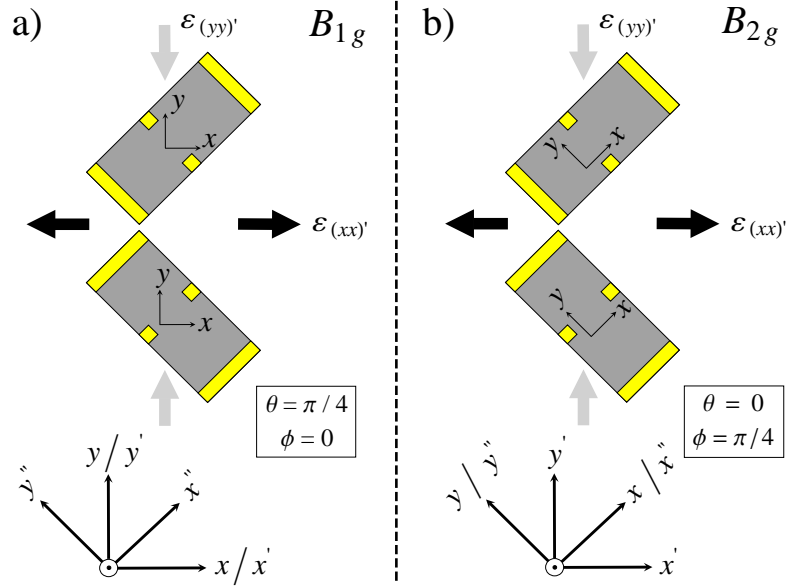


Figure 3.4: Schematic diagrams illustrating transverse elastoresistivity configurations for extracting (a) $m_{xx,xx} - m_{xx,yy}$ (with $(\theta, \phi) = (\pi/4, 0)$) and (b) $2m_{xy,xy}$ (right, with $(\theta, \phi) = (0, \pi/4)$). In (a), one measures the sum of the transverse resistive response to strain $(\Delta\rho/\rho)_{(xy)''} + (\Delta\rho/\rho)_{(yx)''}$ to a strain $\epsilon_{(xx)'} - \epsilon_{(yy)'}$ with the transport frame rotated by $\pi/4$ radians relative to the crystal and normal strain frames; the summed elastoresistivity then yields the elastoresistivity coefficients $m_{xx,xx} - m_{xx,yy}$. In (b), one measures the sum of the transverse resistive response to strain $(\Delta\rho/\rho)_{(xy)''} + (\Delta\rho/\rho)_{(yx)''}$ to a strain $\epsilon_{(xx)'} - \epsilon_{(yy)'}$ with the normal strain frame rotated by $\pi/4$ radians relative to the crystal and transport frames; the summed transverse elastoresistivity then yields the elastoresistivity coefficient $2m_{xy,xy}$.

As depicted in Figure 3.4 (which can be corroborated with (3.9)), the appropriate configuration to extract $m_{xx,xx} - m_{xx,yy}$ ($\propto \chi_{B_{1g}}$) via such transverse measurements is to measure the transverse elastoresistivity with currents and transverse voltages directed along the $[110]$ and $[1\bar{1}0]$ crystallographic directions and with strains oriented along the crystalline axes (mathematically, $(\theta, \phi) = (\pi/4, 0)$); conversely, extracting $2m_{xy,xy}$ ($\propto \chi_{B_{2g}}$) requires measuring the superposed transverse elastoresistivity with currents and transverse voltages directed along the principal crystalline axes and with strains directed along the $[110]$ and $[1\bar{1}0]$ crystallographic directions (mathematically, $(\theta, \phi) = (0, \pi/4)$).

The previous discussion was framed in a manner that emphasized the essential similarity between the longitudinal and transverse configurations; however, there is an additional simplification in the transverse configuration that essentially halves the experimentalist's workload. Since $(\Delta\rho/\rho)_{(yx)''}(H_z) = (\Delta\rho/\rho)_{(xy)''}(-H_z)$ from Onsager's relation [55], one can measure the same elastoresistivity coefficients in the transverse configuration by performing the measurements $(\Delta\rho/\rho)_{(xy)''}(\pm H_z)$ and taking the sum. An illustration of this elastoresistivity configuration is given in Figure 3.5 and expressed mathematically as

$$\begin{aligned} & (\Delta\rho/\rho)_{(xy)''}(H_z) + (\Delta\rho/\rho)_{(xy)''}(-H_z) = & (3.10) \\ & - \left[\epsilon_{(xx)'} - \epsilon_{(yy)'} \right] \cdot \left[2m_{xy,xy} \cos(2\theta) \sin(2\phi) + (m_{xx,xx} - m_{xx,yy}) \sin(2\theta) \cos(2\phi) \right]. \end{aligned}$$

Instead of dismounting the same crystal and re-mounting in a new configuration, as is required for the differential longitudinal configuration, one need only reverse the orientation of the magnetic field, which is usually simply accomplished *in situ*. We emphasize that the appropriate elastoresistivity coefficients are given by the *symmetric* combination (i.e., sum) of transverse voltages, in contrast to Hall coefficient measurements, which are given by the anti-symmetric (i.e., difference) combination in magnetic field. A final comment is that in zero magnetic field, $(\Delta\rho/\rho)_{(xy)''} = (\Delta\rho/\rho)_{(yx)''}$, and so only a single measurement is required:

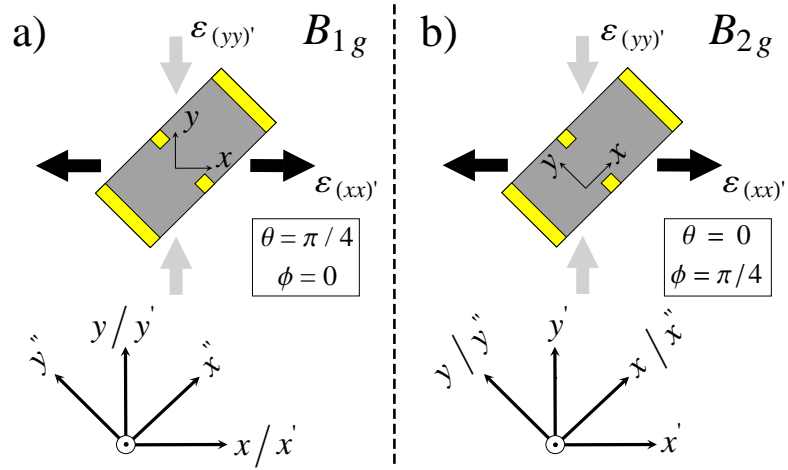


Figure 3.5: Transverse elastoresistivity configurations for extracting (a) $m_{xx,xx} - m_{xx,yy}$ (with $(\theta, \phi) = (\pi/4, 0)$) and (b) $2m_{xy,xy}$ (with $(\theta, \phi) = (0, \pi/4)$). Mounted in these configurations and in the presence of a finite field, the appropriate elastoresistivity coefficients can be measured from $(\Delta\rho/\rho)_{(xy)''}(H_z) + (\Delta\rho/\rho)_{(xy)''}(-H_z)$; in zero field, the same coefficients can be extracted with a single measurement $(\Delta\rho/\rho)_{(xy)''}(H_z = 0)$. The primary advantage of the transverse technique is that one can measure the same elastoresistivity coefficients from a single mounting without A_{1g} contamination.

$$\begin{aligned}
(\Delta\rho/\rho)_{(xy)''}(H_z = 0) &= (\Delta\rho/\rho)_{(yx)''}(H_z = 0) = & (3.11) \\
-\frac{1}{2} \left[\epsilon_{(xx)'} - \epsilon_{(yy)'} \right] &\cdot \left[2m_{xy,xy} \cos(2\theta) \sin(2\phi) + (m_{xx,xx} - m_{xx,yy}) \sin(2\theta) \cos(2\phi) \right].
\end{aligned}$$

3.4.2 Sources of Error

As for the differential longitudinal configuration, systematic errors affecting determination of the relevant elastoresistivity coefficients from transverse measurements are of two types: those that only affect the magnitude of the measured coefficients and those that can admix symmetry channels. In particular, uncertainties in sample dimensions, angular misalignment, and strain magnitude errors (all relevant to differential longitudinal configurations) can also manifest in the transverse technique. In addition, misalignment of the contacts used to measure the transverse voltages can lead to some amount of longitudinal resistivity ρ_{xx} seeping into an intended measurement of ρ_{xy} , in which case it is necessary to determine an appropriate method to correctly subtract such longitudinal contamination. In this section, we address each of these concerns as they relate to the transverse scheme, quoting a few main results (whose full derivation appears in Appendices 3.B, 3.C, and 3.D) and emphasizing the advantages of the transverse setup. In particular we note the principal advantage of the transverse technique is that the measurement does not suffer from A_{1g} contamination.

(a) Angular misalignment: Alignment errors propagate in analogous ways as for the differential longitudinal case (Section 3.3.2). Assuming that we intended to measure $(\Delta\rho/\rho)_{(xy)''}(H_z)$ and $(\Delta\rho/\rho)_{(yx)''}(H_z)$ in a (θ, ϕ) configuration but actually mounted at $(\theta + \delta\theta_{xy}, \phi + \delta\phi_{xy})$ and $(\theta + \delta\theta_{yx}, \phi + \delta\phi_{yx})$ (respectively), we obtain the analog of (3.7) for the propagated error and (3.8) for the contamination from the other symmetry channel (one need only interchange subscripts $xx \leftrightarrow xy$ and $yy \leftrightarrow yx$; see Appendix 3.B); again, in the high symmetry configurations, the leading errors are at

second order in the angular misalignment and consequently lead to negligibly small systematic errors.

(b) Unequal strain experienced by the two samples: Strain offset errors are fundamentally different than in the differential longitudinal configuration, which is the primary advantage of the transverse geometry. In zero magnetic field, the quantity $(\Delta\rho/\rho)_{(xy)''}$ is fundamentally immune to strain offset errors (indeed, there is no offset since only a single sample is needed, in contrast to the differential technique). Furthermore, the isotropic strains that are experienced by the crystal cannot generate a transverse voltage: that is, rotationally invariant (A_{1g}) strains cannot produce directionally oriented (B_{1g} or B_{2g}) resistivity changes (see Appendix (3.C.6), with $m_{xy,xx} = m_{xy,zz} = 0$ in vanishing field). In a finite field, a second measurement is needed, but since Onsager gives $(\Delta\rho/\rho)_{(yx)''}(H_z) = (\Delta\rho/\rho)_{(xy)''}(-H_z)$, one can measure the induced resistivity changes without re-gluing the crystal; therefore, one can be sure that the strain offset errors in the $(\Delta\rho/\rho)_{(xy)''}(\pm H_z)$ measurements are exactly zero. *This is the primary advantage of the transverse technique.*

(c) Subtracting ρ_{xx} contamination from a transverse measurement: One additional complication in measuring $(\Delta\rho/\rho)_{(xy)''}(H_z)$, however, is subtracting out any unwanted contributions from ρ_{xx} in a putative ρ_{xy} measurement due to unintentional contact misalignment. In a typical Hall measurement of ρ_{xy} , one can use the fact that the transverse force on the electrons is odd in the magnetic field and hence anti-symmetrize the data in field to subtract out ρ_{xx} . This approach does not work for transverse elastoresistivity, where the symmetry-motivated elastoresistivity coefficients of interest are themselves even in the magnetic field (despite coming from a measurement of $(\Delta\rho/\rho)_{(xy)''}(H_z)$). Instead, one needs to characterize the amount of longitudinal ρ_{xx} contamination in terms of the geometry of the electrical contacts themselves. Parametrizing this geometrical misalignment by a parameter

Δ_ℓ , one accounts for such contamination by simultaneously measuring the longitudinal elastoresistance $(\Delta\rho/\rho)_{(xx)''}(H_z)$ from a second pair of contacts (Figure 3.6) and precisely subtracting out the down-weighted contribution $\Delta_\ell \left[(\Delta\rho/\rho)_{(xx)''}(H_z) \right]$ from $(\Delta\rho/\rho)_{(xy)''}(H_z)$. The full subtraction procedure is derived and outlined in Appendix 3.D.

(d) Geometric effects: Geometric effects manifest in a fundamentally different manner in the transverse method relative to the differential longitudinal method. The relative change in transverse resistance $(\Delta R/R)_{xy}$ is a sum of the intrinsic elastoresistivity $(\Delta\rho/\rho)_{xy}$ and a geometric term related to the strain-induced change in thickness of the crystal $\Delta t/t$. For a pure B_{1g} or B_{2g} distortion, $\Delta t \equiv 0$, but even in a nonideal realization in which there is also some isotropic component to the strain (and therefore a finite Δt), the contribution to the measured $(\Delta R/R)_{xy}$ is down-weighted by the unstrained ρ_{xy} , which for a tetragonal material is precisely zero in zero magnetic field. Thus, while geometric effects contribute a small, temperature-independent, additive factor of order unity to the measured elastoresistivity coefficients in the differential longitudinal configuration (that are still negligible on approaching the phase transition), these sorts of geometric effects are even smaller in the transverse scheme (see further discussion in Appendix 3.D). However, in converting between measured relative changes in resistance $(\Delta R/R)_{xy}$ and intrinsic relative changes in resistivity $(\Delta\rho/\rho)_{xy}$, a multiplicative factor relating to the length l and width w of the crystal is required: $(\Delta\rho/\rho)_{xy} = \frac{l}{w} (\Delta R/R)_{xy}$ (derivation in Appendix 3.D). Errors in the determination of the in-plane dimensions of the crystal are temperature-independent and do not admix elastoresistivity coefficients of different symmetries.

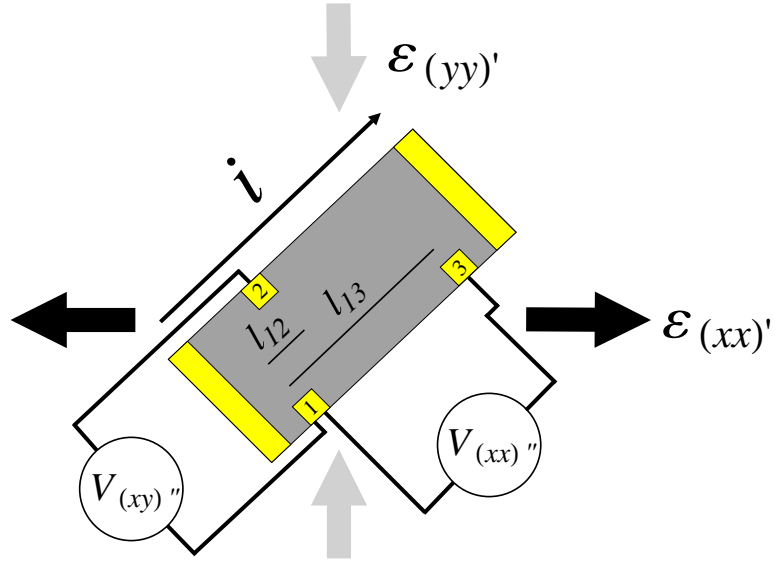


Figure 3.6: Schematic diagram showing contact geometry for a practical transverse elasto-resistance measurement. Contacts 1 and 2 are used to measure $R_{(xy)''}$; however, partial misalignment can lead to $R_{(xx)''}$ contamination in a nominal $R_{(xy)''}$ measurement. This contamination can be accounted for by subtracting out a down-weighted longitudinal contribution, with the down-weighting given by the factor Δ_ℓ . Δ_ℓ is defined as the ratio of the misalignment distance l_{12} to the distance between longitudinal contacts l_{13} , which is related to the ratio of the transverse and longitudinal voltages on a free-standing crystal: $\Delta_\ell \equiv l_{12}/l_{13} = V_{(xy)''}(H=0, \text{free-standing})/V_{(xx)''}(H=0, \text{free-standing})$ (see Appendix 3.D). This subtraction procedure is analogous to the anti-symmetrization procedure that is used for Hall effect measurements. To use this geometry to probe $\chi_{B_{1g}}$ or $\chi_{B_{2g}}$ requires mounting the crystal such that $(\theta, \phi) = (\pi/4, 0)$ or $(\theta, \phi) = (0, \pi/4)$, respectively, as described in the main text.

3.5 Transverse Elastoresistivity Measurements of BaFe_2As_2

In order to demonstrate the efficacy of the new transverse configuration, we chose to measure the $2m_{xy,xy}$ elastoresistivity coefficient of the representative iron-pnictide BaFe_2As_2 . Since we have already extracted this coefficient using the differential longitudinal method [70], this allows for a direct comparison between the two configurations. As we demonstrate below, values of $2m_{xy,xy}$ extracted from the two techniques agree in their temperature dependence, revealing a nematic instability in the B_{2g} symmetry channel.

3.5.1 Experimental Methods

Single crystals of BaFe_2As_2 were grown from a self-flux method as described elsewhere [79, 80]. The crystals grow as thin plates, with the c -axis perpendicular to the plane of the plates and natural facets along the in-plane principal tetragonal axes. A representative, as-grown, rectangular ($1.6 \text{ mm} \times 0.67 \text{ mm} \times 0.029 \text{ mm}$) crystal was selected for the transport measurements. X-ray diffraction was used to confirm that the crystallographic [100] and [010] axes were oriented along the length/width of the sample. Electrical contacts (with current sourced along the [100] tetragonal direction) were affixed to gold-sputtered pads with Dupont 4929N silver paste.

Prior to gluing the sample to the PZT stack, the temperature dependence of the resistances $R_{(xx)''}$ and $R_{(xy)''}$ were measured in zero magnetic field for the free-standing, unstrained crystal in order to pre-characterize the contact geometry. The unstrained $R_{(xx)''}$ is also used for normalizing the elastoresistance data. The samples were then glued to the top surface of a PZT piezoelectric stack (Part Number PSt 150/5×5/7 cryo 1, from Piezomechanik GmbH) using ITW Devcon five minute epoxy spread uniformly across the bottom of the crystal (Figure 3.7). The orientation of the crystal axes of the sample with respect to the principal axes of the PZT stack was initially determined by eye, such that the long axis of the transport bar was at an angle ϕ of approximately 45° with respect to the PZT stack. The angle was

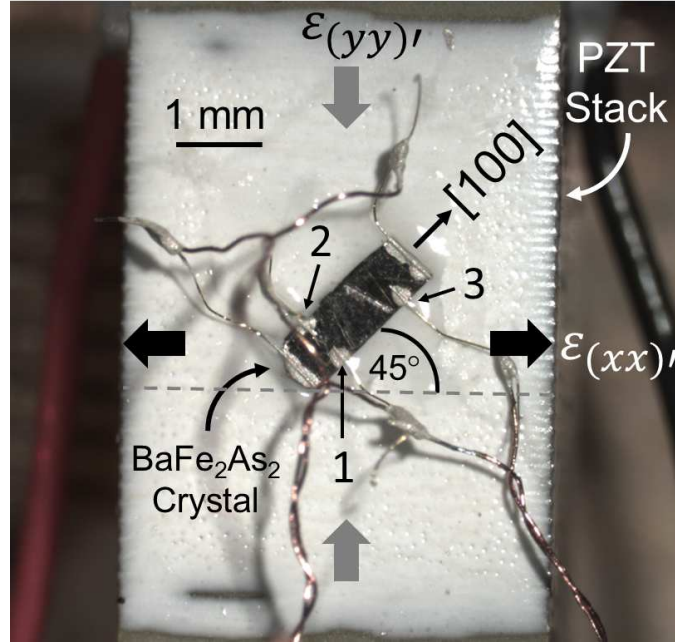


Figure 3.7: Photograph showing a BaFe_2As_2 crystal affixed to the surface of a PZT stack and mounted in the transverse elastoresistivity configuration $(\theta, \phi) = (0, \pi/4)$, appropriate for measuring $2m_{xy,xy}$ ($\propto \chi_{B_{2g}}$). Contacts 1, 2, and 3 are labeled with reference to Figure 3.6. The twisted pairs used for performing the voltage measurements are evident.

subsequently determined more precisely from measurements of the photograph shown in Figure 3.7 to be $45.4^\circ \pm 0.2^\circ$. Mutually transverse strain gauges (Part Number WK-05-062TT-350, from Vishay Precision Group) were glued to the other side of the PZT stack in order to measure the strains $\epsilon_{(xx)'}^{\prime}$ and $\epsilon_{(yy)'}^{\prime}$ *in situ*.

The PZT stack was mounted on the coldhead of a specially adapted probe and cooled in exchange gas in a Janis flow cryostat. Temperature was controlled with a Lake Shore 340 temperature controller, with a stability of ± 50 mK.³ The resistances of both the sample and the strain gauges were measured using Stanford Research Systems SR830 lock-in amplifiers; for the sample, Stanford Research Systems Model

³Temperature stability is an important consideration for these measurements, with the degree of stability needed dictated by the particular material at hand. A requisite condition is that the strain-induced response $\Delta\rho(T, \epsilon + \Delta\epsilon)$ be much larger than the thermally-induced resistivity change $\Delta\rho(T + \Delta T, \epsilon)$; equivalently, this condition requires $\Delta T \ll \frac{d\rho}{d\epsilon} \cdot \Delta\epsilon / \frac{d\rho}{dT}$, where $\frac{d\rho}{d\epsilon}$ is related to an appropriate combination of the material's elastoresistivity coefficients.

SR560 preamplifiers were also used. AC excitation currents of 1 mA and 0.1 mA were used for the sample and strain gauges, respectively.

Elastoresistance data at a fixed temperature were acquired from changes in the resistances of the sample ($R_{(xx)''}$ and $R_{(xy)''}$) and of both strain gauges while sweeping the voltage applied to the PZT between -50 V and $+150$ V. The voltage was swept stepwise in 4 V increments with a delay of 0.25 s between steps; the measured elastoresistance did not depend on this sweep rate scheme, nor were there any observed heating effects [57]. Three full voltage loops were taken for each temperature setpoint; after completing these loops, the temperature was then stepped to a new setpoint and allowed to stabilize before performing the next elastoresistance measurement. All elastoresistance measurements were performed in zero applied magnetic field.

3.5.2 Results

The temperature dependence of the longitudinal and transverse resistances for the free-standing (unstrained) sample are shown in Figure 3.8. The longitudinal resistance R_{xx} follows the usual temperature dependence for this material, exhibiting a downturn at the coupled structural-magnetic phase transition at $T_{S,N} = 134$ K. A finite R_{xy} is measured even for the unstrained sample (middle panel of Figure 3.8) due to misalignment of the contacts used for the transverse voltage measurement. As can be seen, for temperatures above $T_{S,N}$, the ratio $R_{xy}/R_{xx} = \Delta_\ell$ is temperature-independent, with a value of $\sim 0.041 \pm 0.01$. A small deviation from this constant value can be discerned for temperatures just above $T_{S,N}$, presumably due to residual strains in the sample [81]. The subsequent discussion and analysis refers solely to temperatures above $T_{S,N}$, for which the material is tetragonal; below this temperature, the crystal structure is orthorhombic, and the transverse resistance reflects an admixture of effects arising from longitudinal contamination, electronic anisotropy associated with the orthorhombicity, twin domain populations, and twin boundary motion.

Representative strain-induced resistance changes $\Delta R_{(xy)''}$, $\Delta R_{(xx)''}$, and $\Delta_\ell \Delta R_{(xx)''}$ for three voltage sweeps at 100 K are shown in Figure 3.9. The elastoresistive response

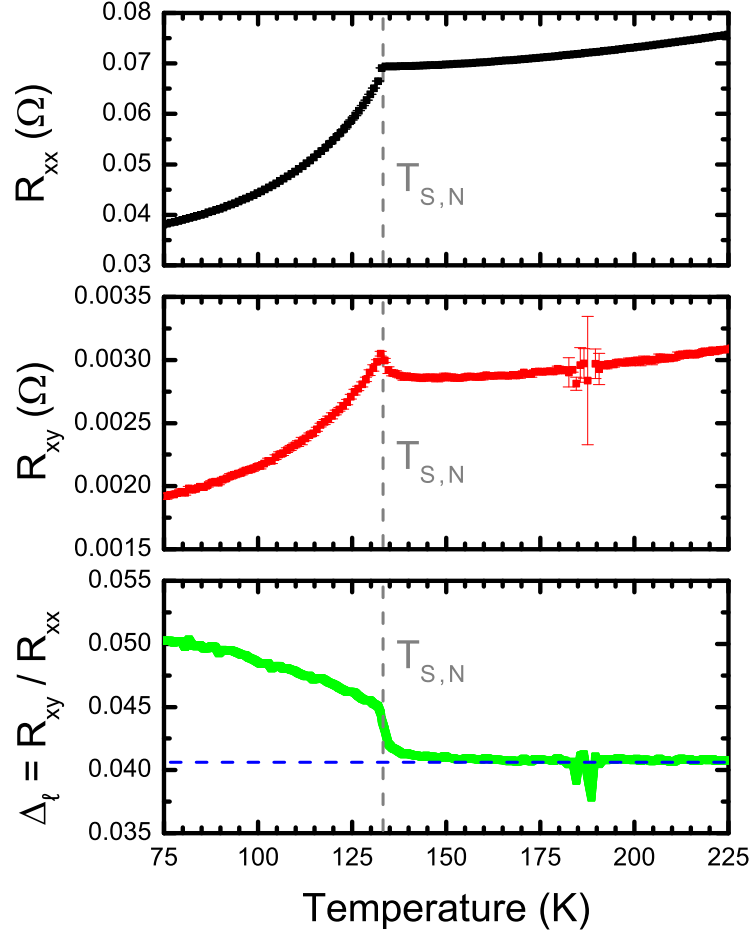


Figure 3.8: Resistance measurements for the BaFe_2As_2 sample showing R_{xx} (top panel), R_{xy} (middle panel), and the ratio $\Delta_\ell \equiv R_{xy}/R_{xx}$ (bottom panel). For temperatures above the coupled structural and magnetic transition at $T_{S,N}$ (vertical dashed gray line), Δ_ℓ is small and temperature-independent; by taking the average value for temperatures > 150 K, we estimate $\Delta_\ell \sim 4.1 \pm 0.1\%$ (horizontal dashed blue line). Since this measurement was performed on a free-standing (unglued) sample in zero magnetic field, the measured R_{xy} in the tetragonal state is due to R_{xx} contamination from contact misalignment; Δ_ℓ characterizes the physical extent of this misalignment.

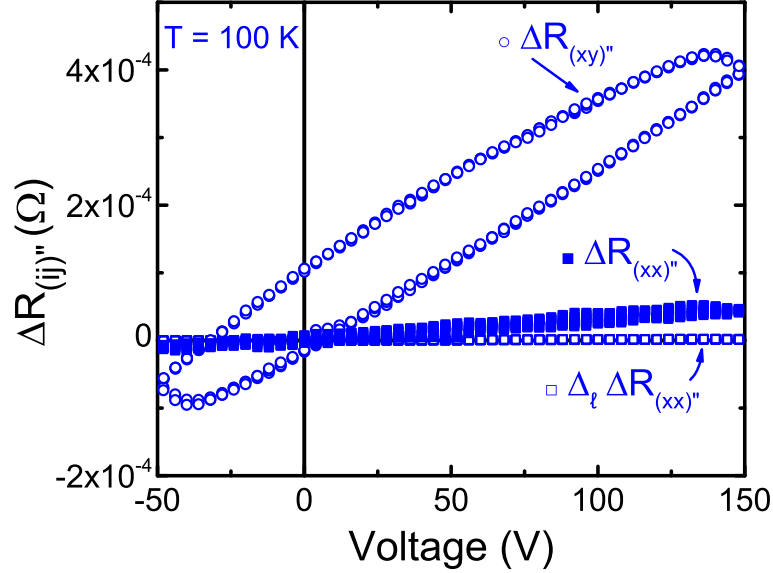


Figure 3.9: Representative data for BaFe_2As_2 showing strain-induced changes in resistance $\Delta R_{(xy)}''$, $\Delta R_{(xx)}''$, and $\Delta_\ell \Delta R_{(xx)}''$ at a temperature of 100 K as a function of the voltage applied to the PZT stack. Values of Δ_ℓ are extracted from Figure 3.8 as described in the main text. In order to correct for ρ_{xx} contamination, the relatively small amount $\Delta_\ell \Delta R_{(xx)}''$ is subtracted from $\Delta R_{(xy)}''$.

in $\Delta R_{(xy)}''$ is significantly larger than $\Delta R_{(xx)}''$, by a factor of ~ 9 at 150 V. To subtract out the ρ_{xx} contamination, one down-weights $\Delta R_{(xx)}''$ even further by Δ_ℓ ; the resulting correction ($\sim 0.4\%$) is essentially negligible on the scale of the $\Delta R_{(xy)}''$ response. The hysteretic behavior evident in $\Delta R_{(xy)}''$ is an intrinsic property of the PZT stack.

Representative transverse elastoresistance data, which have been corrected for the small longitudinal contamination as described above, are shown in Figure 3.10 as a function of applied shear strain ($\epsilon_{xy} = -\frac{1}{2}(\epsilon_{(xx)'} - \epsilon_{(yy)'})$) for a variety of temperatures. The applied shear strain is relative to the strain experienced by the crystal with 0 V applied to the PZT stack. Because of the combined effects of gluing to the PZT stack and differential thermal contraction between the crystal and PZT, the applied shear strain is *not* relative to the zero strain state of the crystal. As

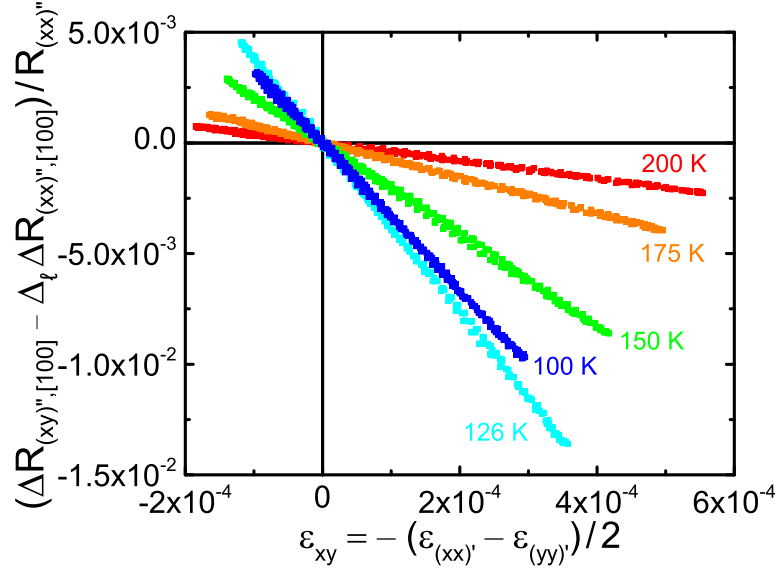


Figure 3.10: Representative data showing the temperature dependence of the elasto-resistive response of BaFe_2As_2 in the transverse configuration $(\theta, \phi) = (0, \pi/4)$ as a function of the induced shear strain ($\epsilon_{xy} = -\frac{1}{2}(\epsilon_{(xx)'} - \epsilon_{(yy)'})$) experienced by the crystal. This is the appropriate configuration for measuring $2m_{xy,xy}$ ($\propto \chi_{B_{2g}}$). Slopes have been corrected for ρ_{xx} contamination, as described in the main text and Appendix 3.D. All responses were linear in the applied strain for all measured temperatures.

can be seen, all measured elasto-resistances are linear in (relative) shear strain for all measured temperatures. The elasto-resistivity coefficient $2m_{xy,xy}$ at each temperature is extracted from the slopes in Figure 3.10 and a multiplicative factor of the crystal's length to its width used to convert the resistance ratio to a resistivity ratio $((\Delta\rho/\rho)_{(xy)'}) = \frac{l}{w} (\Delta R_{(xy)''}/R_{xx})$; see Appendix 3.D). The temperature dependence of the resulting values of $2m_{xy,xy}$ is shown in Figure 3.11. As has been previously shown [70,82], $2m_{xy,xy}$ progressively increases on cooling, reaches its peak at the coupled structural and magnetic transition temperature, and then gradually decreases on further cooling. The maximum value of $2m_{xy,xy}$ is ~ 52 , much larger than that of a typical metal (~ 1).

In accordance with our previous analysis of differential longitudinal elasto-resistance measurements [58,61], the diverging temperature dependence of $2m_{xy,xy}$ can be

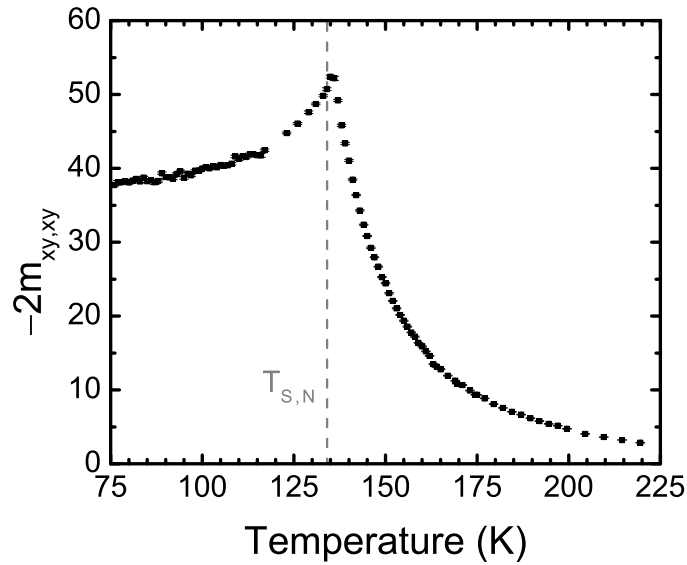


Figure 3.11: Temperature dependence of the elasto-resistivity coefficient $2m_{xy,xy}$ of BaFe_2As_2 from the transverse configuration. Error bars represent 95% confidence intervals from the linear fits to the elasto-resistive slopes at each temperature. The vertical dashed bar marks the coincident structural and magnetic transition temperature $T_{S,N}$ of the sample.

fit well to the Curie-Weiss form

$$2m_{xy,xy} = \frac{\lambda}{a_0(T - \theta)} + 2m_{xy,xy}^0. \quad (3.12)$$

Directly fitting the temperature dependence of $2m_{xy,xy}$ to the Curie-Weiss form (3.12), the temperature-independent fit parameter $2m_{xy,xy}^0$ can be estimated and then used to plot the temperature dependence of the inverse susceptibility $[-2(m_{xy,xy} - m_{xy,xy}^0)]^{-1}$ (which, for an exact Curie-Weiss form, is linear in temperature). Fitting over the temperature range of 136 K to 220 K results in an estimate of $2m_{xy,xy}^0 = 6.7 \pm 0.5$, which we use to plot the temperature dependence of $[-2(m_{xy,xy} - m_{xy,xy}^0)]^{-1}$ as in Figure 3.12. Further details on the evaluation of the goodness of fit and on the temperature window used are discussed in Appendix 3.E. The slope and intercept of $[-2(m_{xy,xy} - m_{xy,xy}^0)]^{-1}$ yield estimates of $\lambda/a_0 = -909 \pm 16$ K and $\theta = 120 \pm 0.9$ K, as given in Table 3.1. As we have previously discussed, the observation of such a Curie-Weiss susceptibility with a Weiss temperature θ close to the coupled structural and magnetic transition definitively establishes the ferroelastic phase transition in BaFe₂As₂ to be pseudo-proper (i.e., strain is not the primary order parameter of the transition but does have the same symmetry as the order parameter) [58, 61]. The physical origin of the electronic nematic order that drives this phase transition remains a subject of ongoing research (for example, see Fernandes *et al.* [65] for a recent review and discussion).

The estimated Curie-Weiss fit parameters from the transverse method can also be compared to the parameter estimates from earlier measurements of $2m_{xy,xy}$ by the differential longitudinal [82] and modified Montgomery methods [70] (see Table 3.1). All three measurements agree in their divergent temperature dependence, which evinces the existence and onset of a nematic order parameter. The differential longitudinal and transverse measurements agree within $\sim 4.0\%$ in their estimate of θ (which characterizes a bare mean field nematic critical temperature) and agree within $\sim 1.3\%$ in their estimates of λ/a_0 ; meanwhile, there is a larger discrepancy between the estimates of θ and λ/a_0 as obtained from the modified Montgomery and transverse methods.

The quantitative variations in the estimated fit parameters between the three

Table 3.1: Fit Parameters from Transverse, Differential Longitudinal, and Modified Montgomery Methods

Parameter	Transverse	Diff. Longitudinal [82]	Modified Montgomery [70]
$2m_{xy,xy}^0$	6.7 ± 0.5	4.7 ± 0.98	7.7 ± 0.3
λ/a_0 (K)	-909 ± 16	-897 ± 84	-1540 ± 13
θ (K)	120 ± 0.9	124.9 ± 1.6	109 ± 0.7

Fit to $2m_{xy,xy} = \frac{\lambda}{a_0(T-\theta)} + 2m_{xy,xy}^0$; uncertainties represent 95% confidence intervals from a least squares fitting routine.

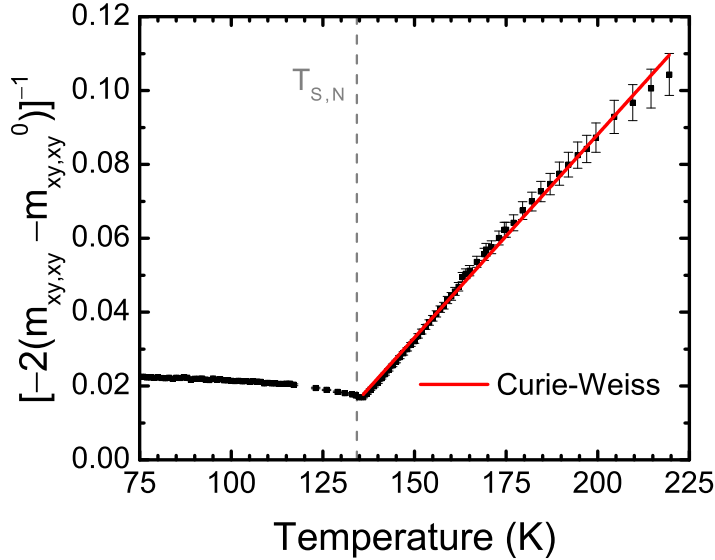


Figure 3.12: Temperature dependence of $[-2(m_{xy,xy} - m_{xy,xy}^0)]^{-1}$, proportional to the inverse nematic susceptibility $\chi_{B_{2g}}^{-1}$ in this configuration. Error bars represent 95% confidence intervals from both the linear fits to the elastoresistive slopes at each temperature and the estimation of $2m_{xy,xy}^0$. The red line shows a linear fit (i.e., Curie-Weiss functional form) between 136 K and 220 K, with fit parameters given in Table 3.1. The vertical dashed line marks the coincident structural and magnetic transition temperature $T_{S,N}$ of the sample ($T_{S,N} = 134$ K).

methods presumably reflect systematic differences in the physical environment in which the three experiments are performed. Strictly, elastoresistivity coefficients are defined in the limit of vanishing strain; however, this limit is not precisely realized in any of the three methods. The elastoresistivity coefficients as extracted from the differential longitudinal and transverse methods are measured relative to the strain state of the crystal with 0 V applied to the PZT (i.e., relative to a state with some residual built-in isotropic and anisotropic strain due to adhesion to the strain-transmitting substrate and differential thermal contraction), while the elastoresistivity coefficients as extracted from the modified Montgomery method are measured relative to a “ B_{2g} neutral point” [70] where the anisotropic strain is tuned to zero by applying a finite voltage to the PZT (until the longitudinal resistivities ρ_{xx} , ρ_{yy} are equal) but where the isotropic strain is explicitly nonzero. Furthermore, since the physical dimensions of the crystals vary between the three studies (“matchstick” rectangular bars for the differential longitudinal measurements; square or rectangular plates with a nearly 2:1 aspect ratio for the modified Montgomery and transverse methods), the effect of strain relaxation due to the geometry of the crystals could plausibly contribute to systematic variation in the fit parameter estimates as well. The exact reasons for the quantitative differences, however, are not yet perfectly understood.

3.6 Conclusion

In writing this paper, we have had two overarching goals. First, building on the elastoresistivity formalism that we have introduced in recent publications [55, 58], we have proposed an alternative method to probe the B_{1g} and B_{2g} components of the elastoresistivity tensor for a tetragonal material via transverse elastoresistivity measurements. We have quantified the effects of various experimental nonidealities that affect both the earlier differential longitudinal elastoresistance methods and the new transverse elastoresistance method and have shown that the transverse scheme has certain specific advantages. In particular, the transverse technique enables measurement of $m_{xx,xx} - m_{xx,yy}$ or $2m_{xy,xy}$ via a single measurement. Importantly, since isotropic strains cannot induce a transverse elastoresistivity $(\Delta\rho/\rho)_{(xy)''}$, and since $2m_{xy,xy}$ was

extracted from a single measurement, the new method is fundamentally immune to A_{1g} -like strains and strain offset errors.

Second, we have used the representative iron-pnictide BaFe_2As_2 to explicitly demonstrate the viability of the transverse elastoresistivity configuration. The new method corroborates the earlier finding of a Curie-Weiss-like $2m_{xy,xy}$ elastoresistivity coefficient in this material, signaling the divergent nematic susceptibility in the B_{2g} symmetry channel. To our knowledge, this is the first discussion and measurement of transverse elastoresistance for any material.

3.A Elastoresistivity Tensor for D_{4h} and Transformation Properties

The explicit form of the elastoresistivity tensor for D_{4h} point group symmetry is [55]

$$m_{ij,kl}^{D_{4h}}(H_z) = \begin{pmatrix} m_{xx,xx} & m_{xx,yy} & m_{xx,zz} & 0 & 0 & 0 & 0 & 0 & 0 & 0 \\ m_{xx,yy} & m_{xx,xx} & m_{xx,zz} & 0 & 0 & 0 & 0 & 0 & 0 & 0 \\ m_{zz,xx} & m_{zz,xx} & m_{zz,zz} & 0 & 0 & 0 & 0 & 0 & 0 & 0 \\ 0 & 0 & 0 & m_{yz,yz} & m_{yz,yz} & m_{yz,zx} & m_{yz,zx} & 0 & 0 & 0 \\ 0 & 0 & 0 & m_{yz,yz} & m_{yz,yz} & -m_{yz,zx} & -m_{yz,zx} & 0 & 0 & 0 \\ 0 & 0 & 0 & m_{yz,zx} & m_{yz,zx} & m_{yz,yz} & m_{yz,yz} & 0 & 0 & 0 \\ 0 & 0 & 0 & -m_{yz,zx} & -m_{yz,zx} & m_{yz,yz} & m_{yz,yz} & 0 & 0 & 0 \\ m_{xy,xx} & m_{xy,xx} & m_{xy,zz} & 0 & 0 & 0 & 0 & m_{xy,xy} & m_{xy,xy} & 0 \\ -m_{xy,xx} & -m_{xy,xx} & -m_{xy,zz} & 0 & 0 & 0 & 0 & m_{xy,xy} & m_{xy,xy} & 0 \end{pmatrix}. \quad (3.A.1)$$

This tensor has 10 independent coefficients, all implicitly dependent on the magnetic field. Those coefficients (of which there are seven) that have an even number of x or an even number of y indices are correspondingly even functions of the magnetic field due to the σ_x and σ_y symmetry constraints (where σ_x and σ_y are mirror operations about the yz and xz planes, respectively). Conversely, those coefficients (of which there are three, demarcated by surrounding boxes) that have an odd number of x or

an odd number of y indices are odd functions of the magnetic field (and hence vanish in zero magnetic field). The symmetry properties of this tensor are described in detail elsewhere [55].

In a given elastoresistivity measurement, what one measures is $(\Delta\rho/\rho)_{(ij)''}$ (i.e., the normalized resistivity change in the transport frame) to an applied strain $\epsilon_{(kl)'}$ in the strain frame, and what one seeks to extract are terms in the elastoresistivity tensor $m_{ij,kl}$ in the crystal frame. These quantities are related by suitable transformation matrices $\hat{\alpha}_\theta, \hat{\alpha}_\phi$ according to (3.5) of the main text with the $\hat{\alpha}_\phi, \hat{\alpha}_\theta$ given by rotational transformations of the form

$$\hat{\alpha}_\phi = \begin{pmatrix} \cos^2(\phi) & \sin^2(\phi) & 0 & 0 & 0 & 0 & 0 & \cos(\phi)\sin(\phi) & \cos(\phi)\sin(\phi) \\ \sin^2(\phi) & \cos^2(\phi) & 0 & 0 & 0 & 0 & 0 & -\cos(\phi)\sin(\phi) & -\cos(\phi)\sin(\phi) \\ 0 & 0 & 1 & 0 & 0 & 0 & 0 & 0 & 0 \\ 0 & 0 & 0 & \cos(\phi) & 0 & 0 & -\sin(\phi) & 0 & 0 \\ 0 & 0 & 0 & 0 & \cos(\phi) & -\sin(\phi) & 0 & 0 & 0 \\ 0 & 0 & 0 & 0 & \sin(\phi) & \cos(\phi) & 0 & 0 & 0 \\ 0 & 0 & 0 & \sin(\phi) & 0 & 0 & \cos(\phi) & 0 & 0 \\ -\cos(\phi)\sin(\phi) & \cos(\phi)\sin(\phi) & 0 & 0 & 0 & 0 & 0 & \cos^2(\phi) & -\sin^2(\phi) \\ -\cos(\phi)\sin(\phi) & \cos(\phi)\sin(\phi) & 0 & 0 & 0 & 0 & 0 & -\sin^2(\phi) & \cos^2(\phi) \end{pmatrix} \quad (3.A.2)$$

and analogously for $\hat{\alpha}_\theta$.

Prior to discussing the implications of these transformations for the elastoresistivity tensor, it is elucidating to focus first on the effect of these rotational transformations on the strain and normalized change in resistivity tensors individually. If the crystal frame is oriented relative to the strain frame by an angle ϕ , then the strains experienced by the crystal are related to the shearless strains in the normal strain frame by $\epsilon_{kl} = \hat{\alpha}_\phi \epsilon_{(kl)'}$; explicitly, this gives

$$\begin{pmatrix} \epsilon_{xx} \\ \epsilon_{yy} \\ \epsilon_{zz} \\ \epsilon_{yz} \\ \epsilon_{zy} \\ \epsilon_{zx} \\ \epsilon_{xz} \\ \epsilon_{xy} \\ \epsilon_{yx} \end{pmatrix} = \begin{pmatrix} \epsilon_{(xx)'} \cos^2 \phi + \epsilon_{(yy)'} \sin^2 \phi \\ \epsilon_{(xx)'} \sin^2 \phi + \epsilon_{(yy)'} \cos^2 \phi \\ \epsilon_{(zz)'} \\ 0 \\ 0 \\ 0 \\ 0 \\ -\frac{1}{2}(\epsilon_{(xx)'} - \epsilon_{(yy)'}) \sin(2\phi) \\ -\frac{1}{2}(\epsilon_{(xx)'} - \epsilon_{(yy)'}) \sin(2\phi) \end{pmatrix}. \quad (3.A.3)$$

By rotating the crystal relative to the normal strain frame, the shearless strains in the normal strain frame are experienced as both normal and shear strains in the crystal frame, with the amount of shear characterized by $\sin(2\phi)$ according to $\epsilon_{xy} = \epsilon_{yx} = -\frac{1}{2}(\epsilon_{(xx)'} - \epsilon_{(yy)'}) \sin(2\phi)$.

Exactly analogous relations exist for transport measurements expressed in the transport and crystal frames. Assuming that the two frames are rotated relative to each other by an angle θ , then what one measures in the transport frame is related to the normalized change in resistivity in the crystal frame by $(\Delta\rho/\rho)_{(ij)''} = \hat{\alpha}_\theta (\Delta\rho/\rho)_{ij}$. Working this out explicitly for in-plane transport measurements,

$$(\Delta\rho/\rho)_{(xx)''} (H_z) = (\Delta\rho/\rho)_{xx} \cos^2 \theta + (\Delta\rho/\rho)_{yy} \sin^2 \theta + \frac{1}{2} \left((\Delta\rho/\rho)_{xy} + (\Delta\rho/\rho)_{yx} \right) \sin(2\theta) \quad (3.A.4a)$$

$$(\Delta\rho/\rho)_{(yy)''} (H_z) = (\Delta\rho/\rho)_{xx} \sin^2 \theta + (\Delta\rho/\rho)_{yy} \cos^2 \theta - \frac{1}{2} \left((\Delta\rho/\rho)_{xy} + (\Delta\rho/\rho)_{yx} \right) \sin(2\theta) \quad (3.A.4b)$$

$$(\Delta\rho/\rho)_{(xy)''} (H_z) = (\Delta\rho/\rho)_{xy} \cos^2 \theta - (\Delta\rho/\rho)_{yx} \sin^2 \theta - \frac{1}{2} \left((\Delta\rho/\rho)_{xx} - (\Delta\rho/\rho)_{yy} \right) \sin(2\theta) \quad (3.A.4c)$$

$$(\Delta\rho/\rho)_{(yx)''} (H_z) = -(\Delta\rho/\rho)_{xy} \sin^2 \theta + (\Delta\rho/\rho)_{yx} \cos^2 \theta - \frac{1}{2} \left((\Delta\rho/\rho)_{xx} - (\Delta\rho/\rho)_{yy} \right) \sin(2\theta). \quad (3.A.4d)$$

The form of (3.A.4) emphasizes that the amount of $(\Delta\rho/\rho)_{xy}$ and $(\Delta\rho/\rho)_{yx}$ signal in a $(\Delta\rho/\rho)_{(xx)''}$ or $(\Delta\rho/\rho)_{(yy)''}$ measurement is characterized by $\sin(2\theta)$, and likewise for the amount of $(\Delta\rho/\rho)_{(xx)}$ and $(\Delta\rho/\rho)_{(yy)}$ in a $(\Delta\rho/\rho)_{(xy)''}$ or $(\Delta\rho/\rho)_{(yx)''}$ measurement.

For the in-plane transport measurements that are the subject of this work, the transformation properties of the relevant elastoresistivity coefficients are given by performing the transformation (3.5) with the specific elastoresistivity tensor (3.A.1):

$$m_{(xx)'', (xx)'} = m_{(yy)'', (yy)'} = m_{xx,xx} - m_{xy,xy} \sin(2\theta) \sin(2\phi) - \frac{1}{2} (m_{xx,xx} - m_{xx,yy}) \left[1 - \cos(2\theta) \cos(2\phi) \right] \quad (3.A.5a)$$

$$m_{(xx)'', (yy)'} = m_{(yy)'', (xx)'} = m_{xx,yy} + m_{xy,xy} \sin(2\theta) \sin(2\phi) + \frac{1}{2} (m_{xx,xx} - m_{xx,yy}) \left[1 - \cos(2\theta) \cos(2\phi) \right] \quad (3.A.5b)$$

$$m_{(xx)'', (zz)'} = m_{(yy)'', (zz)'} = m_{xx,zz} \quad (3.A.5c)$$

$$m_{(xy)'', (xx)'} = m_{xy,xx} - m_{xy,xy} \cos(2\theta) \sin(2\phi) - \frac{1}{2} (m_{xx,xx} - m_{xx,yy}) \sin(2\theta) \cos(2\phi) \quad (3.A.5d)$$

$$m_{(xy)'', (yy)'} = m_{xy,xx} + m_{xy,xy} \cos(2\theta) \sin(2\phi) + \frac{1}{2} (m_{xx,xx} - m_{xx,yy}) \sin(2\theta) \cos(2\phi) \quad (3.A.5e)$$

$$m_{(yx)'', (xx)'} = -m_{xy,xx} - m_{xy,xy} \cos(2\theta) \sin(2\phi) - \frac{1}{2} (m_{xx,xx} - m_{xx,yy}) \sin(2\theta) \cos(2\phi) \quad (3.A.5f)$$

$$m_{(yx)'', (yy)'} = -m_{xy,xx} + m_{xy,xy} \cos(2\theta) \sin(2\phi) + \frac{1}{2} (m_{xx,xx} - m_{xx,yy}) \sin(2\theta) \cos(2\phi) \quad (3.A.5g)$$

$$m_{(xy)'', (zz)'} = -m_{(yx)'', (zz)'} = m_{xy,zz}. \quad (3.A.5h)$$

Expressing the in-plane transport quantities $(\Delta\rho/\rho)_{(ij)''}$ in terms of applied normal strains $\epsilon_{(kl)'}$, plugging in the transformed elastoresistivity coefficients from (3.A.5), and taking the symmetry-motivated combinations $(\Delta\rho/\rho)_{(xx)''} - (\Delta\rho/\rho)_{(yy)''}$ and $(\Delta\rho/\rho)_{(xy)''} + (\Delta\rho/\rho)_{(yx)''}$, we arrive at expressions (3.6) and (3.9) of the main text.

As a final comment, and in order to connect with the experimental setup described in our previous work [58, 61], we note that for configurations in which the current is sourced coincidentally with the normal strain axes, $\phi = -\theta$ and

$$m_{(ij)'', (kl)'} = \hat{\alpha}_\theta m_{ij,kl} \hat{\alpha}_{-\theta} = \hat{\alpha}_\theta m_{ij,kl} \hat{\alpha}_\theta^{-1}. \quad (3.A.6)$$

3.B Quantifying Current and Strain Alignment Errors

As described in the main text (and illustrated in Figures 3.3, 3.4), the high-symmetry configurations for the differential longitudinal elastoresistance measurement are given by (3.6) with $(\theta, \phi) = (0, 0)$ or $(-\pi/4, \pi/4)$, while the high-symmetry configurations for the superposed transverse elastoresistance measurement are given by (3.9) with $(\theta, \phi) = (\pi/4, 0)$ or $(0, \pi/4)$. In an actual measurement, however, slight misalignment relative to these high symmetry directions can be anticipated. In this section we quantify the consequences of such misalignments.

Suppose that in a measurement of $(\Delta\rho/\rho)_{(xx)''}$, it was intended that the crystal frame be oriented relative to the transport and normal strain frames according to some (θ, ϕ) , but the actual configuration was given by $(\theta + \delta\theta_{xx}, \phi + \delta\phi_{xx})$. Similarly, suppose that in an attempt to measure $(\Delta\rho/\rho)_{(yy)''}$, the intended orientation of the crystal frame to be oriented relative to the transport and normal strain frames was (θ, ϕ) , but the actual configuration was given by $(\theta + \delta\theta_{yy}, \phi + \delta\phi_{yy})$. In general, we take $\delta\theta_{xx} \neq \delta\theta_{yy}$ and $\delta\phi_{xx} \neq \delta\phi_{yy}$ so that we treat all alignment errors independently. We now show how such errors propagate in the experimental determination of the relevant elastoresistivity coefficients.

For this type of misalignment, the combination $(\Delta\rho/\rho)_{(xx)''}(H_z) - (\Delta\rho/\rho)_{(yy)''}(H_z)$ is given by

$$\begin{aligned}
 & (\Delta\rho/\rho)_{(xx)''} - (\Delta\rho/\rho)_{(yy)''} = & (3.B.1) \\
 & -\frac{1}{2}(\epsilon_{(xx)'} - \epsilon_{(yy)'})2m_{xy,xy} \left[\sin 2(\theta + \delta\theta_{xx}) \sin 2(\phi + \delta\phi_{xx}) + \sin 2(\theta + \delta\theta_{yy}) \sin 2(\phi + \delta\phi_{yy}) \right] \\
 & + \frac{1}{2}(\epsilon_{(xx)'} - \epsilon_{(yy)'}) (m_{xx,xx} - m_{xx,yy}) \left[\cos 2(\theta + \delta\theta_{xx}) \cos 2(\phi + \delta\phi_{xx}) \right. \\
 & \qquad \qquad \qquad \left. + \cos 2(\theta + \delta\theta_{yy}) \cos 2(\phi + \delta\phi_{yy}) \right],
 \end{aligned}$$

This expression naturally reduces to (3.6) for perfect angular alignment (i.e., $\delta\theta_{xx} = \delta\theta_{yy} = \delta\phi_{xx} = \delta\phi_{yy} = 0$). Expanding this expression to quadratic order in the

angular errors about the high-symmetry configurations $(\theta, \phi) = (0, 0)$ and $(\theta, \phi) = (-\pi/4, \pi/4)$, we find

$$\begin{aligned}
 (\Delta\rho/\rho)_{(xx)''} - (\Delta\rho/\rho)_{(yy)''} &\approx -(\epsilon_{(xx)'} - \epsilon_{(yy)'})2m_{xy,xy} \left[2(\delta\theta_{xx}\delta\phi_{xx} + \delta\theta_{yy}\delta\phi_{yy}) \right] \quad (3.B.2a) \\
 &+ (\epsilon_{(xx)'} - \epsilon_{(yy)'}) (m_{xx,xx} - m_{xx,yy}) \left[1 - ((\delta\theta_{xx})^2 + (\delta\theta_{yy})^2 + (\delta\phi_{xx})^2 + (\delta\phi_{yy})^2) \right] \\
 &\quad \left[(\boldsymbol{\theta}, \boldsymbol{\phi}) = (\mathbf{0}, \mathbf{0}) \right]
 \end{aligned}$$

$$\begin{aligned}
 (\Delta\rho/\rho)_{(xx)''} - (\Delta\rho/\rho)_{(yy)''} &\approx (\epsilon_{(xx)'} - \epsilon_{(yy)'})2m_{xy,xy} \left[1 - ((\delta\theta_{xx})^2 + (\delta\theta_{yy})^2 + (\delta\phi_{xx})^2 + (\delta\phi_{yy})^2) \right] \\
 &- (\epsilon_{(xx)'} - \epsilon_{(yy)'}) (m_{xx,xx} - m_{xx,yy}) \left[2(\delta\theta_{xx}\delta\phi_{xx} + \delta\theta_{yy}\delta\phi_{yy}) \right]. \quad (3.B.2b) \\
 &\quad \left[(\boldsymbol{\theta}, \boldsymbol{\phi}) = (-\pi/4, \pi/4) \right]
 \end{aligned}$$

As can be seen from (3.B.2), for the high-symmetry configurations, the amount of error introduced enters at second order in the angular misalignments.

Consideration of alignment errors for the transverse elastoresistance configuration proceeds in an analogous manner. Suppose that for a high-symmetry configuration (θ, ϕ) , the measurements of $(\Delta\rho/\rho)_{(xy)''}$ and $(\Delta\rho/\rho)_{(yx)''}$ are actually characterized by $(\theta + \delta\theta_{xy}, \phi + \delta\phi_{xy})$ and $(\theta + \delta\theta_{yx}, \phi + \delta\phi_{yx})$, respectively, with $\delta\theta_{xy} \neq \delta\theta_{yx}$ and $\delta\phi_{xy} \neq \delta\phi_{yx}$. A measurement of $(\Delta\rho/\rho)_{(xy)''}(H_z) + (\Delta\rho/\rho)_{(yx)''}(H_z)$ is then given by

$$\begin{aligned}
 &(\Delta\rho/\rho)_{(xy)''} + (\Delta\rho/\rho)_{(yx)''} = \quad (3.B.3) \\
 &-\frac{1}{2}(\epsilon_{(xx)'} - \epsilon_{(yy)'})2m_{xy,xy} \left[\cos 2(\theta + \delta\theta_{xy}) \sin 2(\phi + \delta\phi_{xy}) + \cos 2(\theta + \delta\theta_{yx}) \sin 2(\phi + \delta\phi_{yx}) \right] \\
 &-\frac{1}{2}(\epsilon_{(xx)'} - \epsilon_{(yy)'}) (m_{xx,xx} - m_{xx,yy}) \left[\sin 2(\theta + \delta\theta_{xy}) \cos 2(\phi + \delta\phi_{xy}) \right. \\
 &\quad \left. + \sin 2(\theta + \delta\theta_{yx}) \cos 2(\phi + \delta\phi_{yx}) \right].
 \end{aligned}$$

which reduces to (3.9) for perfect angular alignment. Again expanding this expression

to quadratic order in the angular errors about the high-symmetry configurations $(\theta, \phi) = (\pi/4, 0)$ and $(\theta, \phi) = (0, \pi/4)$, we find

$$\begin{aligned} (\Delta\rho/\rho)_{(xy)''} + (\Delta\rho/\rho)_{(yx)''} &\approx (\epsilon_{(xx)'} - \epsilon_{(yy)'})2m_{xy,xy} \left[2(\delta\theta_{xy}\delta\phi_{xy} + \delta\theta_{yx}\delta\phi_{yx}) \right] \\ &\quad - (\epsilon_{(xx)'} - \epsilon_{(yy)'}) (m_{xx,xx} - m_{xx,yy}) \left[1 - ((\delta\theta_{xy})^2 + (\delta\theta_{yx})^2 + (\delta\phi_{xy})^2 + (\delta\phi_{yx})^2) \right] \\ &\quad \left[(\theta, \phi) = (\pi/4, 0) \right] \end{aligned} \quad (3.B.4a)$$

$$\begin{aligned} (\Delta\rho/\rho)_{(xy)''} + (\Delta\rho/\rho)_{(yx)''} &\approx -(\epsilon_{(xx)'} - \epsilon_{(yy)'})2m_{xy,xy} \left[1 - ((\delta\theta_{xy})^2 + (\delta\theta_{yx})^2 + (\delta\phi_{xy})^2 + (\delta\phi_{yx})^2) \right] \\ &\quad + (\epsilon_{(xx)'} - \epsilon_{(yy)'}) (m_{xx,xx} - m_{xx,yy}) \left[2(\delta\theta_{xy}\delta\phi_{xy} + \delta\theta_{yx}\delta\phi_{yx}) \right]. \\ &\quad \left[(\theta, \phi) = (0, \pi/4) \right] \end{aligned} \quad (3.B.4b)$$

Once again, the errors enter at second order about the high-symmetry configurations.

3.C Quantifying Strain Magnitude Errors

A second type of error to consider is the case of a differential or superposed elastoresistance measurement in which the two samples are perfectly aligned but experience unequal strains. We do not make any specific assumptions about the physical origin of this difference, which might be different depending on the specific experimental configuration that is chosen. For the specific technique that we have used in which thin crystals are adhered to the side surface of a piezoelectric stack, such a difference can arise from imperfect strain transmission by the epoxy used to adhere the crystals to the stack or from strain relaxation due to geometric considerations.

Suppose that an experiment is characterized by a fixed (θ, ϕ) configuration but that different relative amounts of strain are experienced by the two samples during a differential longitudinal elastoresistance measurement (i.e., the strains which induce a finite $(\Delta\rho/\rho)_{(xx)''}$ are slightly different than those causing $(\Delta\rho/\rho)_{(yy)''}$). In other words,

$(\Delta\rho/\rho)_{(xx)''}$ is measured in response to a strain $\epsilon_{(kl)'}^{(1)}$ and $(\Delta\rho/\rho)_{(yy)''}$ is measured in response to a slightly different strain $\epsilon_{(kl)'}^{(2)}$, with $\epsilon_{(kl)'}^{(1)}$ and $\epsilon_{(kl)'}^{(2)}$ given by

$$\epsilon_{(kl)'}^{(1)} = \begin{pmatrix} \epsilon_{(xx)'} + \delta\epsilon_{(xx)'}^{(1)} \\ \epsilon_{(yy)'} + \delta\epsilon_{(yy)'}^{(1)} \\ \epsilon_{(zz)'} + \delta\epsilon_{(zz)'}^{(1)} \\ 0 \\ 0 \\ 0 \\ 0 \\ 0 \\ 0 \end{pmatrix} \quad \text{and} \quad \epsilon_{(kl)'}^{(2)} = \begin{pmatrix} \epsilon_{(xx)'} + \delta\epsilon_{(xx)'}^{(2)} \\ \epsilon_{(yy)'} + \delta\epsilon_{(yy)'}^{(2)} \\ \epsilon_{(zz)'} + \delta\epsilon_{(zz)'}^{(2)} \\ 0 \\ 0 \\ 0 \\ 0 \\ 0 \\ 0 \end{pmatrix}. \quad (3.C.1)$$

The associated resistivity changes are given by

$$(\Delta\rho/\rho)_{(xx)''} = m_{(xx)'',(xx)'}\epsilon_{(xx)'}^{(1)} + m_{(xx)'',(yy)'}\epsilon_{(yy)'}^{(1)} + m_{(xx)'',(zz)'}\epsilon_{(zz)'}^{(1)}, \quad (3.C.2a)$$

$$(\Delta\rho/\rho)_{(yy)''} = m_{(yy)'',(xx)'}\epsilon_{(xx)'}^{(2)} + m_{(yy)'',(yy)'}\epsilon_{(yy)'}^{(2)} + m_{(yy)'',(zz)'}\epsilon_{(zz)'}^{(2)}, \quad (3.C.2b)$$

with the individual elastoresistivity coefficients transforming according to (3.A.5). Explicitly incorporating the angular dependence of the $m_{(ij)'',(kl)'}$, the symmetric combination $(\Delta\rho/\rho)_{(xx)''}(H_z) - (\Delta\rho/\rho)_{(yy)''}(H_z)$ is given as

$$\begin{aligned} & (\Delta\rho/\rho)_{(xx)''} - (\Delta\rho/\rho)_{(yy)''} = & (3.C.3) \\ & (\epsilon_{(xx)'} - \epsilon_{(yy)'}) \left[(m_{xx,xx} - m_{xx,yy}) \cos 2\theta \cos 2\phi - 2m_{xy,xy} \sin 2\theta \sin 2\phi \right] \\ & + \frac{1}{2} (\delta\epsilon_{(xx)'}^{(1)} + \delta\epsilon_{(xx)'}^{(2)} - \delta\epsilon_{(yy)'}^{(1)} - \delta\epsilon_{(yy)'}^{(2)}) \left[(m_{xx,xx} - m_{xx,yy}) \cos 2\theta \cos 2\phi - 2m_{xy,xy} \sin 2\theta \sin 2\phi \right] \\ & + \frac{1}{2} (\delta\epsilon_{(xx)'}^{(1)} - \delta\epsilon_{(xx)'}^{(2)} + \delta\epsilon_{(yy)'}^{(1)} - \delta\epsilon_{(yy)'}^{(2)}) \left[m_{xx,xx} + m_{xx,yy} \right] + (\delta\epsilon_{(zz)'}^{(1)} - \delta\epsilon_{(zz)'}^{(2)}) \left[m_{xx,zz} \right], \end{aligned}$$

where we have organized each term based on the particular irrep of D_{4h} to which it corresponds. The leading term in (3.C.3) is simply (3.6) (i.e., the combination of B_{1g}

and B_{2g} quantities dictated by the specific (θ, ϕ) configuration), but we also measure error terms in proportion to the amount of $\delta\epsilon_{A_{1g,1}} \equiv \frac{1}{2}(\delta\epsilon_{(xx)'}^{(1)} - \delta\epsilon_{(xx)'}^{(2)} + \delta\epsilon_{(yy)'}^{(1)} - \delta\epsilon_{(yy)'}^{(2)})$, $\delta\epsilon_{A_{1g,2}} \equiv \delta\epsilon_{(zz)'}^{(1)} - \delta\epsilon_{(zz)'}^{(2)}$, and $\delta\epsilon_{B_{1g}} \equiv \frac{1}{2}(\delta\epsilon_{(xx)'}^{(1)} + \delta\epsilon_{(xx)'}^{(2)} - \delta\epsilon_{(yy)'}^{(1)} - \delta\epsilon_{(yy)'}^{(2)})$ strain that is also applied during the measurement. Note that the degree of error in the differential elastoresistance measurement is at first order in the magnitude of the relative strain offset.

An analogous expression can be worked out for the superposed transverse elastoresistance configuration as well. Suppose that $(\Delta\rho/\rho)_{(xy)''}$ is measured in response to a strain $\epsilon_{(kl)'}^{(3)}$ and $(\Delta\rho/\rho)_{(yx)''}$ is measured in response to a slightly different strain $\epsilon_{(kl)'}^{(4)}$, with $\epsilon_{(kl)'}^{(3)}$ and $\epsilon_{(kl)'}^{(4)}$ given by

$$\epsilon_{(kl)'}^{(3)} = \begin{pmatrix} \epsilon_{(xx)'} + \delta\epsilon_{(xx)'}^{(3)} \\ \epsilon_{(yy)'} + \delta\epsilon_{(yy)'}^{(3)} \\ \epsilon_{(zz)'} + \delta\epsilon_{(zz)'}^{(3)} \\ 0 \\ 0 \\ 0 \\ 0 \\ 0 \\ 0 \end{pmatrix} \quad \text{and} \quad \epsilon_{(kl)'}^{(4)} = \begin{pmatrix} \epsilon_{(xx)'} + \delta\epsilon_{(xx)'}^{(4)} \\ \epsilon_{(yy)'} + \delta\epsilon_{(yy)'}^{(4)} \\ \epsilon_{(zz)'} + \delta\epsilon_{(zz)'}^{(4)} \\ 0 \\ 0 \\ 0 \\ 0 \\ 0 \\ 0 \end{pmatrix}. \quad (3.C.4)$$

The corresponding changes in resistivity are then

$$(\Delta\rho/\rho)_{(xy)''} = m_{(xy)'',(xx)'}\epsilon_{(xx)'}^{(3)} + m_{(xy)'',(yy)'}\epsilon_{(yy)'}^{(3)} + m_{(xy)'',(zz)'}\epsilon_{(zz)'}^{(3)}, \quad (3.C.5a)$$

$$(\Delta\rho/\rho)_{(yx)''} = m_{(yx)'',(xx)'}\epsilon_{(xx)'}^{(4)} + m_{(yx)'',(yy)'}\epsilon_{(yy)'}^{(4)} + m_{(yx)'',(zz)'}\epsilon_{(zz)'}^{(4)}, \quad (3.C.5b)$$

with the individual elastoresistivity coefficients transforming according to (3.A.5). Explicitly incorporating the angular dependence of the $m_{(ij)'',(kl)'}$, the symmetric combination $(\Delta\rho/\rho)_{(xy)''}(H_z) + (\Delta\rho/\rho)_{(yx)''}(H_z)$ is given as

$$\begin{aligned}
& (\Delta\rho/\rho)_{(xy)''} + (\Delta\rho/\rho)_{(yx)''} = \tag{3.C.6} \\
& - (\epsilon_{(xx)'} - \epsilon_{(yy)'}) \left[(m_{xx,xx} - m_{xx,yy}) \cos 2\theta \sin 2\phi + 2m_{xy,xy} \sin 2\theta \cos 2\phi \right] \\
& - \frac{1}{2} (\delta\epsilon_{(xx)'}^{(3)} + \delta\epsilon_{(xx)'}^{(4)} - \delta\epsilon_{(yy)'}^{(3)} - \delta\epsilon_{(yy)'}^{(4)}) \left[(m_{xx,xx} - m_{xx,yy}) \cos 2\theta \sin 2\phi + 2m_{xy,xy} \sin 2\theta \cos 2\phi \right] \\
& + \frac{1}{2} (\delta\epsilon_{(xx)'}^{(3)} - \delta\epsilon_{(xx)'}^{(4)} + \delta\epsilon_{(yy)'}^{(3)} - \delta\epsilon_{(yy)'}^{(4)}) \left[m_{xy,xx} \right] + (\delta\epsilon_{(zz)'}^{(3)} - \delta\epsilon_{(zz)'}^{(4)}) \left[m_{xy,zz} \right].
\end{aligned}$$

Just as in the differential longitudinal case, the measured errors in the transverse superposed elastoresistance configuration appear in proportion to the amount of $\delta\epsilon_{A_{1g,1}} \equiv \frac{1}{2}(\delta\epsilon_{(xx)'}^{(3)} - \delta\epsilon_{(xx)'}^{(4)} + \delta\epsilon_{(yy)'}^{(3)} - \delta\epsilon_{(yy)'}^{(4)})$, $\delta\epsilon_{A_{1g,2}} \equiv \delta\epsilon_{(zz)'}^{(3)} - \delta\epsilon_{(zz)'}^{(4)}$, and $\delta\epsilon_{B_{1g}} \equiv \frac{1}{2}(\delta\epsilon_{(xx)'}^{(3)} + \delta\epsilon_{(xx)'}^{(4)} - \delta\epsilon_{(yy)'}^{(3)} - \delta\epsilon_{(yy)'}^{(4)})$ strain that are inadvertently applied during the measurement, and the degree of error is at first order in the magnitude of the relative strain offset. However, since $(\Delta\rho/\rho)_{(yx)''}(H_z) = (\Delta\rho/\rho)_{(xy)''}(-H_z)$, one can constrain these strain offsets to be precisely zero since the measurements can be performed under the same mounting conditions (only inverting the magnetic field environment). That is, for a measurement performed on one single crystal, $\delta\epsilon_{(xx)'}^{(4)} = \delta\epsilon_{(xx)'}^{(3)}$, $\delta\epsilon_{(yy)'}^{(4)} = \delta\epsilon_{(yy)'}^{(3)}$, and $\delta\epsilon_{(zz)'}^{(4)} = \delta\epsilon_{(zz)'}^{(3)}$, such that $\delta\epsilon_{A_{1g,1}} = \delta\epsilon_{A_{1g,2}} = 0$. Rephrased in terms of group theory, the strain error does not mix symmetry channels (a measurement of the B_{1g} response is not contaminated by any A_{1g} signal), but the absolute magnitude of the strain experienced by the sample is incorrectly recorded as $\epsilon_{(xx)'}$ rather than $\epsilon_{(xx)'} + \delta\epsilon_{(xx)'}^{(3)}$, and $\epsilon_{(yy)'}$ rather than $\epsilon_{(yy)'} + \delta\epsilon_{(yy)'}^{(4)}$. Thus, provided one can isolate $(\Delta\rho/\rho)_{xy}$ and $(\Delta\rho/\rho)_{yx}$ (i.e., subtract out ρ_{xx} contributions which ‘‘contaminate’’ a nominally ρ_{xy} measurement, which we describe in the following Appendix 3.D), the transverse configuration is immune to contamination from other symmetry channels arising from relative strain magnitude errors. As discussed in the main text, this is the primary advantage of the transverse elastoresistance technique.

3.D Isolating Transverse Elastoresistivities in a Longitudinally-Contaminated Elastoresistance Measurement

In this section we describe in detail the process by which a longitudinal resistivity (ρ_{xx}) “contamination” can be subtracted from an erstwhile transverse resistivity (ρ_{xy}) measurement. Such a situation is often encountered in the context of Hall effect measurements, for which a nominally transverse signal R_{xy}^{measured} (due to a \hat{z} -oriented magnetic field $\mathbf{H} = H_z \hat{z}$) is contaminated by a contribution from the longitudinal resistance R_{xx} such that

$$R_{xy}^{\text{measured}} = R_{xy} + \alpha R_{xx}, \quad (3.D.1)$$

where α is a (not generally small) parameter characterizing the amount of R_{xx} contamination. Such a contamination can arise, for example, from curved current paths within the crystal or from imperfectly aligned voltage contacts. In the Hall effect measurement case, to isolate the Hall resistance signal, one typically measures R_{xy}^{measured} for both positive and negative magnetic field and uses the fact that the longitudinal (transverse) signal is even (odd) in H_z :

$$R_{xy}^{\text{measured}}(H_z) - R_{xy}^{\text{measured}}(-H_z) = 2R_{xy}(H_z). \quad (3.D.2)$$

In this appendix, we will describe the analog to this magnetic field anti-symmetrization for a transverse elastoresistance measurement. In contrast to the Hall effect, though, we cannot rely on a simple parity-in-field argument since contamination of a nominal $2m_{xy,xy}$ or $m_{xx,xx} - m_{xx,yy}$ measurement can come from elastoresistivity coefficients that are either even (e.g., $m_{xx,zz}$) or odd (e.g., $m_{xy,xx}$) in the magnetic field. Nevertheless, by pre-characterizing the contact geometry, it is still possible to isolate the symmetry-connected elastoresistivity coefficients which are related to thermodynamic susceptibilities.

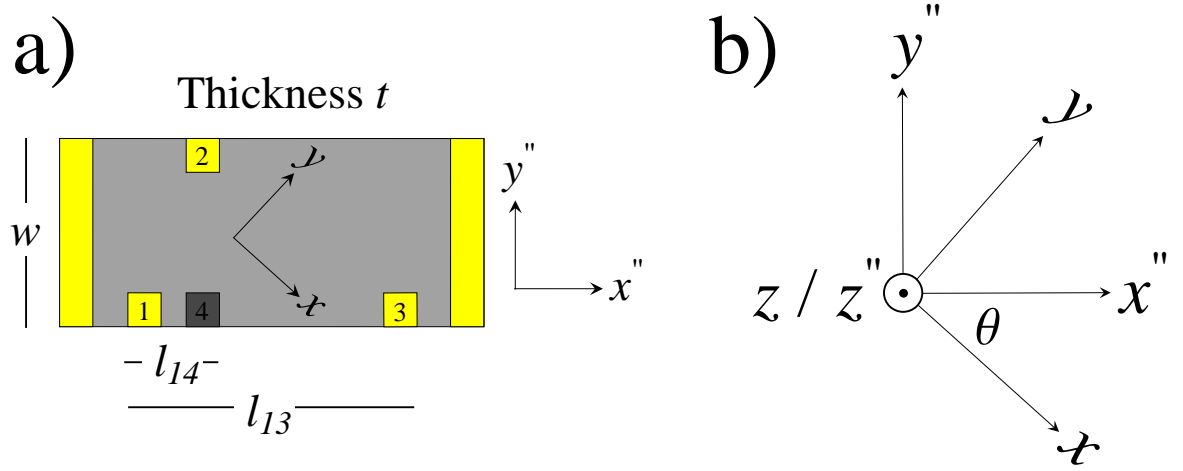


Figure 3.13: (a) Schematic diagram illustrating contact misalignment in a transverse measurement. The transverse voltage is to be measured between contacts 1 and 2, while the longitudinal voltage can be measured between contacts 1 and 3. The degree of transverse contact misalignment (horizontal offset between contacts 1 and 2) has been greatly exaggerated for pedagogical purposes. Contact 4 (dark gray) is a hypothetical contact which is perfectly vertically aligned with contact 2, which means that the relative voltages between these contacts $V_2 - V_4 = 0$ in zero magnetic field for zero strain. (b) Primitive crystal frame and its relative alignment to the transport frame.

In performing a transverse resistivity measurement, the most straightforward manner in which one might encounter longitudinal contamination is due to imperfect contact geometry (as in Figure 3.13) or to nonlinearly directed current paths within the crystal. While microscopic details to do with the specific mechanism of current non-uniformity would dictate how such a longitudinal contamination would be subtracted out, we instead focus on how to subtract out the longitudinal contamination due to contact misalignment, otherwise assuming a homogeneous material with uniformly directed current paths.

Consider an experimental configuration as in Figure 3.13 in which one sources a current $\vec{I} = I \cdot \hat{x}'' = [wtj_{(x)''] \cdot \hat{x}''$ along the x'' direction in the transport frame (with $j_{(x)'}$ the magnitude of the current density in the transport frame, w the crystal width, and t the crystal thickness). One then seeks to isolate the true transverse resistivity

$\rho_{(xy)''}$ (in the transport frame) from a measurement $R_{(xy)''}^{\text{measured}}$ which contains longitudinal contamination $\rho_{(xx)''}$ due to imperfectly aligned contacts 1 and 2. One most conveniently characterizes this contamination by writing Ohm's law in the transport frame as

$$\begin{aligned} E_{(i)''} &= \rho_{(ij)''} j_{(j)''} & (3.D.3) \\ \begin{pmatrix} E_{(x)''} \\ E_{(y)''} \\ E_{(z)''} \end{pmatrix} &= \begin{pmatrix} \rho_{(xx)''} & \rho_{(xy)''} & 0 \\ \rho_{(yx)''} & \rho_{(yy)''} & 0 \\ 0 & 0 & \rho_{(zz)''} \end{pmatrix} \begin{pmatrix} j_{(x)''} \\ 0 \\ 0 \end{pmatrix} = j_{(x)''} \begin{pmatrix} \rho_{(xx)''} \\ \rho_{(yx)''} \\ 0 \end{pmatrix} \end{aligned}$$

and then expressing the resistances in terms of measured voltages, uniform electric fields, and crystal dimensions:

$$\begin{aligned} R_{(xx)''}^{\text{measured}} &= \frac{V_3 - V_1}{I_{(x)''}} = \frac{E_{(x)''} l_{13}}{I_{(x)''}} = \frac{l_{13}}{l_{14}} \frac{V_4 - V_1}{I_{(x)''}} \equiv \frac{1}{\Delta_\ell} \frac{V_4 - V_1}{I_{(x)''}} & (3.D.4) \\ R_{(yx)''}^{\text{measured}} &= \frac{V_2 - V_1}{I_{(x)''}} = \frac{V_2 - V_4}{I_{(x)''}} + \frac{V_4 - V_1}{I_{(x)''}} = \frac{E_{(y)''} w}{j_{(x)''} w t} + \Delta_\ell R_{(xx)''}^{\text{measured}} = \frac{\rho_{(yx)''}}{t} + \Delta_\ell R_{(xx)''}^{\text{measured}}, \end{aligned}$$

where V_i denotes a voltage measured at the i -th contact in Figure 3.13 and $\Delta_\ell \equiv \frac{l_{14}}{l_{13}}$ characterizes the degree of misalignment of the transverse contacts 1 and 2. Solving for $\rho_{(yx)''}$ in (3.D.4), one obtains

$$\rho_{(yx)''} = t \left(R_{(yx)''}^{\text{measured}} - \Delta_\ell R_{(xx)''}^{\text{measured}} \right) \equiv t R_{(yx)''}, \quad (3.D.5)$$

where $R_{(yx)''}$ represents the resistance that would be measured in the absence of contact misalignment. Isolating $R_{(yx)''}$ thus requires down-weighting the simultaneously measured quantity $R_{(xx)''}^{\text{measured}}$ by the parameter Δ_ℓ , which is most readily determined via a zero-field, zero-strain measurement of the contacts. Specifically, in the absence of either strain or a magnetic field, there cannot be a transverse voltage for a crystal with D_{4h} symmetry; therefore, $V_2 = V_4$ and, with the assumption of a uniform electric field within the material,

$$\Delta_\ell \equiv \frac{l_{14}}{l_{13}} = \frac{V_4 - V_1}{V_3 - V_1} \stackrel{\hat{\epsilon}=\hat{0}, H_z=0}{=} \frac{V_2 - V_1}{V_3 - V_1}. \quad (3.D.6)$$

The equations (3.D.5) and (3.D.6) express how one corrects for contact misalignment in order to isolate the resistance $R_{(yx)''}$; however, as prescribed in (3.4) of the main text, the meaningful quantity for elastoresistivity is the ratio of *resistivities*, not resistances. The relationship between the two is elucidated by considering the transverse quantities $(\Delta\rho/\rho)_{(yx)''}(H_z)$ and $(\Delta\rho/\rho)_{(xy)''}(H_z)$, where

$$\begin{aligned} \left(\frac{\Delta\rho}{\rho}\right)_{(yx)''} &= \frac{\Delta\rho_{(yx)''}}{\sqrt{\rho_{(xx)''}(\hat{\epsilon}=\hat{0})\rho_{(yy)''}(\hat{\epsilon}=\hat{0})}} \\ \left(\frac{\Delta\rho}{\rho}\right)_{(xy)''} &= \frac{\Delta\rho_{(xy)''}}{\sqrt{\rho_{(xx)''}(\hat{\epsilon}=\hat{0})\rho_{(yy)''}(\hat{\epsilon}=\hat{0})}} \end{aligned} \quad (3.D.7)$$

and where the normalization factor contains the unstrained *longitudinal* resistivities $\rho_{(xx)''}$ and $\rho_{(yy)''}$. Since $\rho_{(yx)''} = tR_{(yx)''}$ (and likewise for $\rho_{(xy)''}$), the linearized strain-induced resistivity change is given by $\Delta\rho_{(yx)''} = t\Delta R_{(yx)''} + R_{(yx)''}\Delta t$; substituting into (3.D.7), and using the fact that for a tetragonal material $\rho_{(xx)''}(\hat{\epsilon}=\hat{0}) = \rho_{(yy)''}(\hat{\epsilon}=\hat{0})$,

$$\left(\frac{\Delta\rho}{\rho}\right)_{(yx)''} = \frac{t\Delta R_{(yx)''} + R_{(yx)''}\Delta t}{\left(\frac{wt}{l_{13}}\right) R_{(xx)''}(\hat{\epsilon}=\hat{0})}, \quad (3.D.8)$$

and likewise for $\left(\frac{\Delta\rho}{\rho}\right)_{(xy)''}$. When the strain is of a B_{1g} or B_{2g} character (i.e., area-preserving), the thickness change due to strain Δt is precisely zero and so the second term in the numerator of (3.D.8) vanishes (i.e., $R_{(yx)''}\Delta t = 0$). When the strain is predominantly of a B_{1g} or B_{2g} character but also possesses an area-deforming (A_{1g}) component (as is a more realistic approximation to our specific experimental realization), Δt is finite; nevertheless, provided the measured resistance change is dominated by changes in the resistivity under strain as opposed to geometric effects, it will still be true that $R_{(yx)''}\Delta t \ll t\Delta R_{(yx)''}$. In either case then, $\Delta\rho_{(yx)''} \approx t\Delta R_{(yx)''}$, and, combining (3.D.5) and (3.D.8),

$$\left(\frac{\Delta\rho}{\rho}\right)_{(yx)''} \approx \frac{l_{13}}{w} \left[\left(\frac{\Delta R_{(yx)''}^{\text{measured}}}{R_{(xx)''}}\right) - \Delta_\ell \left(\frac{\Delta R_{(xx)''}^{\text{measured}}}{R_{(xx)''}}\right) \right], \quad (3.D.9)$$

and likewise for $\left(\frac{\Delta\rho}{\rho}\right)_{(xy)''}$. In (3.D.9), it is to be understood that the approximation becomes an exact equality under conditions of pure B_{1g} or B_{2g} strain. This is the procedure we used to subtract longitudinal resistance ‘‘contamination’’ and obtain the data described in the main text.

In zero magnetic field and for appropriate mounting configurations, a single measurement with contact misalignment accounted for according to (3.D.9) is sufficient for extracting the relevant elastoresistivity coefficients; in a finite field, one requires an extra measurement that is performed after reversing the magnetic field. Upon taking the symmetry-motivated sum $(\Delta\rho/\rho)_{(yx)''}(H_z) + (\Delta\rho/\rho)_{(xy)''}(H_z)$ (and using (3.D.9) and the Onsager relations), the generalized expression for finite H_z is given by

$$\begin{aligned} \left(\frac{\Delta\rho}{\rho}\right)_{(yx)''}(H_z) + \left(\frac{\Delta\rho}{\rho}\right)_{(xy)''}(H_z) &= \left(\frac{\Delta\rho}{\rho}\right)_{(yx)''}(H_z) + \left(\frac{\Delta\rho}{\rho}\right)_{(yx)''}(-H_z) = \\ & \frac{l_{13}}{w} \left[\left(\frac{\Delta R_{(yx)''}^{\text{measured}}(H_z)}{R_{(xx)''}(H_z)}\right) - \Delta_\ell \left(\frac{\Delta R_{(xx)''}^{\text{measured}}(H_z)}{R_{(xx)''}(H_z)}\right) \right. \\ & \quad \left. + \left(\frac{\Delta R_{(yx)''}^{\text{measured}}(-H_z)}{R_{(xx)''}(-H_z)}\right) - \Delta_\ell \left(\frac{\Delta R_{(xx)''}^{\text{measured}}(-H_z)}{R_{(xx)''}(-H_z)}\right) \right]. \end{aligned} \quad (3.D.10)$$

Equations (3.D.9) and (3.D.10) express the transverse elastoresistivity analog to anti-symmetrization in a magnetic field for Hall resistance measurements. By measuring $(\Delta R_{(yx)''}^{\text{measured}}/R_{(xx)''})$ and $(\Delta R_{(xx)''}^{\text{measured}}/R_{(xx)''})$ simultaneously, and having pre-characterized Δ_ℓ in zero magnetic field (using (3.D.6), measured under conditions of zero strain), one can simply subtract the two elastoresistance measurements (with the longitudinal contribution weighted by Δ_ℓ and an overall geometric correction by $\frac{l_{13}}{w}$) in order to isolate $(\Delta\rho/\rho)_{(yx)''}$. The same subtraction procedure works for measuring either $m_{xx,xx} - m_{xx,yy}$ or $2m_{xy,xy}$ since the above derivation is independent of the relative orientation of the transport and crystal frames.

3.E Evaluating Goodness of Fit of Curie-Weiss Model to the Measured Elastoresistivity Coefficient $2m_{xy,xy}$

The elastoresistivity coefficient $2m_{xy,xy}$ exhibits a monotonic increase with decreasing temperature from the highest temperature measured (220 K in the present work) down to 136 K, which is just above the coupled structural and magnetic transition temperature $T_{S,N} \approx 134$ K. In this section, we briefly describe the procedures used to fit the data to a Curie-Weiss temperature dependence above the phase transition, which is physically motivated based on a mean-field description of the nematic susceptibility [58, 61].

As discussed in the main text, the $2m_{xy,xy}$ elastoresistivity data were fit to a Curie-Weiss temperature dependence of the form $2m_{xy,xy}^{\text{Curie-Weiss}} = \frac{\lambda}{a_0(T-\theta)} + 2m_{xy,xy}^0$ (see (3.12) of the main text). In order to evaluate the goodness of fit of the Curie-Weiss form to the measured data, we illustrate in Figure 3.14 a bullseye plot as a function of a varying temperature window. A bullseye plot is a contour map of the root mean square error (RMSE) of the observed data from an expected model as a function of a varying window in the independent variable. In the ideal case where the expected model perfectly conforms to the measured data over a particular range, the RMSE will obtain a local minimum over this range and the output of the contour map will resemble a bullseye-like pattern. Since narrowing the independent variable window also diminishes the sample size over which the fit is performed and relaxes constraints on the parameters in the fit model, bullseye plots also display a general trend of decreasing RMSE as one increases (decreases) the low (high) end cutoff in the independent variable window; one therefore expects a general trend of decreasing RMSE as one approaches the bottom right region of the contour map.

In the context of the present measurement, the expected model is a Curie-Weiss temperature dependence and the color output of the bullseye plot in Figure 3.14 corresponds to the residual difference (for each temperature window) between the inverse susceptibility $(2m_{xy,xy} - 2m_{xy,xy}^0)^{-1}$ and a linear function of temperature.

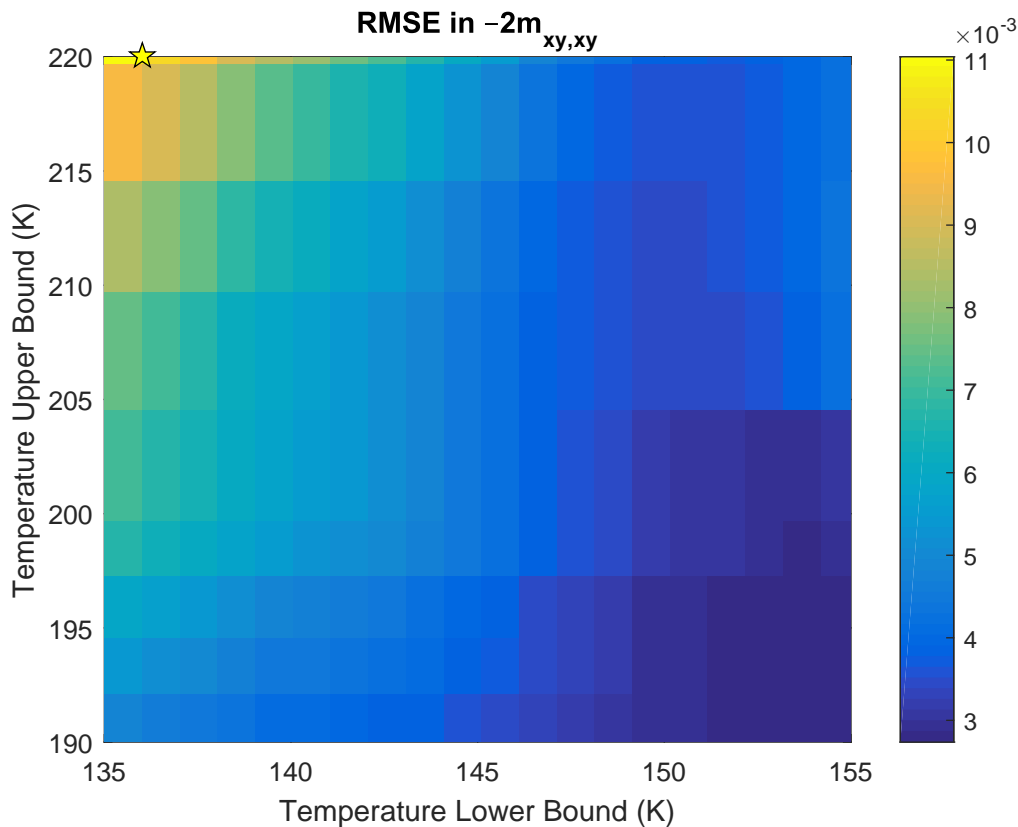


Figure 3.14: Bullseye plot of the $2m_{xy,xy}$ elasto-resistivity coefficient, illustrating the minimized RMSE from the Curie-Weiss form as a function of a varying temperature window. While an ideal fit over a particular range would produce a local minimum in the RMSE in that range and hence a bullseye-like pattern in the contour map, no such bullseye pattern is observed for the present data. This indicates that there is no “optimal” temperature range over which the data best conforms to the Curie-Weiss form. Without such a best-fit range, we opt to fit over the maximal range from 220 K (the highest temperature measured) down to 136 K (just above $T_{S,N} \approx 134$ K).

For each fixed window, we first estimate the temperature-independent parameter $2m_{xy,xy}^0$ by a least RMSE minimization procedure between the measured $2m_{xy,xy}$ and the Curie-Weiss form; with this $2m_{xy,xy}^0$, we then estimate the best-fit parameters λ/a_0 and θ by minimizing the RMSE between the $(2m_{xy,xy} - 2m_{xy,xy}^0)^{-1}$ and a linear fit. The low temperature cutoff for the windows varies between 135 K and 155 K, while the high temperature cutoff for the windows varies between 190 K and 220 K. As displayed in Figure 3.14, a bullseye-like pattern is not observed; the only discernible feature is a general trend of decreasing RMSE as the temperature window is narrowed. This indicates the absence of an “optimal” temperature range over which the elasto-resistivity coefficient $2m_{xy,xy}$ displays Curie-Weiss behavior; therefore, we choose to fit the data over the maximal range from 220 K (the highest temperature measured) down to 136 K (just above $T_{S,N}$). This range is demarcated by a star in the top-left portion of Figure 3.14 and yields the fit parameters given in the main text (see Table 3.1).

The most easily interpretable parameter from the Curie-Weiss fit is the Weiss temperature θ . To characterize the dependence of the Weiss temperature on the particular temperature window used for the fit, we also plot a contour map of the best-fit estimates of θ as a function of a varying temperature window (Figure 3.15). The star in the top-left region of Figure 3.15 again corresponds to the maximal temperature range, which we use due to the absence of any particular best fit range. The distribution of Weiss temperatures is heavily concentrated around ~ 120 K for the ranges close to the maximal window, which is the value of θ quoted in the main text.

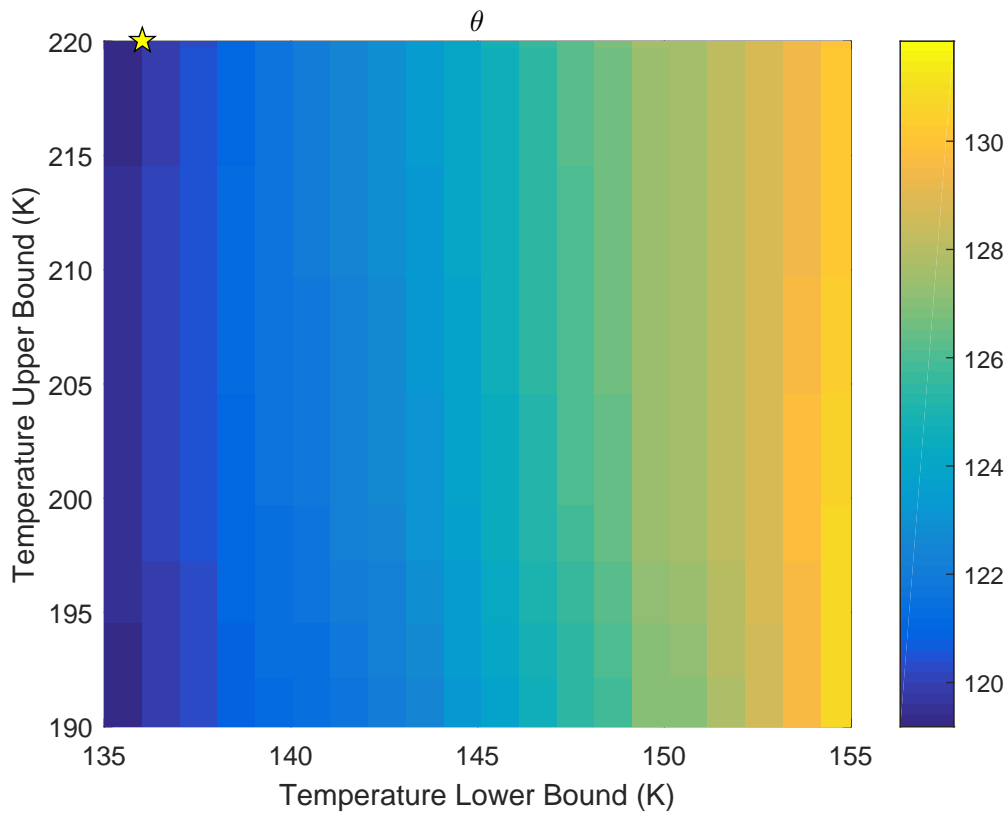


Figure 3.15: Contour map of estimated Weiss temperatures θ as a function of a varying temperature window. The star in the top-left region again corresponds to the maximal temperature range, which we use due to the absence of any particular best fit range. The distribution of Weiss temperatures is heavily concentrated around ~ 120 K for the ranges close to the maximal window, which is the value of θ quoted in the main text.

Chapter 4

Evidence for a Nematic Component to the Hidden Order Parameter in URu_2Si_2 from Differential Elastoresistance Measurements

In this chapter, differential elastoresistance measurements are presented which probe the nematic susceptibility of URu_2Si_2 . Our measurements reveal that the fluctuating order has a nematic component, confirming reports of twofold anisotropy in the broken symmetry state and strongly constraining theoretical models of the Hidden Order phase. This chapter is taken nearly verbatim from [57].

4.1 Introduction

The heavy fermion compound URu_2Si_2 undergoes a continuous phase transition at $T_{HO} \sim 17$ K, the precise nature of which has not been fully established, despite considerable experimental [11–14] and theoretical [33–35, 83–87] attention. Determination of the symmetry (or symmetries) that are broken in the “Hidden Order” phase is not

just of purely academic interest, but also has a direct bearing on the symmetry of the superconducting gap that develops below $T_c = 1.5$ K. Of particular relevance to the present work, several recent measurements have provided evidence that the Hidden Order phase breaks the fourfold rotational symmetry of the high temperature tetragonal crystal lattice [21, 42, 52, 53]; however, the degree of anisotropy that is observed depends heavily on the crystal size (as determined via torque measurements [52]) and also on the crystal quality (for X-ray diffraction measurements [21]), leading to some contention as to whether or not these are intrinsic effects. In the current work, we take a complementary approach and probe the fluctuating order in the temperature regime *above* T_{HO} . Our results demonstrate first that the fluctuating order has a nematic component, confirming that the Hidden Order phase spontaneously breaks fourfold rotational symmetry, and second that other symmetries must also be broken at the phase transition.

To measure a general susceptibility of a system, one must apply the appropriate conjugate field (i.e., the physical quantity that couples linearly to the given order) and measure the linear response. For a tetragonal material, such as URu₂Si₂ above the Hidden Order transition, the conjugate field to electronic nematic order is anisotropic biaxial in-plane strain (either $\epsilon_{aniso} = (\epsilon_{xx} - \epsilon_{yy})$ or $\epsilon_{aniso} = \gamma_{xy}$ for spontaneous order in the [100] or [110] directions, corresponding to B_{1g} and B_{2g} representations of the D_{4h} point group, respectively). The nematic susceptibility for each of these orientations is then $\chi_N \propto \lim_{\epsilon_{aniso} \rightarrow 0} \frac{d\psi}{d\epsilon_{aniso}}$, where ψ represents any thermodynamic quantity measuring the induced anisotropy in mutually orthogonal directions ([100] and [010], or [110] and $[1\bar{1}0]$ respectively [61]; also see ‘‘Elastoresistance Measurements’’ subsection in the Supplementary Discussion). For a continuous electronic nematic phase transition, χ_N diverges towards the phase transition, signaling an instability towards nematic order. Such behavior was recently observed for the representative underdoped iron pnictide Ba(Fe_{1-x}Co_x)₂As₂, demonstrating that the structural phase transition that precedes the onset of collinear antiferromagnetic order in that material is driven by electronic nematic order [58, 61, 88].

There are also classes of order for which there is a single transition to an ordered state that has a nematic *component*, while simultaneously breaking additional

symmetries. A simple example would be a unidirectional incommensurate density wave with order parameter $\Delta_i = \Delta(Q_i)$, for which both translational and tetragonal symmetries are simultaneously broken at the same transition (Q_i corresponds to the ordering wavevector of the density wave, and $i = x$ or y). In such a case, anisotropic strain is not conjugate to the order parameter (i.e., the coupling term in the free energy expansion is not bilinear). Nevertheless, the inherent nematicity associated with the unidirectional density wave motivates introduction of a nematic order parameter \mathcal{N} which couples linearly to $(|\Delta_x|^2 - |\Delta_y|^2)$ and to which anisotropic strain *is* linearly coupled (see “Nematic \times (?) Symmetry” subsection in the Supplementary Discussion). For such a situation, and with the assumption of a continuous transition, an analysis based on standard Ginzburg-Landau theory for coupled order parameters reveals that the nematic susceptibility follows a Curie-Weiss temperature dependence at high temperatures (as the density wave fluctuations orient in the anisotropic strain field) but then develops an additional divergence close to the transition temperature, experimentally distinguishing the behavior from that of a “pure” nematic transition. We find that Hidden Order in URu₂Si₂ appears to fall into this latter class, having a nematic component but also breaking additional symmetries at the Hidden Order phase transition (see “Nematic Susceptibility: Theory” subsection in the Supplementary Discussion).

Our measurements are based on a novel technique that probes the differential response in the electrical resistivity to anisotropic biaxial strain in mutually perpendicular directions. We measure the induced resistivity anisotropy, N (defined by $N = (\rho_{yy} - \rho_{xx})/\frac{1}{2}(\rho_{yy} + \rho_{xx}) \sim ((\Delta R/R)_{yy} - (\Delta R/R)_{xx})$), which, by symmetry, is proportional to ψ in the limit of asymptotically small values. The induced anisotropy is characterized by specific terms in the associated elasto-resistivity tensor m_{ij} that relate changes in the resistivity to strains experienced by the material [58]. In the regime of infinitesimal strains (linear response), the elasto-resistivity coefficients ($m_{11} - m_{12}$) and $2m_{66}$ are linearly proportional to the bare (unrenormalized) nematic susceptibility, $\chi_{N_{[100]}}$ and $\chi_{N_{[110]}}$, for strains in the [100] and [110] directions respectively [58]. The proportionality constant relating the resistivity anisotropy to the nematic order parameter is governed by microscopic physics but does not contain any singular

contributions. Consequently, any divergence of the induced resistivity anisotropy is directly related to divergence of the nematic susceptibility. Since this is ultimately a derivative of a transport measurement, the technique is especially sensitive to static or fluctuating order which affects the Fermi surface.

As described below, our measurements reveal a strongly anisotropic differential elastoresistance between the B_{1g} and B_{2g} symmetry channels. In the B_{2g} channel for temperatures well above T_{HO} , the $2m_{66}$ elastoresistivity coefficient follows a Curie-Weiss dependence. This behavior directly implies that the fluctuating order has a nematic component. However, we also find a striking additional divergence in $2m_{66}$ close to the phase transition which tracks the heat capacity. This additional contribution to the differential elastoresistance demonstrates that while Hidden Order in URu_2Si_2 must break fourfold rotational symmetry, it also breaks other symmetries and hence is not purely nematic.

4.2 Results

Representative measurements of $(\frac{\Delta R}{R})_{yy}$ for five different temperatures are shown in Figure 4.1(b) and (c) for $[\bar{1}\bar{1}0]$ and $[100]$ oriented crystals respectively, revealing a linear response. The sign of $(\frac{\Delta R}{R})_{xx}$ is *opposite* to that of $(\frac{\Delta R}{R})_{yy}$ due to the anisotropic strain (i.e., the imposed symmetry breaking), distinct from changes in resistance observed under conditions of hydrostatic pressure [38]. This procedure was performed for both the $(\frac{\Delta R}{R})_{xx}$ and $(\frac{\Delta R}{R})_{yy}$ orientations on the same sample by removing the crystal from the piezo with acetone between each measurement. The slopes $\frac{\Delta R}{R}$ versus strain for each orientation were found using a linear fit and the difference was taken. The resulting elastoresistivity coefficients $2m_{66}$ and $m_{11} - m_{12}$ are plotted in Figure 4.2 as a function of temperature.

The data shown in Figures 4.1 and 4.2 reveal a striking anisotropy in the elastoresistivity coefficients, with $2m_{66}$ values considerably larger, and also more strongly temperature-dependent, than $m_{11} - m_{12}$. For comparison, the elastoresistivity coefficients of simple metals are small (of order one) and essentially isotropic [58]. It is worth remarking that the differential elastoresistance of URu_2Si_2 is comparable to

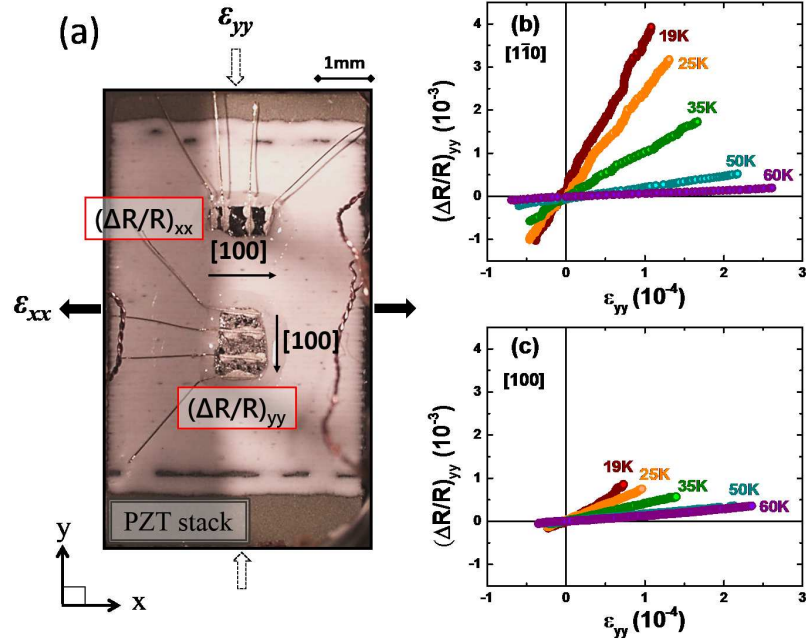


Figure 4.1: **Measurement of elastoresistivity coefficients.** Anisotropic strain is achieved by gluing thin crystals of URu_2Si_2 to the side of a PZT piezoelectric stack such that ϵ_{xx} is opposite in sign to ϵ_{yy} . The Cartesian axes are defined relative to the piezo stack itself, with the x -(y -)direction parallel to the short (long) axis of the piezo. (a) Photograph of $[100]$ oriented URu_2Si_2 crystals mounted in the $(\frac{\Delta R}{R})_{yy}$ and $(\frac{\Delta R}{R})_{xx}$ directions on the surface of a PZT piezoelectric stack. Strain gauges mounted on the opposite face of the piezo stack measure ϵ_{yy} and ϵ_{xx} , which are related by the effective Poisson ratio of the PZT stack, $\nu_p \equiv -\frac{\epsilon_{xx}}{\epsilon_{yy}}$. Panels (b) and (c) show representative $(\frac{\Delta R}{R})_{yy}$ elastoresistance data for five different temperatures as a function of ϵ_{yy} for $[1\bar{1}0]$ and $[100]$ orientations, respectively. Data are plotted for both warming and cooling cycles and are identical within the resolution of the experiment. The resistive response to anisotropic strain is considerably larger (by a factor of ~ 4) for measurements made in the $[1\bar{1}0]$ direction compared to the $[100]$ direction.

that of BaFe_2As_2 , for which the response along the [100] and [110] orientations is also strongly anisotropic, with $2m_{66}$ values reaching ~ 40 approaching the tetragonal-to-orthorhombic phase transition in that material.

Recalling that $2m_{66}$ is proportional to the nematic susceptibility in the [110] direction ($\chi_{N_{[110]}}$), the large values of $2m_{66}$ (red data points in Figure 4.2) and the strong temperature dependence both indicate a diverging nematic susceptibility in the B_{2g} (d_{xy} symmetry) channel, and hence motivate fitting the data to the Curie-Weiss form ($2m_{66} = C/[(T - \theta)] + 2m_{66}^0$). Since the elastoresistance only develops significant values below approximately 60 K, the range of temperatures over which this fit can be applied is necessarily small. Nevertheless, if we attempt fits over different temperature ranges, the best fit, defined by a reduced chi-squared statistic closest to 1, occurs for a range from approximately 30 K up to the maximum of 60 K, with a Weiss temperature $\theta = 15.2 \pm 0.3$ K (see ‘‘Curve Fitting’’ subsection in the Supplementary Discussion). Extrapolation of the best fit function to lower temperatures (shown as a green line in Figure 4.2) reveals significant deviation from Curie-Weiss-like behavior for temperatures below approximately 30 K. The onset of this deviation at 30 K is coincident with a suppression in $(T_1T)^{-1}$ seen in recent NMR experiments [89], suggestive of a common origin, possibly associated with the progressive development of strongly fluctuating order.

In contrast, $m_{11} - m_{12}$, which is proportional to $\chi_{N_{[100]}}$, is small and exhibits only a weak temperature dependence (cyan data points in Figure 4.2); additional measurements on a separate crystal confirmed the small value of $m_{11} - m_{12}$ (see ‘‘Elastoresistance Measurements’’ subsection in the Supplementary Discussion). Given the large values of $2m_{66}$, it is likely that this weak temperature dependence derives from slight sample misalignment (i.e., a small amount of contamination from $2m_{66}$ in the [100] orientation due to imperfectly constrained current paths within the crystal). For the remaining discussion we focus solely on the $2m_{66}$ data.

The most striking aspect of the temperature dependence of the elastoresistivity coefficients is the sharp downward anomaly observed at T_{HO} . The $2m_{66}$ data are re-plotted in Figure 4.3(a) on an expanded scale for the temperature window from 15.5 K to 19 K, spanning T_{HO} . The anomaly exactly aligns with the sharp peak in

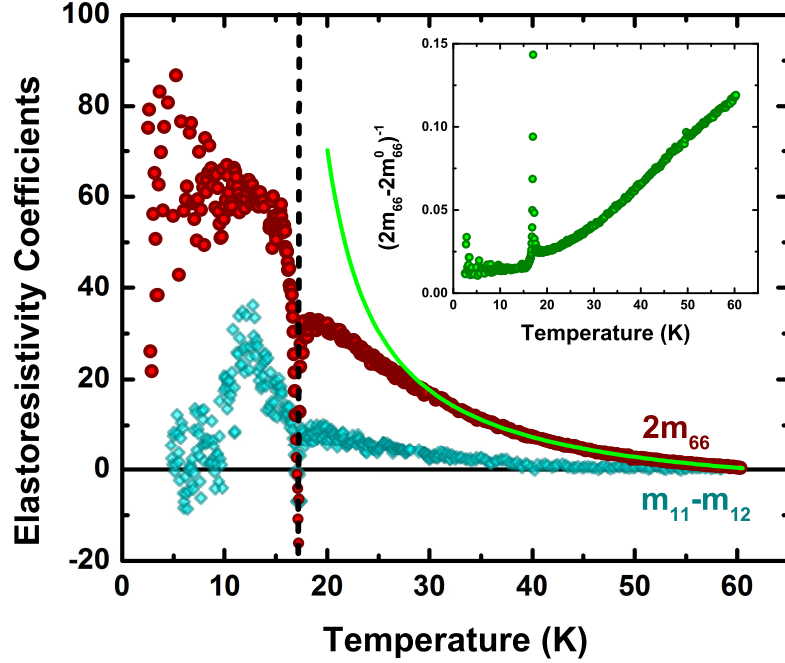


Figure 4.2: **Temperature dependence of the elastoresistivity coefficients.** The $2m_{66}$ (red circles) and the $m_{11} - m_{12}$ (cyan diamonds) elastoresistivity coefficients reveal a large directional anisotropy, with $2m_{66}$ reaching very large values close to and below the Hidden Order transition. The dashed vertical black line indicates the Hidden Order transition, $T_{HO} = 17.17$ K, determined from the peak in the temperature derivative of the resistivity. The green curve is a fit of $2m_{66}$ to a Curie-Weiss temperature dependence $2m_{66} = \frac{C}{T-\theta} + 2m_{66}^0$ from 60 K to 30 K, as described in the main text. The fit is extrapolated below 30 K to emphasize deviations from Curie-Weiss behavior below this temperature. The best-fit values for the parameters are $C = 375$ K, $\theta = 15.2$ K, and $2m_{66}^0 = -7.9$. The inset shows $(2m_{66} - 2m_{66}^0)^{-1}$ versus temperature, with $2m_{66}^0$ determined from the green fit in the main figure.

the temperature derivative of the in-plane resistivity $\frac{d\rho}{dT}$ (Figure 4.3(b,c)), indicating that the effect is associated with the thermodynamic phase transition at T_{HO} . For comparison, heat capacity measurements were also performed for the same crystal that was used for the $[1\bar{1}0]$ oriented measurements. The data closely follow the temperature dependence of $\frac{d\rho}{dT}$ [90], reminiscent of the theoretical treatment of critical fluctuations in metallic antiferromagnets by Fisher and Langer [91], with slight differences in the peak position attributed to small differences in thermometry between the two different systems used for transport and thermodynamic measurements.

4.3 Discussion

The observation of the Curie-Weiss temperature dependence of the $2m_{66}$ elastoresistivity coefficient, combined with the large anisotropy between $2m_{66}$ and $m_{11} - m_{12}$, strongly implies a nematic character to the fluctuations associated with the Hidden Order phase. However, the sharp downward anomaly in $2m_{66}$ at T_{HO} , which apparently closely follows the anomaly in the heat capacity at T_{HO} , is not consistent with a “pure” nematic behavior, implying that Hidden Order does *not* couple bilinearly to anisotropic strain. Motivated by these results, we consider below a Ginzburg-Landau model of a more complex system described by a multicomponent (vector) order parameter (see “Nematic \times (?) Symmetry” subsection in the Supplementary Discussion).

As described previously, the nematic susceptibility of a material that suffers an electronic nematic instability follows a Curie-Weiss temperature dependence, as has been observed for the iron pnictides [58, 61, 88]. However, a nematic response is also possible if the ordered state breaks fourfold spatial rotation symmetry but does not couple to strain as a bilinear term in the free energy. In this scenario, the Hidden Order state would be described by a two-component vector order parameter $\vec{\Delta} = (\Delta_x, \Delta_y)$. Motivated by the inherent nematicity in such a system, the nematic response can be modeled in mean field theory by introducing a separate nematic order parameter \mathcal{N} , which couples to the strain in the form

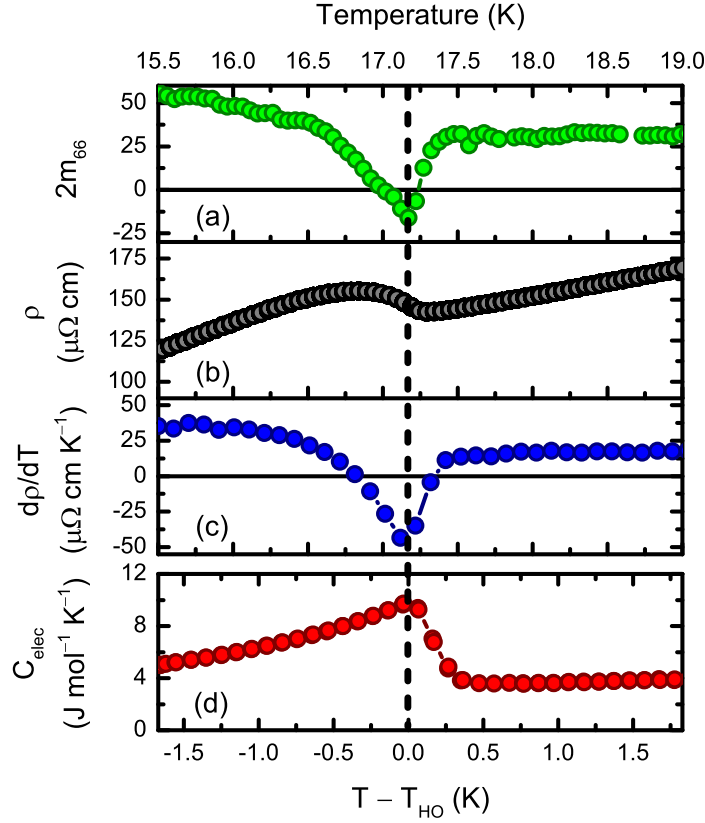


Figure 4.3: **Temperature dependence of $2m_{66}$ and heat capacity near T_{HO} .** Temperature dependence of (a) the $2m_{66}$ elasto-resistivity coefficient, (b) the in-plane resistivity ρ , (c) the temperature derivative of the in-plane resistivity $\frac{d\rho}{dT}$, and (d) the electronic specific heat in the immediate vicinity of T_{HO} , all measured on the same $[1\bar{1}0]$ oriented crystal. The phonon component to the specific heat was subtracted out by using ThRu_2Si_2 , such that $C_{elec}(\text{URu}_2\text{Si}_2) = [C(\text{URu}_2\text{Si}_2) - C(\text{ThRu}_2\text{Si}_2)]$. Data for all four panels are plotted as a function of $T - T_{HO}$, with the absolute temperature scale for the transport measurements shown on the upper axis. The temperature range in absolute units for all four plots is the same. The position ($T_{HO} = 17.17$ K) and width of the peak in $2m_{66}$ exactly match that of $\frac{d\rho}{dT}$, while there is a slight temperature offset ($T_{HO} = 17.47$ K) relative to the heat capacity measurement (but with the same width). Differences between T_{HO} obtained from transport and electronic specific heat are attributed to slight differences in thermometry between the two measurements.

$$\Delta F = (\epsilon_{aniso} + \lambda \mathcal{N})(|\Delta_x|^2 - |\Delta_y|^2), \quad (4.1)$$

where λ is a coupling constant. The theory does not depend on the microscopic origin of \mathcal{N} , which could be an independent order parameter or parasitic to the Hidden Order. Within such a theory, an additional contribution to the nematic susceptibility occurs close to the Hidden Order transition which is proportional to the singular part of the heat capacity associated with the critical behavior:

$$\chi_{\mathcal{N}} \sim \frac{1}{T - T_{\mathcal{N}}} (1 + \beta \Delta C_v), \quad (4.2)$$

where the constant β depends on the strengths of the couplings between \mathcal{N} , $\vec{\Delta}$, and ϵ_{aniso} (see “Nematic \times (?) Symmetry: Functional Form” subsection in the Supplementary Discussion). This effect is analogous to anomalies observed in the elastic moduli and thermal expansion coefficients at a structural phase transition, first described by Testardi [92]. Intuitively, the relationship between the nematic susceptibility and heat capacity arises because it is the *square* of Hidden Order which generates a nematic distortion; within mean field considerations, both nematic and energy density fluctuations (i.e., the heat capacity) are related to the square of the order parameter (see “Nematic \times (?) Symmetry: Mean Field Intuition” subsection in the Supplementary Discussion), so these two quantities necessarily mirror each other near the phase transition.

The close correspondence between the predictions of this Ginzburg-Landau treatment and the observed data strongly suggest that Hidden Order in URu₂Si₂ is described by a two-component order parameter that breaks fourfold symmetry. Since the $2m_{66}$ coefficient diverges but $m_{11} - m_{12}$ does not, the orientation of the nematic fluctuations is along the [110] and [$\bar{1}\bar{1}0$] directions, consistent with the orientation deduced by measurements in the broken symmetry state [52].

The significance of this result is not so much the deduction that other symmetries are broken in the Hidden Order phase. Over a period of many years, a growing body of evidence points to partial gapping of the Fermi surface and a possible doubling of the unit cell in the c -direction [12, 37, 39, 40, 44, 45, 47, 48, 93–97]. Rather, our

result is significant because it confirms the more controversial conclusions drawn from earlier torque [52], NMR [53], cyclotron resonance [42], and X-ray diffraction [21] measurements that the Hidden Order phase spontaneously breaks fourfold lattice symmetry. Our results, which are ultimately based on statements about symmetry, do not identify a specific microscopic model for Hidden Order, but they clearly place tight constraints, namely that the Hidden Order phase is described by a vector order parameter that breaks fourfold symmetry.

The same coupling to the crystal lattice that yields the resistive response to strain must also cause an orthorhombic distortion below T_{HO} , consistent with reports of high resolution X-ray diffraction measurements [21]. Whether or not this anisotropy is observed in thermodynamic measurements of macroscopic crystals is then a matter of the resolution of the specific measurement and the relative population of the two orthogonal orthorhombic domain orientations (which will be influenced by both crystal size and quality, via effects associated with pinning of domain walls). Both aspects illustrate the distinct advantage of probing the nematic susceptibility in the temperature regime $T > T_{HO}$, for which there are no domains (one is simply probing the susceptibility of the symmetric phase) and for which the resistivity anisotropy is extremely sensitive to subtle perturbations of the Fermi surface.

Despite these advances, important questions remain. In particular, since nematic fluctuations in the B_{2g} channel couple linearly to the shear modulus, one anticipates a softening of the C_{66} elastic constant approaching the Hidden Order phase transition. However, earlier measurements of the elastic moduli [98,99] do not show such a softening. At least in principle, weak coupling between the nematic order parameter and the crystal lattice (consistent with the small magnitude of the orthorhombic distortion observed in X-ray diffraction experiments [21]) would limit any appreciable renormalization of C_{66} to small values of the reduced temperature close to the phase transition (see “Nematic Susceptibility: Theory” subsection in the Supplementary Discussion). Nevertheless, the present results, in conjunction with other measurements that reveal a twofold anisotropy in the Hidden Order phase [52], clearly motivate a careful reinvestigation of the elastic properties of URu₂Si₂ for samples of a comparably high RRR.

4.4 Methods

In order to probe a thermodynamic susceptibility, one measures the response of an order parameter to an application of its conjugate field. In this context, the elastoresistivity measurements presented here track the induced resistivity anisotropy as a function of anisotropic biaxial strain. For a tetragonal material, the elastoresistivity tensor (which relates the normalized resistivity change to the strain experienced by a material) is defined by

$$\begin{pmatrix} (\Delta\rho/\rho)_{xx} \\ (\Delta\rho/\rho)_{yy} \\ (\Delta\rho/\rho)_{zz} \\ (\Delta\rho/\rho)_{yz} \\ (\Delta\rho/\rho)_{zx} \\ (\Delta\rho/\rho)_{xy} \end{pmatrix} = \begin{pmatrix} m_{11} & m_{12} & m_{13} & 0 & 0 & 0 \\ m_{12} & m_{11} & m_{13} & 0 & 0 & 0 \\ m_{31} & m_{31} & m_{33} & 0 & 0 & 0 \\ 0 & 0 & 0 & m_{44} & 0 & 0 \\ 0 & 0 & 0 & 0 & m_{44} & 0 \\ 0 & 0 & 0 & 0 & 0 & m_{66} \end{pmatrix} \begin{pmatrix} \epsilon_{xx} \\ \epsilon_{yy} \\ \epsilon_{zz} \\ \epsilon_{yz} \\ \epsilon_{zx} \\ \epsilon_{xy} \end{pmatrix} \quad (4.3)$$

Anisotropic strain is achieved by gluing thin crystals of URu₂Si₂ to the surface of a PZT piezoelectric stack. The high-quality crystals used for these experiments were characterized by residual resistance ratios (RRR) of 170 (for the [1 $\bar{1}$ 0] oriented measurements) and 81–87 (for the [100] oriented measurements) (see Supplementary Table I). The elastoresistivity coefficients $m_{11} - m_{12}$ and $2m_{66}$ are determined from the difference of $(\Delta R/R)_{yy}$ and $(\Delta R/R)_{xx}$ for a given set of strains for [100] and [1 $\bar{1}$ 0] oriented crystals respectively [58]. To first order this is also equal to the induced resistivity anisotropy N , expressed below in terms of the anisotropic biaxial strain $(\epsilon_{yy} - \epsilon_{xx})$:

$$N_{[100]} \approx ((\Delta R/R)_{yy} - (\Delta R/R)_{xx})_{[100]} = (\epsilon_{yy} - \epsilon_{xx})(m_{11} - m_{12}) \quad (4.4)$$

$$N_{[1\bar{1}0]} \approx ((\Delta R/R)_{yy} - (\Delta R/R)_{xx})_{[1\bar{1}0]} = (\epsilon_{yy} - \epsilon_{xx})2m_{66} \quad (4.5)$$

where x and y refer to the axes along which the piezo stack induces biaxial strain, indicated in Figure 4.1(a) and following the description given in previous work [58].

For each temperature, five voltage cycles were performed. Voltage applied to the piezo stack was increased/decreased in a stepwise fashion. The time delay between steps was varied from 0.25 s to 2 s with no change in the measured elastoresistance, indicating the absence of any appreciable heating effects. Data shown in all figures were taken using a delay of 0.5 s. The strain was measured using mutually perpendicular strain gauges glued to the back surface of the piezo stack.

4.A Nematic Susceptibility: Theory

In the main text, we have understood our differential elastoresistance measurements (proportional to the nematic susceptibility) within a Ginzburg-Landau theory of coupled order parameters. In this section, we describe the theoretical expectation for the temperature dependence of the nematic susceptibility for two relevant cases: 1) a system described by a single nematic order parameter coupled to a crystal lattice, and 2) the closely related case of a system possessing a two-component order parameter that breaks four-fold lattice symmetry (as would be appropriate, for example, for a unidirectional incommensurate density wave). The main result is that while in the former case the nematic susceptibility above the phase transition follows a Curie-Weiss temperature dependence, in the latter case the nematic susceptibility also receives a correction proximate to the phase transition which scales as the singular contribution to the heat capacity.

In applying this framework to URu_2Si_2 , we assume that the Hidden Order transition is continuous (or, at worst, weakly first order). This assumption is validated by the large mean field-like heat capacity anomaly in zero field; however, recent high resolution X-ray measurements reveal a small but apparently abrupt orthorhombicity onset at T_{HO} [21], which suggests that the phase transition may be weakly first order. In this case, the measurements reported here can still reasonably be interpreted within a framework of a fluctuational regime present above T_{HO} . As an aside, we note that if indeed the transition is weakly first order, the critical fluctuations would be cut off for small values of the reduced temperature, which might account for the absence of any appreciable renormalization of C_{66} through the Hidden Order

phase transition [98, 99].

4.A.1 Electronic Nematic Transition

To model a second order electronic nematic phase transition with coupling to the tetragonal lattice, one can Taylor expand the free energy to quartic order in terms of the nematic order parameter \mathcal{N} and the structural order parameter ε :

$$f = \frac{1}{2}a_0(T - T_{\mathcal{N}})\mathcal{N}^2 + \frac{1}{4}b\mathcal{N}^4 + \frac{1}{2}c\varepsilon^2 + \frac{1}{4}d\varepsilon^4 - \lambda\mathcal{N}\varepsilon. \quad (4.A.1)$$

In this expansion, the bilinear term $\lambda\mathcal{N}\varepsilon$ is the lowest order coupling allowed by symmetry, $T_{\mathcal{N}}$ is the bare nematic temperature which would characterize this transition in the absence of coupling to the lattice, and a_0, b, c, d, λ are positive coefficients. Due to the bilinear coupling, a nonzero \mathcal{N} induces a finite ε , which compels the $C_4 \rightarrow C_2$ point group symmetry breaking of the lattice.

In order to compute the nematic susceptibility from this free energy, we find the values of \mathcal{N} which minimize f by differentiating with respect to \mathcal{N} :

$$\frac{\partial f}{\partial \mathcal{N}} = a_0(T - T_{\mathcal{N}})\mathcal{N} + b\mathcal{N}^3 - \lambda\varepsilon = 0. \quad (4.A.2)$$

This defines a cubic equation for \mathcal{N} which can be solved in terms of ε ; however, we are interested in the linear response $\frac{\partial \mathcal{N}}{\partial \varepsilon}$, which we can find by implicit differentiation:

$$\begin{aligned} \frac{\partial}{\partial \varepsilon} \left(\frac{\partial f}{\partial \mathcal{N}} \right) &= [a_0(T - T_{\mathcal{N}}) + 3b\mathcal{N}^2] \left(\frac{\partial \mathcal{N}}{\partial \varepsilon} \right) - \lambda = 0 \\ \Rightarrow \left(\frac{\partial \mathcal{N}}{\partial \varepsilon} \right) &= \frac{\lambda}{a_0(T - T_{\mathcal{N}}) + 3b\mathcal{N}^2}. \end{aligned} \quad (4.A.3)$$

The nematic susceptibility is given as $\chi_{\mathcal{N}} \equiv \lim_{\varepsilon \rightarrow 0} \frac{\partial \mathcal{N}}{\partial \varepsilon}$, and since $\mathcal{N} = 0$ for $T > T_{\mathcal{N}}$, above the transition we have the Curie-Weiss form:

$$\chi_{\mathcal{N}} = \frac{\lambda}{a_0(T - T_{\mathcal{N}})} \quad (T > T_{\mathcal{N}}). \quad (4.A.4)$$

4.A.2 Nematic \times (?) Symmetry

A nematic response is also possible if the Hidden Order state breaks four-fold spatial rotation symmetry but does not couple to strain as a bilinear term in the free energy (unlike the purely electronic nematic transition described in the previous subsection of the Supplementary Discussion). In this scenario, the Hidden Order state can be described by a two-component vector order parameter $\vec{\Delta}$, the nematic response can be modeled in mean field theory by introducing a separate nematic order parameter \mathcal{N} , and the two are coupled in the form of Equation (4.1) of the main text. In this section, we show that within such a theory, a sharp jump in the nematic susceptibility occurs at the Hidden Order transition and is proportional to the singular heat capacity shift of Hidden Order. This correction to the nematic susceptibility can be seen from both mean field considerations—where the jump occurs infinitesimally below the transition—and upon including Gaussian fluctuations.

The notion of a “multicomponent” order parameter depends in turn on whether the Hidden Order phase preserves or breaks lattice translation symmetry (corresponding to a $\vec{Q} = 0$ and finite \vec{Q} order parameters, respectively). In the former case, a multicomponent order parameter must belong to a multidimensional irreducible representation (irrep) of the space group—examples are the E_g and E_u irreps of the D_{4h} point group. There are two possible realizations of multicomponent order parameters at finite \vec{Q} : (1) the order parameter is a scalar but can order in one of two directions Q_x and Q_y (e.g., unidirectional density wave order). The corresponding multicomponent order parameter is the set $\Delta(Q_x), \Delta(Q_y)$. The specific example cited has B_{1g} symmetry, and there is an equivalent case with B_{2g} symmetry (unidirectional density wave running along $[110]$ and $[1\bar{1}0]$ directions); (2) the finite \vec{Q} order itself belongs to a multidimensional irrep such as the E_g group. For this case, \vec{Q} could be a high symmetry point (D_{4h} examples are $Q = (0, 0, \ell)$ or (π, π, ℓ) , where ℓ represents a modulation along the z -axis).

A natural question here concerns the origin of \mathcal{N} . While mean field theory simply treats $\vec{\Delta}$ and \mathcal{N} as coupled order parameters, and so is agnostic about their origin, it is possible that \mathcal{N} is an avatar of the difference in fluctuations of the two components of $\vec{\Delta}$. This has been argued to be the case in the iron pnictide superconductors [100],

and below we outline how the nematic order parameter arises in such a scenario. Another possibility is that there may be some intrinsic nematic ordering tendency which is preceded by the Hidden Order transition, in which case it must be included in the free energy from the start. As we show below, the free energies for these two possibilities are identical, and so the sharp discontinuity in the susceptibility occurs in either case, provided the Hidden Order transition occurs first.

Nematic \times (?) Symmetry: Mean Field Intuition

We consider here the mean field theory of a two-component vector order parameter $\vec{\Delta} = (\Delta_x, \Delta_y)$ coupled to a nematic order parameter \mathcal{N} . The minimal symmetry-allowed mean field free energy expansion takes the form

$$\begin{aligned} f = & \frac{1}{2}r_0(T - T_{HO}) (|\Delta_x|^2 + |\Delta_y|^2) + \frac{1}{4}u (|\Delta_x|^4 + |\Delta_y|^4) \\ & + w|\Delta_x|^2|\Delta_y|^2 - \gamma h (|\Delta_x|^2 - |\Delta_y|^2) \\ & + \frac{1}{2}a_0(T - T_{\mathcal{N}})\mathcal{N}^2 + \frac{1}{4}b\mathcal{N}^4 - \alpha h\mathcal{N} - \lambda\mathcal{N} (|\Delta_x|^2 - |\Delta_y|^2). \end{aligned} \quad (4.A.5)$$

In order that the free energy be bounded from below, we take the coefficients a_0, b, r_0 , and u to be positive, but the parameters α, γ , and λ are of indeterminate sign. T_{HO} and $T_{\mathcal{N}}$ are the bare Hidden Order and nematic transition temperatures (respectively) which would characterize those phase transitions in the absence of both the external strain field h , and the coupling term $-\lambda\mathcal{N} (|\Delta_x|^2 - |\Delta_y|^2)$, and we assume that $T_{HO} > T_{\mathcal{N}}$ so that the nematic order onsets parasitically at the Hidden Order transition. The coefficient w determines whether the Z_2 symmetry is broken at the transition—for $w > 0$ only one component orders below T_{HO} , while for $w < 0$ both components become non-zero and there is no Z_2 symmetry breaking. Finally, note that we will formally take the external strain field h to zero in computing the nematic susceptibility.

We will henceforth assume that $w > 0$ so that the system spontaneously breaks Z_2 symmetry at the transition, and we also assume that Δ_x is the component which orders (i.e., $\Delta_y = 0$ throughout). The free energy in (4.A.5) then reduces to

$$\begin{aligned}
f &= \frac{1}{2}a_0(T - T_{\mathcal{N}})\mathcal{N}^2 + \frac{1}{4}b\mathcal{N}^4 - \alpha h\mathcal{N} \\
&+ \frac{1}{2}r_0(T - T_{HO})|\Delta_x|^2 + \frac{1}{4}u|\Delta_x|^4 - \gamma h|\Delta_x|^2 - \lambda\mathcal{N}|\Delta_x|^2.
\end{aligned} \tag{4.A.6}$$

Defining $\tilde{T}_{HO}(h, \mathcal{N}) \equiv T_{HO} + \frac{2\gamma h}{r_0} + \frac{2\lambda\mathcal{N}}{r_0}$, we can recast (4.A.6) in the more suggestive form

$$\begin{aligned}
f &= \frac{1}{2}a_0(T - T_{\mathcal{N}})\mathcal{N}^2 + \frac{1}{4}b\mathcal{N}^4 - \alpha h\mathcal{N} \\
&+ \frac{1}{2}r_0(T - \tilde{T}_{HO}(h, \mathcal{N}))|\Delta_x|^2 + \frac{1}{4}u|\Delta_x|^4.
\end{aligned} \tag{4.A.7}$$

This form emphasizes that the effect of the $\gamma h|\Delta_x|^2$ and $\lambda\mathcal{N}|\Delta_x|^2$ terms is essentially to shift the bare Hidden Order temperature T_{HO} .

The phase transition occurs when Δ_x acquires a nonzero expectation value, which is found in mean field theory by computing the stationary points of f :

$$\begin{aligned}
\frac{\partial f}{\partial |\Delta_x|} &= r_0(T - \tilde{T}_{HO}(h, \mathcal{N}))|\Delta_x| + u|\Delta_x|^3 = 0 \\
\Rightarrow |\Delta_x| &= \begin{cases} 0 & T > \tilde{T}_{HO}(h, \mathcal{N}) \\ \pm \sqrt{\frac{r_0(\tilde{T}_{HO}(h, \mathcal{N}) - T)}{u}} & T < \tilde{T}_{HO}(h, \mathcal{N}). \end{cases}
\end{aligned} \tag{4.A.8}$$

Plugging these back into (4.A.7), we find that

$$f = \begin{cases} f_{\text{nematic}} & T > \tilde{T}_{HO}(h, \mathcal{N}) \\ f_{\text{nematic}} - \frac{r_0^2}{4u}(\tilde{T}_{HO}(h, \mathcal{N}) - T)^2 & T < \tilde{T}_{HO}(h, \mathcal{N}), \end{cases} \tag{4.A.9}$$

where $f_{\text{nematic}} \equiv \frac{1}{2}a_0(T - T_{\mathcal{N}})\mathcal{N}^2 + \frac{1}{4}b\mathcal{N}^4 - \alpha h\mathcal{N}$ is the free energy for a second order phase transition characterized by a single nematic order parameter. This would be the appropriate free energy to model a nematic transition in a liquid crystal, for instance, as it does not include coupling to a crystal lattice.

\mathcal{N} will assume values that minimize the free energy, which we find by differentiation:

$$\frac{\partial f}{\partial \mathcal{N}} = 0 = \begin{cases} \frac{\partial f_{\text{nematic}}}{\partial \mathcal{N}} & T > \tilde{T}_{HO}(h, \mathcal{N}) \\ \frac{\partial f_{\text{nematic}}}{\partial \mathcal{N}} - \frac{r_0 \lambda}{u} (\tilde{T}_{HO} - T) & T < \tilde{T}_{HO}(h, \mathcal{N}) \end{cases} \quad (4.A.10)$$

with $\frac{\partial f_{\text{nematic}}}{\partial \mathcal{N}} = a_0(T - T_{\mathcal{N}})\mathcal{N} + b\mathcal{N}^3 - \alpha h$ and $\frac{\partial \tilde{T}_{HO}}{\partial \mathcal{N}} = \frac{2\lambda}{r_0}$. (4.A.10) defines a cubic equation in \mathcal{N} that we could solve in terms of h ; treating \mathcal{N} as an implicit function of h , we can take the derivative of (4.A.10) with respect to h and solve for the linear response $\frac{\partial \mathcal{N}}{\partial h}$:

$$\frac{\partial \mathcal{N}}{\partial h} = \begin{cases} \frac{\alpha}{a_0(T - T_{\mathcal{N}}) + 3b\mathcal{N}^2} & T > \tilde{T}_{HO}(h, \mathcal{N}) \\ \frac{\alpha + \frac{2\gamma\lambda}{u}}{a_0(T - T_{\mathcal{N}}) + 3b\mathcal{N}^2 - \frac{2\lambda^2}{u}} & T < \tilde{T}_{HO}(h, \mathcal{N}), \end{cases} \quad (4.A.11)$$

where we have used that $\frac{\partial \tilde{T}_{HO}}{\partial h} = \frac{2\gamma}{r_0}$. Above and at $T = T_{HO}$, the system has not transitioned to the Hidden Order state, and hence $\Delta_x = \mathcal{N} = 0$; furthermore, the nematic susceptibility is defined in the limit of vanishing h . In these limits, $\tilde{T}_{HO}(h, \mathcal{N}) = T_{HO}$ and the nematic susceptibility is given by

$$\chi_{\mathcal{N}} = \lim_{h \rightarrow 0} \frac{\partial \mathcal{N}}{\partial h} = \begin{cases} \frac{\alpha}{a_0(T - T_{\mathcal{N}})} & T > T_{HO} \\ \frac{\alpha + \frac{2\gamma\lambda}{u}}{a_0(T - T_{\mathcal{N}}) - \frac{2\lambda^2}{u}} & T < T_{HO}^- \end{cases} \quad (4.A.12)$$

Note that T_{HO}^- indicates a temperature infinitesimally below T_{HO} , and so there is an abrupt change in the nematic susceptibility across the transition temperature. Above T_{HO} , the nematic susceptibility is exactly as for the case of an electronic nematic transition, but there are additional contributions below the ordering temperature. This abrupt change occurs because of the change in the free energy at T_{HO} , which in mean field manifests as a discontinuous second derivative of the energy (or, equivalently, a discontinuity in the heat capacity).

We can relate the parameter u to the magnitude of the heat capacity singularity at T_{HO} by focusing on the Hidden Order contribution to the free energy on cooling through the transition and invoking the thermodynamic identity $C_v = -T \frac{\partial^2 f}{\partial T^2}$:

$$\Delta C_v \equiv -T \frac{\partial^2 f}{\partial T^2}(T_{HO}^-) - (-T \frac{\partial^2 f}{\partial T^2}(T_{HO}^+)) = \frac{r_0^2}{2u} T_{HO}. \quad (4.A.13)$$

Using this result, we find that the nematic susceptibility in terms of the heat capacity anomaly at T_{HO} is

$$\chi_N = \begin{cases} \frac{\alpha}{a_0(T-T_N)} & T > T_{HO} \\ \frac{\alpha}{a_0(T-T_N)} \left[1 + \frac{4\gamma\lambda}{r_0^2 T_{HO}} \Delta C_v + \mathcal{O}(\lambda^2) \right] & T < T_{HO}^- \end{cases} \quad (4.A.14)$$

Thus, across the Hidden Order transition (where Δ_x orders), *the nematic susceptibility receives a correction that is proportional to the specific heat capacity jump of the Hidden Order*. In mean field theory, this only arises just below the Hidden Order transition temperature, but fluctuations above the transition temperature have the same effect. An alternative intuition for this result is that since the nematic order parameter is proportional to $(\Delta_x^2 - \Delta_y^2)$, while the heat capacity is a proportional to $(\Delta_x^2 + \Delta_y^2)$, these two quantities are directly proportional (within mean field theory) in the case of C_4 symmetry breaking.

It should be noted that an anomaly in the nematic susceptibility is also possible when Hidden Order does *not* break four-fold symmetry; however, the magnitude of the anomaly is then not directly proportional to the specific heat capacity jump (within mean field theory). Because (a) the observed anomaly in the nematic susceptibility tracks the specific heat capacity jump, (b) there is a large nematic susceptibility in the symmetric state above T_{HO} indicating tendencies to C_4 symmetry breaking, and (c) several other experimental techniques [21,42,52,53] find evidence for C_4 symmetry breaking at T_{HO} , it seems likely that Hidden Order does indeed possess a nematic component.

Nematic \times (?) Symmetry: Functional Form

In this section, we illustrate how a nematic order parameter can arise from fluctuations of an underlying order with Z_2 symmetry. Here we follow closely the procedure outlined in [100], where we begin with a two-component vector order parameter with the free energy density

$$\begin{aligned}
f_1[\Delta_x, \Delta_y] &= \frac{1}{2}(\partial|\Delta_x|)^2 + \frac{1}{2}(\partial|\Delta_y|)^2 + \frac{r}{2}(|\Delta_x|^2 + |\Delta_y|^2) \\
&+ \frac{v}{2}(|\Delta_x|^2 + |\Delta_y|^2)^2 - \frac{g}{2}(|\Delta_x|^2 - |\Delta_y|^2)^2
\end{aligned} \tag{4.A.15}$$

with $r \propto (T - T_c)/T_c$, $v > g$, and $\partial = \nabla$ the spatial gradient operator. This is a simple re-writing of (4.A.5) with $v = (2w + u)/4$ and $g = (2w - u)/4$. The nematic order parameter in this situation can in fact correspond to the difference in fluctuations of the two components of $\vec{\Delta}$. More formally, we can study such a nematic state by employing a Hubbard-Stratonovich transformation in which we decouple both fourth order terms above. We begin with the original partition function, which is a functional integral over the order parameter fields Δ_x, Δ_y :

$$\begin{aligned}
\mathcal{Z} &\propto \int \mathcal{D}\Delta_x \mathcal{D}\Delta_y e^{-S_{\text{eff}}[\Delta_x, \Delta_y]} \\
S_{\text{eff}}[\Delta_x, \Delta_y] &= \int \frac{d^d \mathbf{k}}{(2\pi)^d} f[\Delta_x(\mathbf{k}), \Delta_y(\mathbf{k})].
\end{aligned} \tag{4.A.16}$$

In writing S_{eff} in this way, we have assumed that Δ_x and Δ_y are frequency and momentum dependent.

To study the nematic phase, we introduce auxiliary scalar fields \mathcal{N} for $|\Delta_x|^2 - |\Delta_y|^2$ and ζ for $|\Delta_x|^2 + |\Delta_y|^2$ and perform a Hubbard-Stratonovich transformation to decouple the quartic order (in Δ_i) terms in the free energy. The Hubbard-Stratonovich transformation is a generalization of the identity

$$e^{-\frac{a}{2}x^2} = \frac{1}{\sqrt{2\pi a}} \int_{-\infty}^{\infty} dy e^{-\frac{y^2}{2a} - ixy}, \tag{4.A.17}$$

which for separate fields \mathcal{N} and ζ yields

$$\mathcal{Z} \propto \int \mathcal{D}\Delta_x \mathcal{D}\Delta_y \mathcal{D}\mathcal{N} \mathcal{D}\zeta e^{-S_{\text{eff}}[\Delta_x, \Delta_y, \mathcal{N}, \zeta]} \quad (4.A.18)$$

$$S_{\text{eff}}[\Delta_x, \Delta_y, \mathcal{N}, \zeta] = \int \frac{d^d \mathbf{k}}{(2\pi)^d} f_2[\Delta_x(\mathbf{k}), \Delta_y(\mathbf{k}), \mathcal{N}(\mathbf{k}), \zeta(\mathbf{k})].$$

This represents a major simplification because we have reduced the theory to one which includes only Gaussian integrals, but this comes at the cost of two additional integrals over the extra auxiliary order parameter fields.

We would like to compute the nematic susceptibility above the temperature at which both $\vec{\Delta}$ and \mathcal{N} order (i.e., $\langle \Delta_x \rangle = \langle \Delta_y \rangle = \langle \mathcal{N} \rangle = 0$), and so, in addition to transforming the free energy in (4.A.5), we also add in the effect of a symmetry breaking strain field h . Proceeding to Gaussian level in the order parameter fields and the fluctuations, this corresponds to the theory

$$\begin{aligned} f_2[\Delta_x(\mathbf{r}), \Delta_y(\mathbf{r}), \mathcal{N}, \zeta] &= \frac{1}{2}(\partial|\Delta_x|)^2 + \frac{1}{2}(\partial|\Delta_y|)^2 \\ &+ \frac{r}{2}(|\Delta_x|^2 + |\Delta_y|^2) - \frac{h}{2}(|\Delta_x|^2 - |\Delta_y|^2) \\ &+ \frac{1}{2}a\mathcal{N}^2 + \lambda(|\Delta_x|^2 - |\Delta_y|^2)\mathcal{N} - \alpha h\mathcal{N} \\ &+ \frac{1}{2}b\zeta^2 + d(|\Delta_x|^2 + |\Delta_y|^2)\zeta, \end{aligned} \quad (4.A.19)$$

where $r \propto (T - T_c)/T_c$ and $a = \frac{1}{g} \propto (T - T_{\mathcal{N}})/T_{\mathcal{N}}$ (Note: we assume that $T_c > T_{\mathcal{N}}$ so that nematic order develops parasitically when $\vec{\Delta}$ orders). The coefficient α reflects the strength and sign of the coupling of \mathcal{N} to the external field, relative to that of $\vec{\Delta}$.

The field ζ (with quadratic coefficient $b = -1/v$) essentially renormalizes the coefficient r in (4.A.19), and so we neglect its fluctuations and analyze the theory by integrating out Δ_x and Δ_y :

$$\begin{aligned} \mathcal{Z} &\propto \int \mathcal{D}\mathcal{N} \left\langle e^{-\int_{\mathbf{k}} \lambda (|\Delta_x|^2 - |\Delta_y|^2) \mathcal{N}} \right\rangle_{\Delta_x, \Delta_y} e^{-\int_{\mathbf{k}} \frac{a}{2} \mathcal{N}^2 - \alpha h \mathcal{N}} \\ &\approx \int \mathcal{D}\mathcal{N} e^{-\int_{\mathbf{k}} \lambda (\langle |\Delta_x|^2 \rangle - \langle |\Delta_y|^2 \rangle) \mathcal{N}} e^{-\int_{\mathbf{k}} \frac{a}{2} \mathcal{N}^2 - \alpha h \mathcal{N}}, \end{aligned} \quad (4.A.20)$$

with $\langle |\Delta_x|^2 \rangle$ given by

$$\begin{aligned} &\int \mathcal{D}\Delta_x (\Delta_x^2) \exp \left[-\frac{1}{2} \int_{\mathbf{k}} (\mathbf{k}^2 + r + h) \Delta_x(\mathbf{k}) \Delta_x(-\mathbf{k}) \right] \\ &= \int \frac{d^d \mathbf{k}}{(2\pi)^d} \frac{1}{[\mathbf{k}^2 + (r/2) + h]} \equiv G(r + h) \end{aligned} \quad (4.A.21)$$

and $\langle |\Delta_y|^2 \rangle$ given by

$$\begin{aligned} &\int \mathcal{D}\Delta_y (\Delta_y^2) \exp \left[-\frac{1}{2} \int_{\mathbf{k}} (\mathbf{k}^2 + r - h) \Delta_y(\mathbf{k}) \Delta_y(-\mathbf{k}) \right] \\ &= \int \frac{d^d \mathbf{k}}{(2\pi)^d} \frac{1}{[\mathbf{k}^2 + (r/2) - h]} \equiv G(r - h). \end{aligned} \quad (4.A.22)$$

Thus, taking the saddle point of the partition function in (4.A.20), we have for small values of the applied field

$$\begin{aligned} a\mathcal{N} - \alpha h + \lambda[G(r + h) - G(r - h)] &= 0 \\ \implies a\mathcal{N} - \alpha h + \lambda \left(\frac{\partial G(r)}{\partial r} \right) h &= 0. \end{aligned} \quad (4.A.23)$$

This in turn implies that the nematic susceptibility above T_c is given by

$$\begin{aligned} \chi_{\mathcal{N}} &= \lim_{h \rightarrow 0} \frac{\partial \mathcal{N}}{\partial h} = \frac{\alpha}{a} \left[1 - \lambda \left(\frac{\partial G(r)}{\partial r} \right) \right] \\ &= \frac{\alpha}{a_0(T - T_{\mathcal{N}})} \left[1 - \lambda \left(\frac{\partial G(r)}{\partial r} \right) \right] \quad (T > T_c). \end{aligned} \quad (4.A.24)$$

What (4.A.24) shows is that in the disordered phase of $\vec{\Delta}$, the nematic susceptibility above the phase transition is the sum of a Curie-Weiss term (the same as for the electronic nematic case) and an additional contribution which, as will be shown below, has a specific heat-like dependence on temperature.

Nematic \times (?) Symmetry: Specific Heat-like Singularity

To see why $\frac{\partial G(r)}{\partial r}$ behaves like the specific heat singularity due to the phase transition, we will express the partition function in terms of the mean field order parameters (including spatial fluctuations), derive the free energy f , and then compute the heat capacity singularity due to the phase transition as $c_{\text{sing}} = \frac{\partial E}{\partial T} = \frac{\partial}{\partial T} \left[-\frac{\partial \ln \mathcal{Z}}{\partial \beta} \right] = \frac{\partial}{\partial T} \left[\frac{\partial f}{\partial \beta} \right]$. Although we focus only on the heat capacity contribution due to the phase transition c_{sing} , there are many other degrees of freedom that contribute to the total heat capacity; however, these other degrees of freedom do not change abruptly at T_c .

Following this procedure, we consider the full partition function (with fluctuations) up to quartic order in the $\vec{\Delta}$ fields:

$$\begin{aligned} \mathcal{Z} &\propto \int \mathcal{D}\Delta_x \mathcal{D}\Delta_y e^{-S_{\text{eff}}[\Delta_x, \Delta_y]} \\ S_{\text{eff}}[\Delta_x, \Delta_y] &= \int \frac{d^d \mathbf{k}}{(2\pi)^d} f[\Delta_x(\mathbf{k}), \Delta_y(\mathbf{k})] \\ f[\Delta_x, \Delta_y] &= \frac{1}{2}(\partial|\Delta_x|)^2 + \frac{1}{2}(\partial|\Delta_y|)^2 + \frac{r}{2}(|\Delta_x|^2 + |\Delta_y|^2) \\ &\quad + \frac{u}{4}(|\Delta_x|^4 + |\Delta_y|^4) + w|\Delta_x|^2|\Delta_y|^2 \end{aligned} \tag{4.A.25}$$

We begin by expanding $\vec{\Delta}$ about its mean field value, i.e., by letting

$$\begin{aligned} |\Delta_x| &= \langle |\Delta_x| \rangle + \psi_x(\mathbf{r}) \\ |\Delta_y| &= \langle |\Delta_y| \rangle + \psi_y(\mathbf{r}), \end{aligned} \tag{4.A.26}$$

where the mean field values of the components of the order parameter are given by

$$\langle |\Delta_x| \rangle = \begin{cases} 0 & \text{if } T > T_c \\ \pm \sqrt{-|r|/u} & \text{if } T < T_c, \end{cases} \quad (4.A.27)$$

and $\langle |\Delta_y| \rangle = 0$ for all temperatures (since the state is unidirectional). Expanding the terms in (4.A.25) to quadratic order in the fluctuations ψ_x and ψ_y ,

$$\begin{aligned} \frac{1}{2}(\partial|\Delta_x|)^2 &= \frac{1}{2}(\partial[\langle |\Delta_x| \rangle + \psi_x])^2 = \frac{1}{2}(\nabla\psi_x)^2 \\ \frac{1}{2}(\partial|\Delta_y|)^2 &= \frac{1}{2}(\nabla\psi_y)^2 \\ \frac{r}{2}(|\Delta_x|^2 + |\Delta_y|^2) &= \frac{r}{2}(\langle |\Delta_x| \rangle^2 + \psi_x^2 + 2\langle |\Delta_x| \rangle\psi_x + \psi_y^2) \\ \frac{u}{4}(|\Delta_x|^4 + |\Delta_y|^4) &\approx \frac{u}{4}[\langle |\Delta_x| \rangle^4 + 4\langle |\Delta_x| \rangle^3\psi_x + 6\langle |\Delta_x| \rangle^2\psi_x^2] \\ w|\Delta_x|^2|\Delta_y|^2 &\approx w\langle |\Delta_x| \rangle^2\psi_y^2. \end{aligned} \quad (4.A.28)$$

Observing that the linear terms in ψ_x cancel, the new theory including fluctuations is given by

$$\begin{aligned} \mathcal{Z} &\propto \int \mathcal{D}\psi_x \mathcal{D}\psi_y e^{-S_{\text{eff}}[\psi_x, \psi_y]} \\ \frac{1}{\mathcal{V}} S_{\text{eff}} &= \frac{r}{2} \langle |\Delta_x| \rangle^2 + \frac{u}{4} \langle |\Delta_x| \rangle^4 \\ &\quad + \frac{1}{2\mathcal{V}} \int \frac{d^d \mathbf{k}}{(2\pi)^d} (\mathbf{k}^2 + \xi_x^{-2}) |\psi_x(\mathbf{k})|^2 \\ &\quad + \frac{1}{2\mathcal{V}} \int \frac{d^d \mathbf{k}}{(2\pi)^d} (\mathbf{k}^2 + \xi_y^{-2}) |\psi_y(\mathbf{k})|^2 \\ &\equiv \frac{r}{2} \langle |\Delta_x| \rangle^2 + \frac{u}{4} \langle |\Delta_x| \rangle^4 \\ &\quad + \frac{1}{2\mathcal{V}} \int \frac{d^d \mathbf{k}}{(2\pi)^d} [G_x^{-1}(\mathbf{k}) |\psi_x(\mathbf{k})|^2 + G_y^{-1}(\mathbf{k}) |\psi_y(\mathbf{k})|^2], \end{aligned} \quad (4.A.29)$$

where we have introduced the length scales

$$\xi_x^{-2} \equiv \frac{1}{2}(r + 3u\langle|\Delta_x|\rangle^2) = \begin{cases} r/2 & T > T_c \\ |r| & T < T_c \end{cases} \quad (4.A.30)$$

$$\xi_y^{-2} \equiv \frac{1}{2}(r + 2w\langle|\Delta_x|\rangle^2) = \begin{cases} r/2 & T > T_c \\ |r|(2w - u)/2u & T < T_c. \end{cases}$$

Using the formula $\ln \det G^{-1} = \text{Tr} \ln G^{-1}$, we can integrate out the fluctuation fields ψ_x, ψ_y in (4.A.29) to obtain the free energy density:

$$f = -\frac{\ln \mathcal{Z}}{\mathcal{V}} = \frac{r}{2}\langle|\Delta_x|\rangle^2 + \frac{u}{4}\langle|\Delta_x|\rangle^4 + \frac{1}{2} \int \frac{d^d \mathbf{k}}{(2\pi)^d} (\ln[\mathbf{k}^2 + \xi_x^{-2}] + \ln[\mathbf{k}^2 + \xi_y^{-2}]). \quad (4.A.31)$$

For $T > T_c$, the two terms in the integral are the same.

We can now compute the heat capacity singularity $c_{\text{sing}} = \frac{\partial}{\partial T} \left[\frac{\partial f}{\partial \beta} \right]$. Since $r \propto (T - T_c)/T_c$, it follows that $\frac{\partial}{\partial T} = \frac{\partial r}{\partial T} \frac{\partial}{\partial r} = \frac{1}{T_c} \frac{\partial}{\partial r}$ and $\frac{\partial}{\partial \beta} = -T^2 \frac{\partial}{\partial T} = \frac{-T_c^2(1+r)^2}{T_c} \frac{\partial}{\partial r} \approx -T_c \frac{\partial}{\partial r}$ (valid for $T \approx T_c$, or $|r| \ll 1$), and hence the heat capacity singularity is given by

$$c_{\text{sing}} = -\frac{\partial^2 f}{\partial r^2}. \quad (4.A.32)$$

Applying this result to (4.A.31) and substituting the r dependence of $\langle|\Delta_x|\rangle$, we find that for $T > T_c$

$$c_{\text{sing}} = \frac{\partial}{\partial r} \left[\int \frac{d^d \mathbf{k}}{(2\pi)^d} \frac{1}{[\mathbf{k}^2 + (r/2)]} \right] \equiv \frac{\partial G(r)}{\partial r} \quad (T > T_c), \quad (4.A.33)$$

where $G(r)$ is the correlation function that we wrote down in the previous section. Hence, $\partial G/\partial r$ is equal to the fluctuational contribution to the heat capacity and proportional to the nematic susceptibility correction in the disordered phase.

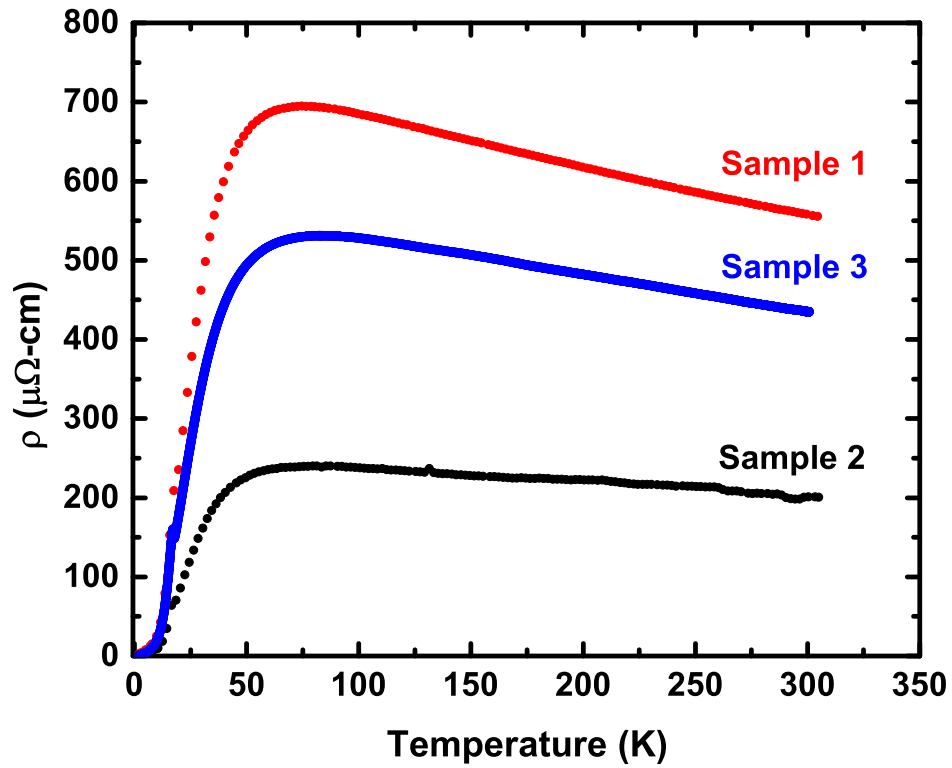
Supplementary Table 4.1: URu₂Si₂ Sample Information (Dimensions in mm)

	Orientation	Length	Width	Thickness	$RRR \equiv R(300K)/R(4.2K)$
Sample 1	[100]	1.05	0.073	0.070	87
Sample 2	[100]	1.38	0.656	0.062	81
Sample 3	[$\bar{1}10$]	1.26	0.288	0.095	170

Note: In the original publication with the definition $RRR \equiv R(300K)/R(4.2K)$, Sample 3 was quoted to have a RRR value of 170. With a different definition of $RRR \equiv R(300K)/R(2K)$ (used in the next chapter in the context of the RRR dependence of the elastoresistive response), Sample 3 is assigned a RRR value of 970.

4.B Crystal Growth

Single crystals of URu₂Si₂ were grown by the Czochralski technique and then electrorefined to improve the purity. The crystals were oriented by Laue diffraction in back-scattering geometry and cut with a wire saw. In some cases, the crystals were cleaved with a razor blade and bar shaped samples were extracted. After elastoresistivity measurements the in-plane orientations of the URu₂Si₂ samples were confirmed using a commercial four-circle single crystal diffractometer in an Eulerian cradle geometry, with CuK_{α1} radiation, of wavelength $\lambda = 1.54 \text{ \AA}$. Fine alignment of the diffraction geometry was done using the (004) out-of-plane orientation peak, which is the one with the strongest intensity for this family of planes. Subsequently, the [112] peaks were identified by moving to the corresponding ω and ξ (azimuthal) positions, and performing ϕ scans (rotation about the out-of-plane axis). $\phi=0$ corresponds to top and bottom sample edges along the horizontal axis. For crystals with edges along the [100] directions, the [112] diffraction peaks were found at ϕ values of 45°, 135°, 225° and 315°. For crystals with edges along the [110] directions, the [112] diffraction peaks were found at ϕ values of 0°, 90°, 180° and 270°. Supplementary Table 4.1 provides details for the three samples measured, where $RRR \equiv \frac{R(300K)}{R(4.2K)}$. The resistivity as a function of temperature for the three samples is plotted in Supplementary Figure 4.4.



Supplementary Figure 4.4: In-plane resistivity as a function of temperature for samples detailed in Supplementary Table 4.1. Sample 1 [100] and Sample 3 [$\bar{1}10$] were used for the elastoresistivity measurements in the main text. Sample 2 [100] was also measured and showed the same temperature dependence in $m_{11} - m_{12}$ as Sample 1.

4.C Elastoresistance Measurements

To emphasize the difference between hydrostatic pressure and in-plane biaxial strain, and also to illustrate that the nematic susceptibility is fundamentally a differential measurement, we present in Supplementary Figure 4.5 the individual elastoresistance measurements on the three samples used in this study. Each data point represents the slope of the change in normalized resistance to applied strain at zero strain, and the points are plotted as a function of temperature. Each point comes from fitting a line to five successive voltage sweeps and averaging the resultant slope. The gray stars correspond to data measured on crystals oriented along the long axis of the piezo (the $(\frac{\Delta R}{R})_{yy}$ configuration), whereas the black boxes denote data obtained from crystals oriented along the short axis of the piezo (the $(\frac{\Delta R}{R})_{xx}$ configuration), as illustrated in Figure 1 of the main text.

For a $[1\bar{1}0]$ oriented crystal, there is a strong, temperature-dependent response in the elastoresistance (Supplementary Figure 4.5(a)). Aside from the raw slopes being much larger than unity (which is unusual for a metal and remarkable in itself), there is also a pronounced difference in the individual elastoresistance measurements, which have *opposite* signs. This is strong evidence that the normalized resistance change is due predominantly to the in-plane biaxial strain (which is a volume preserving deformation), as distinct from hydrostatic pressure which would uniformly change the resistance regardless of the in-plane orientation of the current. The $2m_{66}$ elastoresistivity coefficient (which is proportional to the nematic susceptibility) is extracted from these measurements by subtracting the two curves; because the curves have opposite sign, this subtraction results in slightly higher raw numbers for the nematic susceptibility.

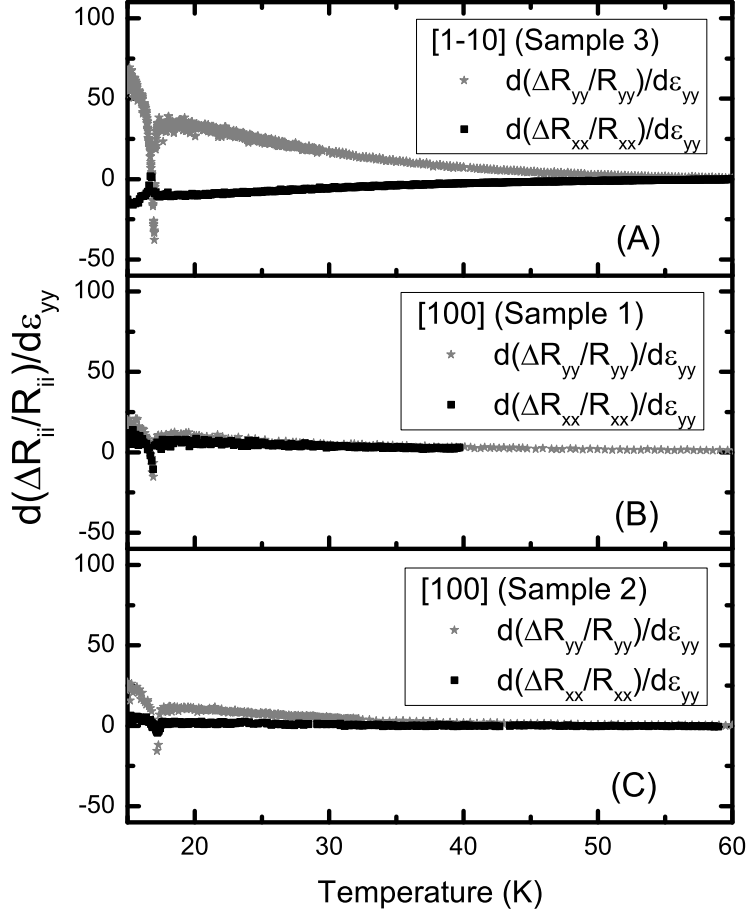
In contrast, we also present the individual elastoresistance data for two different $[100]$ oriented crystals (Supplementary Figure 4.5 (b, c)). The measured slopes for both $[100]$ crystals are considerably smaller than for the $[1\bar{1}0]$ sample; correspondingly, the difference in the curves (i.e., the differential elastoresistance, which is the quantity that is proportional to the nematic susceptibility) is also smaller, illustrating the pronounced anisotropy in the nematic susceptibility tensor ($2m_{66} \gg (m_{11} - m_{12})$)

implies that $\chi_{N,[110]} \gg \chi_{N,[100]}$). As defined, this is the *bare* nematic susceptibility, unrenormalized by interaction with the crystal lattice [101].

In the region near T_{HO} , the elastoresistance measurements on the [100] oriented samples begin to deviate significantly from their small higher temperature values. This likely reflects imperfect alignment of the current paths relative to the x - and y -axes of the piezo stack. If the current paths within the crystal are predominantly in the [100] direction but, due to very slightly misoriented contacts, contain a minor contribution from the [110] direction, this could give rise to a non-zero elastoresistance response for a nominally [100] oriented sample. Additionally, if there is even a small offset between the current direction and the axes of the piezo stack when gluing the crystal down, this could also cause some of the critical behavior associated with the [110] direction to “contaminate” the [100] measurement. Regardless of these subtleties, we still observe a much stronger response in the [110] direction than the [100] in both the individual and differential elastoresistance measurements.

4.D Proximity to Strain-induced Transition

It has previously been established that hydrostatic pressure in excess of approximately 5 kBar stabilizes the competing local moment antiferromagnetic (LMA) groundstate of URu_2Si_2 (for a relatively recent review of key experimental results see [14] and references therein). Recent measurements also revealed a critical uniaxial stress of $\sigma \sim 0.33$ GPa for the HO to antiferromagnetic transition [102]. Furthermore, recent theoretical treatment employing a Ginzburg-Landau model based on the lowest-lying crystal field states predicts a similar stabilization of the LMA state due to uniaxial stress [85]. In this theory, the HO-to-LMA transition is predicted to occur for uniaxial stress $\sigma \sim 0.6$ GPa directed along either the [100] or [110] directions. Therefore, it is important to compare the strains experienced by the crystals in our experiment with those that would be anticipated for such large stresses. Since the elastic moduli of URu_2Si_2 are known [98], we can readily calculate the strain that would result from uniaxial stress of this magnitude. In the following analysis we show that our experiment employs strains that are considerably smaller than those corresponding



Supplementary Figure 4.5: Temperature dependence of the individual elastoresistance measurements (slopes of the normalized resistivity change to strain) for both the $(\frac{\Delta R}{R})_{xx}$ (black boxes) and $(\frac{\Delta R}{R})_{yy}$ (gray stars) configurations for all three samples. (a) $[1\bar{1}0]$ oriented crystal. Along with a very large elastoresistance signal ($(\frac{\Delta R}{R})_{xx}, (\frac{\Delta R}{R})_{yy} \gg 1$), there is a pronounced difference between the individual orthogonal configurations. Because the $(\frac{\Delta R}{R})_{xx}$ orientation has an opposite sign to that of $(\frac{\Delta R}{R})_{yy}$, the difference, which is proportional to the nematic susceptibility, is larger than either individual orientation. (b, c) $[100]$ oriented crystals. There is a decidedly smaller elastoresistance signal in each individual measurement and a correspondingly smaller difference between the $(\frac{\Delta R}{R})_{xx}$ and $(\frac{\Delta R}{R})_{yy}$ configurations. Near T_{HO} , the $[100]$ data resemble those from the $[1\bar{1}0]$ sample, likely reflecting slight sample misalignment on the piezo stack. Sample 2 and Sample 3 are the samples that appear in the main text.

to the critical stress boundaries.

For tetragonal symmetry, strain and stress are related by the tensor equation

$$\begin{pmatrix} \sigma_{xx} \\ \sigma_{yy} \\ \sigma_{zz} \\ \sigma_{yz} \\ \sigma_{zx} \\ \sigma_{xy} \end{pmatrix} = \begin{pmatrix} C_{11} & C_{12} & C_{13} & 0 & 0 & 0 \\ C_{12} & C_{11} & C_{13} & 0 & 0 & 0 \\ C_{13} & C_{13} & C_{33} & 0 & 0 & 0 \\ 0 & 0 & 0 & C_{44} & 0 & 0 \\ 0 & 0 & 0 & 0 & C_{44} & 0 \\ 0 & 0 & 0 & 0 & 0 & C_{66} \end{pmatrix} \begin{pmatrix} \epsilon_{xx} \\ \epsilon_{yy} \\ \epsilon_{zz} \\ \epsilon_{yz} \\ \epsilon_{zx} \\ \epsilon_{xy} \end{pmatrix}. \quad (4.D.1)$$

In writing this tensor equation we have employed the Voigt notation convention, whereby $xx \rightarrow 1$, $yy \rightarrow 2$, $zz \rightarrow 3$, $yz \rightarrow 4$, $zx \rightarrow 5$, and $xy \rightarrow 6$. Answering our main question requires inverting the elastic moduli tensor, C_{ij} , which for tetragonal symmetry gives

$$\begin{pmatrix} \epsilon_{xx} \\ \epsilon_{yy} \\ \epsilon_{zz} \\ \epsilon_{yz} \\ \epsilon_{zx} \\ \epsilon_{xy} \end{pmatrix} = \begin{pmatrix} \frac{C_{11}C_{33}-C_{13}^2}{\alpha(C_{11}-C_{12})} & \frac{C_{13}^2-C_{12}C_{33}}{\alpha(C_{11}-C_{12})} & -\frac{C_{13}}{\alpha} & 0 & 0 & 0 \\ \frac{C_{13}^2-C_{12}C_{33}}{\alpha(C_{11}-C_{12})} & \frac{C_{11}C_{33}-C_{13}^2}{\alpha(C_{11}-C_{12})} & -\frac{C_{13}}{\alpha} & 0 & 0 & 0 \\ -\frac{C_{13}}{\alpha} & -\frac{C_{13}}{\alpha} & \frac{C_{11}+C_{12}}{\alpha} & 0 & 0 & 0 \\ 0 & 0 & 0 & \frac{1}{C_{44}} & 0 & 0 \\ 0 & 0 & 0 & 0 & \frac{1}{C_{44}} & 0 \\ 0 & 0 & 0 & 0 & 0 & \frac{1}{C_{66}} \end{pmatrix} \begin{pmatrix} \sigma_{xx} \\ \sigma_{yy} \\ \sigma_{zz} \\ \sigma_{yz} \\ \sigma_{zx} \\ \sigma_{xy} \end{pmatrix}, \quad (4.D.2)$$

where $\alpha \equiv C_{33}(C_{11} + C_{12}) - 2C_{13}^2$. Explicit inversion of this matrix was done in Mathematica, but the exact form is also given in [103].

In this form, we can now consider the cases of a uniaxial stress of magnitude σ applied in the [100] and [110] directions. Starting with the simpler case, a uniaxial stress of magnitude σ applied in the [100] direction amounts to the case where $\sigma_{xx} = \sigma$ and all other $\sigma_{ij} = 0$, or equivalently that

$$\begin{pmatrix} \epsilon_{xx} \\ \epsilon_{yy} \\ \epsilon_{zz} \\ \epsilon_{yz} \\ \epsilon_{zx} \\ \epsilon_{xy} \end{pmatrix} = \begin{pmatrix} \sigma \left(\frac{C_{11}C_{33}-C_{13}^2}{\alpha(C_{11}-C_{12})} \right) \\ \sigma \left(\frac{C_{13}^2-C_{12}C_{33}}{\alpha(C_{11}-C_{12})} \right) \\ -\sigma \left(\frac{C_{13}}{\alpha} \right) \\ 0 \\ 0 \\ 0 \end{pmatrix}. \quad (4.D.3)$$

For the more complicated case of a uniaxial stress applied in the [110] direction, $\sigma_{xx} = \sigma_{yy} = \sigma_{xy} = \frac{\sigma}{2}$ and all other $\sigma_{ij} = 0$. This result is taken from [60], but it can be seen from two different vantage points: 1) by resolving the applied stress into its x - and y -components while accounting for the enlarged cross sectional area of the plane normal to the [110] direction, or 2) by applying a 45° orthogonal coordinate transformation to the stress tensor. Using this result, we obtain that

$$\begin{pmatrix} \epsilon_{xx} \\ \epsilon_{yy} \\ \epsilon_{zz} \\ \epsilon_{yz} \\ \epsilon_{zx} \\ \epsilon_{xy} \end{pmatrix} = \begin{pmatrix} \frac{\sigma}{2} \left(\frac{C_{11}C_{33}-C_{13}^2}{\alpha(C_{11}-C_{12})} + \frac{C_{13}^2-C_{12}C_{33}}{\alpha(C_{11}-C_{12})} \right) \\ \frac{\sigma}{2} \left(\frac{C_{11}C_{33}-C_{13}^2}{\alpha(C_{11}-C_{12})} + \frac{C_{13}^2-C_{12}C_{33}}{\alpha(C_{11}-C_{12})} \right) \\ -\sigma \left(\frac{C_{13}}{\alpha} \right) \\ 0 \\ 0 \\ \frac{\sigma}{2} \left(\frac{1}{C_{66}} \right) \end{pmatrix} = \begin{pmatrix} \frac{\sigma}{2} \left(\frac{C_{33}}{\alpha} \right) \\ \frac{\sigma}{2} \left(\frac{C_{33}}{\alpha} \right) \\ -\sigma \left(\frac{C_{13}}{\alpha} \right) \\ 0 \\ 0 \\ \frac{\sigma}{2} \left(\frac{1}{C_{66}} \right) \end{pmatrix}. \quad (4.D.4)$$

At this stage, we can now plug in numbers to estimate the strain required to move across the HO-LMA phase boundary. For $(C_{11}, C_{12}, C_{13}, C_{33}, C_{44}, C_{66}) = (255, 48, 86, 313, 133, 188)$ GPa (taken from [98], which are extrapolated to $T = 0$ K), a stress of magnitude $\sigma = 0.6$ GPa applied in the [100] direction induces a strain of

$$\begin{pmatrix} \epsilon_{xx} \\ \epsilon_{yy} \\ \epsilon_{zz} \\ \epsilon_{yz} \\ \epsilon_{zx} \\ \epsilon_{xy} \end{pmatrix} = \begin{pmatrix} 2.62 \times 10^{-3} \\ -2.76 \times 10^{-4} \\ -6.45 \times 10^{-4} \\ 0 \\ 0 \\ 0 \end{pmatrix}, \quad (4.D.5)$$

while a stress of magnitude $\sigma = 0.6$ GPa applied in the [110] direction induces a strain of

$$\begin{pmatrix} \epsilon_{xx} \\ \epsilon_{yy} \\ \epsilon_{zz} \\ \epsilon_{yz} \\ \epsilon_{zx} \\ \epsilon_{xy} \end{pmatrix} = \begin{pmatrix} 1.17 \times 10^{-3} \\ 1.17 \times 10^{-3} \\ -6.45 \times 10^{-4} \\ 0 \\ 0 \\ 1.60 \times 10^{-3} \end{pmatrix}. \quad (4.D.6)$$

This analysis reveals that the strain in the [100] ([110]) direction associated with a uniaxial stress of 0.6 GPa in the [100] ([110]) direction is of order 10^{-3} . In contrast, the largest strain experienced by the samples in our experiments corresponding to a full voltage sweep of the piezo stack, is of order $\frac{\Delta l}{l} \sim 10^{-4}$. Some of the transverse strains associated with the uniaxial stress are nevertheless smaller than 10^{-3} , so the analysis described in the main text to extract the elastoresistivity coefficients was repeated for a smaller range of strains. The temperature dependence of the elastoresistivity coefficients was the same for both small ($\sim 10^{-5}$) and large ($\sim 10^{-4}$) strain regimes, consistent with the linear response observed for the resistance as a function of strain (see for example Figure 1 of the main text). The only difference in the temperature dependence of the elastoresistivity coefficients for the two strain ranges was that the signal-to-noise became worse for the smaller strain range. These effects are discussed in more detail in the subsequent curve fitting subsection of the Supplementary Discussion.

Another source of strain comes from mounting the sample to the piezo stack,

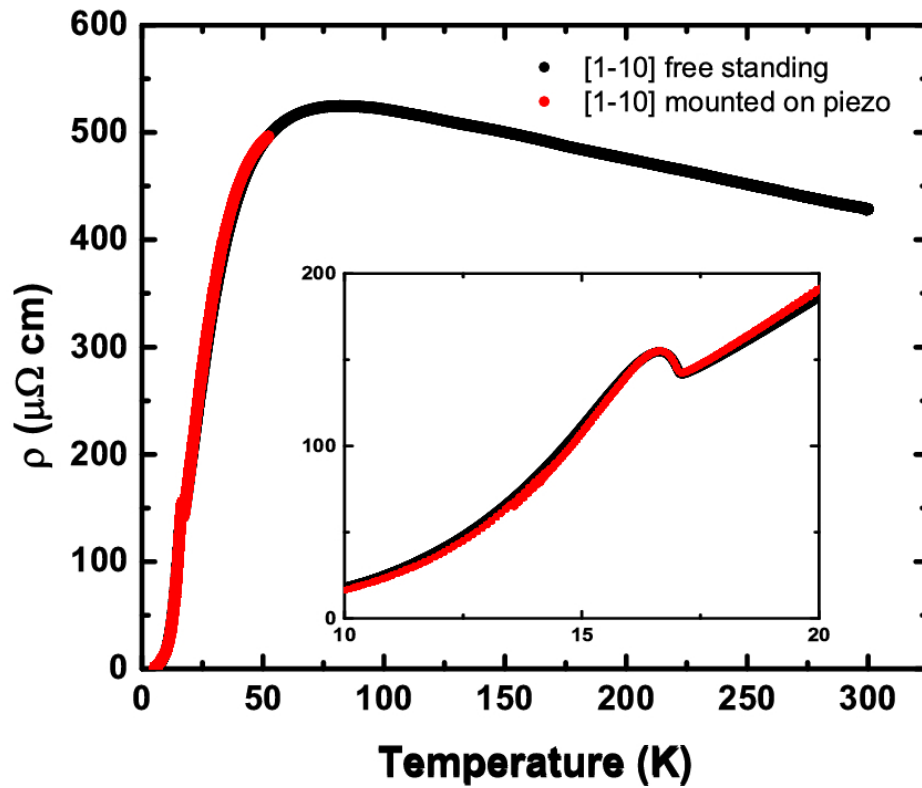
which creates a “built-in” strain from the epoxy, as well as effects arising from the differential thermal contraction [73]. To test for the effects of built-in strain, the resistivity as a function of temperature was measured with the sample free-standing and when glued to the piezo stack (Supplementary Figure 4.6). The two transport curves are nearly identical, showing no discernible shift in the Hidden Order transition temperature.

4.E Curve Fitting

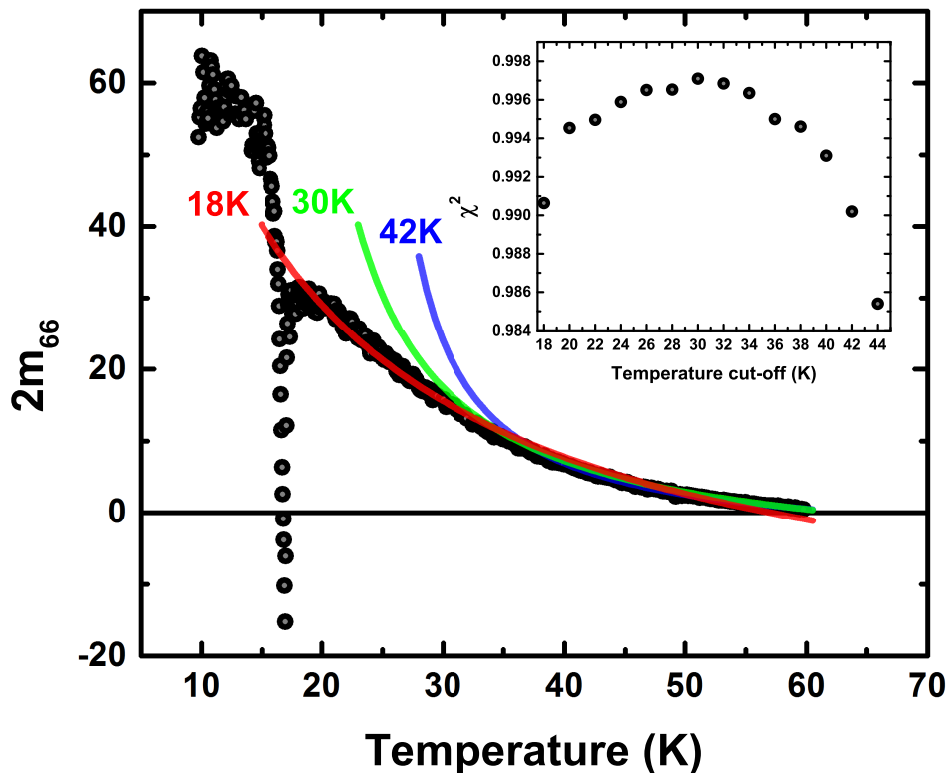
Neglecting the sharp anomaly at T_{HO} , the elastoresistivity coefficient $2m_{66}$ exhibits a monotonic increase with decreasing temperature from 60 K (the highest temperature at which there is a measureable elastoresistance) down to just above T_{HO} . In the following two sections, we briefly describe the procedures used to fit the data first to a Curie-Weiss temperature-dependence (motivated by the Ginzburg-Landau models described in the Supplementary Discussion) and then to a more general power law.

4.E.1 Curie-Weiss Fit

Motivated by the Ginzburg-Landau theory described in the Supplementary Discussion and in the main text, the $2m_{66}$ elastoresistance data were fit to a Curie-Weiss temperature dependence $2m_{66} = \frac{C}{T-\theta} + 2m_{66}^0$. When the data are fit over the full temperature range from 60 K down to 18 K (i.e., to just above the anomaly centered at 17.2 K), a clear systematic deviation can be seen (red curve of Supplementary Figure 4.7), which is confirmed by the reduced χ^2 value (inset Supplementary Figure 4.7). Similar fits were performed between 60 K and different lower-bound cut-off temperatures to find a reduced χ^2 which was closest to 1, which is how we define the best fit (inset to Supplementary Figure 4.7). The best fit determined by this method is found to be for the range between 60 K and 30 K (green curve, Supplementary Figure 4.7), with fit parameters given in the main text.



Supplementary Figure 4.6: In-plane resistivity as a function of temperature on $[1\bar{1}0]$ Sample 3, both free-standing and glued to the piezo stack with zero volts applied. The slight difference between the curves is attributed to differential thermal contraction of the PZT and the URu_2Si_2 sample. There is no discernible shift in T_{HO} between the two curves.



Supplementary Figure 4.7: A plot of the elastoresistivity coefficient $2m_{66}$ as a function of temperature. The data were fit to (4.E.1) with $\alpha = 1$. The red curve is a fit from 18 K to 60 K, the green from 30 K to 60 K, and the blue from 42 K to 60 K. The inset shows the reduced χ^2 for temperature windows of varying sizes (from a lower cut-off temperature to 60 K). The best fit is over the region 30 K to 60 K, as defined by χ_{red}^2 closest to 1.

4.E.2 General Power Law Fit

In addition to fitting the data to a Curie-Weiss temperature dependence, as described above, a more general fit to an arbitrary power law was also attempted. However, with less than a decade in reduced temperature, the data are not well-suited to such a scaling analysis, and the results are not conclusive. We include this analysis here for completeness.

We start by assuming that the elastoresistance is given by a single power law:

$$2m_{66} = 2m_{66}^0 + \frac{C}{(T - \theta)^\alpha} \quad (4.E.1)$$

where $2m_{66}^0$, C , θ and α are treated as fit parameters. Importantly, α is a nonlinear fit parameter, which greatly complicates the problem. One can linearize α (the parameter we are most interested in) by subtracting off $2m_{66}^0$, taking the natural log of both sides, and then taking a temperature derivative. If we could precisely estimate $2m_{66}^0$ and sensibly smooth the data in taking the temperature derivative, then we would be left with the simple task of fitting

$$\frac{d \ln(2m_{66} - 2m_{66}^0)}{dT} = \frac{-\alpha}{T - \theta} \quad (4.E.2)$$

The problem with the procedure leading to (4.E.2) is that if we misestimate $2m_{66}^0$ by some amount δ , then we no longer have a linearized fit form for α :

$$\ln(2m_{66} - 2m_{66}^0) = \ln \left(\delta + \frac{C}{(T - \theta)^\alpha} \right). \quad (4.E.3)$$

Furthermore, there is no sensible way to linearize (4.E.3) via a Taylor expansion since we expect the temperature dependent term to dominate near criticality but to progressively approach zero at higher temperatures. These issues and others have been addressed in the literature [104].

Instead, we choose a graphical method. Assuming the functional form (4.E.1) and fixing a particular α , one can unbiasedly estimate the other three linear parameters (and in particular the temperature independent term $2m_{66}^0$) through a normal fitting routine. Since (4.E.1) is equivalent to

$$\frac{1}{(2m_{66} - 2m_{66}^0)^{1/\alpha}} = \frac{T - \theta}{C^{1/\alpha}} \quad (4.E.4)$$

it is straightforward to compute $\frac{1}{(2m_{66} - 2m_{66}^0)^{1/\alpha}}$ and to graph the result versus temperature. Doing this for many values of α yields the critical exponent, as the right choice will result in a quantity linearly proportional to temperature.

Importantly, this method avoids the pitfalls of nonlinear parameter estimation and numerical differentiation; however, it is still quite susceptible to errors in $2m_{66}^0$, as any error δ results in the highly nonlinear expression

$$\frac{1}{(2m_{66} - 2m_{66}^0)^{1/\alpha}} = \frac{1}{(\delta + \frac{C}{(T-\theta)^\alpha})^{1/\alpha}} \quad (4.E.5)$$

The nonlinearity from misestimating $2m_{66}^0$ expressed in (4.E.5) is worth keeping in mind since $\frac{1}{(2m_{66} - 2m_{66}^0)^{1/\alpha}}$ is *not* linear in temperature for any α spanning the range $0.5 \leq \alpha \leq 3$ (Supplementary Figure 4.8). The fits are done over the temperature range $20 \text{ K} \leq T \leq 60 \text{ K}$, where we are limited on the low end by proximity to the Hidden Order phase transition and on the high end by our ability to resolve the elastoresistive response. Note that the estimate of $2m_{66}^0$ is itself dependent on the particular α chosen, and so varies between curves. Higher values of α yield highly unphysical estimates of θ and are hence neglected.

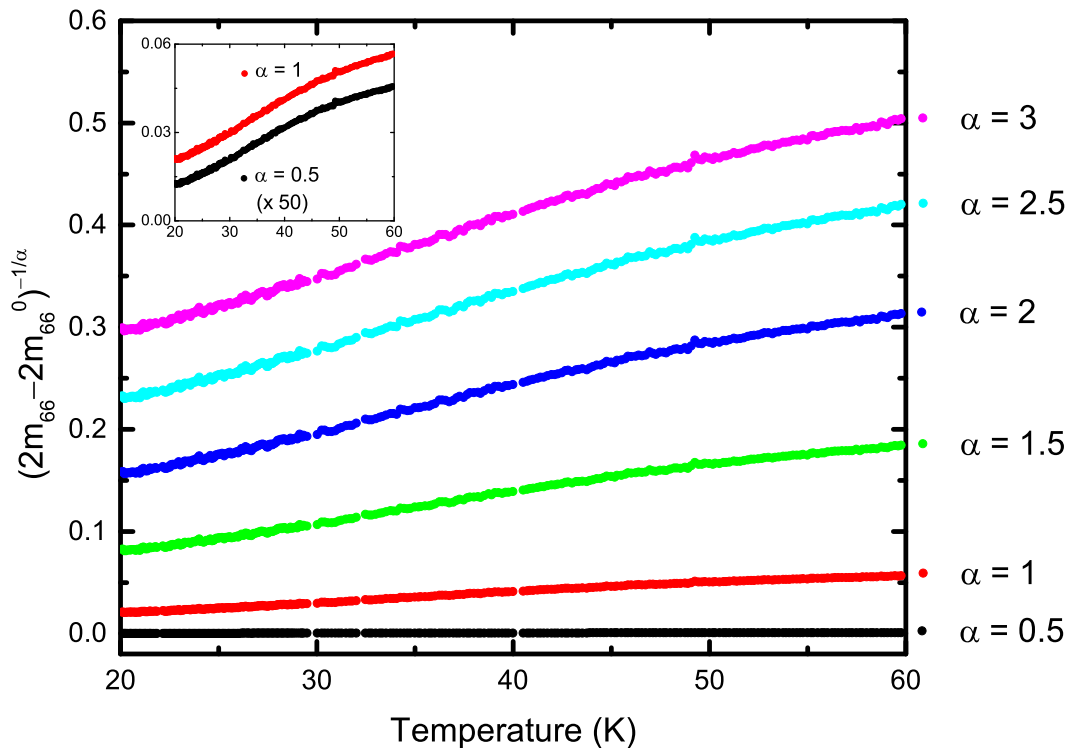
From the temperature dependence of the $2m_{66}$ data (Supplementary Figure 4.8), we do not unequivocally observe a power law divergence with an extractable critical exponent. The task of fitting critical exponents is potentially complicated by our limited range in temperature (less than a decade), and this might be why it is difficult to distinguish between different α 's. The results are also potentially skewed by incorrect

estimations in the temperature independent parameter $2m_{66}^0$. Consequently, the most physically meaningful fit to the data is provided by the Curie-Weiss model described in the main text (i.e., fixing the exponent $\alpha = 1$).

4.F Nonlinear Elastoresistance Near T_{HO}

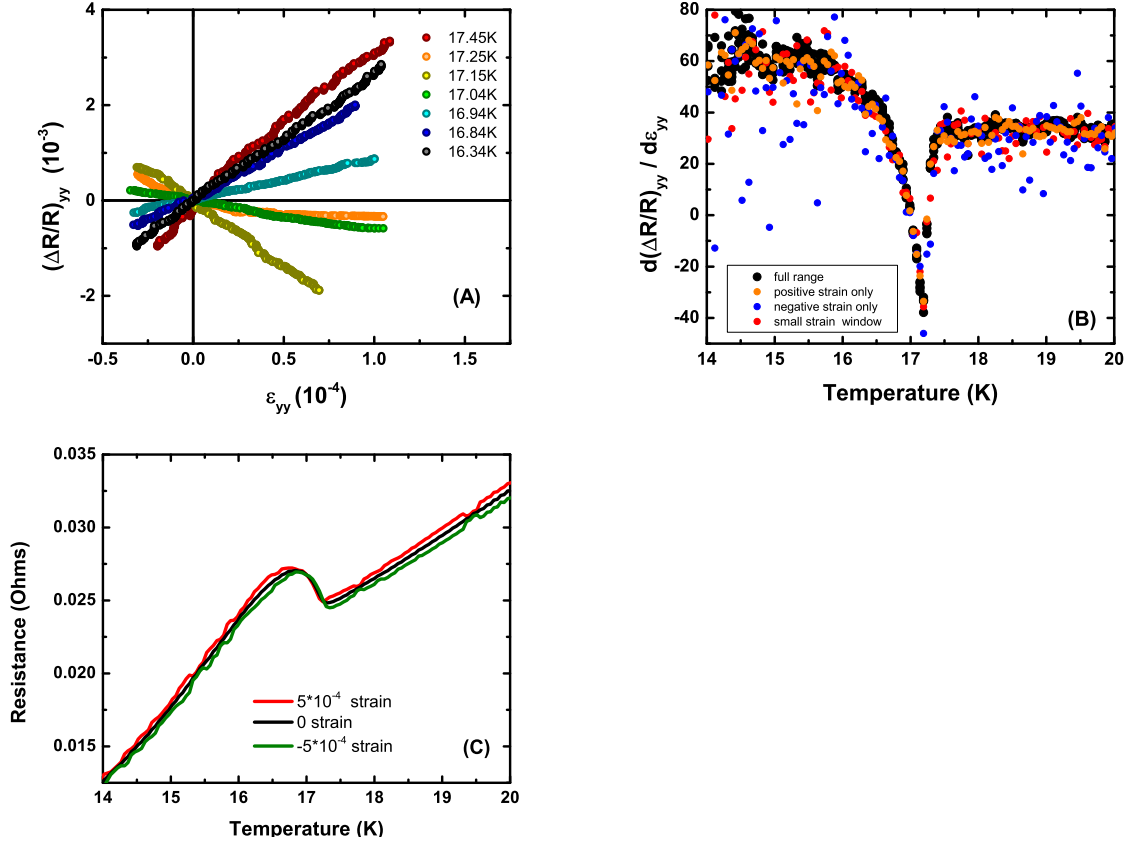
For temperatures more than ~ 150 mK away from T_{HO} , the elastoresistance is linear with strain over the entire range of strain experienced by the material in our experiments (which, in the vicinity of T_{HO} is approximately $-0.5 \times 10^{-4} < \epsilon_{yy} < +1 \times 10^{-4}$); however, very close to $T_{HO} = 17.17$ K, the elastoresistance develops a nonlinear response to strain. This effect can be seen in Supplementary Figure 4.9(a), which shows successive measurements of $(\frac{\Delta R}{R})_{yy}$ for a $[1\bar{1}0]$ oriented crystal as a function of ϵ_{yy} for temperatures spanning T_{HO} . In the nonlinear regime, the magnitude of the elastoresistivity coefficients are slightly *underestimated* if the data are fit to a linear function over the entire data range. This effect can be seen in Supplementary Figure 4.9(b), which shows $(\frac{\Delta R}{R})_{yy}/\epsilon_{yy}$ evaluated for different strain ranges (see Supplementary Figure 4.9 caption for further detail). It is important to note, however, that the sign change of the slope of the elastoresistance is a robust feature, observed for large and small strains and for temperatures that extend beyond the nonlinear regime.

The physical origin of the nonlinear response very close to T_{HO} is unclear. The effect could be associated with critical behavior, or possibly with strain-induced changes in T_{HO} . To investigate the latter idea, we estimate the rate at which T_{HO} is affected by anisotropic strain. We do this by extracting the temperature dependence of the resistivity for fixed values of the strain. This is obtained by performing a linear fit to the elastoresistance over different strain ranges (see Supplementary Figure 4.9 caption for further detail) and using the fit parameter to calculate the resistance for a specific strain (we choose $\pm 5 \times 10^{-4}$). The resulting curves are shown in Supplementary Figure 4.9(c), together with the temperature dependence of the resistivity for the same unstrained crystal (mounted on the piezo, with 0 V applied to the piezoelectric stack). For all temperatures more than ~ 150 mK from T_{HO} , the resistance of the



Supplementary Figure 4.8: Inverse elastoresistivity coefficient (with a subtracted temperature-independent term) versus temperature. For the case where $2m_{66}$ obeys a power law divergence with a critical exponent α , we should observe a curve that is linear in temperature. This linear relationship is not observed for any α spanning the range $0.5 \leq \alpha \leq 3$ over the entire temperature window. The data can be fit to a Curie-Weiss form over a smaller temperature range. Inset: Zoom-in version on the $\alpha = 0.5$ and $\alpha = 1$ curves, highlighting nonlinear behavior. The $\alpha = 0.5$ curve is rescaled by a factor of 50 for illustrative purposes.

strained sample is independent of the fit range used to calculate the elastoresistivity coefficients, consistent with the linear elastoresistive response. Inspection of the curves in Supplementary Figure 4.9(c) indicates that T_{HO} increases (decreases) for negative (positive) strains $\epsilon_{yy} - \epsilon_{xx}$. This effect is consistent with expectations for a phase transition involving a multicomponent order parameter and with the model developed in the Supplementary Discussion, as can be appreciated by inspection of Equation (4.A.7). The analysis indicates a change in T_{HO} of approximately 100 mK per 10^{-3} strain. Close to T_{HO} , such a strain-induced change in T_{HO} would yield a nonlinear response, possibly accounting for some of the nonlinearity at T_{HO} . Significantly, for smaller strains, the change in T_{HO} would be correspondingly smaller. Since the anomaly in $2m_{66}$ is observed for large and small strain ranges alike (Supplementary Figure 4.9(b)), and since the response is linear for all temperatures more than ~ 150 mK from T_{HO} (in comparison to the width of the anomaly, which extends for over 1000 mK), we conclude that the anomaly itself is not primarily associated with strain-induced changes in T_{HO} . Nevertheless, the nonlinear effects described above preclude a critical scaling analysis, at least for the strains employed in the current study.



Supplementary Figure 4.9: (a) $(\frac{\Delta R}{R})_{yy}$ as a function of applied strain ϵ_{yy} around the Hidden Order transition for Sample 3 ($[1\bar{1}0]$). There is a clear sign change in the slope of $(\frac{\Delta R}{R})_{yy}$ at $T_{HO} = 17.17$ K. In a small temperature range (± 0.15 K) about T_{HO} , the resistive response to applied strain is nonlinear. The slopes in (a) are fit and plotted in (b) for different strain regions. Black points refer to the full strain region of -50 V to $+150$ V (which correspond to strains $\sim -0.25 \times 10^{-4}$ to 1×10^{-4}). Orange points in (b) are from slopes fit over a 0 V to 150 V strain region in (a) (strains of ~ 0 to 1×10^{-4}). Blue points in (b) are from slopes fit over a -50 V to 0 V strain region in (a) (strains of $\sim -0.25 \times 10^{-4}$ to 0). Red points in (b) are from slopes fit over a -50 V to 50 V region in (a) (strains of $\sim -0.25 \times 10^{-4}$ to 0.25×10^{-4}). Comparing the black points and the red points in (b), it can be seen that the magnitude of the elastoresistivity coefficients are slightly underestimated if the data are fit to a linear function over the entire strain range and overestimated if fitting only the negative strain region. In (c) we plot resistance as a function of temperature for a fixed strain in the $[1\bar{1}0]$ sample (see main text for further details). From the shift in the point of inflection in the resistance, application of $+5 \times 10^{-4}$ strain (red curve) and of -5×10^{-4} strain (green curve) shifts the transition temperature T_{HO} by approximately 100 mK per 10^{-3} of strain.

Chapter 5

Additional Elastoresistivity Measurements on URu₂Si₂

In this chapter, some observations are presented from additional preliminary elastoresistivity experiments on URu₂Si₂ that extend the experimental study described in Chapter 4. In particular, the $2m_{xy,xy}$ elastoresistivity coefficient of URu₂Si₂ was measured (a) for samples with varying residual resistivity ratio (RRR) values, (b) via the transverse method described in Chapter 3, and (c) in high magnetic fields. The results of these additional preliminary measurements are in broad agreement with previous studies of URu₂Si₂ and corroborate the picture presented in the previous chapter, namely, that Hidden Order is associated with broken fourfold rotational symmetry (in addition to breaking other symmetries). The measurements are, however, incomplete, and are included here in part to motivate additional future experiments.

5.1 Effect of Sample Quality on Elastoresistivity of URu₂Si₂

As mentioned briefly in Section 1.4, certain symmetry properties of Hidden Order are only resolvable in thermodynamic measurements on the cleanest URu₂Si₂ samples, suggesting a novel interplay between crystalline disorder (e.g., impurities, defects,

or internal stress) and electronic nematic order (especially as it couples to the crystal lattice). One cursory metric of sample quality is the residual resistivity ratio (RRR), which is conventionally defined as the ratio of the room temperature resistivity $\rho(300\text{K})$ to its extrapolated zero temperature value $\rho(0\text{K})$. Higher RRR values are associated with low defect or impurity density which generically increase $\rho(0\text{K})$; however, many factors can in principle affect RRR, making it an imperfect measure of sample quality. Nevertheless, it will generally be the case that samples with the most (least) disorder will have lower (higher) RRR values, and so it can serve as a convenient and quantifiable metric for sample quality.

Although the Hidden Order transition temperature (as observed from, for example, heat capacity and transport) has a small dependence on RRR [90], the symmetry properties of Hidden Order seem to have a much more dramatic sample quality dependence. High-resolution X-ray diffraction measurements performed by Tonegawa *et al.* [21] observe such a RRR dependence—the authors explicitly identify a splitting in the temperature dependence of the [880] Bragg peak on cooling through Hidden Order for a sample of $\text{RRR} \approx 670$, but the splitting is not observed for a sample of $\text{RRR} \approx 10$. Okazaki *et al.* [52] observe the onset of twofold oscillations in the magnetic torque (indicative of fourfold rotational symmetry breaking) only in the smallest samples by volume. One explanation of this effect involves the formation of domains (estimated to be of order $10 \mu\text{m}$), with approximately half of the domains oriented along the [110] crystallographic direction and the other half along $[1\bar{1}0]$, thereby canceling in all but the smallest crystals. Questions then arise concerning the origin of these domains and the possibility of detecting them experimentally. Another possible explanation is that these smaller samples had fewer domains or smaller internal stresses; if those domains or internal stresses are also the dominant effect in determining RRR (as opposed to, for example, impurity scattering), the magnitude of the twofold signal in the magnetic torque may be tracking a RRR effect. As the nature of such a RRR effect is still a subject of ongoing debate in the field, we present here preliminary measurements of the RRR dependence of the elastoresistivity in URu_2Si_2 .

Measurements were performed on a variety of URu_2Si_2 samples with RRR values spanning several orders of magnitude. RRR was determined by first measuring the

5.1. EFFECT OF SAMPLE QUALITY ON ELASTORESISTIVITY OF URu_2Si_2 147

temperature dependence of the in-plane longitudinal resistivity for contacts oriented along the crystallographic [110] direction, with the definition $RRR \equiv R(300K)/R(2K)$. Three samples were then chosen for the elastoresistance study, with RRR values of 970 (length 1.26 mm, width 0.29 mm, thickness 0.10 mm), 168 (length 0.90 mm, width 0.29 mm, thickness 0.10 mm), and 7 (length 1.23 mm, width 0.69 mm, thickness 0.05 mm) (Figure 5.1(a)). Having maintained the contacts from the initial RRR measurements, the samples were then prepared for the elastoresistance measurements by gluing to a PZT stack with Devcon five-minute epoxy. The RRR 970 and 168 samples were grown by Ryan Baumbach and Eric Bauer at the National High Magnetic Field Lab in Los Alamos from a Czochralski technique and then electro-refined to purify and destress the crystals. The RRR 7 sample was grown by Sheng Ran and Brian Maple at the University of California, San Diego, also via a Czochralski method.

The temperature dependence of the elastoresistance $d(\Delta\rho/\rho)_{yy,[110]}/d\epsilon_{yy}$ for the three RRR samples is shown in Figure 5.1(b). Even without measuring $d(\Delta\rho/\rho)_{xx,[110]}/d\epsilon_{yy}$ (which would be needed to extract $2m_{xy,xy}$), an appreciable difference is observed between the different samples. The largest measured elastoresistance corresponds to the RRR 970 sample, which also displays the strongest temperature dependence, the largest downward feature which scales as the heat capacity anomaly, and a Hidden Order transition temperature which is higher in temperature as compared to the lowest RRR sample. Additionally, while both the RRR 7 and RRR 168 samples show downward anomalies, the lower RRR sample is observed to have a lower transition temperature and a smaller, broader downward feature. The present observation of a pronounced RRR dependence to the elastoresistivity has also been reproduced elsewhere (T. Shibauchi, Private communication [105]).

These measurements appear to support conclusions drawn from X-ray measurements [21], namely that signatures of broken fourfold symmetry are rapidly suppressed as sample quality is reduced. Although these measurements in isolation do not unambiguously isolate the B_{2g} response (i.e., $d(\Delta\rho/\rho)_{yy,[110]}/d\epsilon_{yy}$ has contributions from both A_{1g} and B_{2g} strains), in light of the differential longitudinal measurements which show the dominant elastoresistivity coefficient to be $2m_{xy,xy}$, it seems most likely that

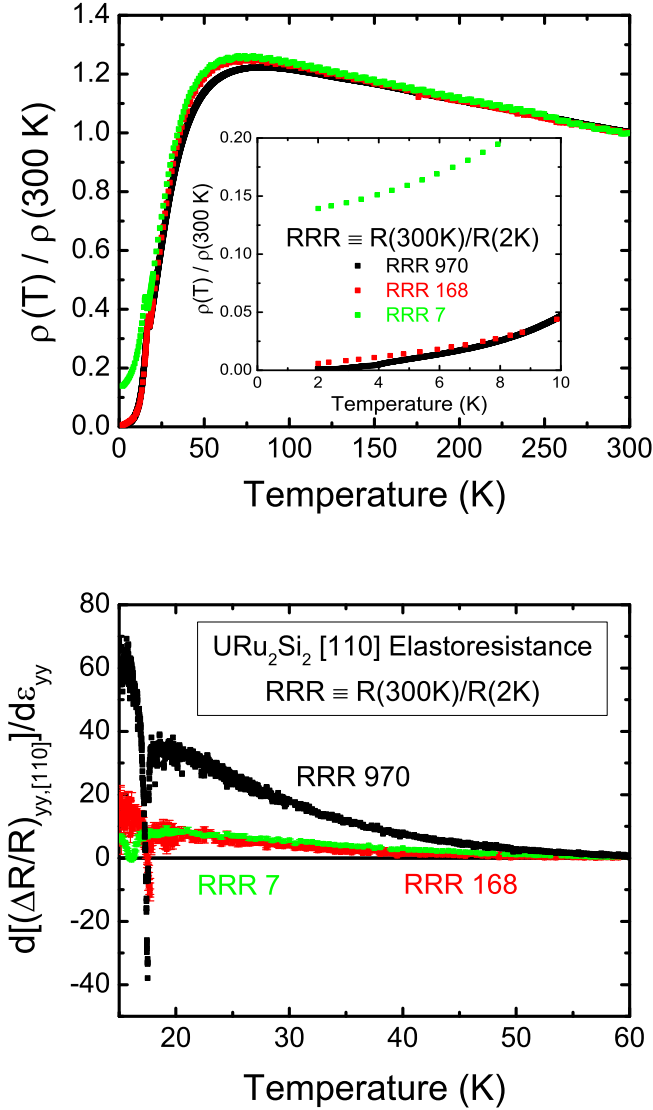


Figure 5.1: (a) Temperature dependence of the in-plane resistivity for three separate URu_2Si_2 samples, with contacts oriented along $[110]$. The quoted RRR value is given by $RRR = R(300 \text{ K})/R(2 \text{ K})$. (b) The elastoresponse $d[(\Delta\rho/\rho)_{yy,[110]}] / d\epsilon_{yy}$ for the three samples presented in (a). The elastoresponse for the RRR 970 and the RRR 168 samples both show an anomaly centered at T_{HO} that tracks the heat capacity. For these two samples, T_{HO} occurs at essentially the same temperature, but the magnitude of the elastoresponse is much smaller for the lower RRR sample. The RRR 7 sample not only shows a smaller elastoresponse but also displays the anomaly at a slightly lower temperature than the higher RRR samples, in agreement with the published RRR dependence of T_{HO} [90].

the origin of the effect is due to disorder reducing the magnitude of $2m_{xy,xy}$. Additional experiments (ideally using a Montgomery or transverse geometry for B_{1g} and B_{2g} strain configurations for samples with different RRR values) are, however, needed to establish that the effect does indeed originate from the anisotropic strain (i.e., not due to A_{1g} strain admixture) and to identify its physical origin, which is still not well-understood.

If $2m_{xy,xy}$ is confirmed to have a strong dependence on sample quality (as measured by RRR), it raises the question of what is the source of this effect. The RRR dependence is possibly associated with local (anisotropic) strains suppressing nematic fluctuations; these local strains may also be the source of the observed RRR dependence of the Hidden Order transition temperature T_{HO} (where lower RRR values also coincide with a lower T_{HO}) [90]. If local strains are the source of the RRR effect, this may also explain why as-grown URu_2Si_2 samples grown from a molten flux naturally have much higher RRR values than as-grown samples from a Czochralski technique [90]. A second contributing factor may be local internal stresses stabilizing “puddles” of the pressure-induced large moment antiferromagnetic (LMAF) phase [106]. If lower RRR samples have a higher relative fraction of residual LMAF puddles due to larger internal stresses, and if these puddles do not lead to an orthorhombic distortion—and there is no *a priori* reason to suppose that they should—then the diverging nematic susceptibility (that is only associated with Hidden Order) must decrease. Both of these effects would reduce the magnitude of the measured $2m_{xy,xy}$.

5.2 Transverse Elastoresistivity Measurements on URu_2Si_2

To obviate concerns about the effects of isotropic (i.e., A_{1g} -like) strain contamination from the initial differential longitudinal method, measurements of the $2m_{xy,xy}$ elastoresistivity coefficient were additionally attempted via the newly proposed transverse method. In light of the RRR effect observed in the previous section, however, samples of a sufficiently high RRR are required to compare to the differential longitudinal

data (which were taken for a sample characterized by RRR 970). Unfortunately, such samples could not be obtained on the time scale of this thesis. Nevertheless, a preliminary transverse elastoresistivity experiment was performed on an available sample with the largest available RRR (≈ 240). In addition to concerns about RRR, these measurements must also be seen as preliminary in light of the physical geometry of the sample, which for radiation safety reasons could not be cut into a rectilinear bar. Such a rectangular shape is appropriate for constraining the current path along an appropriate crystallographic direction; given that the sample measured did not have such a geometry (see photograph in Figure 5.2(a)), some contamination between symmetry channels can be anticipated.

With these concerns in mind, an initial measurement of $2m_{xy,xy}$ from the transverse method was attempted. An as-mounted sample for the transverse elastoresistivity measurement is shown in Figure 5.2(a). Prior to gluing, the contacts were characterized on the free-standing sample (Figure 5.2(b)) and a $\Delta_\ell \approx 13\%$ was determined (see Chapter 3 for the definition of Δ_ℓ , which characterizes misalignment of the transverse contacts). Although not shown in Figure 5.2(b), the measured R_{xy} was found to be negative due to the relative horizontal positioning of contacts 1 and 2 in Figure 5.2(a), a point to which we will return shortly.

The strain-induced responses are shown in Figure 5.3(a). In sharp contrast to the differential longitudinal case, the magnitude of $\Delta R_{(xx)''}$ is actually observed to be slightly larger than $\Delta R_{(xy)''}$, although the down-weighted contribution $\Delta_\ell \Delta R_{(xx)''}$ is still a relatively small fraction of $\Delta R_{(xy)''}$ at all temperatures. Having subtracted out the longitudinal contamination $\Delta_\ell \Delta R_{(xx)''}$ from $\Delta R_{(xy)''}$, the temperature dependence of the transverse elastoresistive slopes as a function of anisotropic strain are shown in Figure 5.3(b). Because of the relative sign of R_{xy} to R_{xx} from the free-standing measurements, the sign of the elastoresistive slopes as a function of anisotropic strain is opposite to that from the differential longitudinal method, and an overall minus sign is needed to convert the slope to an elastoresistivity coefficient. The sign of the transverse elastoresistive slope and the crystal contact dimensions ($l \approx 0.957$ mm and $w \approx 0.63$ mm) are accounted for in Figure 5.4(a), which shows the temperature dependence of the estimated $2m_{xy,xy}$ elastoresistivity coefficient from

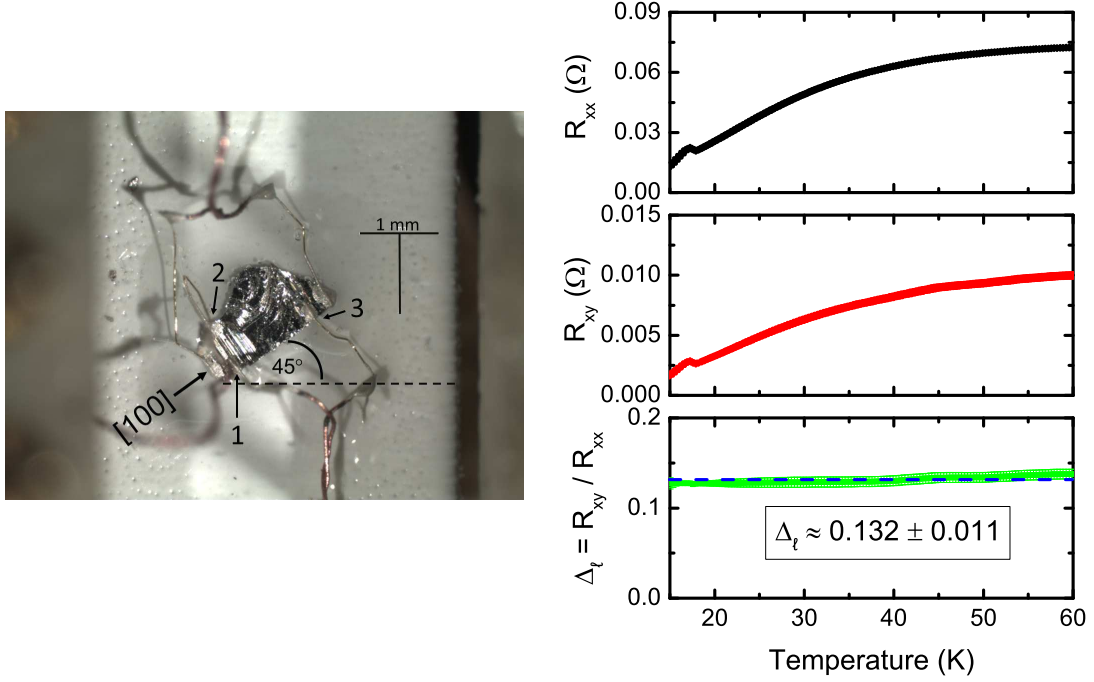


Figure 5.2: (a) Picture of a mounted sample for transverse elastoresistivity measurements. For the orientation of currents (along [100]) and strains (along [110]) relative to the crystallographic axes, the configuration shown admits measurement of the B_{2g} component of the elastoresistivity tensor. $(\Delta\rho/\rho)_{(xy)''}$ and $(\Delta\rho/\rho)_{(xx)''}$ are simultaneously measured, and the difference (with $(\Delta\rho/\rho)_{(xx)''}$ down-weighted by Δ_ℓ) is related to $2m_{xy,xy}$. (b) Measurement of R_{xy} and R_{xx} on the free-standing crystal (i.e., before mounting to a PZT) in order to extract $\Delta_\ell \equiv R_{xy}/R_{xx}$. $\Delta_\ell \approx 13\%$ is observed to be roughly temperature independent. RRR for this sample is ≈ 240 . As noted in the main text, this relatively low value of RRR is not ideal given the strong dependence of $2m_{xy,xy}$ on RRR (Section 5.1). A further nonideality is associated with the sample geometry, which deviates significantly from a perfect rectilinear shape, potentially affecting symmetry-based conclusions.

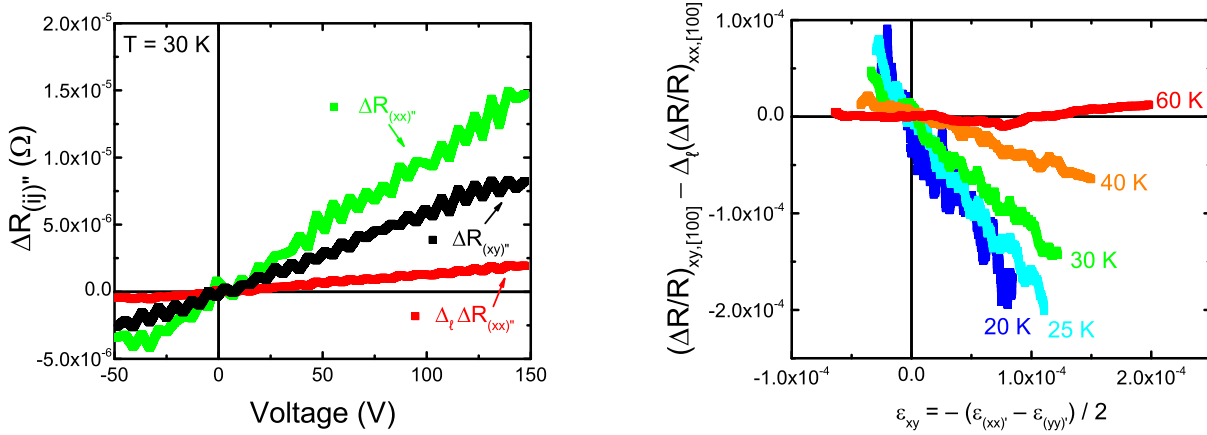


Figure 5.3: (a) Strain-induced resistance changes $\Delta R_{(xy)''}$, $\Delta R_{(xx)''}$, and $\Delta_{\ell} \Delta R_{(xx)''}$ as a function of voltage applied to the PZT. For the sample measured, $\Delta R_{(xx)''}$ is actually larger than $\Delta R_{(xy)''}$, although the down-weighted contribution $\Delta_{\ell} \Delta R_{(xx)''}$ is smaller than $\Delta R_{(xy)''}$. This contrasts sharply with the differential longitudinal measurements performed on a higher RRR sample. (b) Representative transverse elastoresistivity measurements of the down-weighted $(\Delta\rho/\rho)_{xy}$ versus strain for a sample of $\text{RRR} \approx 240$. These slopes are used to extract the elastoresistivity coefficient $2m_{xy,xy}$. All slopes are observed to be roughly linear in the anisotropic strain at all temperatures except for a very small temperature window of $\approx \pm 150$ mK around T_{HO} . Very close to the Hidden Order transition, the elastoresistive slope changes sign, evincing the anomaly in the nematic susceptibility which follows the heat capacity. The absolute magnitude of the elastoresistive slope is smaller than in the earlier differential longitudinal case, presumably due to the RRR effect.

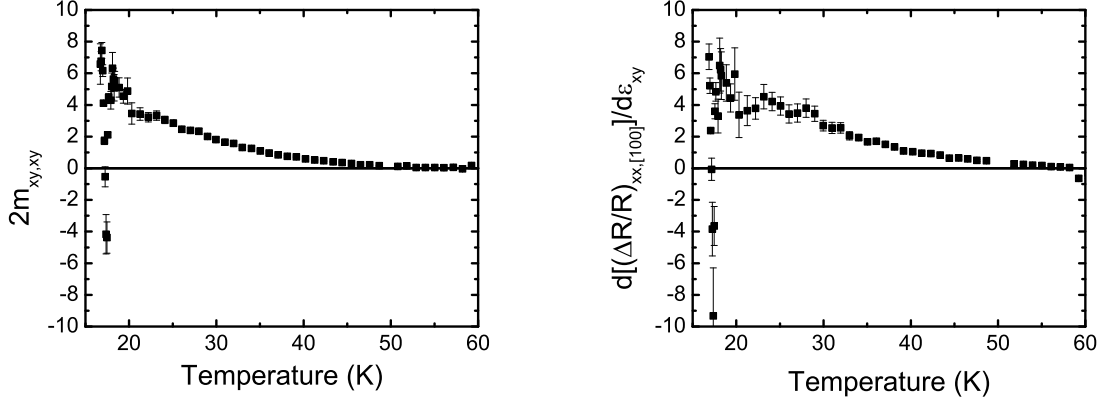


Figure 5.4: (a) Temperature dependence of $2m_{xy,xy}$ as extracted from the transverse method for the sample with RRR 240. The anomaly associated with Hidden Order at T_{HO} is evident, but the absolute magnitude of the elastoresistivity coefficient is comparable to the differential longitudinal case for samples with a similar RRR value (see Figure 5.1(b)). (b) Temperature dependence of $d(\Delta\rho/\rho)_{xx,[100]}/d\epsilon_{xy}$ in the transverse method. The qualitative behavior of $d(\Delta\rho/\rho)_{xx,[100]}/d\epsilon_{xy}$ follows nearly exactly with the estimated $2m_{xy,xy}$, with nearly the same values. This is in sharp contrast to the differential longitudinal measurements on higher RRR samples in which $2m_{xy,xy}$ was significantly larger than the isotropic contributions.

the transverse method. The magnitude of $2m_{xy,xy}$ is similar to that obtained from differential longitudinal elastoresistance measurements for samples with the same RRR (Figure 5.1(b)) but is clearly smaller than what is found for samples with higher RRR values, as described in Section 5.1. Both methods evince the same temperature dependence and downward anomaly which scales as the heat capacity. Because of the relative magnitude of $\Delta R_{(xx)''}$, we also show the temperature dependence of the response $d(\Delta\rho/\rho)_{xx,[100]}/d\epsilon_{xy}$ (Figure 5.4(b)). Induced by both anisotropic and isotropic strains, $d(\Delta\rho/\rho)_{xx,[100]}/d\epsilon_{xy}$ is observed to have the same temperature dependence and roughly the same value as the quoted $2m_{xy,xy}$, in sharp contrast to the differential longitudinal measurements on higher RRR samples in which $2m_{xy,xy}$ was observed to be significantly larger than the isotropic contributions.

The nonidealities of the specific sample used for this initial transverse measurement and the differences from the differential longitudinal method strongly motivate

repeating the transverse elastoresistivity measurements on higher RRR samples, in geometries probing both the B_{1g} and B_{2g} components of the elastoresistivity tensor, and for samples with a more ideal (i.e., better defined rectilinear) geometry. These preliminary transverse elastoresistivity measurements can be understood in a manner consistent with earlier differential longitudinal measurements in light of the RRR effect, but beyond this statement, it is difficult to draw firm conclusions. Though incomplete, these first transverse measurements are nevertheless included here as much to demonstrate that the technique can also be applied to URu₂Si₂. Additional experiments are needed to clarify the origin of the longitudinal response in this geometry.

5.3 Magnetic Field Dependence of Elastoresistivity in URu₂Si₂

Given the elastoresistivity formalism worked out in Chapters 2 and 3 (which explicitly accommodates the presence of a magnetic field by consideration of the Onsager relations), measurements in a general magnetic field environment can be performed via either the differential longitudinal or transverse elastoresistivity methods (from $(\Delta\rho/\rho)_{xx}(\mathbf{H}) - (\Delta\rho/\rho)_{yy}(\mathbf{H})$ or $(\Delta\rho/\rho)_{xy}(\mathbf{H}) + (\Delta\rho/\rho)_{xy}(-\mathbf{H})$, respectively, for appropriately oriented coordinate frames). This class of elastoresistivity measurements may be particularly elucidative for the subset of SCES for which an externally applied magnetic field functions as a tuning parameter that stabilizes different proximate ground states. For these materials, the magnetic field dependence of the elastoresistance can directly probe the quantum critical regime, potentially offering insights into the physics of any associated quantum phase transitions. As discussed in Section 1.4, URu₂Si₂ is an example of such a SCES, as Hidden Order can be suppressed to zero temperature by application of a c -axis oriented magnetic field (Figure 1.3(c)). The magnetic field dependence of Hidden Order can be seen, for example, in the specific heat [19]—whereas the onset of Hidden Order is associated with a second-order-like heat capacity anomaly in zero field, the anomaly evolves on application of an increasing magnetic field into a sharp first-order-like feature (Figure 5.5). The heat

5.3. MAGNETIC FIELD DEPENDENCE OF ELASTORESISTIVITY IN URu_2Si_2

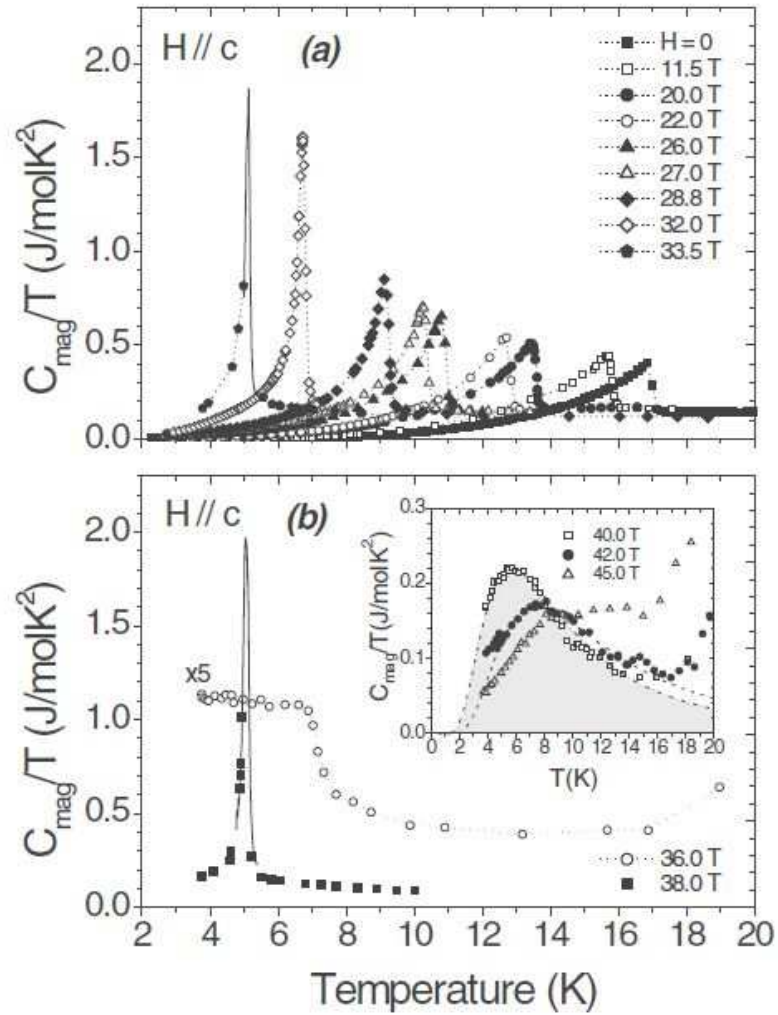


Figure 5.5: Reproduced from Jaime *et al.* [19]. The zero field heat capacity jump in URu_2Si_2 is reminiscent of a mean field second order phase transition. On increasing the magnetic field, the heat capacity anomaly evolves into a sharp first-order-like feature and also shifts downward towards zero temperature. Both of these behaviors are qualitatively followed in the elastoresistance.

capacity anomaly also shifts down in temperature, being fully suppressed at a field of ≈ 35.1 T.

Experiments probing the magnetic field dependence of the differential elastoresistance of URu₂Si₂ were performed at the National High Magnetic Field Laboratory (DC Field Facility) in Tallahassee. The same sample was used as for the differential longitudinal measurements in zero field [57]; however, the data presented here should be considered preliminary, as the sample fractured on preparation for the high field measurements and the RRR of the sample was reduced (after the experiment the RRR was checked and found to be 168, considerably lower than the initial value of 970 before the sample was damaged). Measurements were done in Cell 9 (31 T resistive magnet), Cell 12 (35 T resistive magnet), and in the Hybrid Cell (45 T hybrid resistive and superconducting magnet) in liquid ⁴He refrigerators. Initial experiments were only performed in geometries characterizing the $2m_{xy,xy}$ elastoresistivity coefficient (see Figure 5.6(a) for a picture of as-mounted samples). Elastoresistance data at a fixed temperature and field were acquired from changes in the resistances of the samples and strain gauges while sweeping the voltage applied to the PZT between -50 V and $+150$ V. The voltage was swept stepwise in 4 V increments with a delay of 0.25 s between steps. Three full voltage loops were taken for each temperature setpoint; after completing these loops, the temperature and/or field was then stepped to a new setpoint and allowed to stabilize before performing the next elastoresistance measurement. The resistances of the samples and strain gauges were measured using Stanford Research Systems SR830 lock-in amplifiers; for the samples, Stanford Research Systems Model SR560 preamplifiers were also used. AC excitation currents of 1 mA and 0.1 mA were used for the samples and strain gauges, respectively.

The temperature dependence of the differential elastoresistance at different magnetic fields is extracted from the slopes of the normalized changes in resistance to strain. Representative data for $H = 20$ T are shown in Figure 5.6(b). All slopes are observed to be linear in the anisotropic strain at all temperatures and fields except for a very small temperature window ($\approx \pm 150$ mK) around T_{HO} , as was the case for the zero field measurements (see Figure 4.9). The elastoresistive slopes increase in magnitude with decreasing temperature until just above T_{HO} , where they then abruptly

5.3. MAGNETIC FIELD DEPENDENCE OF ELASTORESISTIVITY IN URu_2Si_2

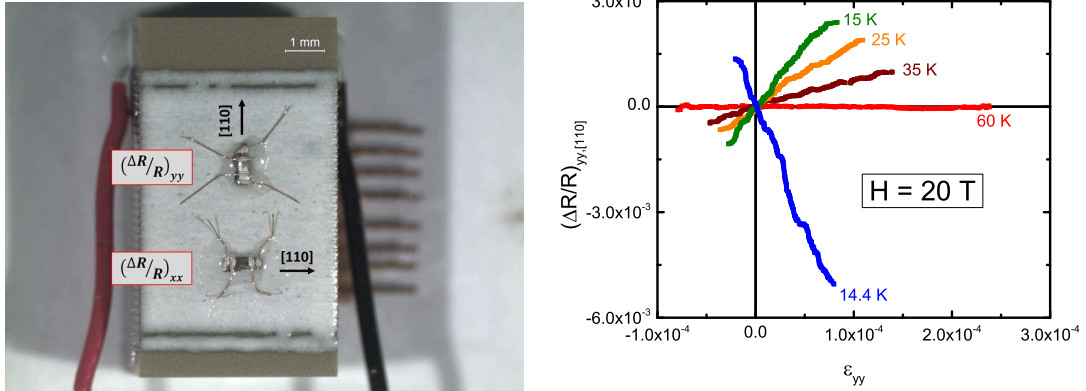


Figure 5.6: (a) Picture of mounted samples for differential longitudinal elastoresistivity measurements in a high magnetic field. For the orientation of currents (along $[110]$) and strains (along $[100]$) relative to the crystallographic axes, the configuration shown admits measurement of the B_{2g} component of the elastoresistivity tensor. The top sample corresponds to measurements of $(\Delta\rho/\rho)_{yy,[110]}$, the bottom sample corresponds to measurements of $(\Delta\rho/\rho)_{xx,[110]}$, and the difference is related to $2m_{xy,xy}$. (b) Representative measurements of $(\Delta\rho/\rho)_{yy,[110]}$ versus strain at a magnetic field of $H = 20$ T directed along the crystallographic c -axis. These slopes (and similar ones from measurements of $(\Delta\rho/\rho)_{xx,[110]}$) are used to extract the elastoresistivity coefficient $2m_{xy,xy}(H_z = 20$ T). In agreement with the zero field measurements, all slopes are observed to be linear in the anisotropic strain at all temperatures except for a very small temperature window around T_{HO} . Very close to the Hidden Order transition (which is ≈ 17.5 K in zero field but shifts down in an applied magnetic field), the elastoresistive slope changes sign, evincing the anomaly in the nematic susceptibility which follows the temperature dependence of the heat capacity.

change sign, similar to the behavior seen in zero field (see Figures 4.2 and 4.3).

The temperature dependence of the differential elastoresistance at different magnetic fields is presented in Figure 5.7 and displays two prominent trends. First, a pronounced downward feature is observed at the Hidden Order transition temperature T_{HO} . The qualitative behavior of this downward feature accords with the field dependence of the specific heat anomaly, as both become narrower, taller, and shift to lower temperatures in increasing field. This lends credence to our original model of Hidden Order derived from a Landau theory of a vector order parameter, which predicts such an anomaly in the nematic susceptibility which follows the heat capacity close to T_{HO} if the vector order parameter has nematic fluctuations. Second, there is a large susceptibility for an extended regime above T_{HO} which persists even as the phase transition goes from second to first order. Notably, the onset temperature of a resolvable elastoresistive response shifts downwards with increasing field. The differential elastoresistance also more slowly onsets with increasing field, consistent with a fluctuational regime being suppressed as the transition becomes more first-order-like.

The elastoresistance also diverges at fixed temperature while sweeping towards the critical magnetic field in the Hidden Order state (Figure 5.7(d)). Both $d(\Delta\rho/\rho)_{yy,[110]}/d\epsilon_{yy}$ and $d(\Delta\rho/\rho)_{xx,[110]}/d\epsilon_{yy}$ are large and opposite in sign for $H < H_c$, and they both oppositely diverge at the critical field. Data for fields $H > H_c$ suffer from a poorer signal-to-noise due to the large negative magnetoresistance of URu₂Si₂ in this regime [107], and so it is difficult to make firm statements about the elastoresistive response in this field range. However, the divergence of the elastoresistance for $H < H_c$ is clear and demonstrates that the nematic susceptibility diverges on tuning through the Hidden Order phase boundary with magnetic field from below H_c .

5.3. MAGNETIC FIELD DEPENDENCE OF ELASTORESISTIVITY IN URu_2Si_2 159

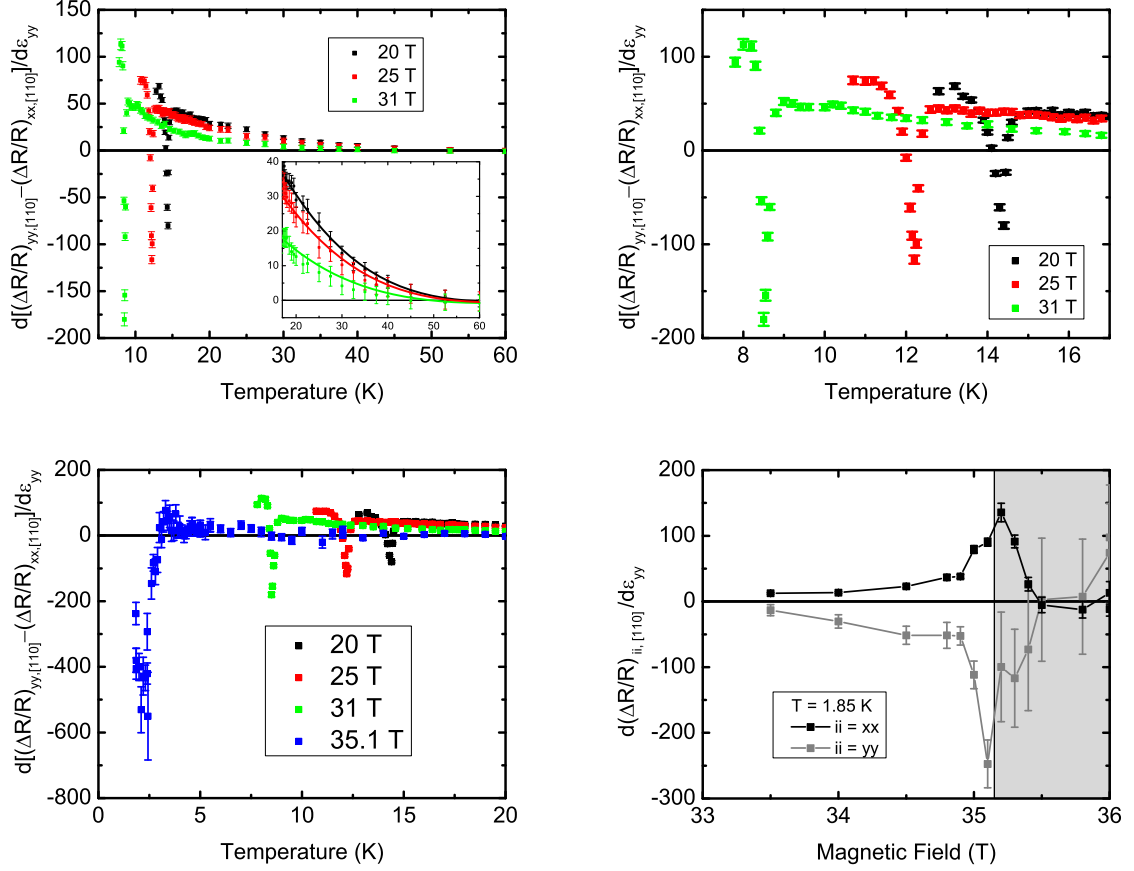


Figure 5.7: (a) (Top Left) Differential elastoresistance measurements for a range of fields approaching the critical magnetic field of ≈ 35.1 T at which Hidden Order is suppressed. The measurements are proportional to the elastoresistivity coefficient $2m_{xy,xy}$, although the data need to be normalized by $(1 + \nu_p)$ (where ν_p is the Poisson ratio of the PZT) to obtain the exact elastoresistivity coefficient. Both the onset of a resolvable elastoresistive response and the heat capacity anomaly shift downwards in temperature with increasing field. (b) (Top Right) Expanded view of (a) at low temperatures. The differential elastoresistance tracks the field dependence of Hidden Order; furthermore, the height of the anomaly increases with increasing field and the width of the anomaly decreases with increasing field. These observations are consistent with the field dependence of the heat capacity. (c) (Bottom Left) A version of (a) but also including data taken at the critical magnetic field. A large response is observed, but the heat capacity anomaly is harder to resolve because of the sharp first-order nature of the transition and the large negative magnetoresistance of URu_2Si_2 near this field. (d) (Bottom Right) Differential elastoresistance at a base temperature of 1.85 K as a function of magnetic field. The elastoresistance diverges on approaching the critical magnetic field from below, but the signal-to-noise becomes limiting on the high magnetic field side due to the large negative magnetoresistance.

Chapter 6

Concluding Remarks and Future Outlook

The utility of elastoresistivity as a valuable experimental tool for identifying subtle forms of broken symmetry was introduced and discussed in this thesis, particularly as it relates to strongly correlated electron systems (SCES), where strong electronic and magnetic interactions can give rise to novel phase transitions. The symmetry properties of the elastoresistivity tensor were presented, including the first discussion in the context of non-cubic systems and in the presence of a magnetic field. This formalism also motivated a new class of transverse elastoresistivity measurements, first proposed and experimentally demonstrated in this thesis and which possess several experimental advantages. Additionally, elastoresistivity measurements were performed on the specific SCES URu_2Si_2 , providing evidence that the Hidden Order parameter breaks the fourfold rotational symmetry of the high temperature tetragonal state (in addition to other symmetries). Preliminary measurements of the magnetic field and RRR dependence of the elastoresistivity of URu_2Si_2 were also presented.

In this final chapter, I review the current status both of elastoresistivity measurements and of the state of understanding of Hidden Order in URu_2Si_2 at the conclusion of my thesis work. Regarding the elastoresistivity technique, I discuss the specific advancements undertaken in this thesis, highlight several remaining sources of systematic error from our specific implementation, and outline potential future directions.

Regarding Hidden Order, I summarize and critique the evidence of fourfold rotational symmetry breaking gathered from both elastoresistivity and other measurements, address open questions about time-reversal symmetry and the existence of an ordered magnetic dipole moment, and offer a perspective about which microscopic theories are consistent with the experimental evidence.

6.1 Elastoresistivity Technique: Current Status

In this thesis, the symmetry properties of the elastoresistivity tensor were presented, including the first discussion in the context of non-cubic systems and in the presence of a magnetic field. The various irreducible components of the elastoresistivity tensor can be connected to order parameters of corresponding symmetry within the Landau paradigm for continuous phase transitions, allowing elastoresistivity to identify the subtle forms of broken symmetry that can arise within the context of SCES. The presentation given here paid particular attention to electronic nematic order, a particular type of electronically-driven anisotropic state that has recently attracted attention in the context of SCES.

The formal treatment of the elastoresistivity tensor also motivated a new class of transverse elastoresistivity measurements, first proposed and experimentally demonstrated in this thesis. The transverse method possesses several experimental advantages over the earlier differential longitudinal scheme, as discussed in Sections 3.3.2 and 3.4.2. These advantages are directed towards a particular category of systematic error which mixes responses from different symmetry channels, examples of which include angular misalignment of the current or strain relative to the crystal axes or unequal strain experienced by two samples used in a differential measurement. Both of these examples not only result in errors in the magnitude of the extracted elastoresistivity coefficients but can also complicate symmetry-based conclusions relating to an associated order parameter. A principal advantage of the transverse method is that it enables a direct measurement of the induced resistivity anisotropy from a single measurement and therefore eschews unequal strain errors (a primary source of symmetry-admixing error).

While we have presented an appropriate formalism to describe the elastoresistivity tensor, and while we have outlined general approaches that can be used to measure the B_{1g} and B_{2g} components of this tensor, there remains further opportunity to improve the specific realization of the experiment. In particular, as discussed in Sections 3.3.2 and 3.4.2, there are several sources of systematic error related to our specific implementation which affect the magnitude of the measured elastoresistivity coefficients and which could, at least in principle, be improved by refinements to the technique. Among these include quantifying strain transmission, reducing strain inhomogeneity, and eliminating bias strain due to (a) differential thermal contraction of the sample and PZT substrate and (b) possible uncontrolled strains arising from the epoxy used to adhere the crystal to the PZT surface. Modified techniques can be readily envisaged that further reduce these sources of systematic error; moreover, numerical modeling of these effects may also prove insightful in terms of quantifying their relative magnitudes and guiding future efforts to minimize each error source.

6.2 Hidden Order in URu₂Si₂: Current Status

6.2.1 Hidden Order and Fourfold Rotational Symmetry

Previous Evidence for Broken Fourfold Rotational Symmetry

Evidence for broken fourfold rotational symmetry in the Hidden Order state of URu₂Si₂ was introduced in Section 1.4.3. To remind readers, this evidence includes:

- X-ray Diffraction

The temperature dependence of the [880] Bragg peak splits on cooling through T_{HO} , directly resolving a small (of the order of 10^{-5}), B_{2g} type orthorhombic distortion that can only be resolved for the highest RRR samples [21]. The fact that lower quality URu₂Si₂ samples suffer from small parasitic dipole moments along the tetragonal c -axis provides compelling evidence that disorder affects the Hidden Order ground state, perhaps providing an intuition for the observed RRR dependence. Since the publication of the high-resolution X-ray results,

this conclusion has been challenged by Amitsuka *et al.* [54]. The temperature dependence of the peak splitting observed by Tonegawa *et al.* [21] is, however, extremely compelling evidence for an orthorhombic distortion that onsets precisely at the critical temperature at which Hidden Order onsets. It is difficult to conceive of any argument that would cause such peak splitting based, for example, on crystal mosaicity that would onset precisely at T_{HO} without also invoking an onset of orthorhombicity.

- Magnetic Torque

Okazaki *et al.* [52] observe the onset of twofold oscillations in the Hidden Order state in the magnetic torque. This result is indicative of fourfold rotational symmetry breaking; however, it is only observed in the smallest samples measured by volume. One explanation of this effect involves the formation of domains (estimated to be of order $10 \mu\text{m}$), with approximately half of the domains oriented along the $[110]$ crystallographic direction and the other half along $[1\bar{1}0]$, thereby canceling in all but the smallest crystals. Another possible explanation is that these smaller samples had fewer domains or smaller internal stresses; if those domains or internal stresses are also the dominant effect in determining RRR (as opposed to, for example, impurity scattering), the magnetic torque may be tracking a RRR effect.

- Cyclotron Resonance

Tonegawa *et al.* [42, 43] observe in-plane cyclotron mass anisotropy from cyclotron resonance measurements. The angle dependence of the cyclotron mass for the three main Fermi surface sheets can be determined from quantum oscillations on samples with a long mean free path. The Fermi surface shapes largely correspond to those obtained from band structure calculations in the pressure-stabilized antiferromagnetic state, which display a nearly isotropic angular dependence; however, the frequency dependence of the α hole pocket (the largest pocket, centered around the Γ point) shows an anomalous splitting near the $[110]$ direction, explicitly breaking the tetragonal symmetry.

- Nuclear Magnetic Resonance

Kambe *et al.* [53] measure the angular dependence of the ^{29}Si NMR line width under an in-plane field rotation. From the line width, they infer a cusp in the angular dependence of the Knight shift. This cusp can be explained by line broadening associated with a superposition of two sinusoidal curves (having twofold symmetry) arising from nematic domains aligned along the $[110]$ and $[\bar{1}\bar{1}0]$ directions.

Evidence for Broken Fourfold Rotational Symmetry from Elastoresistivity Measurements

In this thesis (and concurrent with publication of the X-ray measurements described above), we have performed a series of elastoresistivity measurements that indicate that fluctuations of the Hidden Order state have a nematic character, and hence that Hidden Order breaks fourfold rotational symmetry. The primary evidence that implies this conclusion is that the $2m_{xy,xy}$ elastoresistivity coefficient grows monotonically as temperature is lowered, first following a Curie-Wiess temperature dependence but then subsequently exhibiting deviations as the temperature approaches T_{HO} from above. The observation of an additional anomaly in the elastoresistance close to T_{HO} that appears to follow the same temperature dependence as the heat capacity provides compelling evidence that Hidden Order must, however, break other symmetries. We have presented an argument based on a Ginzburg-Landau treatment of coupled order parameters that anticipates exactly this temperature dependence if Hidden Order breaks C_4 and additional symmetries (see Sections 4.3 and 4.A).

Critique of Experiments Revealing Broken Fourfold Rotational Symmetry

Based on the experimental results discussed above, the weight of evidence points towards the Hidden Order state being characterized by the absence of fourfold rotational symmetry (among other broken symmetries), but with a remarkable sensitivity to disorder. The small degree of orthorhombicity, combined with the apparent sensitivity to disorder, have, however, led to lingering doubts, and it is perhaps useful to

reflect on some of these concerns, which include:

- Elastic Moduli

If the picture of fourfold symmetry breaking is correct, a big open question remains about the behavior of the elastic constants [108], which show softening in the B_{1g} elastic mode and a hardening (with a slight change in slope at Hidden Order) in all other modes. Although in principle weak coupling between a nematic order parameter and the crystal lattice (consistent with the small magnitude of the orthorhombic distortion observed in X-ray diffraction experiments) would limit any appreciable renormalization of the elastic modes consistent with the nematicity, the work of this thesis (along with other measurements) motivates a careful reinvestigation of the elastic properties of URu₂Si₂ for samples of a comparably high RRR.

- A_{1g} Elastoresistivity Coefficients

It would be very difficult to understand the current elastoresistivity data as arising from A_{1g} “contamination” (i.e., an artifact of isotropic strain). In the context of the differential longitudinal elastoresistivity measurements presented in this thesis on high RRR samples, the A_{1g} elastoresistive response would have to have been the dominant effect to the applied strain, which is at odds with the empirical observation that $(\Delta\rho/\rho)_{xx,[110]} - (\Delta\rho/\rho)_{yy,[110]} \gg (\Delta\rho/\rho)_{xx,[110]} + (\Delta\rho/\rho)_{yy,[110]}$. Nevertheless, differential A_{1g} strain is a source of systematic error in the present realization of the differential longitudinal method (in fact, it was a principal motivation for proposing the transverse elastoresistivity method), and future transverse elastoresistivity experiments on higher RRR samples would help adjudicate whether such A_{1g} contamination is indeed negligible. Such transverse elastoresistivity experiments would ideally be performed on rectilinear bars of the same high RRR value in both the B_{1g} and B_{2g} configurations, the comparison of which (if performed on crystals with identical RRR values) would unambiguously reveal the A_{1g} temperature dependence. While this was a goal of this research, we were not able to find appropriate candidate samples that meet the required criteria on the time scale of this thesis, despite

screening dozens of samples. The initial, preliminary transverse elastoresistivity measurements (Section 5.2) are difficult to interpret due to the low RRR and nonideal geometry of the sample measured; however, the data are suggestive, revealing a similar temperature dependence for the B_{2g} channel but also some response in the putative A_{1g} channel. These measurements need to be checked using better shaped, high quality crystals.

- Raman Spectroscopy

Buhot *et al.* [109] and Kung *et al.* [110] both measure signatures associated with Hidden Order from Raman spectroscopy which they assign to an A_{2g} symmetry. While Kung *et al.* do not quote the specific RRR value of the sample they measure, the data they present is in agreement with the data acquired by Buhot *et al.* on a sample of RRR 50, which has been shown to be too small to resolve fourfold rotational symmetry breaking. In order to observe an A_{2g} -like Raman response (which is a $\vec{Q} = 0$ probe), there must be a coupling in the free energy which links the A_{2g} observable ($\equiv \phi_{A_{2g}}(\vec{Q} = 0)$) to the Hidden Order parameter ($\equiv \Delta(\vec{Q}_C)$, since Hidden Order is a finite \vec{Q}_C order). To preserve translation symmetry, the leading coupling term in the free energy would then be of the form $\phi_{A_{2g}}|\Delta|^2$, and, if such a term is also to be invariant under the point group symmetry operations in D_{4h} , $\Delta(\vec{Q}_C)$ must belong to a multi-dimensional irreducible representation of D_{4h} (since the square of all one-dimensional irreps behaves trivially under the point group and hence cannot solely couple to an A_{2g} quantity). Finally, we note that certain classes of E_g order break the vertical and diagonal mirrors to which Raman is sensitive, and hence the assignment of Hidden Order uniquely to an A_{2g} symmetry from these measurements might not be justified.

6.2.2 Hidden Order and Time-Reversal Symmetry

Important questions regarding the time-reversal character of Hidden Order also still remain. By symmetry, a unidirectional Hidden Order state belonging to the E_g irreducible representation that breaks time-reversal symmetry should presumably lead,

as a secondary effect, to a finite ordered magnetic dipole moment in that direction. Such an in-plane dipole moment has not yet been detected from neutron scattering on lower RRR samples, although the lower bound from such experiments is slightly above the predicted moment from a time-reversal symmetry breaking dotriacontapolar picture. Such a small in-plane dipole moment may have been detected by NMR [25] and μ SR [32], although there is no consensus yet in the community. This small in-plane moment is to be distinguished from the parasitic out-of-plane moment directed along the c -axis, which seems to be extrinsic to Hidden Order [27].

6.2.3 Final Conclusions

As described above in Section 6.2.1, the measurements presented in this thesis support recent conclusions that fourfold rotational symmetry is broken in the Hidden Order state of URu_2Si_2 . While the small magnitude of the resulting orthorhombicity, combined with a manifest dependence on sample quality, led to lingering discussion as to whether Hidden Order breaks fourfold symmetry, the weight of evidence now appears to point more convincingly towards this conclusion. As stressed in the work presented in this thesis, the favored interpretation regarding Hidden Order is that the associated order parameter belongs to a multicomponent vector with a nematic component. Elastoresistivity alone is agnostic to which of the two-dimensional (E_g or E_u) irreducible representations of D_{4h} Hidden Order belongs, although E_g is preferred given that non-centrosymmetry has not been reported in the literature.

Combined with evidence for antiferro order with ordering wave vector $\vec{Q}_C = (001)$ (Section 1.4.2), Hidden Order is characterized by an $E_g(\vec{Q}_C)$ order parameter of the high temperature $I4/mmm$ space group. The ordering of this order parameter then reduces the crystallographic (magnetic) space group $I4/mmm$ ($I4/mmm1'$) to either $Cmce$ ($Cmce1'$) or $Fmmm$ (C_{Amce}), depending on whether Hidden Order preserves or breaks time-reversal symmetry. Elastoresistivity alone is also agnostic to the time-reversal character of Hidden Order. If Hidden Order is an $E_g(\vec{Q}_C)$ order that breaks time-reversal symmetry, one anticipates on the basis of symmetry a secondary in-plane magnetic dipole moment, about which there is not yet consensus in the community

(Section 1.4.1).

Which microscopic models are these observations consistent with? One such microscopic model is the dotriacontapolar (rank 5) picture advanced by Ikeda *et al.* [34]. Based on DFT calculations (obtained by tight-binding from 56 orbitals, with spin-orbit coupling, and analyzed beyond the random phase approximation), their calculations indicate that the dominant multipole correlations are associated with magnetic dotriacontapolar order (E_g character that breaks time-reversal symmetry) and static magnetic dipolar order (A_{2g} character that breaks time-reversal symmetry). The dotriacontapolar and dipolar correlations are apparently very nearly degenerate; their relative energies can be tuned with hydrostatic pressure, consistent with the measured $T - P$ phase diagram (Figure 1.3(c)). In this picture, the high rank order is realized due to a strong nesting tendency by \vec{Q}_C , which connects portions of the Fermi surface of angular momentum $j_z = \pm 5/2$ character. In a pseudospin subspace consisting of only the $|j_z = +5/2\rangle \equiv |\uparrow\rangle$ and $|j_z = -5/2\rangle \equiv |\downarrow\rangle$, transitions between $|\uparrow\rangle$ and $|\downarrow\rangle$ accompany a change in angular momentum $\Delta j_z = 5$ allowed only at rank 5. The difficulty in directly detecting a high-rank multipolar order is offered as an explanation for why the nature of Hidden Order has been so elusive. In this context, the significance of the results described in this thesis lies in identifying just one of the symmetries that is broken (of several) in the Hidden Order state.

Bibliography

- [1] P. M. Chaikin and T. C. Lubensky, *Principles of Condensed Matter Physics* (Cambridge University Press, Cambridge, UK 1995).
- [2] P. W. Anderson, *Basic Notions of Condensed Matter Physics* (Benjamin/Cummings Publishing Company, Menlo Park, California, USA 1984).
- [3] J. M. Yeomans, *Statistical Mechanics of Phase Transitions* (Oxford University Press, Oxford, UK 1992).
- [4] Yoichi Ando, Kouji Segawa, Seiki Komiya, and A. N. Lavrov, *Phys. Rev. Lett.* **88**, 137005 (2002).
- [5] V. Hinkov, D. Haug, B. Fauqué, P. Bourges, Y. Sidis, A. Ivanov, C. Bernhard, C. T. Lin, B. Keimer, *Science* **319**, 597 (2008).
- [6] I. R. Fisher, L. Degiorgi, and Z. X. Shen, *Rep. Prog. Phys.* **74**, 124506 (2011).
- [7] M. A. Tanatar, E. C. Blomberg, A. Kreyssig, M. G. Kim, N. Ni, A. Thaler, S. L. Bud'ko, P. C. Canfield, A. I. Goldman, I. I. Mazin, and R. Prozorov, *Phys. Rev. B* **81**, 184508 (2010).
- [8] J.-H. Chu , J. G. Analytis, K. De Greve, P. L. McMahon, Z. Islam, Y. Yamamoto, and I. R. Fisher, *Science* **329**, 824 (2010).
- [9] R. Prozorov, M. A. Tanatar, N. Ni, A. Kreyssig, S. Nandi, S. L. Budko, A. I. Goldman, and P. C. Canfield, *Phys. Rev. B* **80**, 174517 (2009).

- [10] Eduardo Fradkin, Steven A. Kivelson, Michael J. Lawler, James P. Eisenstein, and Andrew P. Mackenzie, *Annu. Rev. Condens. Matter Phys.* **1**, 153 (2010).
- [11] T. T. M. Palstra, A. A. Menovsky, J. van den Berg, A. J. Dirkmaat, P. H. Kes, G. J. Nieuwenhuys, and J.A. Mydosh, *Phys. Rev. Lett.* **55**, 2727 (1985).
- [12] M. B. Maple, J. W. Chen, Y. Dalichaouch, T. Kohara, C. Rosset, M. S. Torikachvili, M. W. McElfresh, and J.D. Thompson, *Phys. Rev. Lett.* **56**, 185 (1986).
- [13] W. J. Schlabitz, W. J. Baumann, R. Pollit, U. Rauchschwalbe, H. M. Mayer, U. Ahlheim, and C. D. Bredl, *Z. Phys. B* **62**, 171 (1986).
- [14] J. A. Mydosh and P. M. Oppeneer, *Rev. Mod. Phys.* **83**, 1301 (2011).
- [15] G. Motoyama, T. Nishioka, and N. K. Sato, *Phys. Rev. Lett.* **90**, 166402 (2003).
- [16] G. Motoyama, N. Yokoyama, A. Sumiyama, and Y. Oda, *J. Phys. Soc. Jpn.* **77**, 123710 (2008).
- [17] E. Hassinger, G. Knebel, K. Izawa, P. Lejay, B. Salce, and J. Flouquet, *Phys. Rev. B* **77**, 115117 (2008).
- [18] P. G. Niklowitz, C. Pfleiderer, T. Keller, M. Vojta, Y.-K. Huang, and J. A. Mydosh, *Phys. Rev. Lett.* **104**, 106406 (2010).
- [19] M. Jaime, K. H. Kim, G. Jorge, S. McCall, and J. A. Mydosh, *Phys. Rev. Lett.* **89**, 287201 (2002).
- [20] J. S. Kim, D. Hall, P. Kumar, and G. R. Stewart, *Phys. Rev. B* **67**, 014404 (2003).
- [21] S. Tonegawa, S. Kasahara, T. Fukuda, K. Sugimoto, N. Yasuda, Y. Tsuruhara, D. Watanabe, Y. Mizukami, Y. Haga, T. D. Matsuda, E. Yamamoto, Y. Onuki, H. Ikeda, Y. Matsuda, and T. Shibauchi, *Nature Comm.* **5**, 4188 (2014).

- [22] Y. Kasahara, H. Shishido, T. Shibauchi, Y. Haga, T. D. Matsuda, Y. Onuki, and Y. Matsuda, *New J. Phys.* **11**, 055061 (2009).
- [23] C. Broholm, J. K. Kjems, W. J. L. Buyers, P. Matthews, T. T. M. Palstra, A. A. Menovsky, and J. A. Mydosh, *Phys. Rev. Lett.* **58**, 1467 (1987).
- [24] K. Matsuda, Y. Kohori, T. Kohara, K. Kuwahara, and H. Amitsuka, *Phys. Rev. Lett.* **87**, 087203 (2001).
- [25] S. Takagi, S. Ishihara, S. Saitoh, H. Sasaki, H. Tanida, M. Yokoyama, and H. Amitsuka, *J. Phys. Soc. Jpn.* **76**, 033708 (2007).
- [26] H. Amitsuka, K. Matsuda, I. Kawasaki, K. Tenya, M. Yokoyama, C. Sekine, N. Tateiwa, T. C. Kbayashi, S. Kawarazaki, and H. Yoshizawa, *J. Magn. Magn. Mater.* **310**, 214 (2007).
- [27] Takasada Shibauchi, Hiroaki Ikeda, and Yuji Matsuda, *Phil. Mag.* **94**, 3747 (2014).
- [28] P. Das, R. E. Baumbach, K. Huang, M. B. Maple, Y. Zhao, J. S. Helton, J. W. Lynn, E. D. Bauer, and M. Janoschek, *New J. Phys.* **15**, 053031 (2013).
- [29] K. A. Ross, L. Harriger, Z. Yamani, W. J. L. Buyers, J. D. Garrett, A. A. Menovsky, J. A. Mydosh, and C. L. Broholm, *Phys. Rev. B* **89**, 155122 (2014).
- [30] Aharon Kapitulnik, Jing Xia, Elizabeth Schemm, and Alexander Palevski, *New J. Phys.* **11**, 055060 (2009).
- [31] E. R. Schemm, R. E. Baumbach, P. H. Tobash, F. Ronning, E. D. Bauer, and A. Kapitulnik, *Phys. Rev. B* **91**, 140506(R) (2015).
- [32] Ikuto Kawasaki, Isao Watanabe, Adrian Hillier, and Dai Aoki, *J. Phys. Soc. Jpn.* **83**, 094720 (2014).
- [33] K. Haule and G. Kotliar, *Nature Phys.* **5**, 796 (2009).

- [34] H. Ikeda, M.-T. Suzuki, R. Arita, T. Takimoto, T. Shibauchi, and Y. Matsuda, *Nature Phys.* **8**, 528 (2012).
- [35] P. Chandra, P. Coleman, and R. Flint, *Nature* **493**, 621 (2013).
- [36] J. A. Mydosh and P. M. Oppeneer, *Phil. Mag.* **94**, 3642 (2014).
- [37] T. T. M. Palstra, A. A. Menovsky, and J. A. Mydosh, *Phys. Rev. B* **33**, 6527(R) (1986).
- [38] M. W. McElfresh, J. D. Thompson, J. O. Willis, M. B. Maple, T. Kohara, and M. S. Torikachvili, *Phys. Rev. B* **35**, 43 (1987).
- [39] J. Schoenes, C. Schönenberger, J. J. M. Franse, and A. A. Menovsky, *Phys. Rev. B* **35**, 5375 (1987).
- [40] C. R. Wiebe, J. A. Janik, G. J. MacDougall, G. M. Luke, J. D. Garrett, H. D. Zhou, Y.-J. Jo, L. Balicas, Y. Qiu, J. R. D. Copley, Z. Yamani, and W. J. L. Buyers, *Nature Phys.* **3**, 96 (2007).
- [41] J. A. Janik, H. D. Zhou, Y.-J. Jo, L. Balicas, G. J. MacDougall, G. M. Luke, J. D. Garrett, K. J. McClellan, E. D. Bauer, J. L. Sarrao, Y. Qiu, J. R. D. Copley, Z. Yamani, W. J. L. Buyers, and C. R. Wiebe, *J. Phys. Condens. Matter* **21**, 192202 (2009).
- [42] S. Tonegawa, K. Hashimoto, K. Ikada, Y.-H. Lin, H. Shishido, Y. Haga, T.D. Matsuda, E. Yamamoto, Y. Onuki, H. Ikeda, Y. Matsuda, and T. Shibauchi, *Phys. Rev. Lett.* **109**, 036401 (2012).
- [43] S. Tonegawa, K. Hashimoto, K. Ikada, Y.-H. Lin, H. Shishido, Y. Haga, T.D. Matsuda, E. Yamamoto, Y. Onuki, H. Ikeda, Y. Matsuda, and T. Shibauchi, *Phys. Rev. B* **88**, 245131 (2013).
- [44] A. F. Santander-Syro, M. Klein, F. L. Boariu, A. Nuber, P. Lejay, and F. Reinert, *Nature Phys.* **5**, 637 (2009).

- [45] R. Yoshida, Y. Nakamura, M. Fukui, Y. Haga, E. Yamamoto, Y. Ōnuki, M. Okawa, S. Shin, M. Hirai, Y. Muraoka, and T. Yokoya, *Phys. Rev. B* **82**, 205108 (2010).
- [46] F. L. Boariu, C. Bareille, H. Schwab, A. Nuber, P. Lejay, T. Durakiewicz, F. Reinert, and A. F. Santander-Syro, *Phys. Rev. Lett.* **110**, 156404 (2013).
- [47] J.-Q. Meng, P. M. Oppeneer, J. A. Mydosh, P. S. Riseborough, K. Gofryk, J. J. Joyce, E. D. Bauer, Y. Li, and T. Durakiewicz, *Phys. Rev. Lett.* **111**, 127002 (2013).
- [48] E. Hassinger, G. Knebel, T. D. Matsuda, D. Aoki, V. Taufour, and J. Flouquet, *Phys. Rev. Lett.* **105**, 216409 (2010).
- [49] M. M. Altarawneh, N. Harrison, G. Li, L. Balicas, P. H. Tobash, F. Ronning, and E. D. Bauer, *Phys. Rev. Lett.* **108**, 066407 (2012).
- [50] N. Harrison, P. J. W. Moll, S. E. Sebastian, L. Balicas, M. M. Altarawneh, J.-X. Zhu, P. H. Tobash, F. Ronning, E. D. Bauer, and B. Batlogg, *Phys. Rev. B* **88**, 241108(R) (2013).
- [51] Michi-To Suzuki and Hiroaki Ikeda, *Phys. Rev. B* **90**, 184407 (2014).
- [52] R. Okazaki, T. Shibauchi, H. J. Shi, Y. Haga, T. D. Matsuda, E. Yamamoto, Y. Onuki, H. Ikeda, and Y. Matsuda, *Science* **331**, 439 (2011).
- [53] S. Kambe, Y. Tokunaga, H. Sakai, T. D. Matsuda, Y. Haga, Z. Fisk, and R. E. Walstedt, *Phys. Rev. Lett.* **110**, 246406 (2013).
- [54] Hiroshi Amitsuka, Evidence for preservation of crystallographic four-fold rotational symmetry in hidden order of URu₂Si₂ [abstract]. In: APS March Meeting; 2016 March 14–18; Baltimore, Maryland. Abstract ID: BAPS.2016.MAR.H1.4.
- [55] M. C. Shapiro, Patrik Hlobil, A. T. Hristov, Akash V. Maharaj, and I. R. Fisher, *Phys. Rev. B* **92**, 235147 (2015).

- [56] M. C. Shapiro, A. T. Hristov, J. C. Palmstrom, Jiun-Haw Chu, and I. R. Fisher, arXiv:1603.03537 (2016). *Accepted for Publication in Review of Scientific Instruments*.
- [57] Scott C. Riggs, M. C. Shapiro, Akash V. Maharaj, S. Raghu, E. D. Bauer, R. E. Baumbach, P. Giraldo-Gallo, Mark Wartenbe, and I. R. Fisher, *Nature Comm.* **6**, 6425 (2015).
- [58] Hsueh-Hui Kuo, Maxwell C. Shapiro, Scott C. Riggs, and Ian R. Fisher, *Phys. Rev. B* **88**, 085113 (2013).
- [59] Patrik Hlobil, Akash V. Maharaj, Pavan Hosur, M. C. Shapiro, I. R. Fisher, and S. Raghu, *Phys. Rev. B* **92**, 035148 (2015).
- [60] Y. Sun, S. Thompson, and T. Nishida, *Strain Effect in Semiconductors: Theory and Device Applications* (Springer, New York, 2010).
- [61] Jiun-Haw Chu, Hsueh-Hui Kuo, James G. Analytis, and Ian R. Fisher, *Science* **337**, 710 (2012).
- [62] Hsueh-Hui Kuo and Ian R. Fisher, *Phys. Rev. Lett.* **112**, 227001 (2014).
- [63] M. D. Watson, T. K. Kim, A. A. Haghighirad, N. R. Davies, A. McCollam, A. Narayanan, S. F. Blake, Y. L. Chen, S. Ghannadzadeh, A. J. Schofield, M. Hoesch, C. Meingast, T. Wolf, and A. I. Coldea, *Phys. Rev. B* **91**, 155106 (2015).
- [64] L. Onsager, *Phys. Rev.* **38**, 2265 (1931).
- [65] See, for example, R. Fernandes, A. Chubukov, and J. Schmalian, *Nature Phys.* **10**, 97 (2014).
- [66] G. F. Koster, *Solid State Phys.* **5**, 173 (1957).
- [67] G. F. Koster, J. O. Dimmock, R. G. Wheeler, and H. Statz, *Properties of the Thirty-Two Point Groups* (MIT Press, Cambridge, Massachusetts, 1963).

- [68] Robert S. Mulliken, *Phys. Rev.* **43**, 279 (1933).
- [69] International Commission, *J. Chem. Phys.* **23**, 1997 (1955).
- [70] Hsueh-Hui Kuo, Jiun-Haw Chu, Johanna C. Palmstrom, Steven A. Kivelson, and Ian R. Fisher, *Science* **352**, 6288, p.958 (2016).
- [71] M. A. Tanatar, A. E. Böhmer, E. I. Timmons, M. Schütt, G. Drachuck, V. Taufour, S. L. Bud'ko, P. C. Canfield, R. M. Fernandes, R. Prozorov, arXiv:1511.04757 (2015).
- [72] M. Shayegan, K. Karrai, Y. P. Shkolnikov, K. Vakili, E. P. De Poortere, and S. Manus, *Appl. Phys. Lett.* **83**, 5235 (2003).
- [73] D. Butkovičová, X. Marti, V. Saidl, E. Schmoranzzerová-Rozkotová, P. Wadley, V. Holý, and P. Němec, *Rev. Sci. Instrum.* **84**, 103902 (2013).
- [74] A. M. Simpson and W. Wolfs, *Rev. Sci. Instrum.* **58**, 2193 (1987).
- [75] Touloukian, Y. S., Kirby, R. K., Taylor R. E., and Desai, P. D., eds., Thermophysical Properties of Matter: The TPRC Data Series, Vol. 12, *Thermal Expansion: Metallic Elements and Alloys*, Plenum, NY (1975) p. 298–299.
- [76] S. L. Bud'ko, N. Ni, S. Nandi, G. M. Schmiedeshoff, and P. C. Canfield, *Phys. Rev. B* **79**, 054525 (2009).
- [77] Physik Instrumente GmbH, “Piezo Material Data”.
- [78] Clifford W. Hicks, Mark E. Barber, Stephen D. Edkins, Daniel O. Brodsky, and Andrew P. Mackenzie, *Rev. Sci. Instrum.* **85**, 065003 (2014).
- [79] A. S. Sefat, R. Jin, M. A. McGuire, B. C. Sales, D. J. Singh, and D. Mandrus, *Appl. Phys. Lett.* **101**, 117004 (2008).
- [80] J.-H. Chu, J. G. Analytis, C. Kucharczyk, and I. R. Fisher, *Phys. Rev. B* **79**, 014506 (2009).

- [81] Haoran Man, Xingye Lu, Justin S. Chen, Rui Zhang, Wenliang Zhang, Huiqian Luo, J. Kulda, A. Ivanov, T. Keller, Emilia Morosan, Qimiao Si, and Pengcheng Dai, *Phys. Rev. B* **92**, 134521 (2015).
- [82] Hsueh-Hui Kuo, “Electronic Nematicity in Iron-Based Superconductors”, Ph.D. Thesis, Stanford University (2014).
- [83] C. M. Varma and Lijun Zhu, *Phys. Rev. Lett.* **96**, 036405 (2006).
- [84] Tanmoy Das, *Phys. Rev. B* **89**, 045135 (2014).
- [85] K. Haule and G. Kotliar, *Euro. Phys. Lett.* **89**, 57006 (2010).
- [86] P. Chandra, P. Coleman, J. A. Mydosh, and V. Tripathi, *Nature* **417**, 831 (2002).
- [87] S. Elgazzar, J. Ruzs, M. Amft, P. M. Oppeneer, and J. A. Mydosh, *Nature Mater.* **8**, 337 (2009).
- [88] H.-H. Kuo, J.-H. Chu, Scott C. Riggs, L. Yu, P. L. McMahon, K. De Greve, Y. Yamamoto, J. G. Analytis, and I. R. Fisher, *Phys. Rev. B* **84**, 054540 (2011).
- [89] K. R. Shirer, J. T. Haraldsen, A. P. Dioguardi, J. Crocker, N. apRoberts-Warren, A. C. Shockley, C.-H. Lin, D. M. Nisson, J. C. Cooley, M. Janoschek, K. Huang, N. Kanchanavatee, M. B. Maple, M. J. Graf, A. V. Balatsky, and N. J. Curro, *Phys. Rev. B* **88**, 094436 (2013).
- [90] R. E. Baumbach, Z. Fisk, F. Ronning, R. Movshovich, J. D. Thompson, and E. D. Bauer, *Philos. Mag.* **94**, 3663 (2014).
- [91] Michael E. Fisher and J. S. Langer, *Phys. Rev. Lett.* **20**, 665 (1968).
- [92] L. R. Testardi, *Phys. Rev. B* **12**, 3849 (1975).
- [93] H. Ohkuni, Y. Inada, Y. Tokiwa, K. Sakurai, R. Settai, T. Honma, Y. Haga, E. Yamamoto, Y. Ōnuki, H. Yamagami, S. Takahashi and T. Yanagisawa, *Philos. Mag. B* **79**, 1045 (1999).

- [94] K. Behnia, R. Bel, Y. Kasahara, Y. Nakajima, H. Jin, H. Aubin, K. Izawa, Y. Matsuda, J. Flouquet, Y. Haga, Y. Ōnuki, and P. Lejay, *Phys. Rev. Lett.* **94**, 156405 (2005).
- [95] R. Escudero, F. Morales, and P. Lejay, *Phys. Rev. B* **49**, 15271 (1994).
- [96] D. A. Bonn, J. D. Garrett, and T. Timusk, *Phys. Rev. Lett.* **61**, 1305 (1988).
- [97] A. Villaume, F. Bourdarot, E. Hassinger, S. Raymond, V. Taufour, D. Aoki, and J. Flouquet, *Phys. Rev. B* **78**, 012504 (2008).
- [98] B. Wolf, W. Sixl, R. Graf, D. Finsterbusch, G. Bruls, B. Lüthi, E. A. Knetsch, A. A. Menovsky, and J. A. Mydosh, *J. Low Temp. Phys.* **94**, 307 (1994).
- [99] T. Yanagisawa, H. Saito, Y. Watanabe, Y. Shimizu, H. Hidaka, and H. Amit-suka, *J. Phys.: Conf. Ser.* **391**, 012079 (2012).
- [100] R. M. Fernandes, A. V. Chubukov, J. Knolle, I. Eremin, and J. Schmalian, *Phys. Rev. B* **85**, 024534 (2012).
- [101] Settling the Chicken and Egg question in iron based superconductors. *Journal Club for Condensed Matter Physics*. <http://www.condmatjournalclub.org/?p=2247>
- [102] Frederic Bourdarot, Nicolas Martin, Stephane Raymond, Louis-Pierre Regnault, Dai Aoki, Valentin Taufour, and Jacques Flouquet, *Phys. Rev. B* **84**, 184430 (2011).
- [103] Arthur Ballato, “Poisson’s Ratio for Tetragonal Crystals”. Army Research Laboratory, doi:10.1109/58.484463 (1995).
- [104] G. Sobotta, *J. Phys. C: Solid State Phys.* **18**, 2065 (1985).
- [105] S. Tonegawa, Y. Tsuruhara, Y. Matsuda, Y. Haga, T. D. Matsuda, E. Yamamoto, Y. Onuki, and T. Shibauchi (unpublished).

- [106] M. Yokoyama, H. Amitsuka, K. Tenya, K. Watanabe, S. Kawarazaki, H. Yoshizawa, and J. A. Mydosh, *Phys. Rev. B* **72**, 214419 (2005).
- [107] G. W. Scheerer, W. Knafo, D. Aoki, M. Nardone, A. Zitouni, J. Béard, J. Billette, J. Barata, C. Jaudet, M. Suleiman, P. Frings, L. Drigo, A. Audouard, T. D. Matsuda, A. Pourret, G. Knebel, and J. Flouquet, *Phys. Rev. B* **89**, 165107 (2014).
- [108] Tatsuya Yanagisawa, *Phil. Mag.*, **94**, 3775 (2014).
- [109] J. Buhot, M.-A. Méasson, Y. Gallais, M. Cazayous, A. Sacuto, G. Lapertot, and D. Aoki, *Phys. Rev. Lett.* **113**, 266405 (2014).
- [110] H.-H. Kung, R. E. Baumbach, E. D. Bauer, V. K. Thorsmølle, W.-L. Zhang, K. Haule, J. A. Mydosh, and G. Blumberg, *Science* **347**, 6228, p.1339 (2015).